An Advanced Three-Dimensional Simulation System for Safety Analysis of Gas Cooled Reactors

Von der Fakultät 4: Energie-, Verfahrens- und Biotechnik der Universität Stuttgart

zur Erlangung der Würde eines Doktors der Ingenieurwissenschaften (Dr.-Ing.) genehmigte Abhandlung

vorgelegt von

Janis Lapins

geboren in Grambach

Hauptberichter:	Prof. Dr.-Ing. habil. Eckart Laurien
Mitberichter:	Prof. Dr. rer. nat. Andreas Pautz

Tag der mündlichen Prüfung: 11. Mai 2015

Institut für Kernenergetik und Energiesysteme der Universität Stuttgart, 2016

This work is dedicated to

my grandmother Maria Theresia Lapins,

and my mother Dr. Gisela Lapins.

“In the beginning there was nothing which exploded!”

(Terry Pratchett)

“There is a theory which states that if ever anyone discovers exactly what the Universe is for and why it is here, it will instantly disappear and be replaced by something even more bizarre and inexplicable.

There is another theory which states that this has already happened”

(Douglas Adams)

Abstract

High temperature reactors are helium-cooled reactors which consist largely of graphite, both fuel elements (pebbles) and the main structure material. It uses a special fuel element made of graphite in which the uranium dioxide in three-fold coated particles is homogeneously dispersed in a graphite matrix. The coatings – especially the silicon carbide layer – create an effective barrier against fission product diffusion. The HTR, in modular design, is laid out that the maximum allowable fuel temperature of 1620°C is never exceeded in any possible accident without actuation of active components and it can solely shutdown the reactor via negative temperature feedback effects. The methods to predict processes in such nuclear plants were mainly developed until the 1990's – the end of operation of the AVR in Germany. Owing to the computational capabilities at the time, only 2-D tools were available for coupled transient analysis.

Since then, computational power increased massively; also end of last century the favourable characteristics lead to re-newed interest in the technology and development. Hence, a logical next step was to develop new or enhance existing programmes in such a way that coupled three-dimensional time-dependent analysis for neutronics and thermal fluid dynamic is enabled.

The neutron transport programme TORT-TD that solves the neutron transport equation in discrete ordinates for stationary as well as transient problems is used for neutronics calculations. The transient solution of the neutron transport equation is performed by making use of a time-dependent neutron source, xenon/iodine dynamics are implemented as well. TORT-TD was validated for light water reactors, and is coupled to HTR thermal hydraulics. For that purpose the variation parameters for the cross section evaluation had to be modified since there are different variation parameters.

The thermal fluid dynamic programme ATTICA^{3D} applies the porous medium approach for flow in packed beds according to Ergun (dominance of friction). This approach uses a quasi-steady state formulation for the momentum equation while time dependent formulations are employed for mass conservation, and energy conservation for both, the solid and gaseous phase. For spatial discretisation of the conservation equations, the finite volume method is used. For material properties, gas densities, heat transfer etc. a set of constitutive equations completes the set of differential equations. Time integration in ATTICA^{3D} is realised applying a modified Newton-Raphson method which linearizes and subsequently solves the set of equations. ATTICA^{3D} can automatically adapt the time step width within user specified limits. Within this work, the mass and

energy conservation equations are modified so that chemical reactions as consequence of water or air ingress can be simulated, i.e. mass sources for CO, CO_2, H_2 and sinks for H_2O and O_2 or heat sources and enthalpy transport. The heat generated by chemical reaction is either added to the solid or the gaseous phase. The corrosion rates were implemented according to experimental findings for fuel and reflector graphite. Steam or air might enter the primary circuit through a break in the steam generator or an opening of the primary circuit. Steam entering the core region will moderate neutrons, reduce the leakage and thereby increase power. The corrosion was validated for the NACOK experiment performed within the RAPHAEL project where temperature evolution under corrosion and total burn-off had to be simulated simultaneously.

The two programmes - TORT-TD and ATTICA^{3D} - exchange data (power distributions or fuel and moderator temperature distribution, possibly hydrogen distribution) by means of a common interface that interpolates values that are exchanged on mutual computational grids by volumetric averaging. As verification for the proper operation of the interface, the steady state of the transient PBMR-400 benchmark was used. After obtaining a coupled steady state, the transient exercises are performed to test the proper working of the interface in time dependent cases. Here, the cold helium ingress, the total control rod withdrawal case and the total control rod ejection case were simulated and compared to results of other partakers of the benchmark. Also, the coupled system was validated for a full power temperature distribution experiment in the Chinese experimental reactor HTR-10 where good agreement could be reached with the measurements.

The coupled HTR simulation system TORT-TD/ATTICA^{3D} was then applied for single control rod ejection cases for both the PBMR-400 and the HTR-PM. These cases require a 180° model of the reactor. As preparatory works, the control rod cross sections were adjusted to yield the same reactivity increase as the grey curtain model for the PBMR and with MCNP5 for the HTR-PM. Since there are strong shielding effects by neighbouring rods, the power increase was moderate due to strong Doppler and moderator feedbacks. For the HTR-PM, coupled calculations for water ingress cases are simulated. This also tested the whole computational sequence, i.e. steam transport into the core by ATTICA^{3D}, then transfer of hydrogen densities (from hydrogen or from steam) to TORT-TD via the interface, interpolation of the macroscopic cross sections which changes the power density, and the feedback to ATTICA^{3D}. Additionally, an anticipated transient without scram is simulated where shutdown of the reactor is achieved by the temperature feedback effects. For both, the design basis accident and the anticipated transient without scram, the power increases – lacking experimental results – were compared to published results produced with the TINTE code and are,

again, in good agreement. As a demonstration case, a three dimensional water ingress case is presented.

Key words: High temperature reactor, transient three-dimensional analysis, thermal fluid dynamics, neutronics, simulation system, safety analysis, accident analysis, coupled analysis, neutron transport, porous medium, TORT-TD, ATTICA^{3D}, single rod ejection, PBMR, HTR-10, HTR-PM.0

Kurzfassung

Hochtemperaturreaktoren (HTR) sind heliumgekühlte Reaktoren, die größtenteils aus Graphit bestehen, sowohl die Brennelemente als auch die hauptsächlichen Strukturmaterialien. Es wird ein spezielles Brennelement verwendet, bestehend aus Graphit, in dem das Urandioxid in dreifach umhüllten Partikeln (sog. "coated particles“) homogen in einer Graphitmatrix verteilt ist. Die Umhüllungen, insbesondere die Silikonkarbidschicht, bildet eine effektive Barriere gegen Spaltproduktdiffusion. Der HTR in modularem Design ist so ausgelegt, dass die maximale zulässige Brennstofftemperatur von 1620°C in sämtlichen zu unterstellenden Unfällen auch ohne Verwendung von aktiven Komponenten nie überschritten wird und sich der Reaktor allein über seine negativen Rückwirkungseffekt der Brennstofftemperatur selbst abschalten kann. Die Methoden um Vorgänge in derlei Kernkraftwerken vorherzusagen wurden hauptsächlich bis Anfang der 90er des Jahre letzten Jahrtausends entwickelt – dem Ende des Betriebs des AVR in Deutschland.

Seit dieser Zeit nahm die Rechenleistung dramatisch zu. Seine günstigen Eigenschaften führten auch zu erneutem Interesse an dieser Technologie und ihrer Weiterentwicklung Ende der 90er des letzten Jahrtausends. Folglich war ein logischer nächster Schritt neue Programme zu entwickeln bzw. bestehende so zu verbessern, dass gekoppelte dreidimensionale zeitabhängige Neutronik/Thermofluiddynamikanalysen ermöglicht werden.

Das Neutronentransportprogramm TORT-TD, das die Neutronentransportgleichung in diskreten Ordinaten für stationäre als auch für transiente Problemstellungen löst, findet für die Neutronikberechnungen Verwendung. Die zeitabhängige Lösung der Transportgleichung wird durch die Verwendung einer zeitabhängigen Neutronenquelle bewerkstelligt, die Jod/Xenon-Dynamik ist ebenfalls implementiert. TORT-TD wurde bereits für Problemstellungen in Leichtwasserreaktoren validiert und wird nun an HTR-Thermofluiddynamik gekoppelt. Zu diesem Zweck mussten auch die Parameter zur Wirkungsquerschnittsvariation verändert werden, da der HTR andere Abhängigkeiten aufweist.

Das Thermofluiddynamikprogramm ATTICA^{3D} verwendet den Ansatz des porösen Mediums nach Ergun zur Beschreibung von Strömungen in Schüttungsbetten (reibungsdominiertes Problem). Dieser Ansatz verwendet eine quasi-stationäre Formulierung der Impulsgleichung während zeitabhängige Gleichungen zur Beschreibung der Massenerhaltungsgleichungen sowie der Energieerhaltungsgleichungen sowohl für Feststoff-

als auch für die Gasphase Anwendung finden. Zur räumlichen Diskretisierung der Erhaltungsgleichungen wurde die Finite-Volumen-Methode gewählt. Zur Schließung des Differentialgleichungssystems wird für Materialeigenschaften, Gasdichten, Wärmeübergang usw. ein Satz konstitutiver Gleichung verwendet. Die zeitliche Integration in ATTICA^{3D} wurde durch Anwendung einer modifizierten Newton-Raphson-Methode bewerkstelligt, die das Gleichungssystem erst linearisiert und anschließend löst. ATTICA^{3D} kann seine Zeitschrittweiten selbstständig im Rahmen eines vom Benutzer vorgegebenen Bereichs anpassen. In dieser Arbeit wurden unter anderem die Massen- und Energieerhaltungsgleichungen derart angepasst, dass chemische Reaktionen als Folgen eines unterstellten Wasser- oder Lufteinbruchs simuliert werden können. Das heißt es wurden Massenquellterme für CO, CO_2 und H_2 und –senkenterme für H_2O und O_2 sowie der Enthalpietransport eingeführt. Die bei der chemischen Reaktion erzeugte oder abgeführte Wärme wird dabei entweder der Gas- oder der Feststoffphase zugeschlagen. Die Korrosionsraten wurden anhand experimentell abgeleiteter Erkenntnissen implementiert. Dampf oder Luft könnten durch Bruch einer Dampferzeugerwendel oder durch eine Öffnung in den Primärkreis eindringen. Dampf, der in den Kern eintritt, wird Neutronen moderieren, die Leckage verringern und dadurch zu einer Leistungserhöhung führen. Die Korrosion wurde mithilfe des NACOK-Experimentes, das im Rahmen des RAPHAEL-Projekts stattfand, validiert, wobei die Temperaturentwicklung sowie der Graphitabbrand gleichzeitig simuliert wurden.

Die zwei Programme – TORT-TD und ATTICA^{3D} – tauschen Daten (Leistungsverteilung oder Brennstoff- und Moderatortemperaturen, möglicherweise auch Wasserstoffdichten) über eine gemeinsame Schnittstelle aus, die die Werte auf die jeweilig zugrundeliegenden Rechengitter mithilfe volumetrischer Mittelung interpoliert. Zur Verifikation der Arbeitsweise der Schnittstelle wurde der stationäre Zustand des transienten PBMR-400 Benchmarks verwendet. Nach der Lösung für den gekoppelten stationären Zustand, wurden verschiedene Übungen (d. h. Unfall-/Störfallszenarien) gelöst um auch die korrekte Arbeitsweise der Schnittstelle in zeitabhängigen Problemstellungen zu testen. Dabei wurden ein Eintritt kalten Heliums, ein vollständiger Auszug und ein vollständiger Auswurf der Steuerstäbe simuliert und mit den Ergebnissen anderer Benchmarkteilnehmer verglichen. Zusätzlich wurde das gekoppelte System anhand eines Temperaturverteilungsexperimentes unter Volllast des chinesischen Experimentalreaktors HTR-10 validiert, wobei gute Übereinstimmungen mit den Messungen erzielt wurden.

Das gekoppelte HTR-Simulationssystem TORT-TD/ATTICA^{3D} wurde nun zu Anwendungsrechnungen für Einzelstabauswurfstransienten sowohl für den PBMR-400 als auch den HTR-PM verwendet. Diese Problemstellungen benötigen ein 180°-Modell des

Reaktors. Vorbereitende Arbeiten waren hierbei die Anpassung Wirkungsquerschnitte der Steuerstäbe, die so eingestellt wurden, dass für den Fall des PBMR-400 Reaktivitätszunahme wie in der Modellierung mit ‚verschmierten Steuerstäben' (‚grey curtain') erreicht wurde. Für den HTR-PM wurde die Anpassung mithilfe von mit MCNP5 erzeugten Ergebnissen vorgenommen. Da sich die benachbarten Steuerstäbe stark abschatten, fällt die Leistungszunahme durch starke Rückwirkungen der Brennstoff- und Moderatortemperatur moderat aus. Für das HTR-PM Konzept wurden gekoppelte Berechnungen für Wassereinbruchsfälle angestellt. Somit konnte auch die ganze Rechensequenz, d.h. der Transport des Dampfes bis in den Kern hinein, das von ATTICA^{3D} simuliert wird, dann die Übergabe der Wasserstoffdichten (im Wasserstoff oder Dampf) über die Schnittstelle an TORT-TD, die Interpolation der makroskopischen Wirkungsquerschnitte dadurch bedingte Leistungsänderung sowie die Rückwirkung auf ATTICA^{3D} getestet werden. Zusätzlich wird ein Wassereinbruch ohne Scram (‚anticipated transient without scram') simuliert, in dem sich der Reaktor lediglich über die Temperaturrückwirkungen selbst abschaltet. Sowohl für den Auslegungsstörfall als auch für den Fall ohne Scram-Signal wurden die Simulationsergebnisse, mangels experimenteller Daten, mit publizierten Ergebnissen, die mit dem TINTE-Programm erstellt wurden, verglichen, und stimmen gut überein. Als Demonstrationsfall wird auch für eine kurze Simulationsdauer ein dreidimensionaler Wassereinbruchsfall präsentiert.

Schlagworte: Hochtemperaturreaktor, transiente dreidimensionale Analysen, Thermofluiddynamik, Neutronik, Simulationssystem, Sicherheitsanalyse, Unfallanalyse, gekoppelte Analysen, Neutronentransport, poröses Medium, TORT-TD, ATTICA^{3D}, Einzelstabauswurf, PBMR, HTR-10, HTR-PM.

Table of content

List of Figures

List of Tables

Nomenclature

Abbreviations

AVR	Arbeitsgemeinschaft Versuchsreaktor (Consortium Experimental Reactor, German experimental high temperature reactor, 46 MW_{th})
eV	Electron Volt, unit of the charge of one electron, measure for energy, 1 eV = 1.6022 x 10^{-19} J
FSV	Fort Saint Vrain reactor, (US block-type high temperature reactor, 342 MW_{th})
H	Hydrogen
HTGR	High Temperature Gas-Cooled Reactor
HTR	High Temperature Reactor
HTR-PM	High Temperature Reactor Pebble Modular (Chinese HTR, 250 MW_{th})
HTR-10	Chinese experimental High Temperature Reactor, 10 MW_{th}
Np	Neptunium
MeV	Mega Electron Volt, 1 MeV = 1 x 10^{6} eV = 1.6022 x 10^{-13} J
MW	Megawatt = 10^{6} Watts
PBMR	Pebble Bed Modular Reactor (South African HTR concept, 400 MW_{th})
Pu	Plutonium
Th	Thorium
THTR	Thorium High Temperature Reactor (German pebble bed reactor, 308 MW_{th})
U	Uranium

Latin Symbols

A	$\left[m^2\right]$	surface area
c_p	$\left[J/(kgK)\right]$	specific heat capacity
$c_{p,0}$	$\left[J/(kg \cdot K)\right]$	gas mixture heat capacity with k components

$c_{p,g}$	$[J/(kg \cdot K)]$	gas mixture heat capacity with k components
$c_{p,k}$	$[J/(kg \cdot K)]$	specific heat capacity of the gas component k
c_i	$[-]$	precursor concentration of group i
$c_i^{(n)}$	$[-]$	precursor concentration of group i at time step n
$c_i^{(n+1)}$	$[-]$	precursor concentration of group i at time step $n+1$
c_k	$[-]$	mass fraction of gas component k
C_k	$[mol/m^3]$	absolute concentration of gas component k
d	$[m]$	pebble diameter
d_h	$[m]$	hydraulic diameter
D	$[m]$	core diameter
e_g	$[J]$	energy transported in the gas phase
E	$[eV]$	neutron energy
E_a	$[J/mol]$	activation energy
F	$[-]$	reaction rate
h	$[J/kg]$	specific enthalpy
h_s	$[J/kg]$	enthalpy of the solid
h_T	$[J/kg]$	temperature dependent enthalpy
h_p	$[J/kg]$	pressure dependent enthalpy
ΔH	$[J/mol]$	chemical reaction enthalpy
k_{eff}	$[-]$	neutron multiplication factor
m	$[kg]$	mass
m_A	$[kg]$	atomic mass
$\dot{m}$	$[kg/s]$	mass flow of helium
$\dot{m}_{CO}$	$[kg/s]$	mass change rate of carbon monoxide

$\dot{m}_{CO_2}$	$[kg/s]$	mass change rate of carbon dioxide
$\dot{m}_{Graphite}$	$[kg/s]$	mass change rate of graphite
$\dot{m}_{H_2}$	$[kg/s]$	mass change rate of hydrogen
$\dot{m}_{H_2O}$	$[kg/s]$	mass change rate of steam
$\dot{m}_k^n$	$[kg/s]$	mass change rate of component k in reaction type n
$\dot{m}_{O_2}$	$[kg/s]$	mass change rate of oxygen
M	$[-]$	Maxwell-Boltzmann distribution
M_C	$[kg/mol]$	molar mass of carbon
M_{CO}	$[kg/mol]$	molar mass of carbon monoxide
M_{CO_2}	$[kg/mol]$	molar mass of carbon dioxide
M_{H_2}	$[kg/mol]$	molar mass of hydrogen
M_{H_2O}	$[kg/mol]$	molar mass of steam
M_{O_2}	$[kg/mol]$	molar mass of oxygen
n	$[1/s]$	neutron density
n_c	$[-]$	total number of components
n_{reac}	$[-]$	number of different chemical reactions
$\dot{n}_{CO}$	$[mol/(s \cdot m^3)]$	molar change rate of carbon monoxide
$\dot{n}_{CO_2}$	$[mol/(s \cdot m^3)]$	molar change rate of carbon dioxide
$\dot{n}_{CO}$	$[mol/(s \cdot m^3)]$	molar change rate of carbon monoxide
$\dot{n}_{H_2}$	$[mol/(s \cdot m^3)]$	molar change rate of hydrogen
$\dot{n}_{H_2O}$	$[mol/(s \cdot m^3)]$	molar change rate of steam
N	$[10^{24}/cm^3]$	nuclide density
Nu	$[-]$	Nusselt number

p	$[Pa]$	pressure
p_{educt}	$[Pa]$	partial pressure of the educt
p_k	$[Pa]$	partial pressure of gas component k
p_{CO_2}	$[Pa]$	carbon dioxide partial pressure
p_{H_2}	$[Pa]$	hydrogen partial pressure
p_{H_2O}	$[Pa]$	steam partial pressure
$p_{product}$	$[Pa]$	partial pressure of the product
Pr	$[-]$	Prandtl number
r	$[m]$	radius
Re	$[-]$	Reynolds number
R_k	$[J/(kg \cdot K)]$	specific gas constant of component k
$RR_{Graphite}$	$[kg/(m^2 s)]$	reaction rate of graphite
S	$[s^{-1}]$	external neutron source
S_g	$[s^{-1}]$	external neutron source per energy group
Δt	$[s]$	time step size
$\Delta t_{\max}$	$[s]$	maximum time step size
T	$[K]$	temperature
T_f	$[K]$	fuel temperature
T_m	$[K]$	moderator temperature
T_r	$[K]$	reflector temperature
u	$[m/s]$	velocity of the fluid
$u_{\sup}$	$[m/s]$	superficial velocity
V	$[m^3]$	volume
V_{gas}	$[m^3]$	volume of the gas phase

V_{solid}	$[m^3]$	volume of the solid phase
V_{total}	$[m^3]$	volume of the solid and the gas phase
$Q_{chem,k}$	$[W/m^3]$	heat source/sink by chemical reaction of gas species k
Q_{conv}	$[W/m^3]$	heat removed by convection
$Q_{nuclear}$	$[W/m^3]$	heat source generated by fission

Greek Symbols

α	$[W/(m^2 \cdot K)]$	heat transfer coefficient
β	$[-]$	delayed neutron fraction
Γ	$[K^{-1}]$	temperature feedback coefficient
ε	$[-]$	porosity
ε_{rad}	$[-]$	emissivity
ϕ	$[(m^2 \cdot s)^{-1}]$	scalar neutron flux
Φ	$[-]$	dependent variable in the conservation equation
κ_g	$[m^2]$	permeability
λ	$[W/(m \cdot K)]$	heat conductivity
λ_{eff}	$[W/(m \cdot K)]$	effective heat conductivity
λ_i	$[s^{-1}]$	decay constant of precursor group
λ_p	$[-]$	pressure drop coefficient
η	$[kg/(m \cdot s)]$	dynamic viscosity
μ_g	$[m]$	passability
ν	$[-]$	average number of neutrons born in fission
ν_g	$[m^2/s]$	kinematic viscosity of the gas (mixture)
ρ	$[kg/m^3]$	density

ρ_g	$\left[kg/m^3\right]$	density of the gas mixture
ρ_s	$\left[kg/m^3\right]$	density of the solid
ρ_k	$\left[kg/m^3\right]$	density of the gas component k
ρ_r	$[-]$	reactivity
Ψ	$\left[\left(m^2 \cdot s\right)^{-1}\right]$	angular neutron flux
Ψ_f	$[-]$	friction coefficient
$\Psi^{(n)}$	$\left[\left(m^2 \cdot s\right)^{-1}\right]$	angular neutron flux at time step n
$\Psi^{(n)}$	$\left[\left(m^2 \cdot s\right)^{-1}\right]$	angular neutron flux at time step $n+1$
Ψ_{Prod}	$[-]$	production ratio of moles of $\frac{CO}{CO_2}$
σ_{SB}	$\left[W/\left(m^2 \cdot K^4\right)\right]$	Stefan-Boltzmann constant
σ	$\left[10^{-24} cm^2\right]$	microscopic cross section
σ_a	$\left[10^{-24} cm^2\right]$	microscopic absorption cross section
σ_f	$\left[10^{-24} cm^2\right]$	microscopic fission cross section
σ_{eff}	$\left[10^{-24} cm^2\right]$	effective microscopic fission cross section
σ_s	$\left[10^{-24} cm^2\right]$	microscopic scattering cross section
σ_t	$\left[10^{-24} cm^2\right]$	total microscopic cross section
σ_γ	$\left[10^{-24} cm^2\right]$	microscopic capture cross section
Σ_f	$\left[cm^{-1}\right]$	macroscopic fission cross section
$\Sigma_{f,g}$	$\left[cm^{-1}\right]$	macroscopic group wise fission cross section
$\Sigma_{gg'}$	$\left[cm^{-1}\right]$	macroscopic scatter cross section from group g' to g
Σ_s	$\left[cm^{-1}\right]$	macroscopic scatter cross section
Σ_t	$\left[cm^{-1}\right]$	total macroscopic cross section

$\Sigma_{t,g}$	$\left[cm^{-1}\right]$	total group wise macroscopic cross section
Σ_x	$\left[cm^{-1}\right]$	macroscopic cross section (x = a, f, s, t, γ)
Σ_{xeff}	$\left[cm^{-1}\right]$	effective macroscopic cross section (x = a, f, s, t, γ)
ω_g	$\left[s^{-1}\right]$	inverse spatially resolved reactor period of group g
Ω	$\left[sr\right]$	solid angle
χ_k	$\left[-\right]$	volume fraction of the gas component
χ_{prompt}	$\left[eV\right]$	prompt neutron spectrum
$\chi^i_{delayed}$	$\left[eV\right]$	delayed neutron spectrum of precursor group i
υ	$\left[cm/s\right]$	neutron velocity
υ_A	$\left[cm/s\right]$	nuclide velocity

Constants

$g = 9.81\frac{m}{s^2}$	gravitational constant
$k = 1.3806448 \cdot 10^{-23}\frac{m^2 kg}{s^2 \cdot K}$	Boltzmann constant
$N_A = 6.02214129 \cdot 10^{23}\frac{1}{mol}$	Avogadro's number
$R = 8.3144621\frac{J}{mol \cdot K}$	general gas constant
$\sigma_{SB} = 5.76 \cdot 10^{-8}\frac{W}{m^2 \cdot K^4}$	Stefan-Boltzmann constant
$\pi = 3.14159265$	Pi
$e = 2.71828182$	Euler's number

1 Introduction

1.1 Motivation

In 2012, there were 437 commercial power reactors producing electricity with a net power output of 372,572 MW_e, worldwide. This equals 12.3% of the world's overall electricity production and 5.1% of the total primary energy use of the world. In the Western world the nuclear share in electricity production is 25.7%, i.e. a significant amount of electricity production originates from nuclear energy that is considered part of the non-carbon emitting forms of energy. Another 68 reactors were under construction, most of them in Asia [1] [2]. After the Fukushima accident in March 2011, there was a halt for many nuclear projects worldwide, but only Germany decided for a final phase-out within the next ten years.

Most of the power reactors in operation are light water reactors (LWR). LWR use light water (H_2O) as coolant. These can be further subdivided into boiling water (BWR) and pressurised water reactors (PWR). Other commercial reactor types using different ways of moderation or coolant are the heavy water reactor (CANDU), the water cooled graphite moderated reactor (RBMK), the gas cooled reactors (MAGNOX, AGR (UK)), the liquid metal fast breeder reactors (LMFBR), and graphite moderated helium-cooled high temperature reactors (Fort St. Vrain Reactor FSV, decommissioned; Thorium High Temperature Reactor THTR, safe enclosure).

There are international efforts, namely the Generation IV International Forum (GIF) that proposed six future reactor types to be developed with respect to higher economics, safety and proliferation resistance [3]. These comprise three fast reactors: the sodium-cooled, the lead-cooled and the gas-cooled fast reactor. The three other reactor types are: the supercritical light water reactor (SCWR), the molten salt reactor (MSR) and the very high temperature reactor (VHTR), all of which with a thermal neutron spectrum.

The VHTR is a derivative of the high temperature reactor (HTR) that was developed in the 50s and 60s as graphite moderated helium-cooled high temperature reactor with a thermal neutron spectrum [4]. Test reactors like the block-type Peach-Bottom reactor [5] and the pebble-type AVR [6] (German: Arbeitsgemeinschaft Versuchsreaktor, English: consortium experimental reactor) were experimental reactors with only a small total power output, i.e. 100 MW_{th}/40MW_e and 46 MW_{th}/15MW_e. Nevertheless, there was useful experience about the fuel and the operation gained. Following these two exper-

imental reactors, the THTR-300 [7], a pebble type demonstration plant, and the block-type FSV reactor were built and operated [8][9]. Both used Uranium-235 (U) as fuel and thorium as breeding material to produce U-233 and both were facing operational problems, and for the THTR combined with political issues.

With erection of the first experimental reactors the programmes to predict the reactor behaviour were developed as well. Owing to the computational capabilities at the time, these applied simplified, i.e. one- or two-dimensional approaches for prediction of operational conditions, steady state and transient, as well as accident transients.

After the Three-Mile-Island reactor core meltdown accident, where the decay heat of the fission products destroyed large parts of the corium, there was a change of paradigm in the development of the HTRs. Instead of increasing the size and, hence the total power output of HTRs, the focus of development was shifted towards a self-acting decay heat removal system. This feature was an already proven concept for the AVR, but for reactors with a higher power density, active decay heat removal was required (THTR, FSV, and other concepts like the HHT-1130, or PNP [4]). In 1984, Siemens-Interatom introduced the concept of a modular high temperature power reactor that could fulfil this claim. This proposal also led to dramatic changes of the design criteria of an HTR [10] [11] [12]. The approach comprised a low power density, a small diameter to height ratio (unlike in LWRs where height to diameter ratio is ≈ 1) to provide the reactor core with a great surface for heat transport to the outside, and most important an integral design that could cope with a total loss of decay heat removal by active components. The only system that has to be available is the passive reactor cavity cooling system at ambient pressure that could remove the heat radiated from the reactor to the reactor cavity walls by natural convection of a water loop. The heat is transported to an air cooled heat exchanger. Also, this concept minimises the amount of nuclear grade components, and tries to employ as much proven conventional technology as possible. The HTR-Module 200 was already licensed in Germany, but never built. Nevertheless, from this concept on, the self-acting decay heat removal is now regarded state of the art for HTR development and was adopted ever since in all later HTR concepts.

In the middle of the 1990's, international efforts were being made to design license, build and finally operate the South African Pebble Bed Modular Reactor (PBMR). At the same time, two research reactors were put into operation; the Chinese pebble bed HTR-10 and the Japanese block-type High Temperature engineering Test Reactor (HTTR), both experimental facilities with small thermal power output (HTR-10: 10 MW_{th}; HTTR: 30 MW_{th}) to gain operational experience [13] [14] [15] [16].

In 2011, the Fukushima accident occurred as a consequence of an earthquake followed by a tsunami that destroyed the plant's emergency infrastructure. The shutdown procedure went as planned. Only when the waves flooded emergency diesel generators, the decay heat removal system was lost. This demonstrates the importance of actively removing decay heat from big power reactors.

The modular HTRs are laid out in such a way that active removing of decay heat is not necessary. Even in a case of depressurisation and a subsequent core heat-up accident, the specific fuel pebble with its dispersed coated particles that contain the uranium dioxide fuel will neither release fuel nor fission products. That necessitates that the power density has to be low (3 – 5 MW/m^3). With a low power density, the resulting decay heat will also be low. This together with a large graphite body that, like a sponge, can collect large portions of heat ensures that the decay cannot lead to inadmissibly high temperatures. A core melt accident as a consequence of loss of decay heat removal can be excluded.

This fact, along with economic benefits that first have to be proven by a prototype plant, might make it attractive to deploy the high temperature reactor technology in the future. The first double block plant is currently being built at the Rongcheng site in China [17]. Co-generation of electricity and heat for process engineering or district heating may help to increase the attractiveness of this technology.

2 State of the Art

The inherently safe modular high temperature gas cooled reactor concept was first introduced by SIEMENS-INTERATOM in 1988 as the HTR-MODULE 200 [10] [11] [12]. The concept of a high temperature reactor where gas is used as coolant is older. But it was due to the development of the modular gas-cooled reactor that safety features have significantly changed and safety could be enhanced.

A distinctive feature of the concept is that all components are standardized and there is only a small fraction of highly-reliable, high-cost nuclear grade components. In case of failure, everything except the reactor pressure vessel can be exchanged. During operation the reactor building is accessible at all times. The only restricted area during operation is the primary cavity.

Similar to the HTR-Module, the HTR-PM concept, a variation of the Module with a higher thermal power of 250 MW_{th} was introduced [17] and is currently being built in Rongcheng in China. Therefore, it is a concept at the brink of realization and will serve from here on as the reference reactor and is being described in the following [18].

2.1 General features of the High Temperature Reactor - Pebble Bed Modular

The HTR-PM is a reactor with a low average power density (≈ 3.2 MW/m^3) compared to commercial light water reactor systems (≈ 100 MW/m^3). Its total thermal output is only 250 MW. Assuming the efficiency to be around 42%, the electrical output is roughly 105 MW_{el}. The coolant of the primary circuit is helium, which enters the core at 250°C and is heated up to 750°C. The heat of the coolant is exchanged to a water/steam cycle via steam generator. The steam drives a steam turbine. But the strengths of the HTR-PM do not only lie in its electricity generating capacity, but rather in the possible coupling of heat and electricity generation (co-generation) together with very promising safety characteristics.

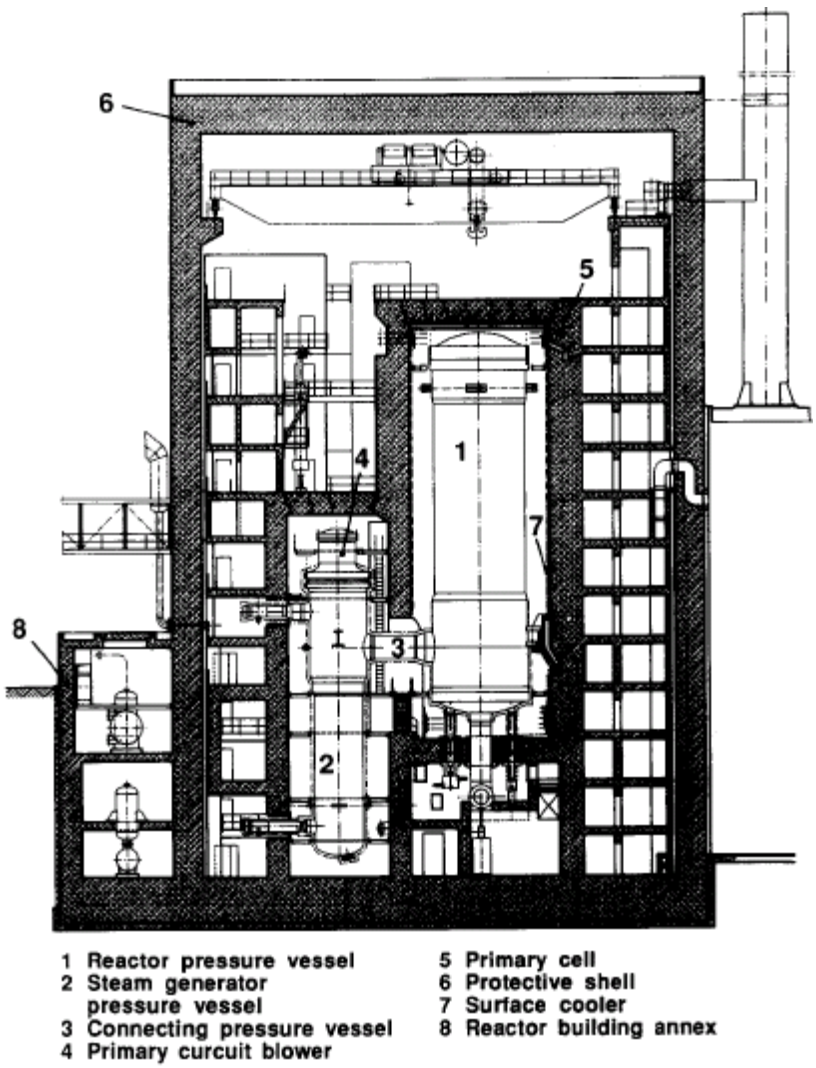

Figure 1: Cross section of the reactor building [11]

The reactor and the nuclear steam supplying system are arranged side by side, see Figure 1 .

The main features of the HTR-PM are:

- The inherent safety features, i.e. due to the interplay of the very low average power density (~3.22 MW/m^3), the great heat capacity and the resistance to heat of the reflector structure together with the good heat conduction characteristics the removal of decay heat solely by heat radiation and conduction is achieved. The design limit temperature is not exceeded. Hence, no significant radioactivity release is expected, even without any active measures. No active core cooling is needed for decay heat removal.
- The fuel elements are billiard ball sized graphite balls of 6 cm diameter. Fissionable material forms small coated particles which are able to retain virtually all fission products up to a temperature of 1620°C [19] [20] [21] [22].

- As fissile material, uranium oxide (UO_2) is used. Each fuel element contains about 7g of Uranium with an initial enrichment of 8.9 % of U-235 [17].
- The reactor core is designed that even in case of accident the critical temperature of 1620°C is not exceeded at any time. These temperatures can only be reached in case of a depressurisation accident. Simple graphite burning contains no risk of exceeding those temperatures since temperatures stay well below the design temperature of the coated particles [19] .
- Thanks to the great retention capabilities of the coated particles a pressure-tight containment known from the light water reactor technology can be omitted without reducing the safety margin for the environment [12] [23].
- The cooling gas, helium, is an inert gas, both chemically and neutron physically.
- All core internals surrounding the pebble bed are made of graphite. No temperature induced failure will occur at the design temperatures.
- The reactor shows a very “lethargic” behaviour with regards to power increase (Doppler Effect in Uranium-238 resonances). The reactor tends to withstand small power or reactivity increases.
- The reactor has eight control rods which are inserted into the side graphite reflector. For long term shutdown, additional absorber spheres of 10 mm diameter (so called Small Absorber Spheres, SAS) are dropped into boring holes inside the reflector. No control or shutdown units have to be inserted into the pebble bed at any time.
- The steam generator is located at the side the reactor pressure vessel (see fig.1), and lower than the reactor pressure vessel to achieve thermo hydraulic decoupling of heat source (reactor core) and heat sink (steam generator). Natural convection prevents hot gas with inadmissibly high temperatures from entering the steam generator.
- High efficiency thanks to both the high temperature difference of hot and cold coolant and due to superheating of the live steam.

2.2 The Primary Circuit

The HTR-PM consists of two modules: the reactor pressure vessel with its graphite internals and the pool-ball sized fuel elements (pebbles) as core, and the steam generator. For connecting the two modules, a coaxial gas duct is used as transfer passage

for the cold (outside) and hot gas (inside), respectively. In order to keep the cooling gas circulating, a one stage helium blower is mounted on top of the steam generator. The blower and steam generator are both placed in the steam generator-pressure vessel. The life steam is transferred to either a conventional steam turbine or is directly used to co-generate process heat or provide process steam for industrial applications. The reactor pressure vessel and the steam generator are both located in separate concrete cavity (primary cavity), each.

2.2.1 The Reactor Pressure Vessel Unit

The reactor pressure vessel is about 25 metres high and has a diameter of around 6 metres. The core with the fuel elements forms the centre of the reactor pressure vessel. It is filled with around 420,000 fuel spheres. The core cavity has a diameter of three meters and an average height of 11 metres. In the vicinity of the core only graphite is used as structural material. At the same time, the graphite serves as neutron reflector. The thickness of the side reflector is about 75 cm. The side reflector has several vertical boring holes. Close to the core, there are borings of about 15 cm of diameter for the eight control rods which are distributed azimuthally. Additionally, there are 22 smaller slot holes for the small absorber spheres that serve as long-term shutdown units. These borings are very close to the core in order to be as effective as possible for the neutron absorption. On the outer side of the reflector, the flow path for the cold helium is located. This helps to keep the non-graphitic structures like core barrel and reactor pressure vessel at low temperatures.

Above the core cavity there are several layers of graphite serving as top reflector and plenum for the cold gas that traverses the core. Therefore, a multitude of small borings penetrate the top reflector providing sufficient flow paths for the coolant. In the centre of the top reflector, there is a charging tube for reloading fuel elements during operation. Since the pebbles are fed into the core cavity through one central opening, the pebble bed forms a cone on the top.

The lower part of the core cavity forms a cone with a 30° angle. This is to guarantee that all fuel elements flow towards the discharging tube without blockage. Like the top reflector, the bottom reflector consists of several graphite layers. The bottom cone has many small borings that provide flow paths for the hot gas that leaves the core. The gas reaches the hot gas plenum where it is mixed and subsequently conveyed to the steam generator via the coaxial gas duct.

When fuel elements are discharged from the reactor, they will be conveyed to a burn-up measurement facility. There, the fuel element’s individual burn-up will be measured.

If the burn-up reaches the design burn-up the fuel element will be sorted out. If not, the fuel element will be recycled (into the core until design burn-up is reached).

Outside the reactor pressure vessel, there is a cavity cooling system. The first task of the cavity cooler is to assure that the concrete that forms the housing for the reactor does not overheat during normal operation. The second and utterly important task is to remove the decay heat in case of accident/incident or shutdown. As mentioned before, the reactor disposes its decay heat only through radiation as soon as the heat reaches the pressure vessel outside. The cooler consists of water pipes that are connected via metal plates. The water circulates on the basis of natural convection, but under accident conditions the heat to be removed increases (~300kW$_{nominal}$, 2 MW$_{accidental}$). This requires the introduction of a pump. The water temperature of this cooling system is ~50 °C.

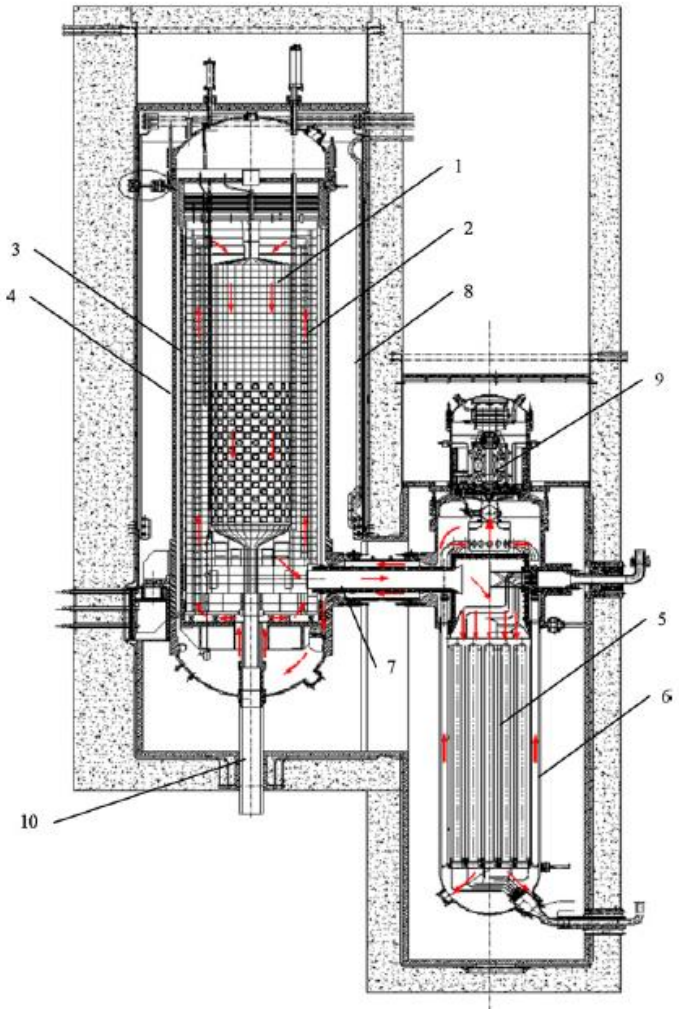

1. Reactor core
2. Side reflector and carbon shield
3. Core barrel
4. Reactor pressure vessel
5. Steam generator
6. Steam generator vessel
7. Coaxial gas duct
8. Water cooling panel (reactor cavity cooling system)
9. Helium blower
10. Fuel discharge tube

Figure 2: Cross section through the primary circuit of the Chinese HTR-PM [17], left the reactor pressure vessel with core internals and pebble bed, on the right: the steam generator with integrated blower.

2.2.2 Control and Shutdown

In order to control the reactor, neutron absorbing rods - the control rods - are used. The control rod is a cylindrical annulus consisting of several layers. Only one of several rings contains boron in form of boron carbide (B_4C). One borated layer of around 1.9 cm thickness is enough since thermal neutrons will not diffuse far into the rod whereas fast neutrons will not be influenced much, not even if the rods were solid [24].

The control rods have to be designed and laid out to override xenon absorption when operating in part load (100% - 40% - 100%). Under equilibrium conditions the rods are inserted to such depth that they release only ≈ 1.3 % of reactivity when all rods are ejected. Introducing ≈ 1.3 % of reactivity into the core was shown to be acceptable in terms of temperature and power of the coated particles.

The HTR-PM is designed with eight control rods and 24 shutdown units. The shutdown units are boring holes in which on demand small absorber spheres (SAS, 10 mm diameter) drop into the side reflector only by gravity. The shutdown units are necessary to keep the reactor sub-critical in a long-term state. In this case, reactivity increase due to temperature decrease of the fuel must be accounted for.

To restart the reactor after a long-term shutdown, the small absorber spheres are removed pneumatically from the reflector one after another, and subsequently conveyed to their storage containers. These containers are located above the top reflector.

2.2.3 The coaxial gas duct

In order to connect the reactor pressure vessel with the steam generator a coaxial gas duct is used. The cold gas flows in the outer annulus, the hot gas flows in counter-current in the inner cylinder. Directing the gas flows that way, the pressure boundary is not subjected to the high temperatures of the hot gas from the reactor.

2.2.4 The Steam Generator

After the hot gas duct, the hot gas is conducted to the steam generator where, after only one pass, the heat is transferred to the water/steam circuit. The helium flows between the steam generator tubes and heats up the water inside the latters.

2.2.5 Auxiliary Installations

In order to operate the HTR-PM, there are two important installations that will assure the reactor to remain operational. These installations are:

1. The fuel handling system

   The fuel handling system has to fulfil two main tasks: load and reload the fuel elements into the core, and also to measure the burn-up, since several core-passes of fuel elements are foreseen. After burn-up measurement, it is decided whether or not to recycle a fuel element.

2. The helium purification system

   The helium purification system is to ensure that the chemical impurities of the gas are kept below specified limits in order to protect fuel-elements, reactor components and metallic internals of the primary circuit. The gas purification system also fulfils the purpose of removing decay heat from the core, and removing ingressed water. For safety reasons, there are two helium purification facilities for each core, one for operation and the other in stand-by mode in order to compensate malfunction of the first system. Also, there is an emergency purification system that - in case needed - has a throughput of the whole primary circuit cooling inventory within one hour, effectively removing impurities or corrosion gases [25].

2.3 The Fuel Elements (Pebbles)

The reactor core nominal volume for an equilibrium core is approximately 77.8 m^3. It is filled with graphite balls (pebbles) of 60mm diameter each containing 7 g of uranium with an enrichment of 8.9 %. The distinctive feature of this fuel element type is that it already contains the moderator. The uranium dioxide is formed in small spherical particles inside a graphite moderator matrix. These particles of 0.5 mm diameter are coated by four layers, see Figure 3:

- a porous carbon buffer layer with a thickness of 0.095 mm, that will take up the fission products, especially fission gases,
- a pyrolitic carbon layer (PyC) with a thickness of 0.045 mm,
- a very dense silicon carbide layer (SiC), with a thickness of 0.035 mm. Various experiments showed that the SiC layer is capable of retaining fission products up to a temperature of 1,600 °C. After less than 1,000 hours of exposure at 1,600 °C, the SiC layer of the coated particle will start to lose its retaining capabilities (Palladium diffusion effect). Maximum fuel temperature during nominal

operation is set to 1,200 °C since caesium diffusion might reach the point of diffusion breakthrough after about 1,000 days (normal pebble lifetime inside the core),

- another PyC layer, with a thickness of 0.04mm.

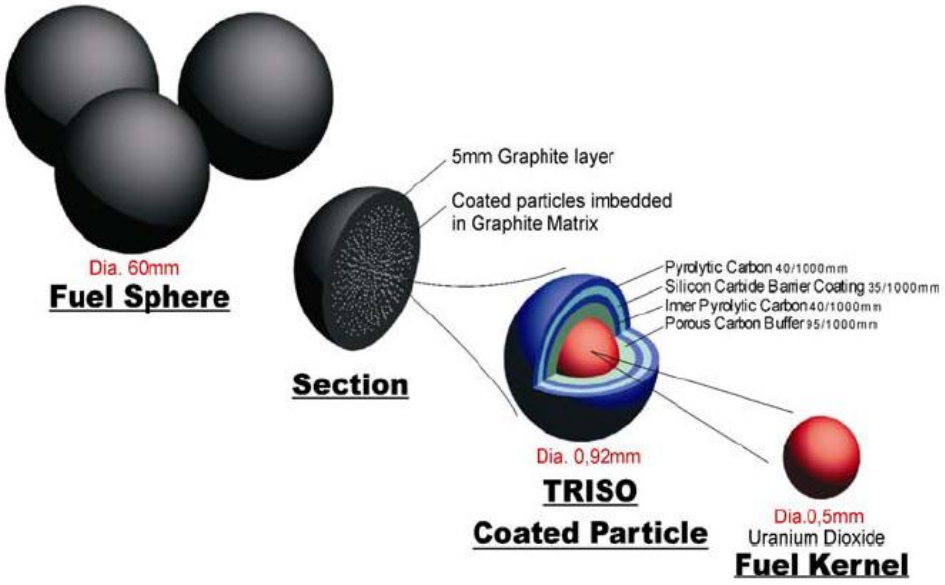

Figure 3: HTR fuel pebble with coated particles [26]

Each fuel pebble contains about 7g UO_2/ pebble leading to around 11,600 coated particles per pebble. The particles are homogeneously dispersed in a graphite matrix of 50 mm diameter coated by a 5 mm thick graphite shell containing no fuel particles. The reactor core is formed by a multitude of randomly distributed pebbles in the core cavity. The packing fraction of solid is 0.61, and hence, the void fraction is 0.39. Heat is mostly generated by fission of U-235 atoms and other fissile material (95 %), only a small part is generated by gamma heating of fission products and actinides. The generated nuclear heat is transported from the coated particle to the pebble surface by means of heat conduction. On the outside of the pebble the heat is transferred by convection and a complicated interplay of heat radiation between pebbles, and, between pebbles and gas, heat conduction. The gaseous coolant transports the heat to the steam generator.

Table 1: Characteristics of spherical elements for the HTR-PM [17]

Diameter of spherical fuel	6 cm
Diameter of fuel region in fuel element	5 cm
Initial enrichment of fuel element	8.9 %
Volumetric filling fraction of pebble bed core	61 %
Fuel	UO_2
Fuel loading mode	Multi-pass

2.4 Safety Features of the HTR-PM

The HTR-PM is designed as an inherently safe reactor. Inherently safe means that even in case of accidents only negligible release of radioactivity will occur. The safety barriers of the fission products of the HTR-PM are nearly equal to the traditional multiple barrier principle for retaining fission products. These barriers are the fissile matrix, the SiC layer and the primary circuit. A pressure tight containment known from traditional nuclear power plants is not necessary due to the high retention ability of the silicon carbide layer and negligible activation of the coolant. Therefore, the whole reactor building, except for the primary cavity, can be entered and maintained at any time of operation and shutdown. However, the safety philosophy of the modular HTR-PM differs from the traditional approach of relying on redundancy and diversity. Instead of making use of costly, highly reliable installations like emergency cooling systems and pressurisers, the HTR's key to safety is simplicity. In accidental case, the actions that have to be taken by the reactor control are always the same [12]:

- Dropping of control rods (in order to stop the chain reaction)
- Shutdown of the helium blower (to stop helium mass flow)
- Shutdown of the water supply to the steam generator (to separate the nuclear core from the conventional plant)
- Closing all valves of connecting pipes to the primary circuit.

These actions will follow any type of incident or accident. There is no accident scenario where special actions other than the above mentioned have to be accounted for. In this

way, it can be excluded that a wrong decision is being made by any controlling personnel.

Basically, there are three major accident categories a reactor has to deal with:

1. Removal of decay heat
2. Control of excess reactivity
3. Control of chemical attacks

All other possible accidents can be sub-classified into these three categories.

2.4.1 Removal of Decay Heat

The removal of decay heat is possible only by means of natural phenomena (conduction, radiation). Hence, the power density and the reactor design must be selected in a way that in case of failure of active core cooling, maximum fuel temperature will never exceed the temperature limit of 1620°C [19]. Thermal fluid dynamic calculations for the HTR-PM showed that during the heat up of the core in the absence of active cooling the temperature limit is not exceeded.

2.4.2 Control of Excess Reactivity

The maximum fuel temperature of 1620°C also determines the maximum admissible reactivity insertion. This leads to a maximum reactivity insertion of ρ_{max} = 1.3 % for the HTR-PM [27]. The control rods must be partially inserted during operation to be able to have an excess reactivity margin when power load is changed. This excess reactivity is crucial since the great loss of neutrons due to Xe-135 absorption must be compensated for. Even in the highly improbable case of an ejection of all control rods at full power, the reactor power will increase instantaneously. But due to the strong epithermal resonance absorption of neutrons in the U-238 (known as Nuclear Doppler effect) the power excursion is almost instantly mitigated reducing the thermal neutron flux. The power will reach previous level. Hence, the reactor is very inert towards changes in its power level.

2.4.3 Control of Chemical Attacks

The reactor must be able to cope with chemical attacks like air or water ingress. During chemical attacks, the release of fission products was estimated by SIEMENS/Interatom for the Module 200. It was calculated by SIEMENS/Interatom that the release of activity

remains within admissible range in all scenarios [12]. The worst scenario is that the reactor is damaged in a way that the reactor vessel forms a “chimney“, i.e. air might traverse the core from the lower to the upper part leading to massive graphite burning of the reflector and the pebble bed. Nevertheless, it is prudent to be prepared for accident management measures to be executed in the time frame of some days after the accident (e.g. providing foam to stop air ingression into the core).

2.5 Issues with the High Temperature Reactor

In recent years, there were discussions whether or not the HTR needs a containment building. This discussion came up after a publication [28] claiming that the fuel elements of the AVR in Jülich, Germany, released far more metallic fission products to the primary circuit than previously expected. Three reasons for fission product release were reported:

- Defective coated particles
- Uranium impurities in the graphite matrix
- Diffusion of fission products out of intact coated particles due to higher temperatures than calculated

The first two bullet points are not of major concern since there was a considerable improvement of the fuel due to introduction of the SiC coating. However, due to higher temperatures the fission product diffusion through the intact coating increases. Also with high burn-up of fuel elements in the hot region (gas flow from top to bottom), the fission products can diffuse out of the coated particles.

This leads to two conclusions: first the burn-up thus far, must remain limited. Secondly, the operational temperatures must stay limited. The very high temperature variant (gas temperatures up to 1000°C or higher) of the HTR is subject to R&D and must first be verified before being technically exploited for co-generation or the like.

Another issue is the final disposal of both irradiated graphite blocks and especially boronated carbon bricks. The carbon bricks in the AVR initially intended to reduce the neutron fluence contain a large amount of tritium (generated by boron capture). Also the ^{14}C, radiocarbon, will create disposal issues, i.e. the amount of ^{14}C of the AVR already takes over large portions of the licensed activity of radiocarbon in the final low and intermediate active waste storage volume in the disposal site ‘Schacht Konrad’ [29]. Additionally, the capture of boron is a major source of tritium (^{3}H) in HTRs.

2.6 Three-Dimensional Problems in High Temperature Reactors

There are several reasons motivating the development of a coupled three-dimensional time dependent simulation system. Three-dimensional situations can arise from:

- non-axis symmetric geometry like in the AVR
- non-axis symmetric fuel loading: the AVR and PBMR had non-central fuel loading tubes; malfunction of fuel loading can lead to non-axis symmetric fuel element distribution (one tube only feeds fresh fuel) which can also lead to the formation of a hot spot
- non axis-symmetric burn-up distribution: more important for the block type-HTR, but can also occur in pebble bed HTRs
- non-axis symmetric control rod ejection/withdrawal or shutdown spheres fall into the side reflector
- densification of pebble bed off-cylindrical centre line
- mechanical blockage of cooling channels or the helium risers.

Especially cases which also need the influence of delayed neutrons, e.g. in a control rod ejection or a combination of scenarios, like a pebble bed densification together with a control rod ejection [30], necessitate the three-dimensional time dependent HTR simulation system.

The above mentioned AVR [6] was a pebble bed test reactor used for qualification of pebble fuel. It used a variety of different fuel elements (9 different fuel elements), i.e. different coatings – BISO (without SiC layer) and TRISO particles – different enrichments, ranging from low to high enriched uranium, some even contained thorium for breeding of U-233. All of them were inserted into the reactor over time. Additionally, the AVR used a two-zone core where the fresh fuel elements were put into the outer part of the core, after reaching a certain burn-up they were inserted into the core centre. With its 9 different fuel elements and 50 burn-up states, the generation of cross section is very elaborate. This, together with some uncertainties of the real gas temperatures (20 % core by-pass through bore-holes was mixed with hot gas before going to the steam generator) makes the simulation of the AVR very challenging. It was therefore decided not to take the AVR as an application case.

2.6.1 Earlier Programs for Safety Analysis in High Temperature Reactors

There is a multitude of different computer programs for HTR analysis. However, these always expose some deficiencies with respect to 3-d transient capabilities of both neutronics and thermal fluid dynamics. An overview of capabilities is presented in Table 2. All but the MGT-3D code are lacking full 3-D capabilities, but the publication date was after the time of this manuscript and transient 3-D results are not published.

Table 2: Overview of simulation tools for HTRs

Name of the program	Neutronics	Thermal fluid dynamics	Reference
RZKIND/THERMIX	2-D	2-D	[31]
ZIRKUS/THERMIX	2-D (steady-state)	2-D	[32]
CFX	-	3-D	[33]
DORT-TD/THERMIX	2-D	2-D	[34]
TINTE	2-D	2-D	[35]
DALTON/THERMIX	3-D	2-D	[36]
CYNOD/RELAP5-3D	2-D	3-D	[37]
WIMS/PANTHERMIX	3-D	2-D	[38]
TH3D	Point kinetics	3-D	[39][40]
NEM/THERMIX	3-D	2-D	[41]
DYN3D-HTR	3-D (block type)	1-D fluid flow, 3-D heat conduction	[42]
SPECTRA	Point kinetics	1-D fluid flow, 2-D conduction	[43]
WKIND/FLOWNEX	1-D	2-D	[44]
MGT-3D	3-D	3-D	[45]

3 Aims of this work

The aims of this work are to introduce an HTR simulation system using well validated data, correlations and methods that are state of the art and follow best estimate standards. The main task is to establish a common interface that allows data exchange between the two initially uncoupled components of the simulation system. This along with modifications introduced in the two major components of the coupled simulation tool TORT-TD/ATTICA3D allows for a three-dimensional time-dependent safety analysis. Especially for processes that cannot be simulated by use of quasi-steady state methods like burn-up calculations or part load is not appropriate and necessitates a treatment that takes into account reactor kinetics, i.e. the effect of delayed neutrons in transient cases.

One component is the time-dependent discrete ordinates neutron transport code TORT-TD, initially introduced as a steady-state discrete ordinate code TORT by the Oak Ridge National Laboratory [46] and enhanced by the Gesellschaft für Reaktor- und Anlagensicherheit mbH (GRS) for time dependent calculations by use of a time dependent neutron source. Detailed description can be found in [47].

The second component of the simulation system is the time dependent three-dimensional thermal fluid dynamics (TFD) code ATTICA^{3D} (Advanced Thermal fluid dynamic Tool for In-vessel and Core Analysis in 3 Dimensions) that was previously introduced as TH3D [35] [40]. It applies the porous media approach in which detailed description of geometry is omitted in favour of the more generalised geometrical description with the help of the porosity ε, the ratio of fluid to total geometrical volume.

These two three-dimensional components are now coupled by means of a common interface. In the steady-state calculation, the interface transfers data from TORT-TD to ATTICA^{3D} and vice versa. The data to be transferred from TORT-TD to ATTICA^{3D} is the mesh-wise power density. After interpolation to the – usually differing – TFD grid, ATTICA^{3D} calculates the temperature distribution of the fuel, moderator and reflector and, if necessary, the hydrogen density. The temperatures for fuel and moderator are taken by TORT-TD to calculate a new power density. This process is repeated until both temperature changes and changes in power density converge, i.e. do not change within certain thresholds provided in the respective inputs. In case of different computational grids, the interface interpolates the data to be transferred to the mutual grids. The neutronic grid is usually much finer in the regions of interest (reactor core and approxi-

mately 1 metre of reflector), compared to the thermal fluid dynamic grid whereas the thermal fluid dynamic grid comprises much larger volumes for simulation.

E.g. while the neutronic problem geometry of interest usually ends 1 metre behind the side reflector, the thermal hydraulic computational grid comprises all the components, core, side reflector helium risers, core barrel, helium gap, reactor pressure vessel, along with radiative heat transfer and/or gas heat conduction and/or convection from the reactor pressure vessel to the reactor cavity cooling system. This is necessary to be able to calculate cases where the decay heat removal system comes into play.

The option to simulate the HTR in three dimensions was not available yet since computing power at the time of origin (70’s and 80’s of last century) was much lower and sufficient for licensing at that time arguing that the most severe accidents do not require more detailed modelling than just a cylindrically symmetric one. The state of computational art also demands for more efficient methods to obtain solutions. Also with increased memory size for computers, the deficiency of only being able to generate 2-dimensional solutions is addressed, and a transient 3-dimensional HTR simulation tool is introduced.

4 Physical and numerical models

4.1 Nuclear Cross Sections

The probability for interaction of neutrons with matter is described by cross sections. These cross sections describe interactions of neutrons with the nuclei of fuel, moderator, reflector and absorbers, etc., basically all materials within the domain of interest. The total microscopic cross section (σ) is subdivided in different possible reactions, e.g. scattering σ_s, absorption σ_a, fission σ_f and capture σ_γ.

The absorption cross section σ_a is the sum of fission and capture cross sections and can be written as

$$\sigma_a = \sigma_f + \sigma_\gamma \tag{4-1}$$

For the scattering, there are two types of scattering accounted for, the elastic and inelastic scattering:

$$\sigma_s = \sigma_{elastic} + \sigma_{inelastic} \tag{4-2}$$

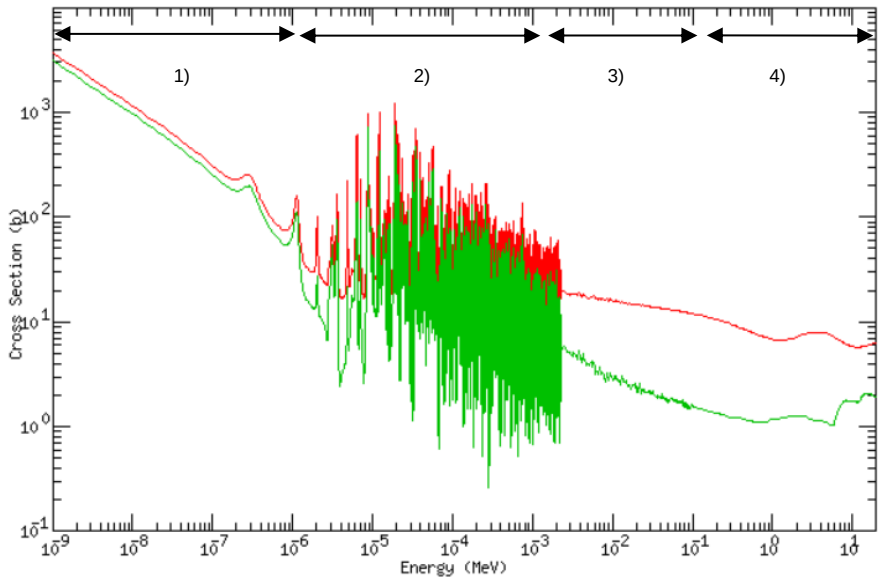

Figure 4: Continuous energy total cross section (red) and fission cross section (green) for a Uranium-235 nucleus from the ENDF-B/VII data files in barn (=10^{-24} cm^2) , the energy ranges (upper arrows) are 1) thermal, 2) resolved resonance, 3) unresolved resonance, and 4) fast range [48].

To obtain the total cross section absorption and scattering fractions are summed up:

$$\sigma_t = \sigma_a + \sigma_s \tag{4-3}$$

At temperatures above 0 K, all nuclides show Brownian motion. This motion influences the relative velocities of neutron and interacting nuclide. The nuclide may move in or against the neutron direction, and hence, the relative velocity between neutron and nuclide will either decrease or increase [49]. The velocity distribution follows a Maxwell-Boltzmann distribution given by

$$M(\upsilon_A, T) = \left(\frac{m_A}{2\pi kT}\right)^{\frac{3}{2}} \cdot \exp\left(\frac{-\frac{1}{2} m_A \cdot \upsilon_A^2}{kT}\right) \tag{4-4},$$

with M as the Maxwell-Boltzmann distribution, υ_A as nuclide velocity, m_A as the atomic mass, k as the Boltzmann constant, and T as the temperature.

The reaction rate F of a monoenergetic neutron beam hitting nuclides in thermal motion is given by the integral over all nuclide velocities v_A

$$F = \int_{v_A} \upsilon_{rel} n N \sigma(\upsilon_{rel}) \cdot M(\upsilon_A, T) d\upsilon_A \tag{4-5},$$

with n as the neutron density of a beam and N as the nuclide density. Introducing an effective cross section σ_{eff} that depends on the neutron velocity one obtains

$$F = \upsilon n N \sigma_{eff}(\upsilon, T) \tag{4-6}.$$

Comparing equations (4-5) and (4-6) yields the equation to define the effective cross section

$$\sigma_{eff}(\upsilon, T) = \int_{\upsilon_A} \frac{\upsilon_{rel}}{\upsilon} \sigma(\upsilon_{rel}) M(\upsilon_A, T) d\upsilon_A \tag{4-7}.$$

A characteristic of equation (4-7) is that it enables the conversion of a known effective cross section at the temperature T to a temperature T' that is higher. This is done with the help of Fourier transformation and convolution, to yield

$$\sigma_{eff}(\upsilon, T') = \int_{\upsilon_A} \frac{\upsilon_{rel}}{\upsilon} \sigma_{eff}(\upsilon_{rel}, T) M(\upsilon_A, T' - T) d\upsilon_A \tag{4-8}$$

i.e. by averaging over a Maxwell-Boltzmann distribution of the temperature difference $(T' - T)$, one obtains the desired temperature transformation. If the energy depend-

ence of the neutron flux density is known, the neutron spectrum $\phi(E)$ can be used as a weighting function for the average effective cross section over the whole energy range, which is

$$\sigma_{eff}(T) = \frac{\int_E \sigma_{eff}(E,T)\phi(E)dE}{\int_E \phi(E)dE} \qquad (4\text{-}9).$$

This is described in more detail in [49]. In the following, whenever σ occurs, this effective cross section σ_{eff} is taken. For ease of reading the index "*eff*" will be dropped. A typical neutron spectrum for an HTR is presented in Figure 5.

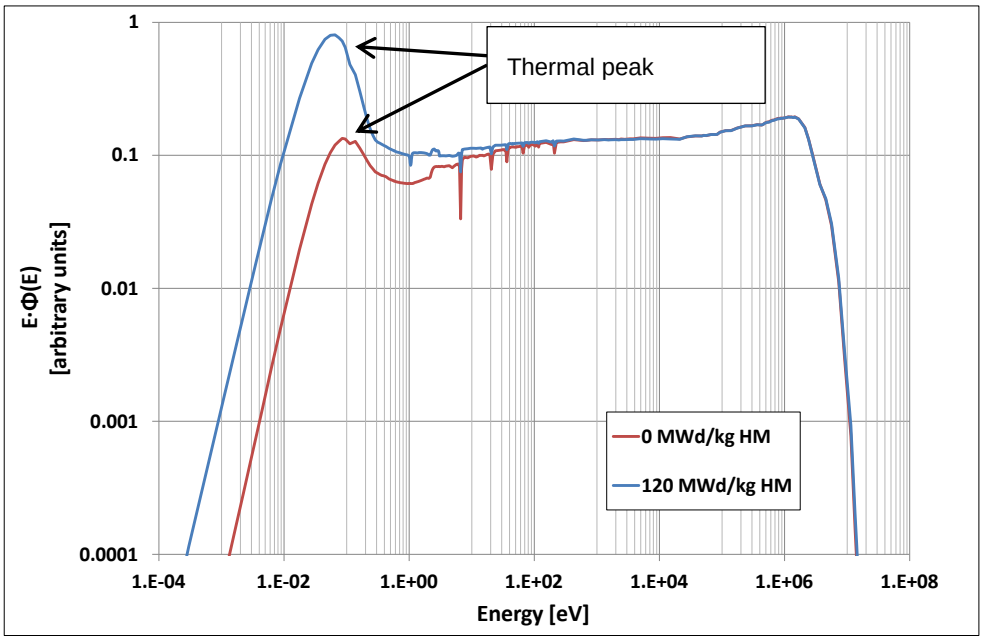

Figure 5: Typical neutron spectrum of a pebble bed with increasing burn-up

While the microscopic cross section only provides the interaction of one neutron with one nucleus of interest, the macroscopic cross section provides the interaction for an ensemble of nuclides; say the fuel region with UO_2 or Plutonium dioxide (PuO_2).The effective macroscopic cross sections Σ_{eff} depend on neutron energy and on the energy (temperature) of the atom it interacts with.

$$\Sigma_x(\vec{r},E,T,t) = N(\vec{r},t)\cdot\sigma_x(E,T) \qquad (4\text{-}10)$$

In the equation above, $N(\vec{r},t)$is the nuclide density, $\sigma_x(E,T)$ is the effective microscopic cross section, and $\Sigma_x(\vec{r},E,T,t)$ is the macroscopic. The subscript x is the re-

spective interaction type which can be total, absorption, fission, scattering, capture or other; *E, T* and *t* denote the respective dependencies of the parameters energy, temperature and time. The change of the nuclide density due to operation of the reactor is referred to as 'burn-up'. With increasing burn-up, the amount of fissile material decreases while the thermal flux and the fission product content increases. For this work, the explicit dependency of the macroscopic cross section on burn-up is neglected, since it is a slowly varying parameter (in the order of days, to weeks), whereas the transients that are considered are on much smaller time scales (seconds, minutes). Only some re-criticality calculation can be in the order of days. But for these transients there is no significant power production present, only decay heat, and, hence, no significant change of nuclide density will occur due to burn-up. Changes of nuclide densities originate mainly from decay of short-lived fission products. For time dependent problems, the fission yields of Iodine-135, a precursor of the reactor poison Xenon-135, are solved analytically to account for xenon poisoning when load changes are imposed. Also, for a comprehensive analysis, the inventory of Pu-239 and Samarium-149 and their precursors Neptunium-239 and Prometium-149, respectively, must be determined.

The decay heat that is produced by fission products and actinides is basically included in the cross section generation but is not a variation parameter for cross section processing. Here, the dependencies for a core region are fuel and moderator temperature, fast and thermal buckling, xenon density and, if necessary, hydrogen density (for water ingress analysis).

The neutron spectrum, i.e. the energy spectrum of the neutrons within a reactor comprises several orders of magnitude, see Figure 4. A usual approach is to subdivide the energy range into a - preferably huge - number of discrete energy groups. For multigroup 3-D modelling, the number should not be higher than 20-30 energy groups for reasons of computational time. But these groups have to be averaged over realistic neutron spectra. Multistep-multigroup procedures can be applied if high orders for transport cross section are needed.

A special treatment is needed for the complicated region of resonances. For the region of unresolved resonances the method of Bondarenko with a background cross section is applied [50]. For the resolved resonance range the slowing down equation is solved for approximately 10,000 – 20,000 energy points. Afterwards, these cross sections are homogenised such that both the reaction rates and the collision probabilities yield the same results as if the resonance region would be calculated point-wise. In general, the higher the number of energy groups, the more detailed the result, but more computational time is needed since for each group a balance equation has to be solved. When

a large number of groups is used, they will be condensed on so-called ‘few group’ cross sections (say 13 neutron groups, four of which are in the thermal range).

To provide a set of parameterised cross section the Nuclear Energy Agency (NEA) computer programme MICROX2 [51] is used for generation of microscopic cross section. MICROX2 accounts for the special nature of the fuel, i.e. the coated particles in random dispersion within a graphite matrix coated by a fuel free graphite shell which, again, is surrounded by the coolant helium and, if applicable, fuel free dummy graphite spheres (needed for start of operation to compensate for excess reactivity) . To provide macroscopic cross sections the HTR steady state programme ZIRKUS/THERMIX [32] is used. The computational sequence of the modular ZIRKUS/THERMIX program is (in order of appearance):

a. Nuclide densities of fresh fuel and reflector (only once in the first run)
b. Microscopic cross sections for the reflector and the fuel element (only once in the first run)
c. With the nuclide densities and the microscopic cross sections, the macroscopic group cross sections are calculated (only once in the first run)

1. Load and reload of fuel elements, mixing of nuclide densities to account for pebble flow within the core, and spectrum calculations.
2. Re-calculation of microscopic cross sections of the fuel element (only after the second run)
3. Re-calculation of macroscopic cross sections for the fuel (only after the second run)
4. Calculation of Dancoff factors
5. Solving of the diffusion equation, determination of the neutron flux
6. With the neutron flux, the power distribution is determined
7. A module to compute the burn-up of the fuel follows.
8. With the then determined burn-up, the decay heat is calculated
9. After all these steps the computational grid is interpolated from the neutronics to the thermal hydraulics computational grid
10. Calculation of solid and gas temperatures, after obtaining the solid temperatures (surface temperatures) the particle temperatures are determined

11. After the calculation of temperatures, they are interpolated back to the neutronics grid

This sequence is repeated until the pebble bed reaches an equilibrium state, i.e. after one reload step the nuclide densities of a burn-up zone does not change anymore. The three steps at the beginning (a,b,c) are only performed once in the beginning, the steps 2 and 3 are executed from the second run, since temperatures change and this will lead to a change of fuel, moderator and reflector temperatures.

From the equilibrium core, the nuclear cross sections are generated for the neutronics code TORT-TD for transient application to the HTR-PM which is shown later in this work. For this reactor geometry, ZIRKUS used 13 neutron groups for the equilibrium core which were condensed to 7 groups for transient calculations. Also, the cross sections were spatially averaged for the reflector part, to reduce the number of material zones to be accounted for. In the core region, the burn-up zones that approximate the pebble flow are replaced by regular cylindrical volumes, see Figure 6. For the core, the number of zones increased slightly from 144 zones in the ZIKRUS calculation to 154 material zones in the TORT-TD calculation. These works, together with cross sections that account for steam content within the core as consequence of a steam generator tube rupture were not performed by the author, but by a colleague: Johannes Bader. However, the explanation is added to clarify how the cross sections for TORT-TD were generated for transient purposes.

Figure 6: Left: sub-division of material zones in ZIRKUS, in the core region the flow lines of the pebble bed are visible, right: sub-division of material zones for TORT-TD [30]

4.2 The multiplication factor and the reactivity

The multiplication factor k_{eff} of a neutron multiplying medium is a measure for the tendency to decrease, increase power or to remain in a steady state. The meaning of the multiplication factor k_{eff} is: for each neutron absorbed in the system, k_{eff} new neutrons will be produced. For a critical system, the power produced remains constant and the multiplication factor is $k_{eff} = 1$, i.e. each neutron lost will be replaced by a new one; the overall population remains the same. To characterise a system that deviates from a steady state, the reactivity ρ_r is introduced.

$$\rho_r = \frac{k_{eff} - 1}{k_{eff}}$$

For a critical reactor, ρ_r equals zero since k_{eff} equals 1. The reactivity is a dimensionless parameter. In literature it can be also given as percentage, or in multiples of the delayed neutron fraction in so-called dollars (1 $ = 1 β) of a considered system or in percent millirho (pcm). (Note: ρ is also the variable for the density in the thermal fluid dynamic calculation, therefore the index r is added) [52].

Systems that have a negative reactivity are called sub-critical, the self-sustaining chain reaction dies out eventually. Systems that have a positive reactivity are referred to as supercritical. Depending on the extent of the reactivity - greater or smaller than the delayed neutron fraction – the system is called delayed supercritical, if $\rho < \beta$ the increase will only increase with the delayed neutrons, or prompt supercritical $\rho > \beta$ if the system also increases with the prompt neutrons coming from fission. The prompt supercritical state leads to a massive increase of the neutron population and must be compensated by internal feedback mechanisms described in the following chapter.

4.3 Important feedback mechanisms in high temperature reactors

The macroscopic cross section multiplied by the energy dependent neutron flux yield the reaction rates *F* at temperature T

$$F_x = \Sigma_{x,eff}(T)\phi = \int_E \Sigma_{x,eff}(E,T)\phi(E)dE \qquad (4\text{-}11)$$

The reaction rates change with temperature, e.g. if the flux remains the same and the temperature leads to a decrease in the macroscopic cross section, the resulting reac-

tion rate will reduce. These reaction rates will vary when temperature or the nuclide density of the system changes. Important feedback mechanisms in HTR are the fuel temperature effect, the moderator temperature effect, and the reflector temperature effect. The moderator and reflector are both made of graphite, but for the distinction of the two different effects, the graphite of the fuel spheres is referred to as moderator whereas the graphite of the reflector bricks is referred to as the reflector.

- The fuel temperature feedback (also referred to as Doppler Effect), $\frac{\partial \rho_r}{\partial T_f}$: Some materials like Thorium-232 (Th-232), U-238 , Pu-238, Pu-240, Pu-242 are resonance absorbers which means that in the resonance energy regions of these nuclides, the absorption cross section is dominating the total cross section of the regarded nuclide, the likelihood of absorption increases with temperature. As most of the energy is released inside the fuel (~95%, the rest is gamma heating), a power increase will instantaneously lead to an increase in fuel temperature (U-235 & U-238) which in turn leads to an increase of absorptions in non-fissile material (U-238). It is the most important feedback in HTRs since the average fuel temperature can increase by several hundred degrees. The fuel temperature feedback is negative [24] [49].

- The moderator effect, $\frac{\partial \rho_r}{\partial T_m}$: The temperature of the moderator material (graphite of fuel spheres) determines the location (in energy) of the thermal flux peak. If the temperature is increased the spectrum hardens and moves the peak to higher energies having a negative impact on the 1/v-range (the thermal peak in Figure 5 moves to the right). The moderator effect is in the range of seconds to minutes and has a negative feedback for temperature increase if uranium is used as fuel. (For plutonium or plutonium and minor actinide fuel which are not considered in this work, this feedback can be positive, since the thermal peak of the neutron spectrum shifts into a fission resonance of the Pu-239, see [27].)

- The reflector effect, $\frac{\partial \rho_r}{\partial T_r}$: The large mass of the graphite reflector of which all the load-carrying structures are made of has a great heat capacity and, hence, big time constants for heat up. Here, the manufacturing impurities are of importance. Impurities are accounted for by means of a boron equivalent, a 1/v-neutron absorber. Unlike the moderator effect, the shift of spectrum to higher energy will lead to a decrease of parasitic absorptions within the moderator. Hence, a temperature increase will lead to a decrease in 1/v absorptions. The reflector effect – because of

the great volume of graphite – has large times of onset, in the range of hours. The reflector feedback is positive [27], but does not occur at the same time like fuel and moderator effect, but with a delay.

- Ingress of steam as moderator, $\frac{\partial \rho_r}{\partial m_{H_2O}}$: If an HTR concept – like the HTR-PM – employs a steam generator where the water pressure (135 bar) is far above the helium pressure (70 bars), a break in a steam generator tube or the whole steam generator plate will lead to ingression of water into the primary circuit. Depending on the location of the break, water or steam will pour into the helium side of the steam generator. With the helium blower running, the steam will be transported to the reactor pressure vessel thereby increasing the moderation of neutrons, first, because the HTR-PM is under-moderated, and secondly, because water slows down neutrons more effectively than graphite. At the same time the leakage towards the reflector will be reduced. (Note: Liquid water or droplets will not enter the reactor pressure vessel since large water masses within the steam generator will stay there due to its geodetic location below the reactor pressure vessel; water droplets that are carried by helium or steam will be effectively separated by the rotating impeller of the blower, see [53]). For smaller amounts of steam until approximately 1,500 kg in the primary circuit - as expected for steam ingress - the feedback is positive. But this is only a theoretical value, because higher amounts of steam are unphysical, since at the time of ingression at nominal pressure the core cannot contain more than 600 kg. Theoretically, if the already physically impossible amount of 1,500 kg is exceeded, the positive effect of the water would be compensated by increased absorptions due to the steam. The use of a steam generator excludes the use of plutonium fuel since the resulting power increase would be unbearably high [27]. The change of reactivity with steam mass in the core region is depicted in Figure 7.

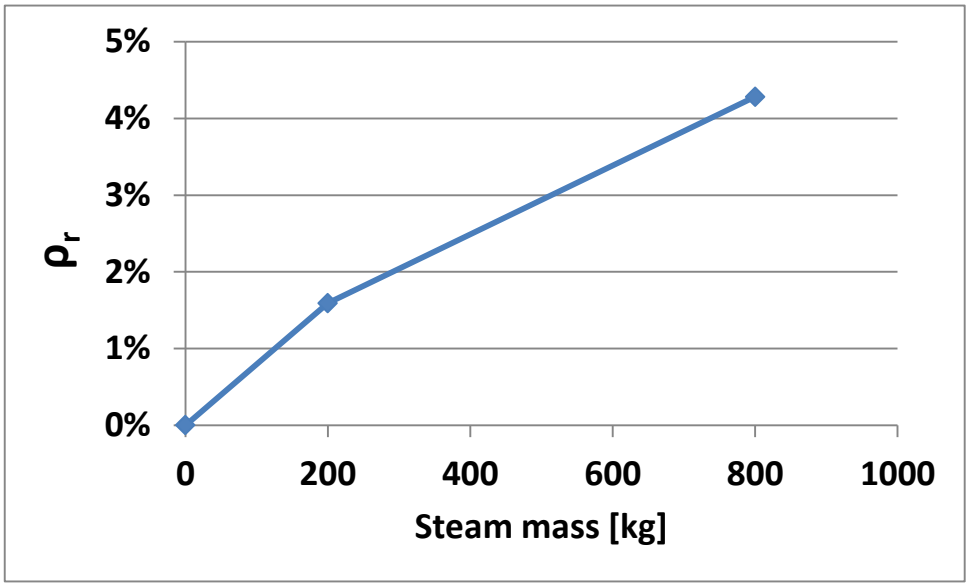

Figure 7: Increase of reactivity in the HTR-PM cross sections with increasing water content within the core region. The impact of steam on the reactivity was analysed with the ZIR-KUS/THERMIX system [32] .Note: From the steam content within the core, the respective hydrogen content is calculated, and added to hydrogen from corrosion if present. The hydrogen density is then taken as a variation parameter for the cross section re-evaluation, see Figure 8.

These feedback effects are important for the understanding of the transient behaviour of the analysed systems (PBMR, HTR-PM) presented in chapters 1 and 1 and explains why the HTR concept behaves so moderately, even in cases with unfavourable conditions like a control rod ejection.

4.4 Coupling Neutronics and Thermal Fluid Dynamics via a common interface to create an HTR simulation system

In order to create a HTR simulation system that has transient 3-dimensional capabilities for processes within the reactor pressure vessel, one needs at least four components, see Figure 8:

1) a set of parameterised weighted nuclear cross sections that cover the whole range of possible states the reactor can experience during a transient (for the HTR-PM 10 fuel temperature, 7 moderator temperatures, 3 xenon densities and 3 values for hydrogen support points for macroscopic cross sections),
2) a 3-dimensional transient neutronics code to solve the neutron transport equation including the delayed neutrons within a domain of interest,
3) a 3-dimensional transient thermal fluid dynamic code to determine the temperature distribution within the reactor pressure vessel, and outside the reactor

pressure vessel up to the reactor cavity cooling system and the heat transport with the coolant,

4) an interface between the neutronics and the thermal fluid dynamics to exchange data between the mutual systems and if necessary to interpolate the values to be transferred to individual respective computational grids.

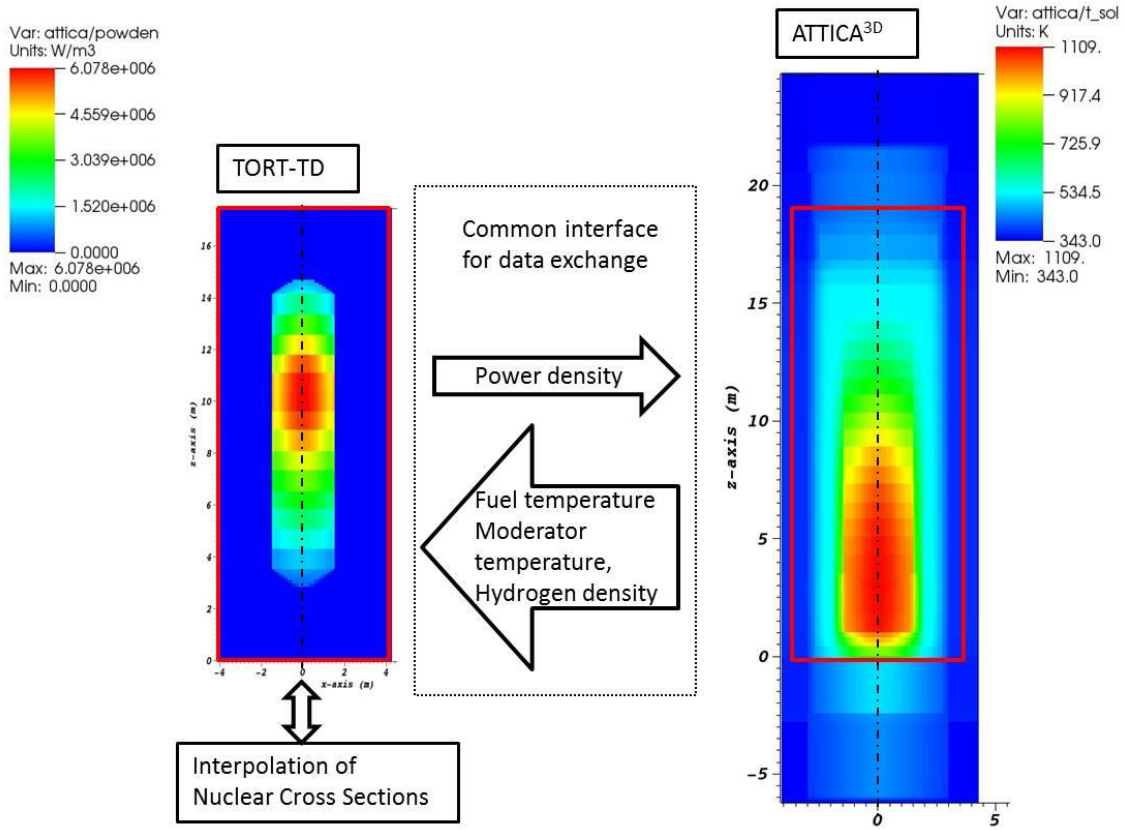

Figure 8: Coupling procedure for TORT-TD and ATTICA3D, both the neutronics model (power density distribution) and the thermal fluid dynamic model (solid temperature distribution) is shown, the red frame on the ATTICA^{3D} side indicates the computational domain of TORT-TD, obviously smaller.

4.4.1 Computation of a Steady-State of the Coupled System

A calculation starts with the neutronics calculation assuming an initial uniform temperature distribution. Alternatively, a previously calculated temperature and xenon/iodine distribution can be read in. Then the cross-sections are evaluated for that temperature and thermal fluid dynamic state and usually interpolated between the support points of the parameterised cross section files. After interpolation of the cross sections, TORT-TD starts with a steady state calculation where the multiplication factor k_{eff} and the

power distribution is determined. Then, this distribution is transferred to ATTICA^{3D} via the integrated interface to TORT-TD that checks the grid of TORT-TD and ATTICA^{3D}. If the computational grids differ - which is usually the case - the values of the power distribution are interpolated to the ATTICA^{3D} grid. This interpolation is done by volumetrically averaging the values. With the interpolated power density distribution, ATTICA^{3D} calculates the temperature distribution of the solid and the gas (also masses, velocities). Applying the heterogeneous temperature model for the pebble fuel, a distinction of moderator and fuel temperature is achieved for the pebble region. Outside the core only one solid temperature (for the fuel free reflector) is calculated. The fuel, moderator and reflector temperatures are passed to the interface that interpolates the values for the TORT-TD computational grid. With the new temperature distribution, TORT-TD evaluates the cross section for the temperature distribution and then re-calculates a power distribution. This cycle is repeated until convergence is achieved. The default threshold for convergence is set to 10^{-6} for the relative change of power for a cell, but is also an optional input parameter in ATTICA^{3D} and can be set by the user (here, 5×10^{-5}). This interaction is depicted in Figure 8. On the lower right, the red frame in the ATTICA^{3D} geometry indicates the extent of the neutronics calculation.

4.4.2 Coupled transient calculations

After obtaining a steady-state using the above mentioned procedure, TORT-TD/ATTICA^{3D} starts the time dependent mode. Time steps are either provided by input or ATTICA^{3D} or TORT-TD. In both programmes, ATTICA^{3D} and TORT-TD there are routines implemented to determine the time step size. While ATTICA^{3D} applies a modified Newton-Raphson method with adaptable time step size that evaluates the truncation error and can in principle make huge time steps, the maximum time step size in TORT-TD is restricted to a maximum time step size of $\Delta t_{\max} \leq 2s$. Therefore the coupled system is also restricted to this time step size. However, this is

The transient mode is started by solving the time-dependent transport and conservation equations for a certain time interval (≈ 2 seconds) without change of other parameters. I. e. all the equations are solved with the time dependent terms present; the solution has to remain the same. A measure to check if the solution can be regarded as converged is the spatially resolved reactor period which has to reach large values ($\omega^{-1} \geq 10^4$ seconds).

TORT-TD starts executing the first time step, ATTICA^{3D} follows, because the response times in neutron physics are generally much smaller than in thermal fluid dynamics.

Otherwise ATTICA^{3D} will reduce the step size and transfers it via the interface to TORT-TD. The coupled system will calculate problems within user provided time step size limits ($\Delta t_{\max} \leq 2s$).

4.5 The neutron transport and diffusion tool (TORT-TD)

TORT-TD is a tool to solve the neutral particle (neutrons, photons) transport equation of phase space elements in a considered reactor (fast reactors, thermal LWR, and thermal HTR). It was originally developed as a steady state three-dimensional neutron transport code to model processes within a reactor, to predict neutron flux in presence of a neutron source, as well as for fluence calculations in buildings [46]. TORT was enhanced for time-dependent capabilities by the Gesellschaft für Anlagen- und Reaktorsicherheit mbH (GRS) by introduction of a time dependent neutron source and the delayed neutron precursor equations (and changing the name into TORT-TD) [54]. TORT-TD is a deterministic programme that applies the discrete ordinate approach to solve the neutron transport equation for each phase space element in cylindrical or Cartesian geometry. The neutron transport equation takes the angular dependence of the neutron flux (anisotropic scattering) into account and is also valid for strong absorber regions and cavity regions. TORT-TD was enhanced for a neutron diffusion solver for reasons of computational time and, therefore, to be able to cope with long-term transients. Here, the transport equation and its implementation in TORT-TD will be described briefly. To study the procedure in more detail, see [47] where general procedures and enhancements for time dependency are described for the two-dimensional transport programme DORT-TD, but the changes for TORT-TD are the same, in principal.

The neutron transport equation is the balance equation of a phase space element accounting for spatial, angular and energetic dependence of the neutron flux. Since the neutron spectrum of a thermal reactor extends over several orders of magnitude on the energy scale, it is a common approach to subdivide the range of energy into intervals, the so-called neutron groups. The highest energy of neutrons is appointed the group index g = 1; the least energy group has the highest index G, $g = 1,...,G$.

The neutron density $n(t)$ is a parameter that depends on a variety of other parameters. It is more common to express the change of neutron density in terms of the angular neutron flux $\Psi(\vec{r},\vec{\Omega},E,t) = \upsilon(\vec{r},\vec{\Omega},E,t) \cdot n(\vec{r},\vec{\Omega},E,t)$, where υ is the velocity of the neutrons, $\vec{\Omega}$ is the direction, E is the energy, and t denotes time. The change of neutron

density with time can have many reasons such as fissions, absorptions, scattering, capture or external sources. The neutron transport equation is a balance equation that takes into account these processes. As starting point, the steady state Boltzmann equation for neutron transport will be described and the introduction of a time dependent source term and the modifications necessary will be explained:

$$\underbrace{\vec{\Omega}\cdot\nabla\Psi\left(\vec{r},\vec{\Omega},E\right)}_{Convection\ \ Term}+\underbrace{\Sigma_t\left(\vec{r},E\right)\Psi\left(\vec{r},\vec{\Omega},E\right)}_{Collision}=$$
$$\underbrace{\iint_{4\pi}\Sigma_s\left(\vec{r},\vec{\Omega}'\rightarrow\vec{\Omega},E'\rightarrow E\right)\Psi'\left(\vec{r},\vec{\Omega}',E'\right)d\Omega'dE'}_{Scattering}+ \qquad (4\text{-}12)$$
$$\underbrace{\frac{\chi(E)}{4\pi}\int\nu\Sigma_f\left(\vec{r},E\right)\phi\left(\vec{r},E\right)dE}_{Fission}+\underbrace{S\left(\vec{r},\vec{\Omega},E\right)}_{Source}$$

where $\vec{\Omega}$ is the direction of a neutron, Ψ is the angular neutron flux, Σ_t, Σ_s and Σ_f are the macroscopic total, scattering and fission cross sections respectively, χ is the Maxwellian fission spectrum, the division by the factor 4π indicates the isotropy of the neutrons generated by fission, ν is the average number of neutrons born in fission, ϕ is the scalar neutron flux (angular flux integrated over all directions) since fission is considered to be isotropic, and S is an external neutron source term. The first term in the equation denotes the convection term. Here, neutrons are lost from the system by spatial diffusion (leakage); the second term describes the loss of neutrons due to any possible reaction (scattering, absorption, fission, capture). Both terms on the left side form a sink for neutrons. On the right hand side, first there is the scatter term $\iint_{4\pi}\Sigma_s\left(\vec{r},\vec{\Omega}'\rightarrow\vec{\Omega},E'\rightarrow E\right)\Psi'\left(\vec{r},\vec{\Omega}',E'\right)d\Omega'dE'$ which accounts for the scattering of neutrons into a distinctive direction with a distinctive energy (under consideration). The second term on the right hand side is the neutrons generated by fission, and the third term is an external neutron source. These are the elements of the neutron transport equation; depending on the problem to be solved some terms can vanish, e.g. for a region without fissile material the fission term disappears, for problems without external neutron source the source terms is zero.

With the right pre-processing of nuclear cross sections and the right normalisation techniques, it can be achieved that results yield essentially the same values as reference solutions like MCNP that treat the whole energy range in a point-wise manner (especially the resonance region).

The multi-group approach introduces balance equations for each neutron group g that subdivides the neutron energy range into a distinctive number of neutron groups. The

different balance equations are coupled via the fission term and the scattering term that can scatter neutrons from group $g' = 1,...,G$ into the considered neutron group g (from the energy interval E' into E and from the direction $\vec{\Omega}'$ into the direction $\vec{\Omega}$). After introducing the energy groups the dependency on the energy disappears and the equation transforms to

$$\begin{aligned}&\vec{\Omega}\cdot\nabla\Psi_g\left(\vec{r},\vec{\Omega}\right)+\Sigma_{t,g}\left(\vec{r}\right)\Psi_g\left(\vec{r},\vec{\Omega}\right)=\\&\sum_{g'=1}^{G}\int_{4\pi}\Sigma_{gg'}\left(\vec{r},\vec{\Omega}'\rightarrow\vec{\Omega}\right)\Psi'_{gg'}\left(\vec{r},\vec{\Omega}'\right)d\Omega'+\frac{\chi_g}{4\pi}\sum_{g'=1}^{G}\nu\Sigma_{f,g}\left(\vec{r}\right)\phi\left(\vec{r}\right)+S_g\left(\vec{r},\vec{\Omega}\right)\end{aligned} \tag{4-13}$$

Delayed neutrons and time dependency

In order to introduce time dependency, it is necessary to also model the delayed neutrons to cover the kinetics of the reactor. The delayed neutrons are emitted over seconds up to a minute by fission products, so called precursors, their fraction of the total number of neutrons is β; its numerical value ranges from 0.5 – 0.7 % for ^{235}U fuel. The number of precursor groups is arbitrary but the widely use of 6 precursor groups yield good results, therefore in this work the number of delayed neutron groups is $i = 1,...,6$. Instead of the whole fission neutrons coming from prompt fission with the prompt spectrum, the term $\frac{\chi(E)}{4\pi}\int\nu\Sigma_f\left(\vec{r},E\right)\phi\left(\vec{r},E\right)dE$ will be multiplied by $\left(1-\beta\right)$, and the delayed neutron fraction is introduced:

$$\begin{aligned}&S_{fission}=S_{prompt}+S_{delayed}\\&=\frac{\left(1-\beta\right)\chi_{prompt}(E)}{4\pi}\int_0^\infty\nu\Sigma_f\left(\vec{r},E\right)\phi\left(\vec{r},E\right)dE+\beta\sum_{i=1}^{6}\frac{\chi^i_{delayed}}{4\pi}(E)\lambda_i c_i\left(\vec{r},t\right)\end{aligned} \tag{4-14}$$

The six groups of delayed neutrons all have their own energy spectrum, indicated by $\chi^i_{delayed}$. λ_i is the respective decay constant and $c_i\left(\vec{r},t\right)$ is the precursor concentration. Also, a new set of equation is introduced, the six precursor concentration equations.

$$\frac{dc_i\left(\vec{r},t\right)}{dt}=\underbrace{-\lambda_i c_i\left(\vec{r},t\right)}_{decay}+\underbrace{\beta_i\int_0^\infty\nu\Sigma_f\left(\vec{r},E'\right)\phi\left(\vec{r},E',t\right)dE'}_{production} \tag{4-15}$$

The change of the precursor concentration with time is the precursor decay plus the production, which is the fraction of the precursor group that is produced by fission.

With the above six equations, the time dependent neutron transport equation transforms to

$$\frac{1}{\upsilon(E)}\frac{d}{dt}\Psi(\vec{r},\vec{\Omega},E,t)=-\vec{\Omega}\cdot\nabla\Psi(\vec{r},\vec{\Omega},E,t)-\Sigma_t(\vec{r},E)\Psi(\vec{r},\vec{\Omega},E,t)$$
$$\iint_{4\pi}\Sigma_s(\vec{r},\vec{\Omega}'\to\vec{\Omega},E'\to E)\Psi'(\vec{r},\vec{\Omega}',E',t)d\Omega'dE'+S_{ext}(\vec{r},\vec{\Omega},E,t) \qquad (4\text{-}16)$$
$$+\frac{(1-\beta)\chi_{prompt}(E)}{4\pi}\int\nu\Sigma_f(\vec{r},E)\phi(\vec{r},E',t)dE+\sum_{i=1}^{6}\frac{\chi^i_{delayed}}{4\pi}(E)\lambda_i c_i(\vec{r},t)$$

The above equation (4-16) along with the six precursor equations (4-15) have to be solved to model realistic time-dependent nuclear systems. The neutron transport equation can only be solved analytically for few selected problems. Generally, for larger heterogeneous reactor systems, numerical solutions are the only way of obtaining a solution. Therefore, the time derivative of the system of equations has to be approximated with the help of the differential quotient.

$$\frac{1}{\upsilon(E)}\frac{d}{dt}\Psi(\vec{r},\vec{\Omega},E,t)\approx\frac{\Psi(t+\Delta t)-\Psi(t)}{\upsilon\Delta t}=\frac{\Psi^{(n+1)}-\Psi^{(n)}}{\upsilon\Delta t}, \qquad (4\text{-}17)$$

where $\Psi^{(n+1)}$ is the flux at time $t+\Delta t$, $\Psi^{(n)}$ is the predecessor at time t, and for the precursor equations:

$$\frac{d}{dt}c_i(\vec{r},t)\approx\frac{c_i(t+\Delta t)-c_i(t)}{\Delta t}=\frac{c_i^{(n+1)}-c_i^{(n)}}{\Delta t} \qquad (4\text{-}18)$$

For TORT-TD an implicit or backward approach for the time discretisation is selected that allows for larger time step size than with an explicit approach . The transport equation and the precursor equations with time discretisation and without external source term are:

$$\frac{1}{\upsilon\Delta t}\left(\Psi^{(n+1)}-\Psi^{(n)}\right)=\left(-\vec{\Omega}\cdot\nabla-\Sigma_t\right)\Psi^{(n+1)}+\iint_{4\pi}\Sigma_s(\vec{\Omega}'\to\vec{\Omega},E'\to E)\Psi'^{(n+1)}d\Omega'dE'$$
$$+\frac{(1-\beta)\chi_{prompt}(E)}{4\pi}\int\nu\Sigma_f(E')\phi^{n+1}dE'+\sum_{i=1}^{6}\frac{\chi^i_{delayed}}{4\pi}(E)\lambda_i c_i^{(n+1)} \qquad (4\text{-}19),$$

and

$$\frac{1}{\Delta t}\left(c_i^{(n+1)}-c_i^{(n)}\right)=-\lambda_i c_i^{(n+1)}+\beta_i\int_0^{\infty}\nu\Sigma_f(E')\phi^{(n+1)}dE' \qquad (4\text{-}20).$$

Rearranging the above equations (4-19),

(4-20) and starting with the precursor equations such that all terms with (n+1) are placed on the left, the terms depending on the previous time step (n) on the right yields for the precursor concentration at time (n+1):

$$c_i^{(n+1)} = \frac{1}{\Delta t}\left(\frac{1}{\Delta t} + \lambda_i\right)^{-1} c_i^{(n)} + \beta_i \int_0^\infty \nu\Sigma_f(E')\phi^{(n+1)} dE' \tag{4-21}$$

Inserting this into the transport equation (4-19) and rearranging yields

$$\begin{aligned}&\left(\frac{1}{\upsilon\Delta t} + \Sigma_t\right)\Psi^{(n+1)} + \vec{\Omega}\cdot\nabla\Psi^{(n+1)} - \iint_{4\pi}\Sigma_s\left(\vec{\Omega}'\to\vec{\Omega}, E'\to E\right)\Psi'^{(n+1)} d\Omega' dE' \\ &-\left(\frac{\chi_{prompt}(E)}{4\pi}(1-\beta) + \sum_{i=1}^{6}\frac{\chi_{delayed}^{i}(E)}{4\pi}\lambda_i\left(\frac{1}{\Delta t} + \lambda_i\right)^{-1}\beta_i\right)\int_0^\infty \nu\Sigma_f(E')\phi^{(n+1)} dE' = \\ &\frac{1}{\upsilon\Delta t}\Psi^{(n)} + \sum_{i=1}^{6}\chi_{delayed}^{i}(E)\lambda_i\frac{1}{\Delta t}\left(\frac{1}{\Delta t} + \lambda_i\right)^{-1} c_i^{(n)}\end{aligned} \tag{4-22}$$

The right side will be a so called time dependent neutron source

$$S' = \frac{1}{\upsilon\Delta t}\Psi^{(n)} + \sum_{i=1}^{6}\frac{\chi_{delayed}^{i}(E)}{4\pi}\lambda_i\frac{1}{\Delta t}\left(\frac{1}{\Delta t} + \lambda_i\right)^{-1} c_i^{(n)} \tag{4-23}$$

and a modified total cross section will be introduced

$$\Sigma_t' = \frac{1}{\upsilon\Delta t} + \Sigma_t \tag{4-24}$$

together with a modified spectrum

$$\chi'(E) = \left(\frac{\chi_{prompt}(E)}{4\pi}(1-\beta) + \sum_{i=1}^{6}\frac{\chi_{delayed}^{i}(E)}{4\pi}\lambda_i\left(\frac{1}{\Delta t} + \lambda_i\right)^{-1}\beta_i\right). \tag{4-25}$$

Inserting all these abbreviations into the equation (4-22) leads to the following equation:

$$\Sigma_t'\Psi + \vec{\Omega}\cdot\nabla\Psi - \iint_{4\pi}\Sigma_s\left(\vec{\Omega}'\to\vec{\Omega}, E'\to E\right)\Psi' d\Omega' dE' - \chi'(E)\int_0^\infty \nu\Sigma_f(E')\phi dE' = S' \tag{4-26}$$

Now, the problem was transformed in a way that the transient solution of the transport equation is formally reduced to a source problem and the same solution methods as for the external source problem can be applied. However, the time step size must be determined.

Determination of flux at next time step

For the determination of time steps one assumes that the spatially resolved group fluxes can be approximated by an exponential function

$$\psi_g^{\tau+1}\left(\vec{r},\vec{\Omega}\right) = \psi_g^{\tau}\left(\vec{r},\vec{\Omega}\right)\cdot e^{\omega_g\left(\vec{r},\vec{\Omega}\right)\Delta t} \tag{4-27}$$

where $\omega_g\left(\vec{r},\vec{\Omega}\right)$ is the inverse spatially resolved reactor period for group g which is given by

$$\omega_g\left(\vec{r},\vec{\Omega}\right)=\frac{1}{\Delta t}\ln\frac{\psi_g^{\tau+1}\left(\vec{r},\vec{\Omega}\right)}{\psi_g^{\tau}\left(\vec{r},\vec{\Omega}\right)} \tag{4-28}$$

The reactor period ω^{-1} is the time when the power increases by a factor of $e\approx 2.7182$.

Using this spatially resolved reactor period will also allow solving problems where the spatial flux is subject to strong changes. This reactor period is also used in TORT-TD to determine the time step size of the next time step by evaluating the numerical truncation error. TORT-TD has been validated for LWR applications with and without thermal hydraulic feedback [54] [75][76].

4.5.1 Other features of TORT-TD

TORT-TD does not only have the option to solve the transport equation in the way described above, but also offers the possibility to apply diffusion theory. This simplification that leaves out angular dependence of scattering is less accurate and exposes deficiencies in areas where strong flux gradients are present (absorbers). Also, the diffusion approach needs an approximation for the flux on the boundaries of the computational domain. Here, use is made of the transport cross section. Generally, the results of the transport equation are more accurate for the above mentioned reasons. Nevertheless, the diffusion option has great advantages with respect to computational times. Therefore, the diffusion option is used for all transient calculations of the HTR-PM (water ingress, ejection of one control rod). For the HTR-10 and the PBMR, the transport option was used.

For transient calculations, additional equations to account for the Iodine-135/Xenon-135 dynamics are implemented. Xe-135 is by far the strongest neutron absorber and accounts for approximately 2.8 % of reactivity [24]. When the reactor is running at constant power, I-135 and Xe-135 are in equilibrium. When the power is lowered, less I-135 is produced and the I-135 concentration will, in the long run, reach the equilibrium at this reduced power level (lower). However, the I-135 decays to Xe-135. This leads to a massive increase in the concentration of Xe-135 which leads to increased absorptions in the xenon. This effect in reality has to be compensated by pulling of the control elements.

Every reactor – after a certain time of operation – produces decay heat because it has a lot of fission products that emit particles and/or energy (alpha, beta, gamma, neutron radiation). To account for this heat production after shutdown of the reactor, decay heat production is implemented in TORT-TD according to the German industrial standard DIN 25 485.

4.6 The thermal fluid dynamic tool (ATTICA^{3D})

The Advanced Thermal fluid dynamic Tool for In-vessel and Core Analysis in 3 Dimensions (ATTICA^{3D}) is the thermal fluid dynamic component of the coupled HTR simulation system TORT-TD/ATTICA^{3D}. Its purpose is to compute the temperature distribution of the solid and the coolant, along with the gas velocities within the reactor pressure vessel and, outside the reactor pressure vessel, the heat transport by radiation, conduction or both to the final heat sink, the reactor cavity cooling system (RCCS).

ATTICA^{3D} was derived by modifying a multi-phase core melt programme MESOCO that allows for several different phases (solid, liquid and gaseous water, gas). Detailed description of method and models can be found in [100].

ATTICA^{3D} makes use of the porous media approach where subdivision between the solid and the fluid volume is done by the porosity parameter ε omitting detailed geometrical description of the respective phases.

$$\varepsilon = \frac{V_{gas}}{V_{solid} + V_{gas}} = \frac{V_{gas}}{V_{total}} \tag{4-29}$$

Here, the porosity ε is the ratio of gas volume to total volume. The porous media approach assumes that a certain component is homogeneously porous throughout the whole component volume. ATTICA^{3D} allows for a thermal non-equilibrium between gas and solid phase.

4.6.1 Conservation equations

In ATTICA^{3D} a mixture of multiple gas components can be simulated. The mixtures are treated as ideal mixtures that are assumed to flow with the same velocity $\vec{u}$. The mass conservation equations are solved for each gas component:

$$\frac{\partial}{\partial \mathrm{t}}\left(\varepsilon \rho_g c_k\right) + \nabla \cdot \left(\varepsilon \rho_g c_k \vec{u}\right) = 0 \tag{4-30}$$

Here, ε denotes the porosity, ρ_g the density of the gas mixture, $\vec{u}$ the velocity vector, c_k the mass fraction of component k. The single gas components are summed up to yield the total mass conservation equation

$$\frac{\partial}{\partial t}\left(\varepsilon \rho_g\right) + \nabla \cdot \left(\varepsilon \rho_g \vec{u}\right) = 0 \tag{4-31}$$

with ρ_g as the gas mixture density and $\vec{u}$ as the velocity. The momentum equation is expressed by a simplified, steady-state approach according to Ergun [62]:

$$\varepsilon \cdot \nabla p = -\vec{R} - \varepsilon \rho_g \vec{g} \tag{4-32}$$

Here, p denotes the pressure, $\vec{R}$ the friction forces and $\vec{g}$ the gravitational acceleration. The simplified equation can be formulated due to the fact that friction forces and gravity body force are dominating over the inertial forces.

The energy conservation equation for the gas has the form

$$\varepsilon \frac{\partial}{\partial t}(\rho_g e_g) + \nabla \cdot (\varepsilon \rho_g \vec{u} h_g) = \nabla\left[\varepsilon \cdot \lambda_{g,eff} \cdot \nabla T_g\right] + Q_{conv} \tag{4-33}$$

Here, e_g, h_g and T_g denote the specific internal energy, specific enthalpy and temperature of the gas, respectively. Heat fluxes due to convection and conduction are considered. An effective heat conductivity $\lambda_{g,eff}$ is applied in order to take into account effects of turbulent dispersion.

For the solid phase, the energy conservation equation is given as

$$(1-\varepsilon)\frac{\partial}{\partial t}(\rho_s h_s) = \nabla\left[(1-\varepsilon) \cdot \lambda_{s,eff} \cdot \nabla T_s\right] - Q_{conv} + Q_{nuclear} \tag{4-34}$$

Here, h_s and T_s denote specific enthalpy and temperature of the solid. Again, an effective heat conductivity for the solid is applied. Q_{conv} and $Q_{nuclear}$ are volumetric heat sources due to convective heat exchange between solid and gas and nuclear heating, respectively.

4.6.2 Constitutive equations

The conservation equations give a set of differential equations that has to be solved iteratively. For closure of the equations, to provide boundary conditions, heat transfer

coefficients, heat conductivities, gas densities use is made of a set of constitutive equations.

4.6.2.1 Friction coefficients

The pressure drop in the pebble bed is calculated according to KTA-rule 3102.3 [82], valid for the range of void fraction 0.36 ≤ ε ≤ 0.42, a diameter d of pebble to total pebble bed diameter ratio of $5 \cdot d \le D$, a minimum bed height $H > 5d$, and a range of Reynolds number $10^0 < \mathrm{Re}/(1-\varepsilon) \le 10^5$. These preconditions are fulfilled for a pebble bed reactor, in general. The Reynolds number is calculated by

$$\mathrm{Re} = \frac{\left(\frac{\dot{m}}{A}\right) d}{\eta} \tag{4-35}$$

and the pressure drop for the pebble bed by the proposed KTA correlation

$$\vec{R} = \frac{dp}{dH} = \Psi \frac{1-\varepsilon}{\varepsilon^3} \frac{1}{d} \frac{1}{2\rho} \left(\frac{\dot{m}}{A}\right)^2 \tag{4-36}$$

Here, $\dot{m}$ denotes the mass flow rate, A the cross section area of the pebble bed, d the pebble diameter, η the dynamic viscosity, dp the pressure loss for the part of the pebble bed, dH height of the considered pebble bed part, ε the porosity, ρ the gas density and Ψ_f as the friction coefficient that can be computed by

$$\Psi_f = \frac{320}{\frac{\mathrm{Re}}{1-\varepsilon}} + \frac{6}{\left(\frac{\mathrm{Re}}{1-\varepsilon}\right)^{0.1}} \tag{4-37}$$

For the other parts the pressure drop is calculated an approach for smooth tubes with the help of the pressure loss coefficient λ which is given by the combined correlation for laminar flow and the Blasius correlation of the Reynolds number for turbulent flow:

$$\lambda_p = \frac{64}{\mathrm{Re}} + 0.3164\ \mathrm{Re}^{-0.25} \tag{4-38}$$

and for the pressure drop

$$\vec{R} = \frac{dp}{dH} = \lambda_p \frac{1}{d} \frac{\rho u^2}{2} \tag{4-39}$$

with u as superficial velocity $u_{superficial} = \frac{u}{\varepsilon}$.

4.6.2.2 Equation of state and transport properties of the gas phase

The solution variables of the gas phase are the pressure p, the gas temperature T_g and the gas component volume fractions χ_k. In the case that multiple gas components are simulated, it is assumed that Dalton's law holds, i.e. sum of partial pressures of the gas components yields total pressure:

$$p = \sum_{k=1}^{N_g} p_k \tag{4-40}$$

The partial pressures p_k can be expressed by the respective volume fraction χ_k using

$$p_k = \chi_k \cdot p \tag{4-41}.$$

The equation of state for the gas is of the form

$$\rho = \rho\left(p, T_g\right) \tag{4-42}$$

and for the gas enthalpy h

$$h = h\left(p, T_g\right) \tag{4-43}$$

The properties of the gas mixture, consisting of N_g components, can then be calculated:

$$\rho_g = \sum_{k=1}^{N_g} \rho_k \tag{4-44}$$

$$c_k = \frac{\rho_k}{\rho_g} \tag{4-45}$$

$$h_g = \sum_{k=1}^{N_g} c_k \cdot h_k \tag{4-46}$$

$$c_{p,g} = \sum_{k=1}^{N_g} c_k \cdot c_{p,k} \tag{4-47}$$

with $c_{p,k}$ as the heat capacity of the component k, c_k as the mass fraction of the gas component k, and the index g as the property of the whole gas mixture

The density ρ of the gas component is then calculated by the ideal gas law for the component k

$$\rho_k = \frac{p_k}{R_k \cdot T_g} \tag{4-48}$$

where R_k is the specific gas constant of the component k for the gas or for pure helium (without any other gas component)

$$\rho_{He} = \frac{p_{He}}{R_{He} \cdot T_g \cdot \left(1 + \frac{4.4486 \cdot 10^{-6}}{T_g^{1.2}}\right)} \tag{4-49}$$

as specified in [82] for the helium properties to be used for HTRs.

This approach of ideal gases can be used instead of using properties of real gases since real gases behave like ideal gases under conditions of low concentration and high temperatures [79][80], which is given in a high temperature reactor.

The gas enthalpy is calculated according to

$$h = h_T + h_p + h_0 \tag{4-50}$$

with

$$h_T = c_{p,0} \cdot \left(T_g - T_0\right) \tag{4-51k}$$

as the temperature dependent enthalpy and T_0 as 273.16 K and for helium a pressure dependent enthalpy

$$h_p = R_{He} \cdot 5.3376 \cdot 10^{-6} \cdot \left(p_k - p_0\right) \cdot T_g^{-0.2} \tag{4-52}$$

with $p_0 = 1 \cdot 10^5 Pa$. For the other gases $h_p = 0$, and $h_0 = 0$ for all gases except steam $h_0 = 2.0364709 \cdot 10^6 J \cdot kg^{-1}$. Gases already implemented in ATTICA^{3D} are helium, nitrogen, hydrogen, oxygen, air and steam.

Other gas properties for the above mentioned gases are given in the Table 3 below.

Table 3: Gas properties as implemented in ATTICA^{3D}

Gas	Gas constant R, $\left[\frac{J}{kg \cdot K}\right]$	Heat capacity c_p, $\left[\frac{J}{kg \cdot K}\right]$	Heat conductivity λ $\left[\frac{W}{m \cdot K}\right]$	Dynamic viscosity η, $\left[\frac{kg}{m \cdot s}\right]$
He	2,077.3	5,195	$\lambda = 2.682 \cdot 10^{-3} \cdot \left(1 + 1.123 \cdot 10^{-3} \cdot p\right) \cdot T^{0.71 \cdot (1 - 2 \cdot 10^{-4} p)}$	$\eta = 3.674 \cdot 10^{-7} * T^{0.7}$
H_2	4,128.1	14,985	$\lambda = 1.097 \cdot 10^{-3} T^{0.8785}$	$\eta = 84.1 \cdot 10^{-7} \cdot \left(\frac{T}{T_0}\right)^{(0.674 - 0.0341 \cdot 10^{-4} T_g)}$
N_2	296.8	1,043	$\lambda = 5.314 \cdot 10^{-4} T^{0.6898}$	$\eta = 166.3 \cdot 10^{-7} \cdot \left(\frac{T}{T_0}\right)^{(0.753 - 1.3 \cdot 10^{-40} T_g + 0.4 \cdot 10^{-7} * T_g^{\,2})}$
O_2	259.2	943	$\lambda = 1.853 \cdot 10^{-4} T^{0.8729}$	$\eta = 191.9 \cdot 10^{-7} \cdot \left(\frac{T}{T_0}\right)^{(0.760 - 1.4 \cdot 10^{-4} T_g + 0.64 \cdot 10^{-7} * T_g^{\,2})}$
Air	287.1	1,011.7	$\lambda = 0.21 \lambda_{O_2} + 0.79 \lambda_{N2}$	$\eta = 0.21 \cdot \eta_{O_2} + 0.79 \cdot \eta_{N2}$
H_2O	461.5	$c_p = c_p\left(h, {}_g T_g\right)$ *	$\lambda = -1.9793 \cdot 10^{-3} + 5.126 \cdot 10^{-5} \cdot T + +4.9441 \cdot 10^{-8} \cdot \mathrm{T}^2$	$\eta = -3.1065 \cdot 10^{-6} \cdot + 4.07 \cdot 10^{-8} T_g$

* $c_{p,H2O} = 1.5763 \cdot 10^3 + T_g \cdot \left(8.4430 \cdot 10^{-1} - 1.27918 \cdot 10^{-4} \cdot T_g\right)$.

4.6.2.3 Solid properties

ATTICA^{3D} has a data base for the commonly used solid materials in high temperature reactors. Some of the solids are actually of gaseous nature, but in cases of narrow gas filled gaps with low radiative heat transfer, this modelling can yield more realistic values since the heat transfer is dominated by the heat conductivity of the gas.

Table 4: Properties of the solids

Material	Mass density ρ, $\left[\frac{kg}{m^3}\right]$	Emissivity ε_{rad}, [–]	Heat capacity c_p, $\left[\frac{J}{kg \cdot K}\right]$	Heat conductivity λ, $\left[\frac{W}{m \cdot K}\right]$
Graphite moderator	1,740	0.8	$c_p = 6.409332 \cdot 10^2 + 3.028911 \cdot T_s - 2.927339 \cdot 10^{-3} \cdot T_s^{\,2} + 1.271449 \cdot 10^{-6} \cdot T_s^{\,3} - 1.979401 \cdot 10^{-10} \cdot T_s^{\,4} - 1.64070 \cdot 10^{-14} \cdot T_s^{\,5} + 5.711734 \cdot 10^{-18} \cdot T_s^{\,6}$, T_s *in* °C	$\lambda = 20$
Graphite reflector	1,790	0.8	$c_p = \frac{10^6}{\rho}(1.239122 + 3.376758 \cdot 10^{-3} \cdot T_s - 2.693509 \cdot 10^{-7} \cdot T_s^{\,2} - 3.429188 \cdot 10^{-9} \cdot T_s^{\,3} + 6.1465372 \cdot 10^{-12} \cdot T_s^{\,4} - 6.265853 \cdot 10^{-15} \cdot T_s^{\,5} + 2.534463 \cdot 10^{-18} \cdot T_s^{\,6})$, T *in* °C	$\lambda = 20$
UO_2	10,400	0.85	$c_p = 2.3769171 \cdot 10^2 + 2.2857672 \cdot 10^{-1} \cdot T_s - 2.3812001 \cdot 10^{-4} \cdot T_s^{\,2} + 1.0315094 \cdot 10^{-7} \cdot T_s^{\,3} - 8.716 \cdot 10^{-12} \cdot T_s^{\,4}$	$\lambda = 8.96285275 - 1.59467091 \cdot 10^{-2} \cdot T_s + 2.05935666 \cdot 10^{-5} \cdot T_s^{\,2} - 1.67532577 \cdot 10^{-8} \cdot T_s^{\,3} + 7.89962261 \cdot 10^{-12} \cdot T_s^{\,4} - 1.92244449 \cdot 10^{-15} \cdot T_s^{\,5} + 1.89402387 \cdot 10^{-19} \cdot T_s^{\,6}$
He	1.4	0.85	5,195	$\lambda = 2.682 \cdot 10^{-3} \cdot (1 + 1.123 \cdot 10^{-3} \cdot p) \cdot T^{0.71 \cdot (1 - 2 \cdot 10^{-4} p)}$
Air	1.4	0.7	1,006	$\lambda = 5.14^{-4} T^7$

4.6.2.4 Calculation of heat transfer by convection

For heat transfer between a free solid surface and an adjacent cell with gas (e.g. in the cavity above the pebble bed) either a constant heat transfer coefficient α can be provided or a heat transfer correlation of Dittus-Boelter can be selected. The constant heat transfer is usually used for boundary conditions while the Dittus-Boelter correlation can only be used within the computational domain. The Dittus-Boelter correlation defines the Nusselt number as

$$Nu = 0.023\,\mathrm{Re}^{0.8}\,\mathrm{Pr}^{0.3} \tag{4-53}$$

with *Reynolds* and *Prandtl* number, $\mathrm{Pr} = \frac{c_p \cdot \eta}{\lambda}$., with c_p as heat capacity, η as the dynamic viscosity and λ as heat conductivity. For the heat transfer coefficient

$$\alpha = \frac{\lambda \cdot Nu}{d_h} \tag{4-54}$$

with λ as the heat conductivity and d_h as the hydraulic diameter.

4.6.2.5 Calculation of heat transfer by thermal radiation

The heat transfer in the void and especially narrow gaps ($l_{gap} << h_{gap}$) is calculated by the Stefan-Boltzmann Law for the averaged zone temperatures T regarding the facing area A:

$$Q_{rad} = \varepsilon_{rad}\sigma_{SB}A\left(T_1^4 - T_2^4\right) \tag{4-55}$$

with the power Q, ε_{rad} as the emissivity of the surface and the Stefan-Boltzmann-Constant $\sigma_{SB} = 5.67 \cdot 10^{-8}$ $\left[\frac{W}{m^2 \cdot K^4}\right]$.

4.6.2.6 Calculation of effective heat conductivities

The energy conservation equations of both solid and gas contain terms with an effective heat conductivity λ_{eff}. This effective heat conductivity has to be computed because in the porous medium approach components with flow are characterised as homogeneous media with a distinctive porosity and a distinctive hydraulic diameter. E.g. for the pebble bed, the porosity is 0.39 and the hydraulic diameter is 0.06 m. In the pebble bed, λ_{eff} takes into account the heat conduction through solid, the heat radiation, convection, as well as gas conduction and radiation. The determination of λ_{eff} for different

parts of the reactor geometry, and especially the pebble bed, are well described in [35] [30].

4.6.3 The Heterogeneous Fuel Temperature Model

To capture the feedback of thermal hydraulics on neutronics a quasi-steady-state heterogeneous temperature model for the fuel pebble (Figure 9) is implemented. This consideration is necessary, since fission heat is mainly generated in the uranium kernel and not in the surrounding graphite. In fast transients, the temperature difference between the fuel kernel and graphite can be substantial. This pronounces strong feedback effects from the fuel Doppler temperature. In the heterogeneous temperature model, the fuel is subdivided into an arbitrary number n of spherical shells, see Figure 9 and Figure 10, in this example n = 6. The heterogeneous temperature model was initially introduced by Hossain [35] but was modified for an additional layer, i.e. the layers were all accounted for (kernel, buffer zone, PyC layer, SiC layer, PyC layer) and not averaged. The different possible heterogeneous temperature models and their consequence on the fuel temperature feedback were investigated in detail in [78] and the conclusion is that there is only a minor difference in the time-dependent and quasi steady state approach to solve the heat conduction equation. The assumption for the investigation was a fast control rod ejection where the reactivity insertion was most severe and the consequences of the temperature models were most pronounced. For other cases like control rod withdrawal or water ingress the time for a particle to reach temperature equilibrium with the surrounding graphite is short in comparison with the time of the transient so the quasi steady-state model is considered sufficient. Therefore, the quasi steady-state heterogeneous temperature model is kept.

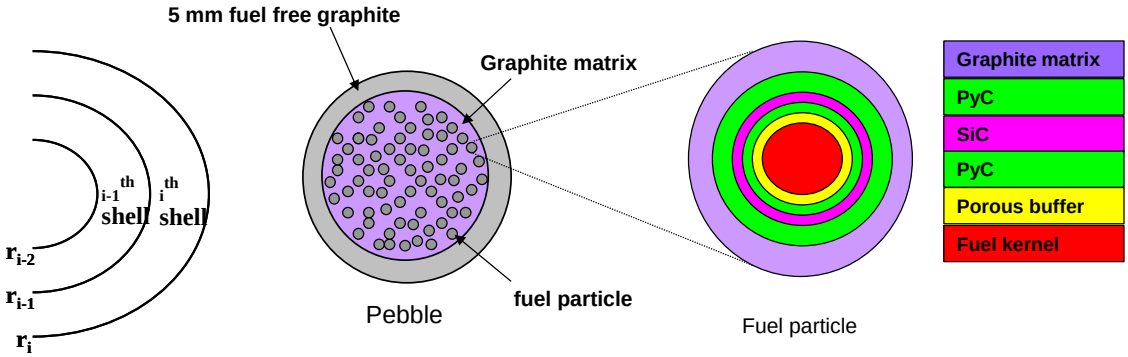

Figure 9: Subdivision of a fuel element when applying the heterogeneous temperature model

Starting from the surface of the fuel element (ith shell or graphite matrix, here i = 6), the steady-state heat conduction equation in spherical geometry for each shell is solved successively towards the fuel element centre (i-1st shell, then i-2nd shell and so on).

$$\frac{d}{dr}\left[r^2\lambda\frac{dT_s}{dr}\right] = -Q_{i,nuc}r^2 \tag{4-56}$$

with r as the radius, λ as the heat conductivity, T_s as the solid temperature and $Q_{i,nuc}$ as the volumetric power produced in the ith shell (assumed constant over a shell).

The surface temperature of the fuel element is taken as the boundary condition to start the calculation. Mean temperatures are calculated for successive fuel shells, until the innermost shell. These temperatures, however, only apply to the graphite shells, not the fuel kernels. Typical temperature profiles for the moderator temperatures are given in Figure 10.

In order to determine the particle temperature within a shell, the respective shell temperature of the surrounding graphite serves as boundary condition and the heat conduction equation is solved for the micro system once more, taking into account the different heat conductivities of the coatings of the particles (Figure 11). After fuel and moderator temperatures are determined, the temperature values are averaged volumetrically and one fuel temperature and moderator temperature per thermal hydraulic mesh is obtained to process nuclear cross sections. Thus, fuel temperature feedback is much more pronounced than it is without the heterogeneous fuel temperature model. In Figure 10 and Figure 11, typical temperature profiles during steady-state are presented for a pebble in the central bottom part of the PBMR.

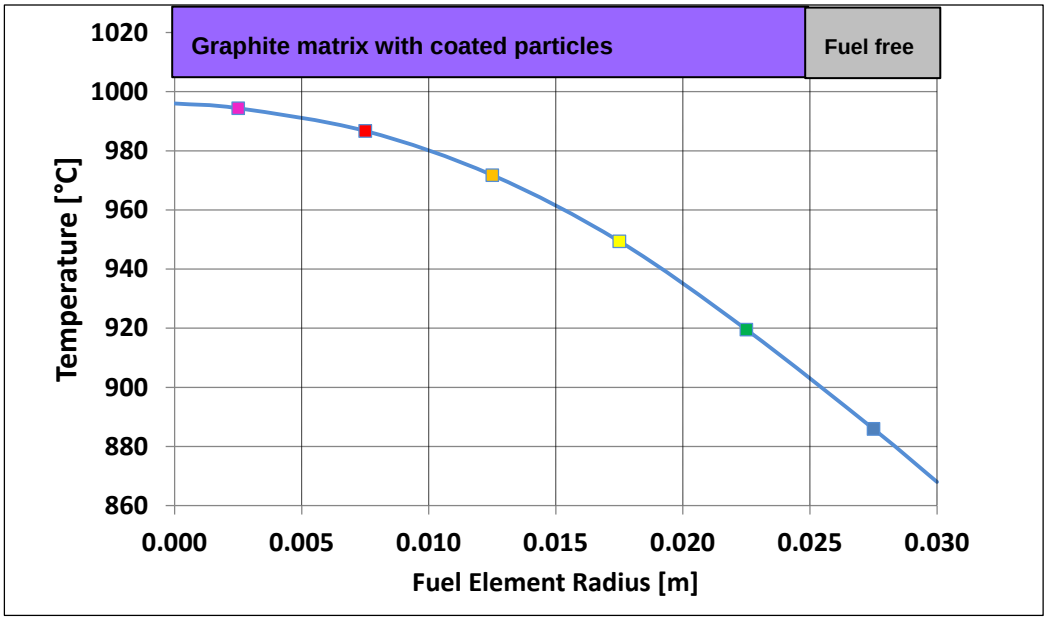

Figure 10: Temperature distribution after solving the heat conduction equation for the fuel pebble, delivering boundary conditions for the coated particle temperature calculation

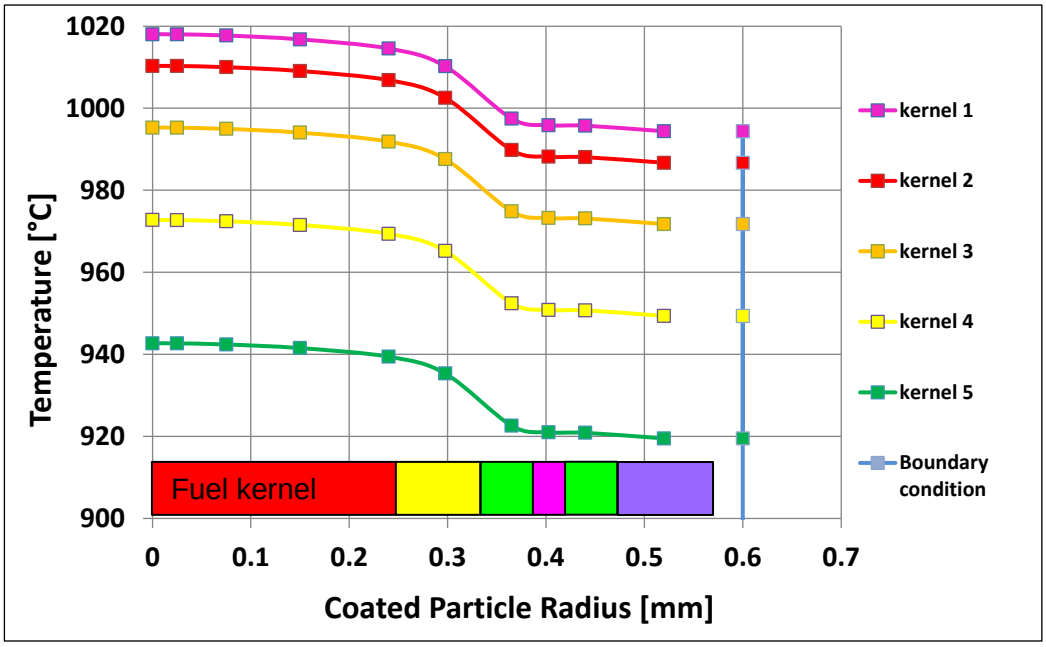

Figure 11: Temperature distribution for the representative kernels per shell. The blue bar on the right side visualises the boundary condition after solving the heat conduction equation and is coloured like the results of the graphite shells from Figure 10. The colouring at the bottom corresponds to the graphite layers in Figure 9

4.7 Numerical solution methods

The general numerical solution approach is to solve the partial differential equation system that consists of the conservation equations of mass, momentum and energy of the phases, together with the constitutive equation introduced above. The approach for the numerical solution of this system in ATTICA^{3D} can be subdivided into two general steps:

- The spatial solution of the equation system: In order to map the three-dimensional space on a discrete grid, the solution domain is discretised spatially by making use of the finite volume method.
- The time integration is done by subdividing time into a sequence of time steps approximating the partial derivatives w.r.t. time of the solution variables by differences that are evaluated at the actual and previous time levels. In ATTICA^{3D} the method of backward differencing formulae is applied.

The implementation of the numerical solution methods was not done within this work. For a description of the methods, see Appendix, chapter 9.1 and in more detail in [100].

4.8 Extensions for air and steam ingress

In an HTR, graphite is abundant within the fuel and the reflector structures. Since graphite is a special kind of carbon, it will react with either oxygen or steam if certain temperature thresholds are exceeded.

Chemical reactions depend on temperature. At low temperatures, i.e. below a certain threshold temperature there is no chemical reaction. For graphite consisting of graphitised carbon and binder the microscopic structure is formed by grain with crystallites and micro-pores which are kept together by binder material. The binder, due to the manufacturing processes, contains macro-pores as a consequence of the disappearance of volatile substances. Graphite is therefore a material with a porous structure. When corrosive substances like steam or oxygen encounter hot graphitic surfaces chemical reaction can occur. For corrosion of nuclear grade graphite with oxygen the threshold temperature is 450°C, for corrosion with steam this temperature was found to be 850°C, [59][62][68][69].

Above the threshold temperatures, there are three ranges of corrosion:

a. The chemical kinetics controlled regime: the temperature of the reaction surface is low enough that diffusion of the reactants is possible throughout the volume, the corrosion attacks the volume of graphite nearly homogeneously

b. The in-pore diffusion controlled regime: with elevated temperatures, the reactants can only diffuse a short distance within the graphite before undergoing reaction, this leads to the formation of a corrosion profile.

c. The boundary layer diffusion controlled regime: at very high temperatures, all corrosion takes place in a thin boundary layer outside the graphite,

The range of temperatures for air and steam ingress is presented in Table 5

Table 5: Temperature dependent regimes for corrosion

	Air ingress [86]	Steam ingress [87]
Chemical range	< 700°C	< 900 °C
In-pore diffusion range	700 – 1,000°C	900 – 1200°C
Boundary layer diffusion controlled regime	> 1,000°C	> 1,200°C

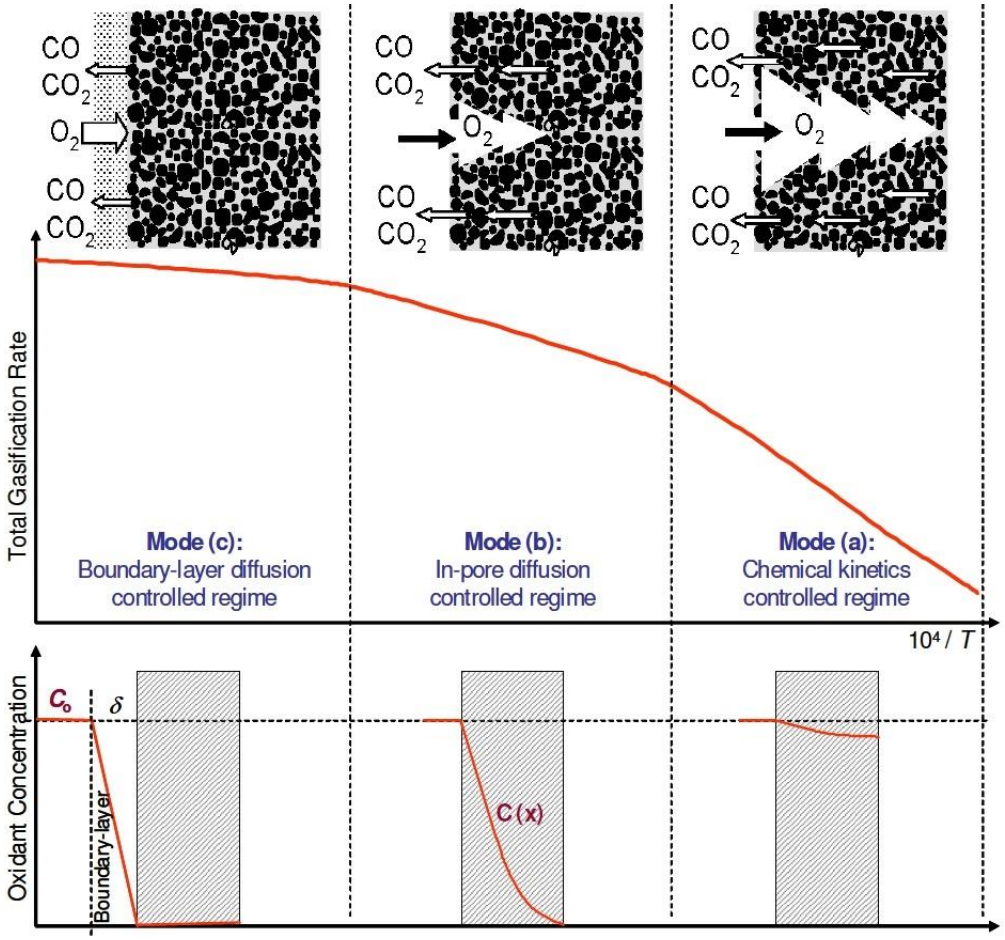

Figure 12: Phenomenology of the graphite corrosion [88]

The most important temperature range for corrosion is the in-pore diffusion controlled regime, for which most of the experiments were performed. Since the chemical range exhibits great uncertainties and low corrosion rates, and in the boundary layer diffusion controlled regime corrosion rates only increase slightly with temperature, only the in-pore diffusion controlled regime is implemented in ATTICA^{3D}. The corrosion rates for the higher temperatures are overestimated by using the correlation for the in-pore diffusion controlled regime which gives conservative estimates. Also, the regime with elevated temperatures is always surrounded by regions of lower temperature where the correlation described below is appropriate. In cases of air ingress, the regions of the boundary layer diffusion range will not see any oxygen needed for the oxidation in case of steam corrosion, the reaction rates are conservatively overestimated. In the 1980s and 90s, significant efforts were made to determine the reaction rates of different candidates for both fuel and reflector graphite (A3-3, A3-27 as fuel sphere materials, V483T, ASR-1RS, ASR-1RG, ATR-2E as reflector graphite). This chapter will describe the introduced modifications needed in order to be able to properly address air and especially water ingress simulations. The latter is important since steam ingress leads

to an increase in moderation and also has long term effects (corrosion of graphite in presence of steam) that can weaken load-carrying structures. The relevant reactions for the air ingress are given in Table 6 below; for water/steam ingress see Table 7.

Table 6: Relevant reactions for the air ingress

Reaction	$\Delta H, \left[\frac{kJ}{kg}\right]$	homogeneous/heterogeneous, primary, secondary
$2 \cdot C + O_2 \rightarrow 2 \cdot CO$	-221	heterogeneous, primary
$C + O_2 \rightarrow CO_2$	-393.3	heterogeneous, primary
$2 \cdot CO + O_2 \rightarrow 2 \cdot CO_2$	-565	homogeneous, secondary
$CO_2 + C \rightarrow 2 \cdot CO$	$+172.47$	heterogeneous, secondary

Table 7: Relevant reactions for the steam ingress

Reaction	$\Delta H, \left[\frac{kJ}{kg}\right]$	homogeneous/heterogeneous
$C + H_2O \rightarrow CO + H_2$	$+131.31$	heterogeneous, primary
$CO + H_2O \rightarrow CO_2 + H_2$	-41.6	homogeneous, secondary
$CO_2 + H_2 \rightarrow CO + H_2O$	$+41.6$	homogeneous, secondary
$CO_2 + C \rightarrow 2 \cdot CO$	$+172.47$	heterogeneous, secondary

In Table 6 and Table 7 above, the relevant reactions are presented. Here, the occurring reactions are classified in heterogeneous/homogeneous and primary/secondary reactions. I.e. the primary reaction is always the reaction of the gas (oxygen or steam) with the hot graphite and hence, heterogeneous since the gas phase reacts with the solid phase. Homogeneous means that gases react in the free gas volume which is independent of the provenience of the graphite. For the water ingress, there can also be methane (CH_4) production, but the precondition is high hydrogen partial pressures. This can be excluded for water ingress since the steam partial pressure is only a fraction of the total pressure (4 bar partial pressure compared to 74 bar of total pressure, [25]).

4.8.1 Introducing new gas components, chemical heat and enthalpy transport into ATTICA^{3D}

In order to capture the produced gas masses additional terms are introduced in the total mass conservation equation. The new terms are highlighted in red.

In ATTICA^{3D}, a mixture of gas components can be simulated. Multiple gas types are implemented and can be used (steam, CO, CO_2, nitrogen, air). Time dependent, compressible mass conservation equations are solved for each component of the gas phase:

$$\frac{\partial}{\partial t}\left(\varepsilon \rho_g c_k\right) + \nabla \cdot \left(\varepsilon \rho_g c_k \vec{u}\right) = \dot{m}_k \tag{4-57}$$

Here, ε denotes the porosity, ρ_g the mass density of the gas, $\vec{u}$ the velocity vector, c_k the mass fraction of component k and $\dot{m}_k$ the volumetric mass production or consumption rate of component k due to chemical reactions.

Total mass conservation equation:

$$\frac{\partial(\varepsilon\rho_g)}{\partial t} + div(\varepsilon\rho_g\vec{u}) = \sum_{k=1}^{nc}\left(\sum_{n=1}^{nreac}\dot{m}_k^n\right) \tag{4-58}$$

with $k = 1,...,n_c$

Here, on the right hand new terms are introduced, the produced gases. c_k denotes the mass fraction of the component k and $\dot{m}_k^n$ is the generated gas mass per second. The sum operator comprises the mass sources from all possible chemical reactions from $n = 1,...,n_{reac}$. Also, for each new gas component k, that is water(steam), hydrogen, carbon monoxide and carbon dioxide, a separate mass conservation equation each is used to ATTICA^{3D}. Here, use of the equations for more than one gas component was made as in MESOCO [74].

Mass conservation equation for the single component:

$$\frac{\partial(\varepsilon\rho_{g,k}c_k)}{\partial t} + div\left(\varepsilon\rho_{g,k}\vec{u}c_k\right) = \sum_{n=1}^{nreac}\dot{m}_k^n \tag{4-59}$$

with $c_k = \frac{m_k}{m_{total}}$ and $\sum_{k=1}^{n_c} c_k = 1$.

Here, the newly introduced terms are on the right hand side are similar to the total mass equation but only for a single component. In the water ingress case there are four reactions considered.

In the energy equations of both solid and fluid new chemical heat sources are introduced. Depending on the nature of the reaction (heterogeneous or homogeneous) different heat sources are used. In the heterogeneous case, chemical heat will be added to the solid, whereas in the other case the heat is added to the fluid. Unlike in literature, chemical heat by endothermal reactions will be subtracted from the solid or fluid; chemical heat of exothermal reactions is added. For the fluid, an additional enthalpy transport for the different components is considered.

Energy conservation for the gas:

$$\varepsilon \frac{\partial}{\partial t}(\rho_g e_g) + \nabla \cdot (\varepsilon \rho_g \vec{u} h_g) = \nabla\left[\varepsilon \cdot \lambda_{g,eff} \cdot \nabla T_g\right] + Q_{conv} + \sum_{n=1}^{nreac} {}^{n}Q_{chem,\mathrm{hom}} + \sum_{k=1}^{nc}\sum_{n=1}^{nreac} \dot{m}_k^n h_k \quad (4\text{-}60)$$

Energy conservation for the solid:

$$(1-\varepsilon)\frac{\partial}{\partial t}(\rho_s h_s) = \nabla\left[(1-\varepsilon) \cdot \lambda_{s,eff} \cdot \nabla T_s\right] - Q_{conv} + Q_{nuclear} + \sum_{n=1}^{nreac} {}^{n}Q_{chem,het} \quad (4\text{-}61)$$

The momentum equation is not changed.

In order to obtain the heat produced or consumed by chemical reaction, experimental data had to be obtained. Here, mainly contributions of the Jülich research centre from the early eighties and nineties were used, see [62][66][68][73]. It has to be mentioned that compared to the experiments performed for air ingress only a small data base is available. This is owed to the fact that corrosion with steam has far less tendency to weaken the graphitic parts compared to air ingress.

It could be shown experimentally that the corrosion behaviour can be described best with a Langmuir-Hinshelwood equation. This equation uses Arrhenius terms, but also accounts for inhibiting effects of product and educt gases on certain reactions.

Langmuir-Hinshelwood equation [66]:

$$RR = \frac{k_{01}\exp\left(\frac{-E_{a1}}{R \cdot T}\right) \cdot p_{educt} \cdot f(Burn-off) \cdot p_{total}}{1 + k_{02}\exp\left(\frac{-E_{a2}}{R \cdot T}\right) \cdot \sqrt{p_{educt}} + k_{03}\exp\left(\frac{-E_{a3}}{R \cdot T}\right) \cdot \sqrt{p_{product}}} \quad (4\text{-}62)$$

Here, *RR* is the reaction rate of a component, e.g. graphite reacts with H2O in form of steam, but this reaction will be slowed down by the abundance of hydrogen. k_{01} de-

notes a so called frequency factors, the exponential term contains the activation energy E_{a1}, the general gas constant and the temperature (Arrhenius term). The Arrhenius term is multiplied by a function of burn-off *f(burn-off)* of graphite. This value ranges from 0.2 for the un-corroded graphite up to 1 for maximum graphite burn-off. The physical reason for this is the opening of previously closed pores within the graphite, offering an increased internal surface for reaction. Also, the partial pressure of the educt and the product are relevant, and the equation can contain a dependence on total pressure p_{total}. In the denominator, one finds two Arrhenius terms multiplied by the partial pressure's square root. Depending on the material and the chemical reaction considered, these inhibiting terms have to be taken into account. For the different graphite types the corrosion behaviour can vary; inhibiting terms may be zero for some graphite specimens.

4.8.2 Water ingress

For the modelling of corrosion due to water ingress experimentally determined reaction rates are employed. These comprise the heterogeneous reactions, since the homogeneous reactions (reaction of carbon monoxide with steam) do not depend on the nature of graphite, i.e. the carbon monoxide does not remember its provenience. The correlation of the primary heterogeneous reaction (eq. (4-63)) is valid for a H_2O partial pressure range of 0.03 bar < p_{H2O} < 5 bar and a graphite burn-off of approximately 2%.

Primary heterogeneous reaction:

The primary heterogeneous reaction ($C + H_2O \rightarrow CO + H_2$) yields a graphite reaction rate RR of:

$$RR_{Graphite} = \frac{6.4 \cdot 10^{11} \cdot \exp\left(-\frac{256{,}000}{8.315 \cdot T}\right) \cdot p_{H_2O}^{0.44}}{1 + 7.5 \cdot 10^{-5} \cdot \exp\left(\frac{121{,}000}{8.315 \cdot T}\right) \cdot p_{H_2}^{0.9} \cdot p_{H_2O}^{-0.4}} \quad \left[\frac{mg}{cm^2 \cdot h} = \frac{10^{-2} kg}{3.6 \cdot 10^3 \ m^2 \cdot s}\right] \quad \text{(4-63)}$$

This correlation is taken out of [68] and will be used as graphite corrosion rate for steam with graphite. Here, p_{H2}, p_{H2O} denote the partial pressures in bar. There are other correlations but these were determined for varying total pressures and graphite burn-off whilst keeping the steam partial pressure constant (at 474 mbar), no partial pressure or temperature dependency is derived, see [69].

With knowledge of the amount of corroded graphite, the gas masses produced (CO, H_2) and consumed (H_2O) in the primary heterogeneous water-shift reaction (C + H_2O → CO + H_2) are easy to determine by stoichiometry. As the units of eq. ((4-63)

are given in kg/s, one only has to multiply the gas mass with the molar mass ratio of $\frac{M_{CO}}{M_C}$ or $\frac{M_{H_2}}{M_C}$ to obtain the produced masses of the subsequent chemical species in kg/s. Also, the nature of the reaction has to be checked. When 1 mole of CO and H_2 are produced each, 1 mole each of H_2O and C are consumed. So, for known graphite corrosion rates the subsequent produced/consumed gas components are:

$$\dot{m}_{Graphite} = -RR_{Graphite} \cdot surface \tag{4-64}$$

For the consumed steam:

$$\dot{m}_{H_2O} = \dot{m}_{Graphite} \cdot \frac{M_{H_2O}}{M_C} \tag{4-65}$$

For the produced hydrogen:

$$\dot{m}_{H_2} = -\dot{m}_{Graphite} \cdot \frac{M_{H_2}}{M_C} \tag{4-66}$$

For the produced carbon monoxide:

$$\dot{m}_{CO} = -\dot{m}_{Graphite} \cdot \frac{M_{CO}}{M_C} \tag{4-67}$$

For the chemical heat (endothermal):

$$Q_{chem,CO} = \dot{n}_{CO} \cdot \Delta H = \dot{n}_{CO} \cdot \left(-131.3 \frac{kJ}{mol} \right) \quad \left[\frac{kJ}{m^3} \right] \tag{4-68}$$

Secondary homogeneous reaction:

The reduction of water in presence of carbon monoxide ($CO + H_2O \rightarrow CO_2 + H_2$) and vice versa is a well-known reaction and was investigated in [60][61]. This reaction only happens in the gas phase.

For the reaction $CO + H_2O \rightarrow CO_2 + H_2$ the corresponding reaction rates are, [60][61]:

$$\dot{n}_{CO2} = \frac{2.32 \cdot 10^{14} \cdot \exp\left(-\frac{33{,}000}{T} \right) \cdot C_{H_2O} \cdot \sqrt{C_{CO}}}{\sqrt{1 + 1.2 \cdot 10^4 \cdot C_{H_2}}} \quad \left[\frac{mol}{m^3 \cdot s} \right] \tag{4-69}$$

In the above equation the concentrations C_k are absolute concentrations, but divided by their units to be dimensionless, and differ from the relative mass fractions introduced in the chapter before. The absolute concentration above for the component k is calculated by:

$$C_k = \frac{c_k \cdot \overline{\rho_{gas}}}{M_k} \tag{4-70}$$

with $\overline{\rho_{gas}}$ as the average density of the gas mixture.

From the production of CO_2 the reaction rates are determined as follows:

$$\dot{m}_{CO_2} = \dot{n}_{CO_2} \cdot V_{gas} \cdot M_{CO_2} \tag{4-71}$$

Average porosities are e.g. 0.39 within the pebble bed, 0.2 for the helium risers and so on.

For the H_2:

$$\dot{m}_{H_2} = \dot{m}_{CO_2} \cdot \frac{M_{H_2}}{M_{CO_2}} \tag{4-72}$$

For the CO:

$$\dot{m}_{CO} = -\dot{m}_{CO_2} \cdot \frac{M_{CO}}{M_{CO_2}} \tag{4-73}$$

For the H_2O:

$$\dot{m}_{CO} = -\dot{m}_{CO_2} \cdot \frac{M_{H_2O}}{M_{CO_2}} \tag{4-74}$$

For the chemical heat (exothermal):

$$Q_{chem,CO_2} = \dot{n}_{CO_2} \cdot \Delta H = \dot{n}_{CO_2} \cdot \left(41.2 \frac{kJ}{mol} \right) \quad \left[\frac{kJ}{m^3} \right] \tag{4-75}$$

For the opposite reaction $CO_2 + H_2 \rightarrow CO + H_2O$, see [60][61]

$$\dot{n}_{H_2O} = \frac{2.9 \cdot 10^{12} \cdot \exp\left(-\frac{28{,}200}{T}\right) \cdot C_{CO_2} \cdot \sqrt{C_{H_2}}}{1 + 3.6 \cdot 10^3 \cdot C_{CO}} \quad \left[\frac{mol}{m^3 \cdot s}\right] \tag{4-76}$$

Here the corresponding equations are

$$\dot{m}_{H_2O} = -\dot{n}_{H_2O} \cdot V_{gas} \cdot M_{H_2O} \tag{4-77}$$

For the H_2:

$$\dot{m}_{H2} = -\dot{m}_{H2O} \cdot \frac{M_{H2}}{M_{H2O}} \tag{4-78}$$

For the CO:

$$\dot{m}_{CO} = -\dot{m}_{H2O} \cdot \frac{M_{CO}}{M_{H2O}} \tag{4-79}$$

For the CO_2:

$$\dot{m}_{CO2} = -\dot{m}_{H2O} \cdot \frac{M_{CO2}}{M_{H2O}} \tag{4-80}$$

For the chemical heat (endothermal):

$$Q_{chem,H2O} = \dot{n}_{H2O} \cdot \Delta H = \dot{n}_{H2O} \cdot \left(-41.2 \frac{kJ}{mol}\right) \quad \left[\frac{kJ}{m^3}\right] \tag{4-81}$$

Secondary heterogeneous reaction (Boudouard reaction, endothermal):

$$CO_2 + C \rightarrow 2 \cdot CO, \quad -172.47\ kJ/mol$$

The corresponding equation for the Boudouard reaction rate is [72]:

$$RR_C = \frac{14.5 \cdot \exp\left(-\frac{25{,}000}{T}\right) \cdot p_{CO_2}}{1 + 3.4 \cdot 10^{-5} \exp\left(\frac{7{,}000}{T}\right) \cdot \sqrt{p_{CO_2}}} \quad \left[\frac{mg}{cm^2 \cdot s} = \frac{10^{-2} kg}{m^2 \cdot s}\right] \tag{4-82}$$

It is questionable if this correlation holds in the higher pressure range, since it was determined for 1 bar pressure and is more relevant in the case of air ingress since there the temperatures are expected to be higher.

$$\dot{m}_{Graphite} = -RR_{CO2} \cdot surface \tag{4-83}$$

for the CO_2:

$$\dot{m}_{CO2} = \dot{m}_{Graphite} \cdot \frac{M_{CO2}}{M_C} \tag{4-84}$$

for the CO:

$$\dot{m}_{CO} = 2 \cdot \dot{m}_{Graphite} \cdot \frac{M_{CO}}{M_C} \tag{4-85}$$

and the chemical heat removed from the system:

$$Q_{chem,Boudouard} = \dot{n}_C \cdot \Delta H = \dot{n}_C \cdot \left(-172.47 \frac{kJ}{mol}\right) \tag{4-86}$$

4.8.3 Calculation of reaction surfaces and volume

Since reaction rates are either provided for a reaction surface (heterogeneous reaction) or for a reaction volume (homogeneous reaction), the respective surfaces or volumes have to be calculated. For the region of the pebble bed the surface is

$$A_{pebblebed} = \frac{6 \cdot V_{cell}(1-\varepsilon)}{d_h} \tag{4-87}$$

with V_{cell} as volume of a considered cell, ε as porosity and d_h as hydraulic diameter. For cases outside the pebble bed the surface is calculated according to

$$A = \frac{4 \cdot V_{cell} \cdot \varepsilon}{d_h} \tag{4-88}$$

For reactions that occur between gases, the free gas volume is used instead of the surface, which is given by

$$V_{reaction} = V_{cell} \cdot \varepsilon = V_{gas} \tag{4-89}$$

4.8.4 Implementation of the graphite burn-off

The graphite burn-off is the relative mass loss due to corrosion of graphite in the fuel or reflector region normalised on the initial solid volume/mass. This parameter tracks the integrated corrosion values over time. It is computed by (explicit approach):

$$burn-off_{cell,timestep} = \frac{\dot{m}_c \cdot dt}{(1-\varepsilon)\cdot V_{cell}} \tag{4-90}$$

with dt as the time step.

After computing the burn-off of one time step in ATTICA^{3D}, the integral value is simply the sum of the burn-off of the actual burn-off results.

$$burn-off_{cell,total} = \sum_{timestep=1}^{max\_timestep} burn-off_{cell,timestep} \tag{4-91}$$

4.8.5 Air ingress

In an air ingress accident, a mixture of 79 % nitrogen and 21 % oxygen enter the primary circuit and eventually the reactor pressure vessel. Since nitrogen is an inert gas, only the oxygen contained in air will undergo corrosion with the reflector and fuel element graphite. Here the reactions presented in Table 6 are considered. The production of CO and CO_2 are two competing reactions with different production ratios at different temperatures.

$$a \cdot C + b \cdot O_2 \rightarrow x \cdot CO + y \cdot CO_2 \tag{4-92}$$

The ratio $\Psi_{Prod} = \frac{nCO}{nCO_2}$ is implemented according to Rossberg and Wicke for coal of type 513 [86] as default, two others are available, a second correlation from [86] and one from Arthur [85]. Experiments have shown that the default production ratio is most suitable for problems concerning corrosion of nuclear grade graphite in an oxygen atmosphere [77].

$$\Psi_{Prod} = \frac{nCO}{nCO_2} = 10^{3.27} \cdot \exp\left(\frac{-14{,}300}{0.239 \cdot R_{gas} \cdot T_{sol}}\right) \tag{4-93}$$

Rearranging the reactions and the production terms for one component, e.g. CO_2, the other component CO can be expressed in terms of the remaining reaction of the corroded graphite. In the corrosion experiments, the mass loss of the graphite samples

was measured. From the results, pressure and temperature dependent reaction rates were derived. In ATTICA^{3D}, the user can select different types of nuclear grade graphite for both pebble and reflector material that are already implemented. Additionally, the user can specify deviating graphite data via input. The implemented graphite specimens and their corresponding corrosion rates are taken from [93][94][95][96] and presented in the following

Table 8: Reaction rates of different graphite specimens with O_2

Graphite type	Reaction rates , $\left[\frac{kg}{m^2 \cdot s}\right]$
A3-3 fuel matrix	$RR_{A3-3} = -\frac{2.34 \cdot 10^{-2} \cdot \exp\left(\frac{-12{,}850}{T}\right) \cdot p_{O_2}}{1 + 0.0039 \cdot \exp\left(\frac{1569}{T}\right) \cdot \sqrt{p_{O_2}}}$
A3-27 fuel matrix	$RR_{A3-27} = -\frac{0.178 \cdot 10^{-2} \cdot \exp\left(\frac{-9{,}768}{T_s}\right) \cdot p_{O_2}}{1 + 0.0143 \cdot \exp\left(\frac{141}{T_s}\right) \cdot \sqrt{p_{O_2}}}$
V483T	$RR_{V483T} = -0.7 \cdot 10^{-2} \cdot \exp\left(\frac{-12{,}000}{T_s}\right) \cdot p_{O_2}$
ASR-1RS	$RR_{ASR-1RS} \approx -0.9 \cdot 10^{-2} \cdot RR_{V483T}$
ASR-1RG	$RR_{ASR-1RG} \approx -1.6 \cdot 10^{-2} \cdot RR_{V483T}$
ATR-1E	$RR_{ATR-1E} \approx -2.1 \cdot 10^{-2} \cdot RR_{V483T}$

For the Boudouard reaction, the correlation for the matrix graphite A3-3 is implemented according to Moormann [93]:

$$RR_{A3\text{–}3,Boudouard} = -\frac{14.5\cdot 10^{-2}\cdot \exp\left(\frac{-25{,}000}{T_s}\right)\cdot p_{CO_2}}{1+3.4\cdot 10^{-5}\cdot \exp\left(\frac{7{,}000}{T_s}\right)\cdot \sqrt{p}_{CO_2}} \tag{4-94}$$

Since the Boudouard reaction is significant above 950 °C only, the correlation is for the fuel matrix graphite only. In accidents, only the core region can have temperatures far beyond that temperature.

4.8.5.1 Mass changes for solid-gas reaction

With given reaction rates of graphite, the production rates for CO and CO_2 can be derived by some stoichiometry and the production ration Ψ presented above.

For the CO_2 produced

$$\dot{m}_{CO_2} = \frac{-RR_C\cdot A}{1+\Psi_{\mathrm{Prod}}}\cdot\frac{M_{CO_2}}{M_C},\left[\frac{kg}{s}\right] \tag{4-95}$$

where $\dot{m}_{CO2}$ denotes the mass change in CO_2, M_C and M_{CO2} denote molar weight of the respective material in kg/mol.

For CO the mass change is the difference of the graphite corrosion rate and the produced CO_2

$$\dot{m}_{CO} = \left(-\dot{m}_C\cdot\frac{M_{CO}}{M_C} - \dot{m}_{CO2}\frac{M_{CO}}{M_{CO_2}}\right), \tag{4-96}$$

The consumed O_2 can then be computed by the produced CO_2 and CO:

$$\dot{m}_{O_2} = -0.5\cdot\dot{m}_{CO}\cdot\frac{M_{O_2}}{M_{CO}} - \dot{m}_{CO2}\frac{M_{O_2}}{M_{CO_2}}, \tag{4-97}$$

4.8.5.2 Mass change rates of the gas-gas reactions

For the homogenous reaction $2\cdot CO + O_2 \rightarrow 2\cdot CO_2$ the mass change rates are

$$\dot{n}_{CO} = -1.2\cdot 10^6\cdot\exp\left(\frac{-12000}{T_g}\right)\cdot c_{CO}\cdot c_{O_2},\left[\frac{mol}{m^3\cdot s}\right] \tag{4-98}$$

where instead of the solid temperature the gas temperature is used, c_{CO} and c_{O2} denote the absolute concentrations. This formula is semi-empiric and the units do not conform. Nevertheless, this formula proved to be adequate to predict the post-combustion of CO [97]. In order to determine the mass change, the molar reaction rate $\dot{n}_{CO}$ has to be multiplied with the molecular weight of CO and with the gas volume.

$$\dot{m}_{CO} = \dot{n}_{CO} \cdot M_{CO} \cdot V_{gas}, \tag{4-99}$$

The gas mass of a certain gas component produced is balanced and inserted on the right side of the mass conservation of this component. In order to balance the energy production or consumption as consequence of chemical reaction, the produced or consumed heat is added to the right hand side of either the energy conservation of the solid (heterogeneous reaction) or of the gas (homogeneous reaction). For the homogeneous post-combustion of CO, this leads to:

$$Q_{chem,CO} = -\dot{n}_{CO} \cdot \Delta H \cdot V_{gas} = -\dot{n}_{CO} \cdot \left(282 \frac{kJ}{mol} \right) \quad \left[\frac{kJ}{m^3 \cdot s} \right], \tag{4-100}$$

The calculation of other possible reactions is implemented analogously.

5 Verification and Validation

This chapter treats verification of the coupled HTR simulation system by computing and comparing to results for the transient calculational benchmark of the South African concept PBMR-400 and validation for the extensions of chemical attacks ATTICA^{3D}, validation of the coupled system TORT-TD/ATTICA^{3D} for the Chinese experimental reactor HTR-10.

5.1 Verification with the PBMR-400 Benchmark

The PBMR-400 Benchmark by the OECD/NEA/NSC [13][46] is a computational benchmark exercise for the South-African HTR concept with an overall thermal power of 400 MW. South Africa put a lot of effort in designing and realising their unique HTR-concept. But due to various reasons (financial, economic, licensing, safety, technological, administrative etc.) this concept was abandoned in 2010. Nevertheless, this development along with the Chinese development triggered a new interest in the technology and a couple of benchmarks were published in order to compare and possibly qualify the simulation codes.

The latest benchmark description published was the coupled neutronic/thermal hydraulic steady state and transient benchmark for the PBMR-400 concept with an annular core for the spherical fuel elements and a helium turbine instead of a steam cycle.

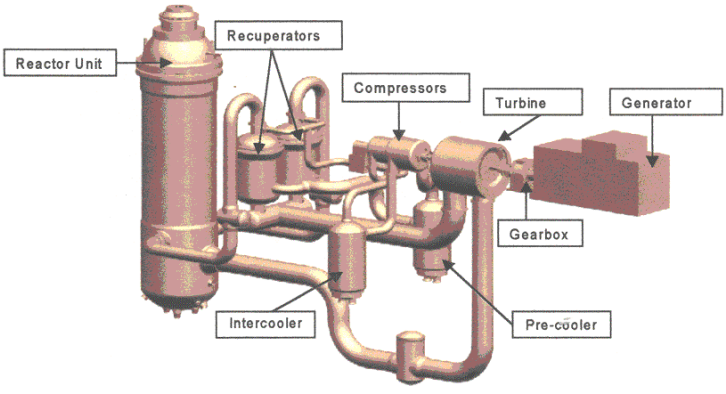

Figure 13: PBMR-400 concept with a single-shaft concept and a helium turbine [13]

The benchmark description contained detailed information about geometrical properties and simplifications (flattening of top and bottom of the pebble bed), material properties (heat conductivities, capacities, densities) and also a recommendation which correlations, and models to use. Also, it contained a set of data for the generation two-group

nuclear cross sections with a small programme to bring the cross sections in the right order. This forms an excellent basis for comparison calculations. The benchmark comprised three major exercises:

- uncoupled steady-state exercises
    - a neutron physics calculation with a fixed set of cross sections
    - a thermal fluid dynamic calculation with a fixed power distribution
- a coupled neutonic/thermal fluid dynamic steady-state calculation
- several coupled neutronic/thermal fluid dynamic transient exercises

By increasing the complexity of the calculations each participant could check how good their respective solutions are in comparison to others. The results had to be submitted stepwise (uncoupled results, coupled steady-state, coupled transients) and were available to other participants via a common homepage by the NEA. The transient exercises were the incidents or accidents an HTR has to cope with in order to be licensed. Here a loss of forced circulation with and without pressurisation, a re-criticality case without any Scram, an ingress of colder helium, and several control rod ejection and withdrawal cases (all, multiple, single) had to be performed. In the following chapters some selected transients are presented in order to demonstrate the capabilities of the coupled system TORT-TD/ATTICA^{3D} for pebble bed HTRs.

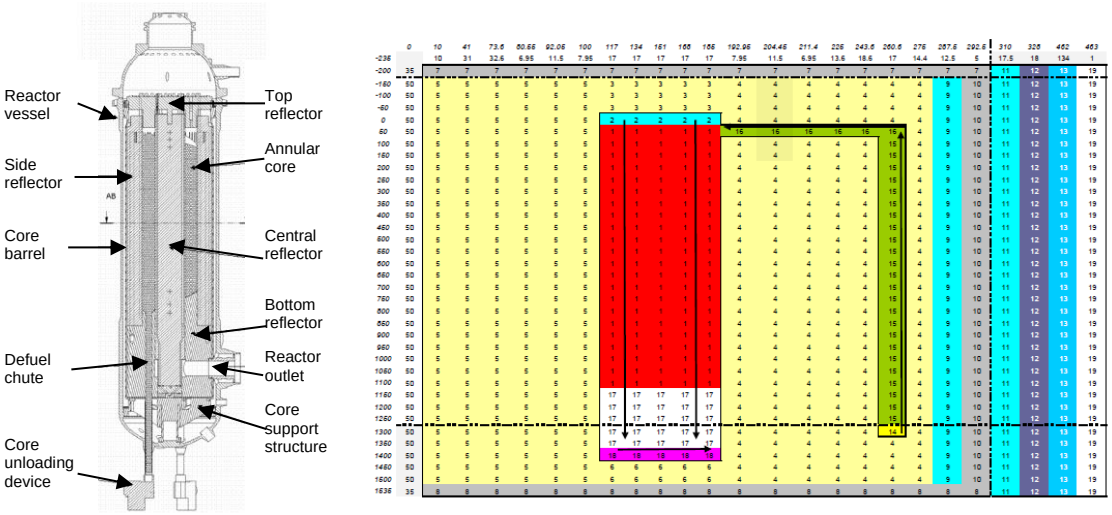

Figure 14: Left: Cross section of the PBMR reactor pressure vessel with core, right: 2-d thermal fluid dynamic model for the PBMR-400 benchmark, core (red), central and side reflectors (yellow), gas flow region (green, red, white and pink), the neutronic model is indicated by the dotted black line [13]

5.1.1 The coupled steady state

In order to have a comparable starting point for the transient calculations, the first coupled calculation to be performed is the coupled steady state. The result for the k_{eff} = 0.988

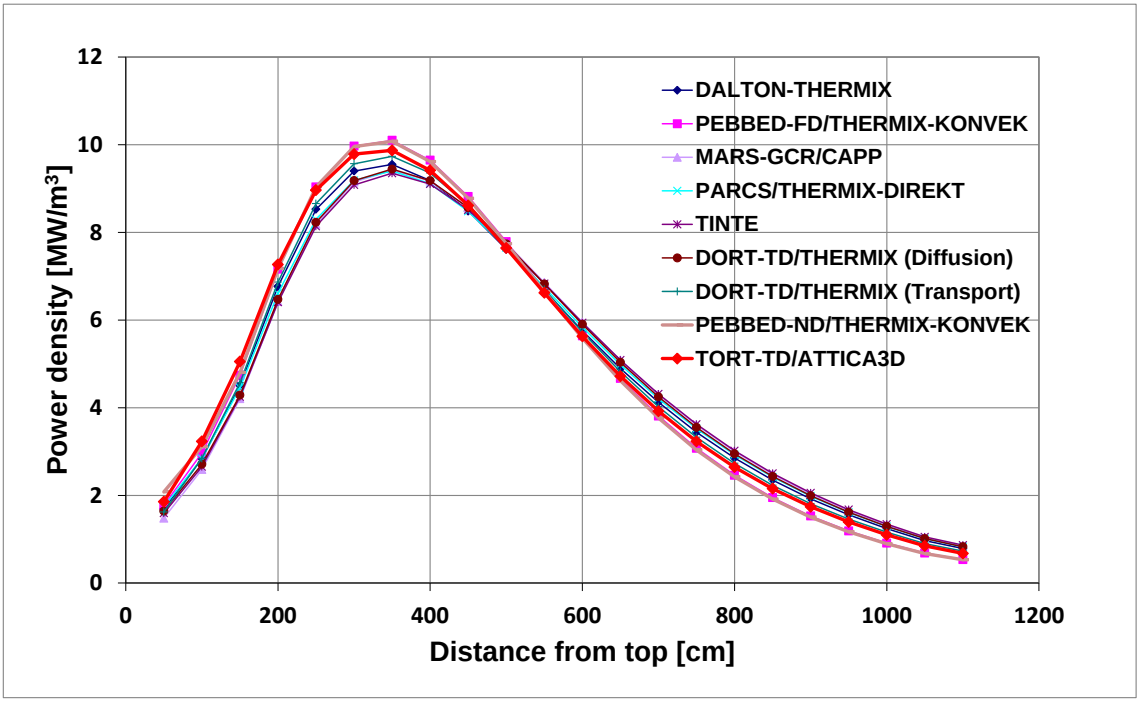

Figure 15: Axial power density distribution for the PBMR-400 benchmark, [26]

Figure 15 shows the axially averaged power distribution over the height of the PBMR-400 core, together with results of other participants of the benchmark. The results of TORT-TD/ATTICA^{3D} agree well with the other results. Figure 16 and Figure 17 show the obtained mean fuel and moderator temperatures that were obtained. The TORT-TD/ATTICA^{3D} results are slightly higher than the results of the benchmark participants. This can be explained by the heterogeneous fuel temperature model that was used while the benchmark description proposed to subdivide the fuel element into 6 shells of 0.5 cm thickness and use the whole fuel element as moderator temperature, the whole inner sphere with particles (r = 2.5 cm) as fuel temperature, and the innermost sphere as maximum fuel temperature.

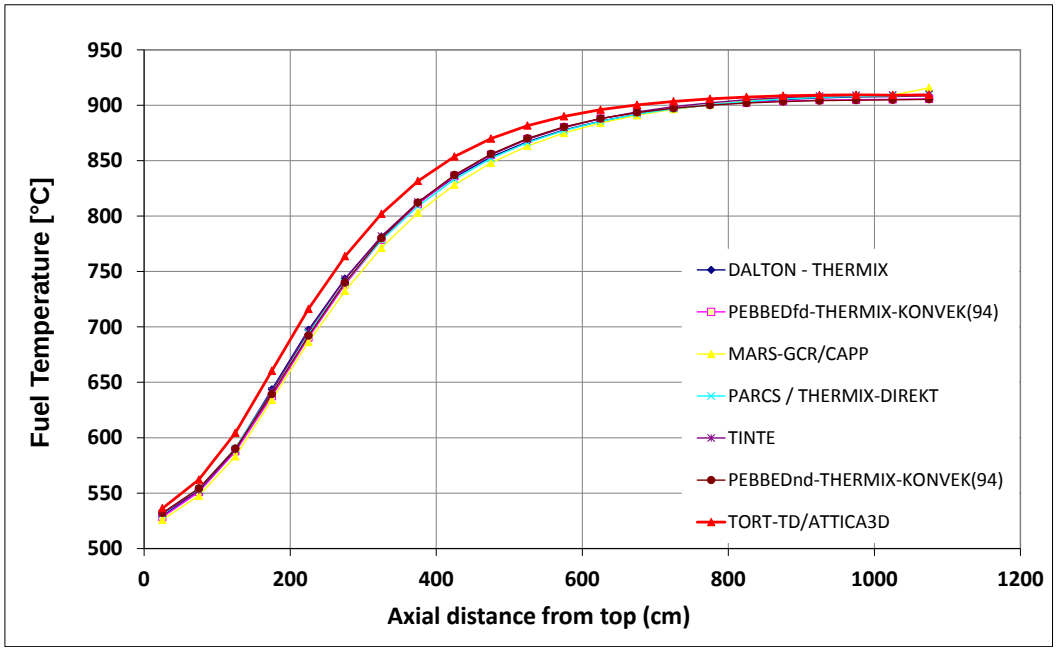

Figure 16: Averaged fuel temperatures of the coupled steady-state PBMR-400 benchmark exercise, [26]

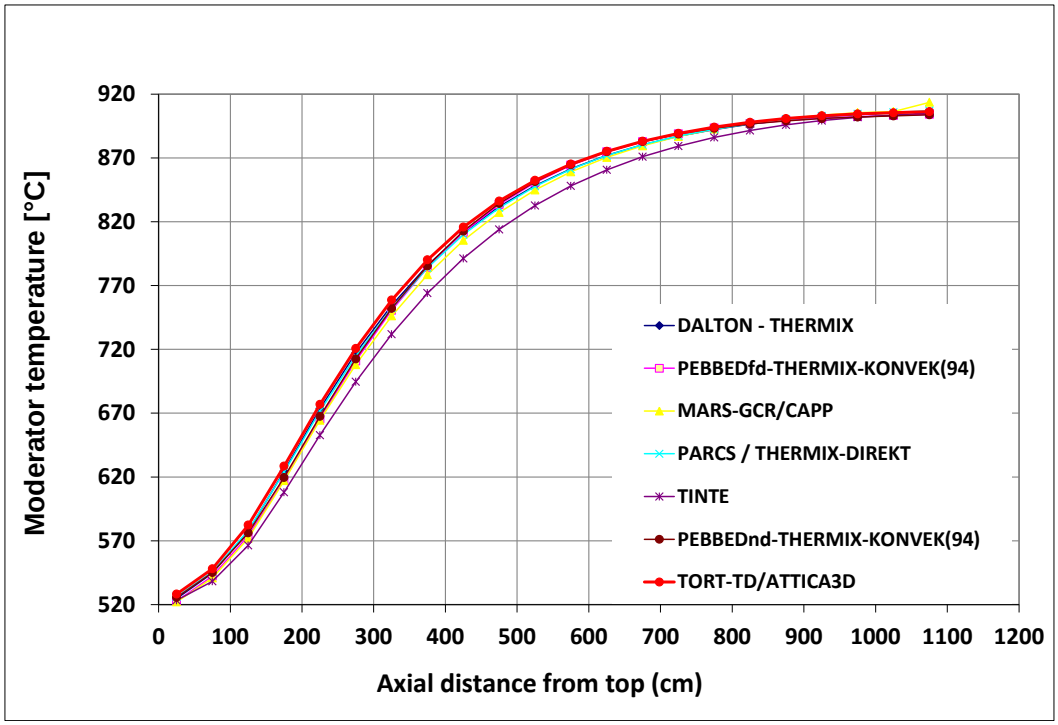

Figure 17: Averaged moderator temperatures of the coupled steady-state PBMR-400 benchmark exercise, [26]

5.1.2 Cold helium ingress

The coolant helium in the primary circuit of an HTR experiences massive thermal expansion during the start of the reactor (inlet/outlet temperature 500°C/900°C). This ne-

cessitates a helium storage system, i.e. some tanks where helium is stored to be re-used after maintenance. The helium will be taken out of the system during heat-up until full power is reached with the design pressure (here 90 bars). The excess helium is stored at a much lower temperature than in the primary circuit. There are of course, pipes to connect to the reactor pressure vessel to transport the gas out of the system.

Due to malfunction or mal-operation, a valve connected to the helium storage system is assumed to open at t = 0 seconds, then colder helium is mixed with the helium from the primary circuit. This will result in a decrease of inlet temperature. For the benchmark exercise, it is assumed that the inlet temperature will decrease over 10 seconds from 500°C to 450°C. The inlet temperature in this case is kept at 450°C for 290 seconds before it is linearly increased over 10 seconds back to the nominal inlet temperature of 500°C. Feedback of the secondary circuit, e.g. increase of the inlet temperature, is neglected for this transient problem.

In Figure 18 the resulting power increase from the ingress of cold helium is presented. The power increases since the moderator temperature is lowered, see Figure 19. This leads to a spectral effect shifting the relatively hard neutron spectrum (high temperatures) to lower energies thereby softening the spectrum, which, in turn, has a positive effect on the fission rates. The steep rise of the power is a consequence of this spectral shift. After ten seconds, the power rises only slightly. Here, the softening of the spectrum leads to a quick increase in fissions which increases the fuel temperature, Figure 20. After the initial decrease of the fuel and moderator temperature (at 50 seconds) the power rise increases the fuel and moderator temperature which, in turn, limits the power rise (100 – 300 seconds). After the inlet temperature goes back to the nominal value moderator and fuel temperature face a maximum value which, in turn, is responsible for the power decrease.

The fuel temperature evolution displays the highest change of all the results. It can be explained by the more detailed fuel model in ATTICA^{3D}. The proposed fuel temperature model of the benchmark recommended a simpler model; the fuel temperature is the mean temperature of the inner pebble part that contains coated particles. This method “dilutes” the result of TORT-TD/ATTICA^{3D} because the whole moderator volume of the inner 2.5 cm sphere is averaged instead of taking the real fuel content. This is more pronounced in cases of fast reactivity increase like the control rod withdrawal, and even more for the rod ejection case.

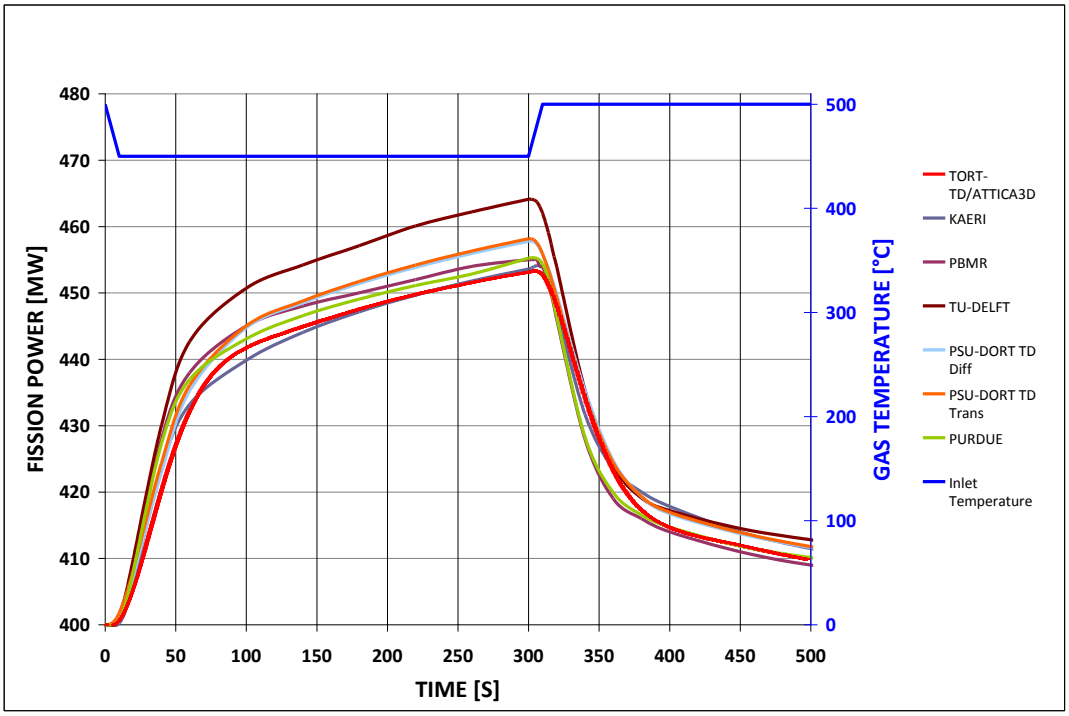

Figure 18: On the left y-axis: fission power in MW, respective results of TORT-TD/ATTICA^{3D} along with the participants' result of the benchmark. On the right axis: gas temperature change over time, [26]

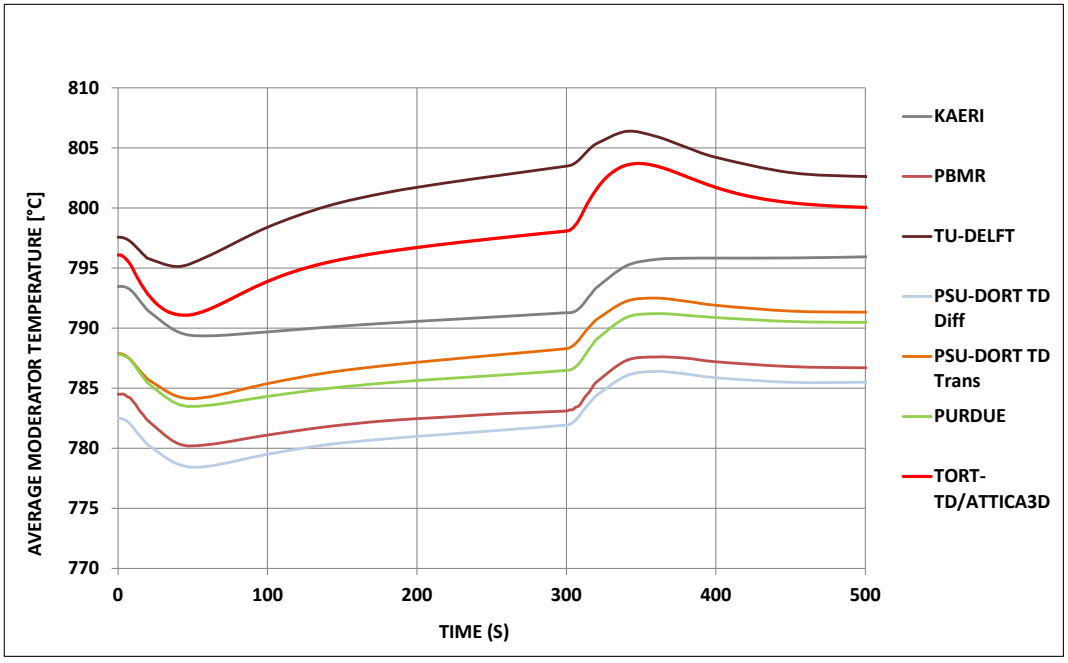

Figure 19: Average moderator temperatures of participants and TORT-TD/ATTICA^{3D}, [26]

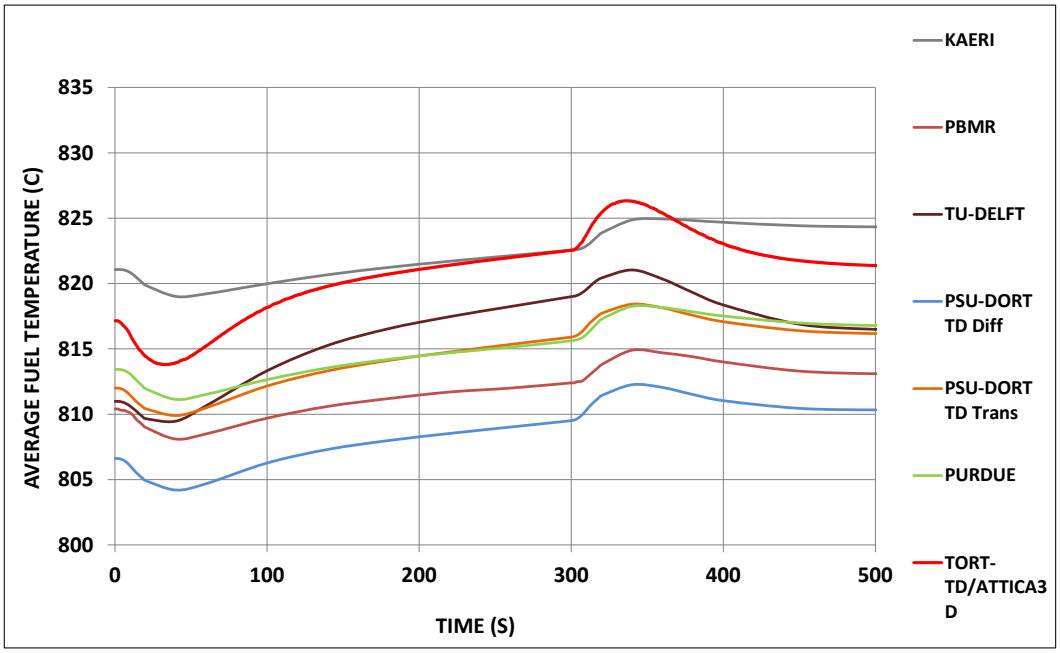

Figure 20: Average fuel temperatures for the cold helium ingress case, [26]

5.1.3 Control rod withdrawal

For the total control rod withdrawal case, it is assumed that all 24 control rods that are inserted in their nominal operation position (1.5 metres from top of the core) are withdrawn over 200 seconds to their outermost position which is 50 cm above the top of the pebble bed. After that the control rods remain at this position. It is assumed that thermal fluid dynamic boundary conditions remain the same, e.g. mass flow, inlet temperature, pressure, and there is no feedback of primary circuit dynamics like increase of inlet temperature.

The rod withdrawal leads to an increase of power. First, there is a steep rise in the total produced power. The reason is that the rods in nominal position have the greatest impact; the flux at that position compared is the highest. The more the rods are withdrawn the smaller the impact on the flux and hence of a further withdrawal. This can be seen in Figure 21. Figure 22, Figure 23, and Figure 24 show the maximum fuel temperature, the average fuel temperature and the average moderator temperatures, respectively. For the safety, the most important temperature is the maximum temperature because it will determine the first failing fuel element, more precisely the first failing particle.

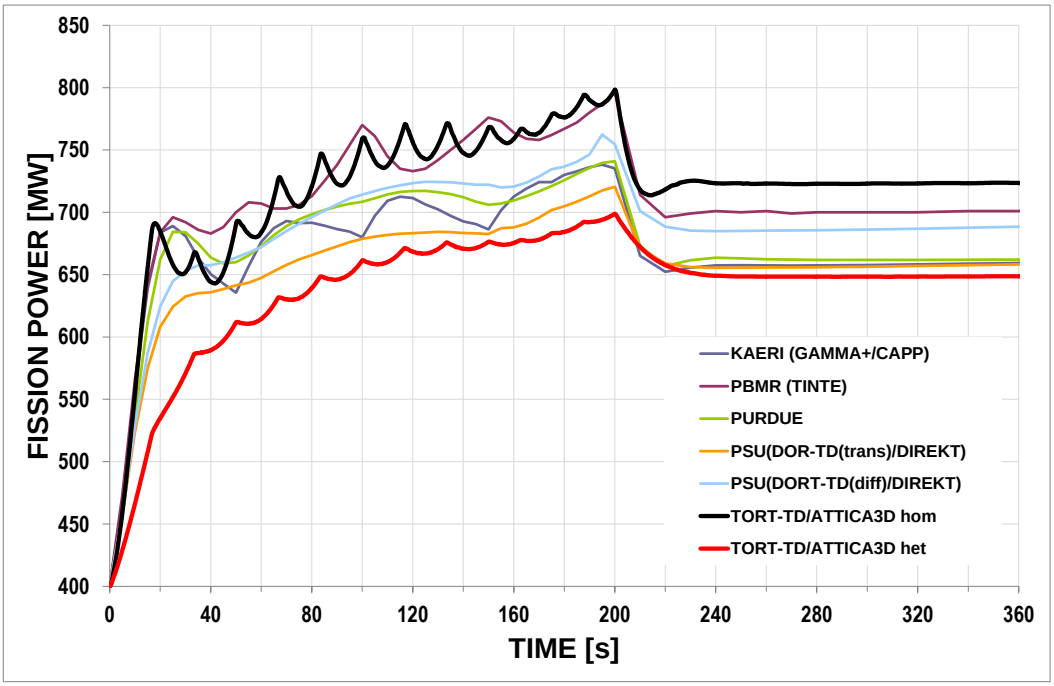

Figure 21: Fission power evolution for a control rod withdrawal case with operational speed (1 cm/s), rods are withdrawn over the first 200 seconds [26]

The average fuel temperatures are the highest for TORT-TD/ATTICA^{3D} of all benchmark participants. The heterogeneous fuel temperature model is responsible for this. As the benchmark proposed a fuel element model made out of 5 shells, the outermost without fuel, the average moderator temperatures of the inner four shells are taken as fuel temperature. This averaging procedure leads to a systematic underestimate of the fuel temperature for the stationary temperature (when compared to the heterogeneous fuel temperature model implemented in ATTICA^{3D}) and has less feed-back effect in the transient case, since the thermal inertia of the inner sphere including moderator is higher. Since the feed-backs are stronger in the TORT-TD/ATTICA$_{3D}$ results for the heterogeneous fuel modelling (het) the power increase is more moderate than compared to other participants. The highest power increase can be observed when omitting description of the fuel, TORT-TD/ATTICA$^{3D}_{hom}$ where basically only the surface temperatures are used. In the homogeneous case, the heat is assumed to be deposited all over the 3 cm fuel sphere leading to a much higher volume to heat up for feedback effects.

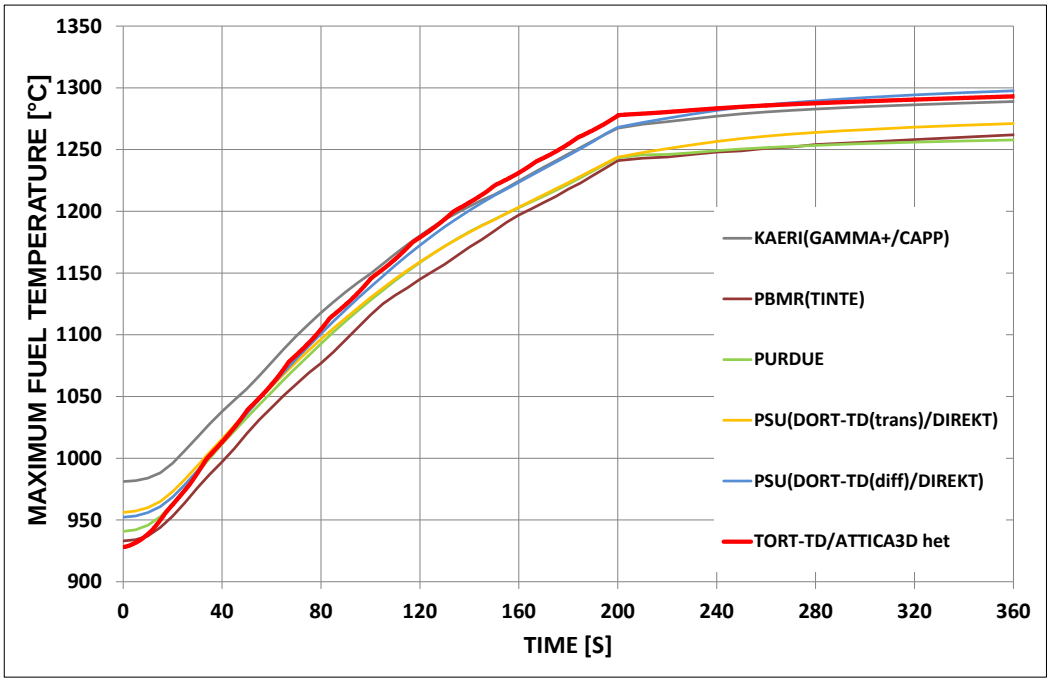

Figure 22: Maximum fuel temperature in case of a total control rod withdrawal [26].

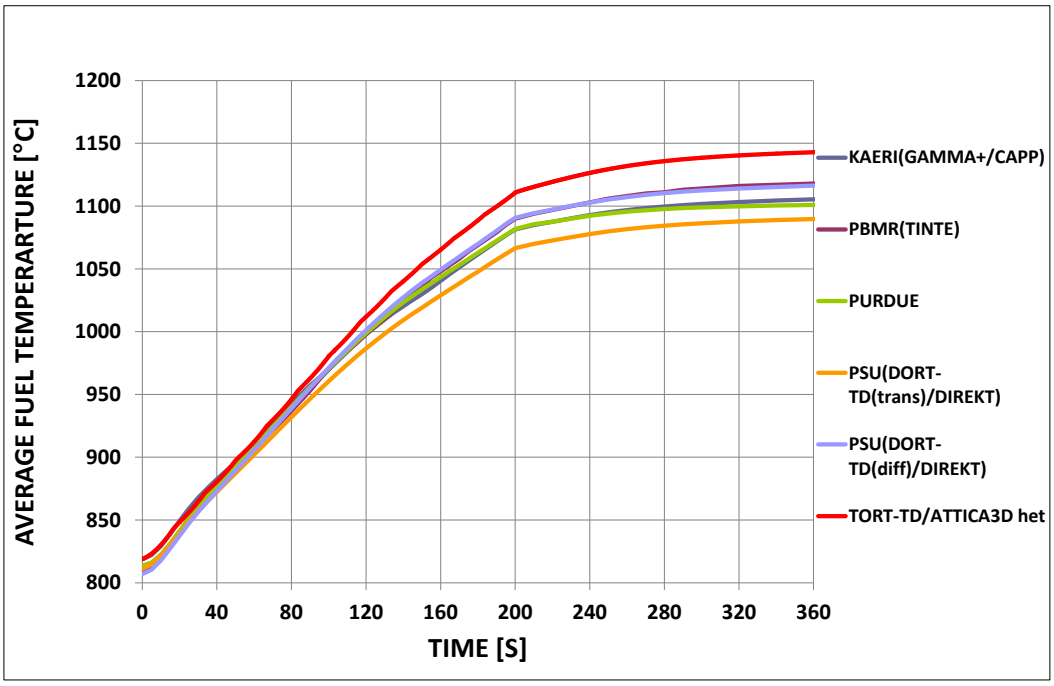

Figure 23: Average fuel temperature for the control rod withdrawal case, note: the fuel temperature of the homogeneous case is depicted in the average moderator temperatures due to the absence of a fuel temperature model [26]

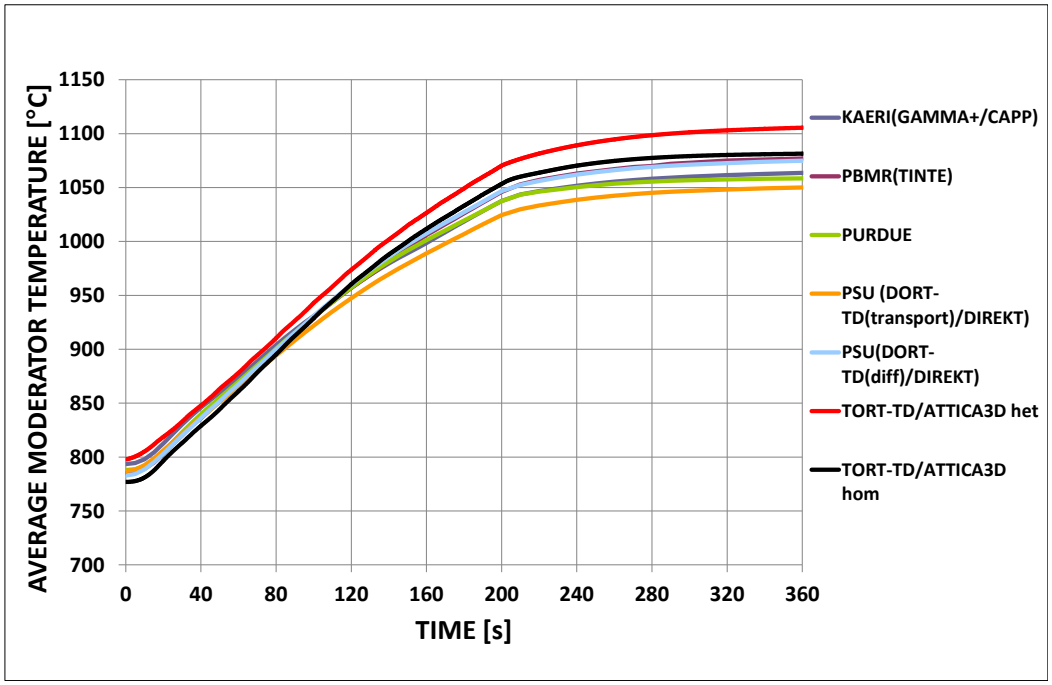

Figure 24: Average moderator temperature for the total control rod withdrawal case of the PBMR-400 benchmark, note: with the detailed fuel temperature model, the average moderator temperature is also higher; the homogeneous case only takes pebble surface temperatures thereby neglecting the temperature profile towards the centre [26]

5.1.4 Control rod ejection

In the total control rod ejection case, it is assumed that all control rods are ejected within 0.1 seconds from the nominal position. This imposes a super-prompt transient onto the simulation system. Here, the importance of the heterogeneous fuel temperature model is even more pronounced than in the control rod withdrawal case.

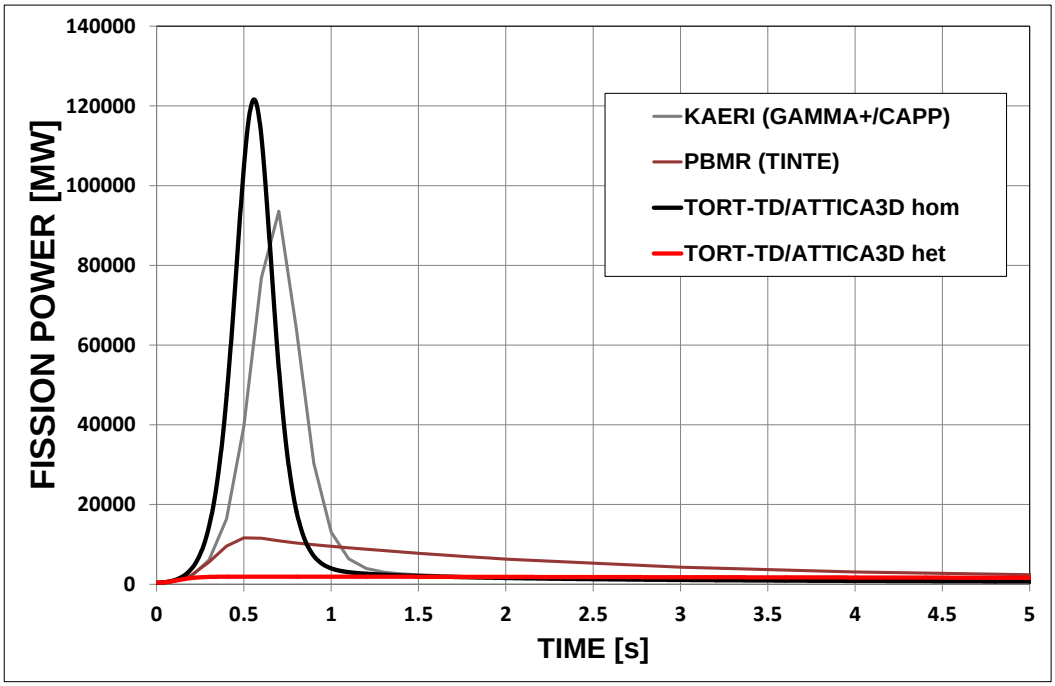

Figure 25: Power increase in a total control rod ejection case [26]

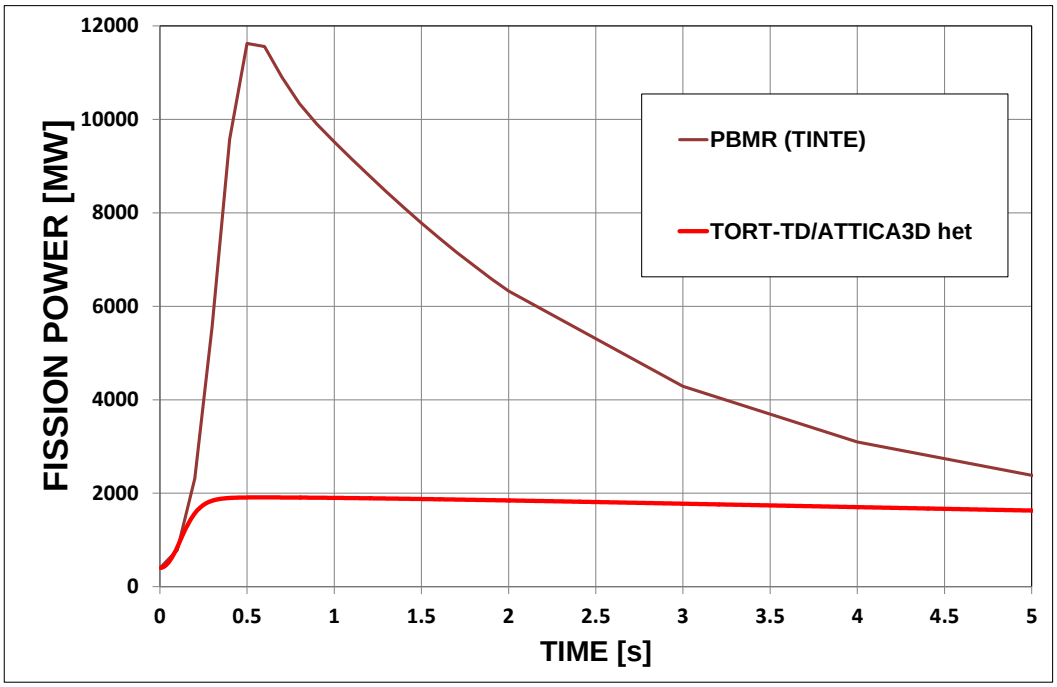

Figure 26: Comparison between TINTE and TORT-TD/ATTICA^{3D} with heterogeneous temperature model for the fuel [26]

Figure 25 and Figure 26 both show the power increase in case of an ejection of all the control rods. Obviously, the different fuel temperature models have a major contribution to the results and lead to a drastic spread in the results. While the homogeneous TORT-TD/ATTICA^{3D} result shows the peak at roughly 12,000 MW (factor 300), the het-

erogeneous model only yields a total power of less than 2000 MW (less than factor 5). The two published results are also wide apart. But, this divergence can be explained when taking a look at the fuel and moderator temperatures. Of course, like in the total control rod withdrawal case, the most important parameter for the fuel integrity is the maximum kernel temperature, while the average fuel and moderator temperatures (locally resolved) are the ones TORT-TD gets from ATTICA^{3D} after running the fuel temperature model and are then used for cross section interpolation.

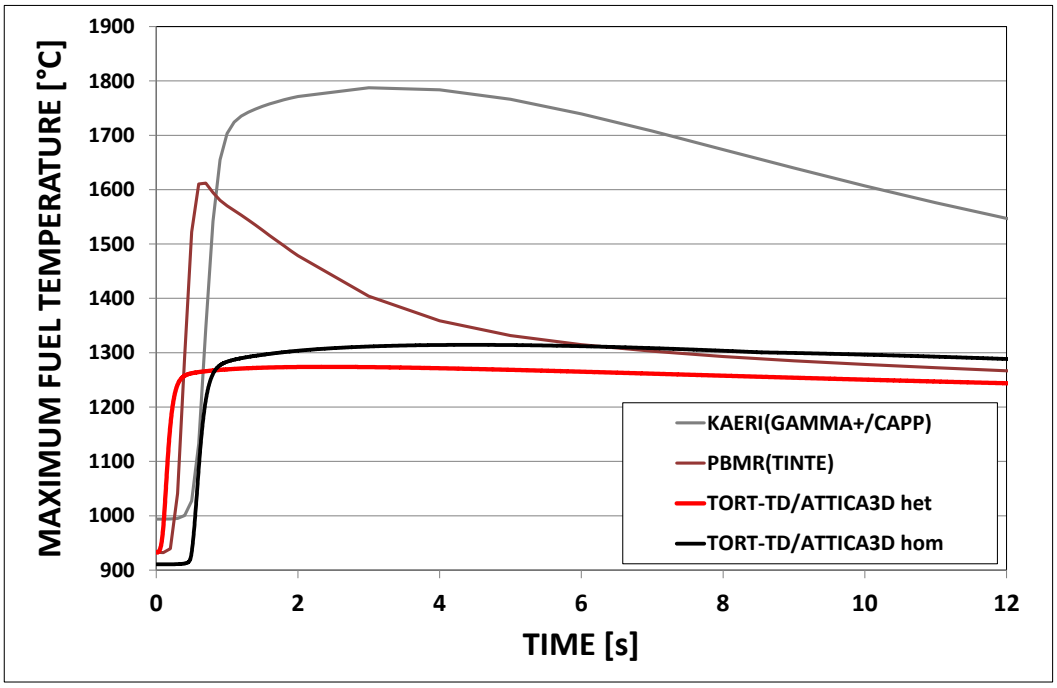

Figure 27: Maximum fuel temperature increase for the total control rod ejection case [26]

In Figure 27 it is apparent that maximum fuel temperatures differ by 400 – 500 °C. While for the KAERI and PBMR results maximum design temperature is exceeded (PBMR too, as there has to be a safety margin) the results of TORT-TD/ATTICA^{3D} results – even for the case without temperature model – yield temperatures well within the range of design limits. It is clear that these differences need explanation. When looking at the moderator temperatures in Figure 28, it is obvious that PBMR with the programme TINTE uses a time dependent fuel temperature model. This was also provided in the benchmark description, but it was not implemented in ATTICA^{3D}. A detailed analysis of the different fuel temperature models was performed in [78]. Here, the finding was that the homogenous modelling bears errors, e.g. for our model it yields power increase of a factor 400 whereas the heterogeneous temperature model yields a factor of only 5. The reason for this massive deviation lies within the response time of the fuel temperature. When magnifying the time axis, see Figure 29, it becomes obvious that the heterogeneous TORT-TD/ATTICA^{3D} solution responds instantaneously to the reactivity in-

crease. The temperature after 0.1 seconds is already increased by 50 Kelvin (denoted by 1)); after 0.2 seconds (denoted by 2)) the net temperature increase used for the cross section re-evaluation is around 150 Kelvin, whereas the closest reactor response at that time (PBMR) increased by less than 50 Kelvin. This quick temperature increase is also the reason why the heterogeneous TORT-TD/ATTICA^{3D} model does not exhibit such strong increase. I.e. the temperature increase is a consequence of the power increase, but the fuel temperature increase is at the same time the mechanism to limit the power increase factors. The heterogeneous model does not exhibit such inertia because it only takes the fuel particle volume (≈0.9% of the pebble volume) as primary location of fission heat deposition. Of course, with the fuel temperature model proposed by the benchmark, the fuel temperature feed-back would start later and the consequence is a higher power excursion.

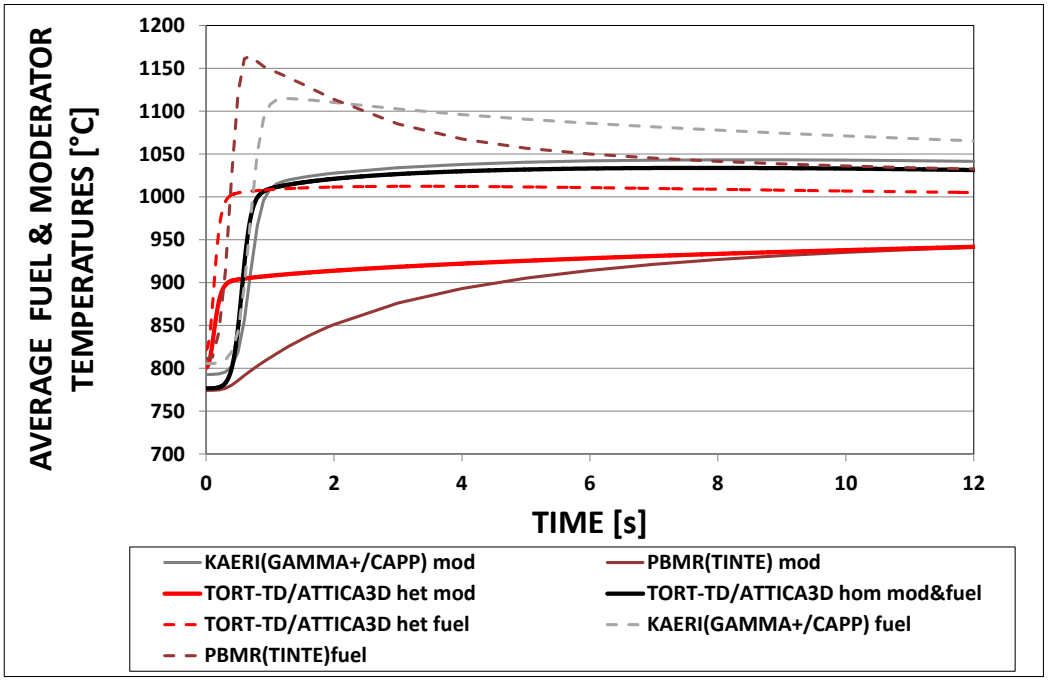

Figure 28: Average fuel and moderator temperatures for the control rod ejection case [26]

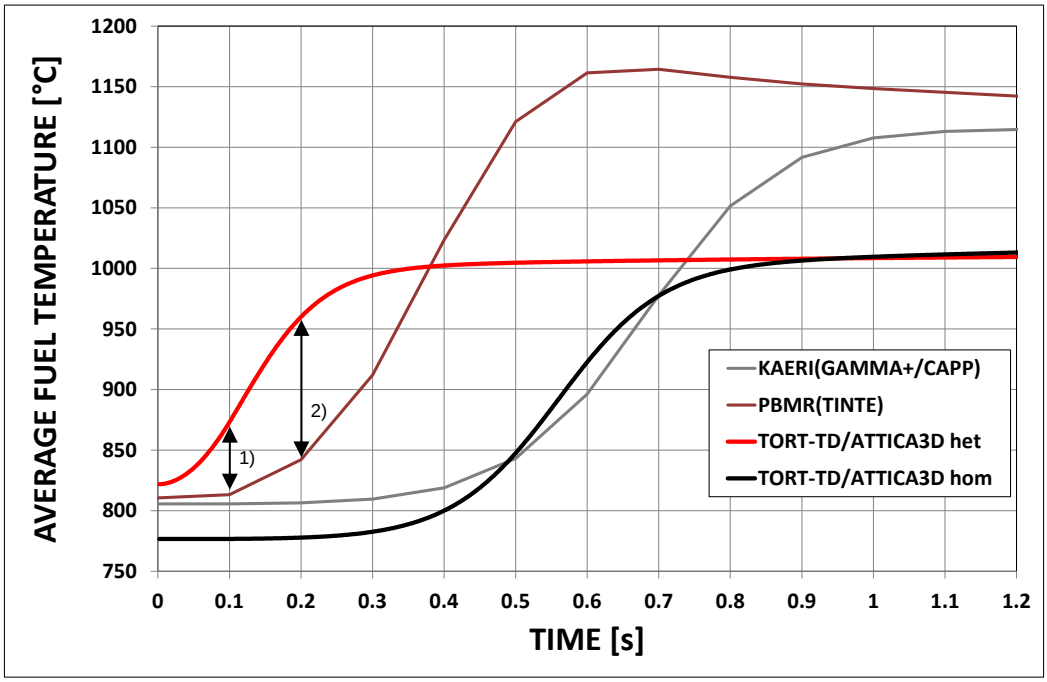

Figure 29: Fuel temperature increase within the first 1.2 seconds of the control rod ejection case; 1) TORT-TD/ATTICA^{3D} has a temperature increase of 50 Kelvin 2) TORT-TD/ATTICA$^{3D}_{het}$ fuel temperature increase is already 150 Kelvin and more than 100 K higher than results of TINTE solution [26].

5.2 Validation of corrosion module with the NACOK facility

The NACOK facility of the Jülich Research Centre is an experiment that is used for investigation of graphite corrosion (NAturzug im COre mit Korrosion, English: natural convection in the core with corrosion). It consists of two upright columns with an inter-connection at the top and bottom that should simulate the hot helium chamber, a part of an HTR core, the connection of the upper gas plenum and the cold helium riser,. In an air ingress case, flow inversion is assumed after a certain time delay leaving the bottom reflector and the pebble bed exposed to corrosion. Further information about the experimental facility and the experiments can be found in [59] where a whole set of different mass flows and heating temperatures were investigated.

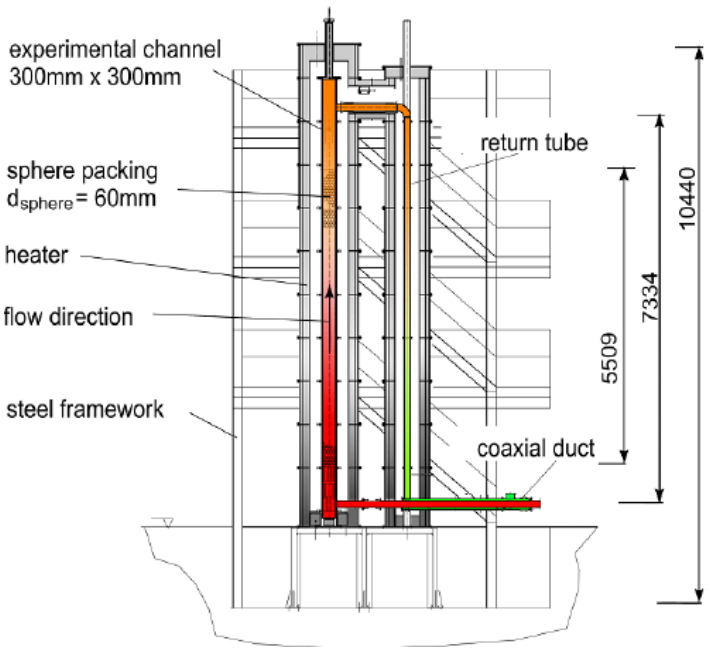

Figure 30: NACOK facility, dimensions in mm, pebble bed test section (red-orange) on the left, return tube on the right section in (orange-green), [83]

5.2.1 Natural Convection in NACOK Experiment

To test if ATTICA^{3D} is capable of simulating the natural convection flow in the NACOK experiment, the measured mass flows are compared to ATTICA^{3D} results. In the mass flow experiments it was tested how much air is sucked in by two differently heated temperature columns; the pebble bed column and the return column (see Figure 30, red and yellow, respectively). While for the return tube the temperature was changed in steps of 200 Kelvin ranging from 200 – 800 °C, the pebble bed was heated to at least 50 K above the return tube temperature, and was increased to up to 1000 °C. The results are presented in Figure 31. There are also results of the well-recognised THERMIX/DIREKT, a thermal fluid dynamic tool for HTRs, included. One is the standard version, which is for reactor calculations and one was modified to match the experiment. Of course, the version modified for the NACOK experiment agrees best with the experimental results (DIREKT NACOK). The non-modified version displays – along with the ATTICA^{3D} results – some deviations, especially in the low temperature range of the return pipe (200 and 400 °C), but improves the higher the return pipe temperatures are. Until, at high temperatures, all three code versions yield acceptable results.

Since the temperatures most likely to occur in a depressurisation accidents are the higher ones and remain high for a long time the natural convection capabilities were found to be sufficiently well modelled and can qualitatively reproduce the behaviour in a deviant geometry like the NACOK experiment.

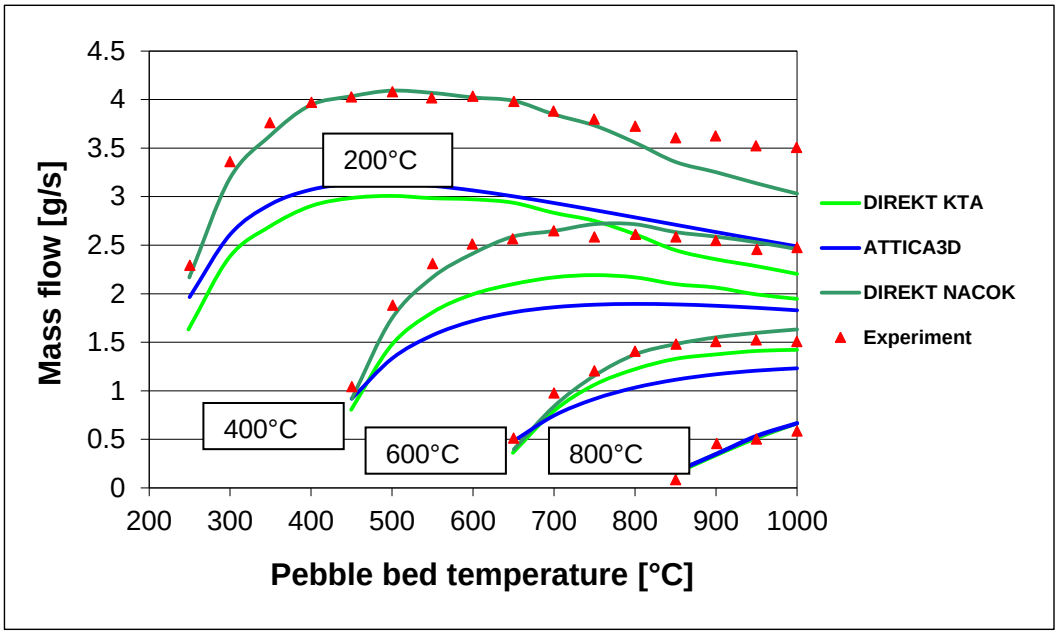

Figure 31: Mass flows at different temperatures for the NACOK experimental facility, temperatures in the boxes are downcomer temperatures, temperatures on the x-axis are pebble bed temperatures, experimental values and DIREKT results from [59] .

5.2.2 Validation of the corrosion module with the NACOK experiment

For the newly implemented corrosion module described in 4.8, test calculations are performed for validation. Here, also the NACOK experiment was selected, but with a different setup than shown in Figure 30. Instead of a pebble bed that was filled into the setup, a reflector block corrosion experiment was used as validation case. This experiment was conducted within the framework of the RAPHAEL project (funded by the European Commision) and made available to contributors of the project.

The test data was obtained in a NACOK reflector corrosion experiment described in [83]. Here, two different graphite reflector materials were tested; one produced by SGL Carbon, and the other from UCAR (United Carbon), both graphite manufacturers that offer nuclear grade graphite. The test was carried out arranging two different block elements (Figure 32 and Figure 33) from two different manufacturers in three layers on top of each other, 12 in total. For the corrosion experiment, the return pipe was not in use. Only an upright column with the reflector blocks and above a ceramic pebble bed of 10 cm height (for pressure drop) was installed. In order to bring the setup to experimental temperatures, the facility steel walls were heated by radiation. The heat was provided by an electrical heater with a heating temperature of 900°C. Additionally, the experiment was flooded by nitrogen at 900°C for 9 hours.

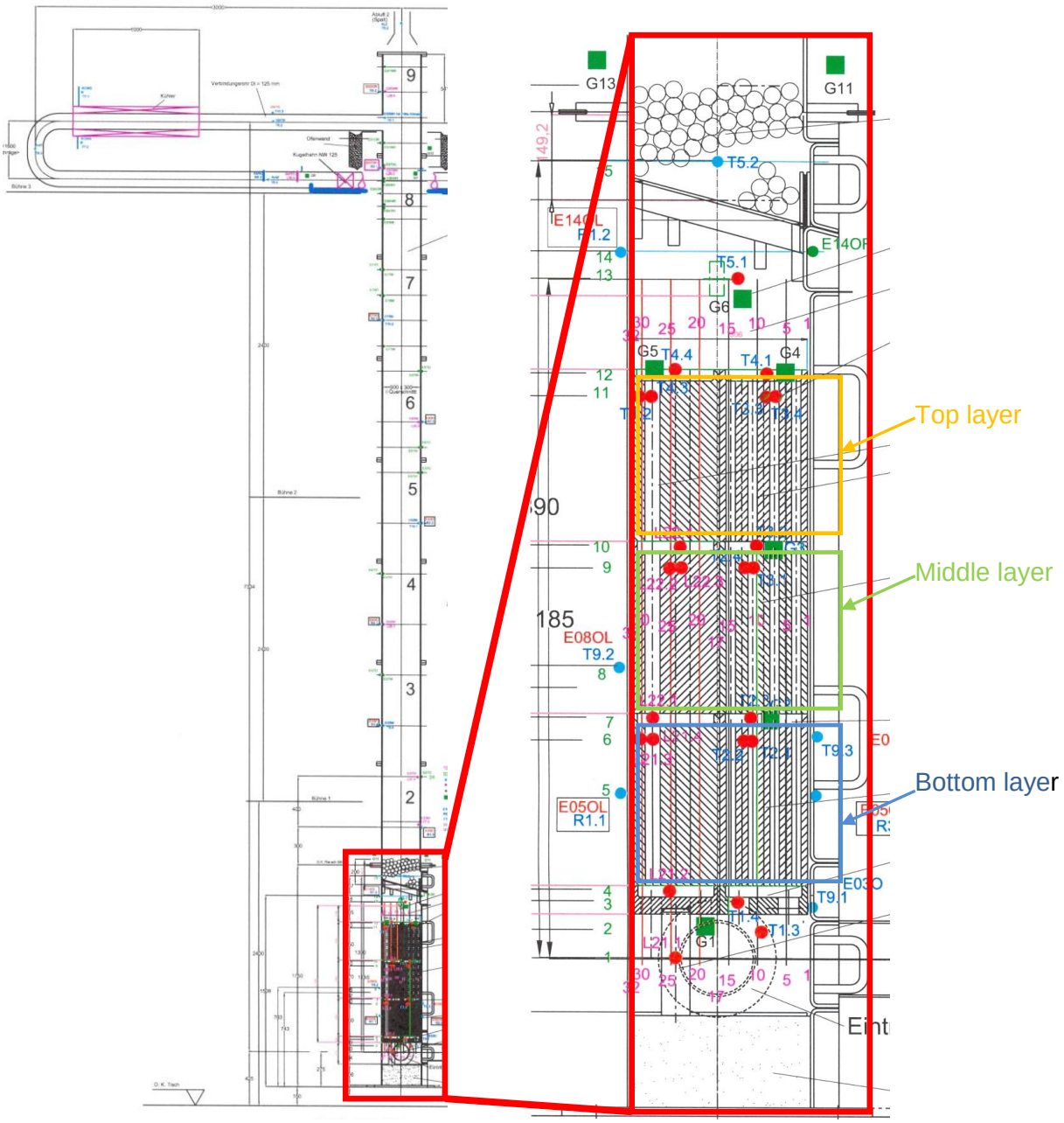

Figure 32: NACOK experiment with reflector graphite blocks for corrosion experiment, left: overall setup, right: magnified section of interest with top (yellow), middle (green) and bottom (blue) layer, [83].

When the experiment was started, the lowest layer had a temperature between 680 – 760°C, the middle layer between 760 – 800°C and the uppermost layer had initial temperatures ranging from 790 – 830°C. When the experimental conditions were obtained, the hot nitrogen valve was closed and a valve that allowed a maximum air flow of 5 g/s was opened to let ambient air (21% oxygen, 79% nitrogen) at 20°C from the experimental hall flow into the experiment. The measured mass flow throughout the experiment was 4.32 g/s. The outer heating was kept constant at 900°C. After opening of the valve the experiment was left for 8.5 hours during which the temperatures were meas-

ured. At the end of the experiment, all graphite blocks were weighed and the relative mass loss was determined by weighing the graphite blocks.

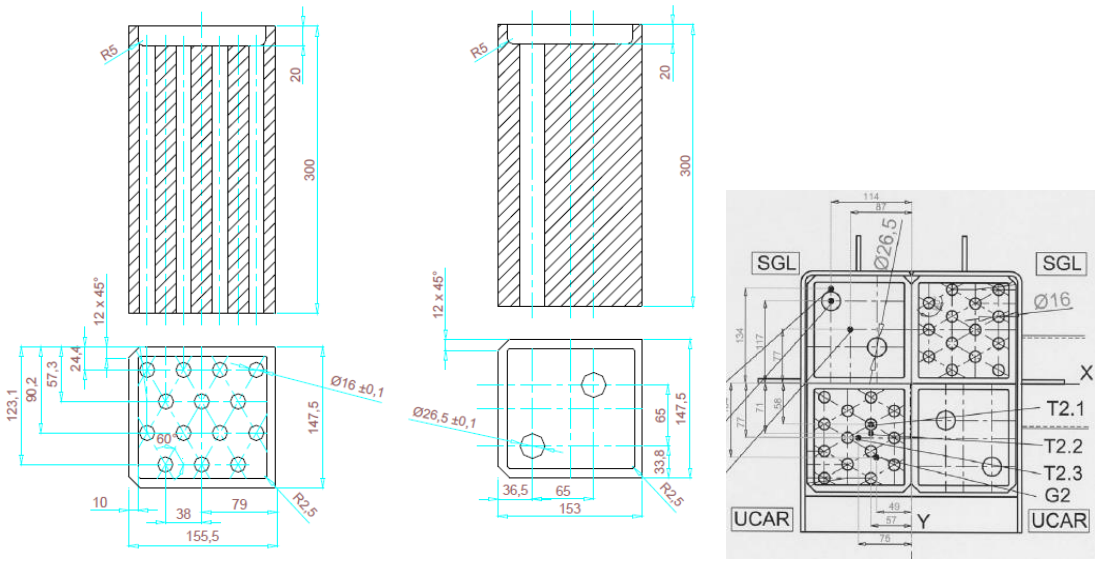

Figure 33: Geometry of the two different specimens of reflector graphite and arrangement for the corrosion test [83]

For the simulation case with, the initial solid temperatures were set as described above. As boundary condition, a heat sink/source of 900°C is assumed with a heat transfer coefficient of 400 W/(m*K) at the side of the blocks and the pebble bed. With this configuration, the experiment was calculated with stand-alone ATTICA^{3D}. Each of the blocks was subdivided into 9 squares in x,y-direction and in 4 layers in z-direction. The geometrical arrangement as well as the initial temperature distribution is depicted in Figure 34.

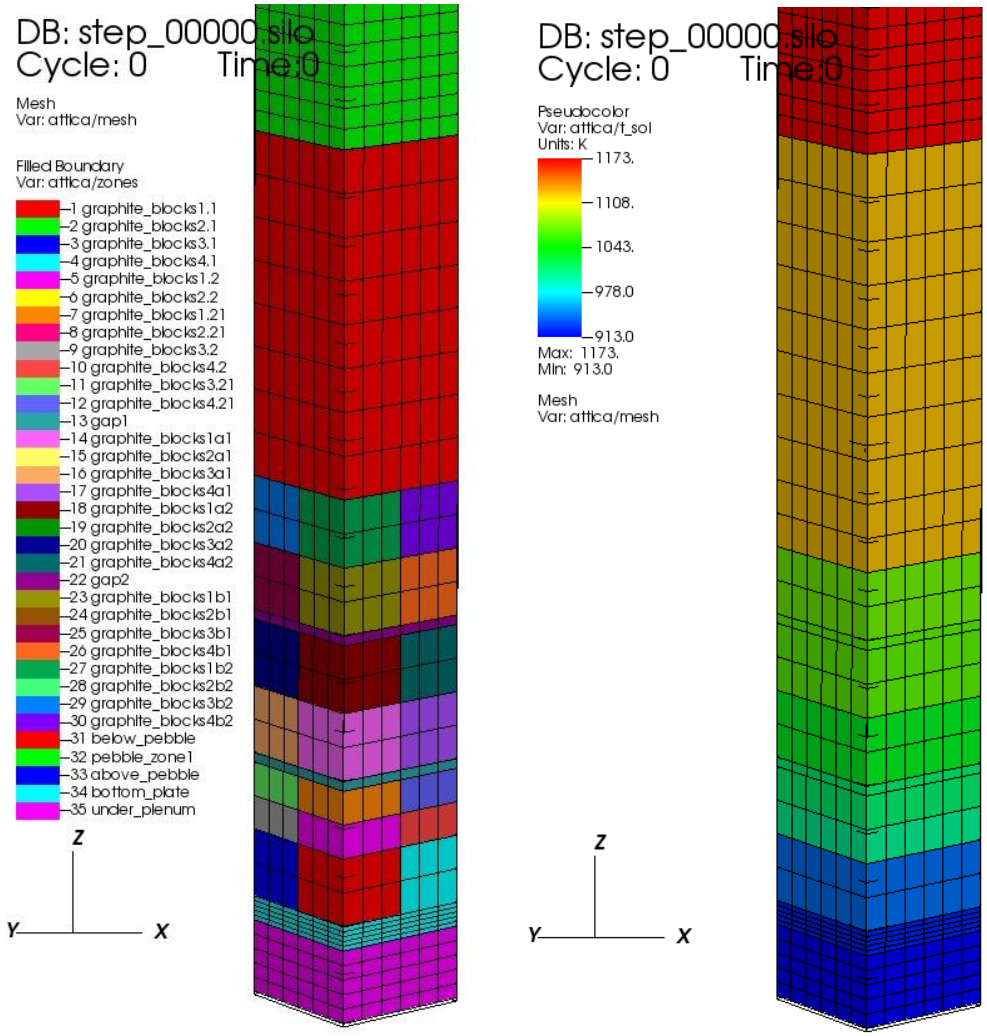

Figure 34: NACOK simulation model in ATTICA3D with zone subdivision (left) and initial temperatures (right).

Figure 35 shows the subdivision of the corrosion zone with the three graphite block layers. The plane with the highest corrosion is the third layer with burn-off starting from the bottom. The burn-off after 2 seconds is insignificant, of course, but already displays three-dimensional corrosion capabilities which are caused by different running times of oxygen from the inlet to the plane.

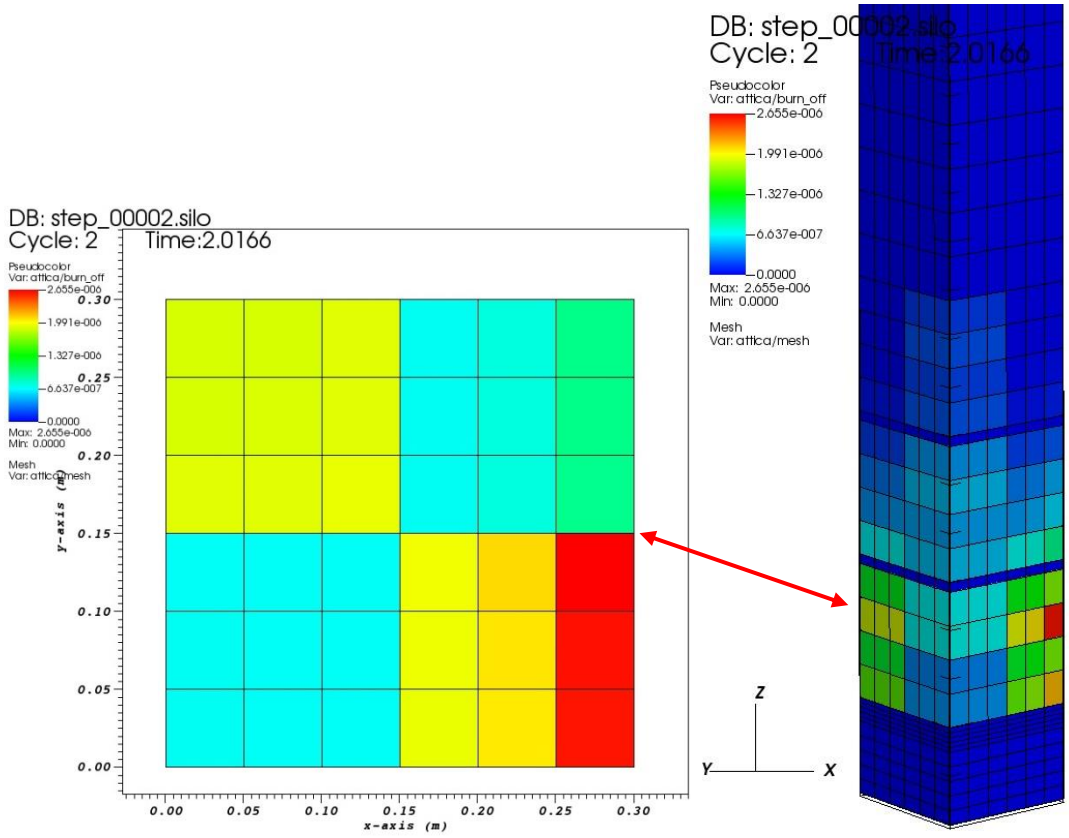

Figure 35: Snapshot of the burn-off of graphite in the NACOK experiment after 2 seconds in the upper middle of the lowest graphite reflector block; the inlet of the experiment is on the right side, this explains the different burn-off in the x,y-plane. The right picture shows a 3-d view of the region of interest.

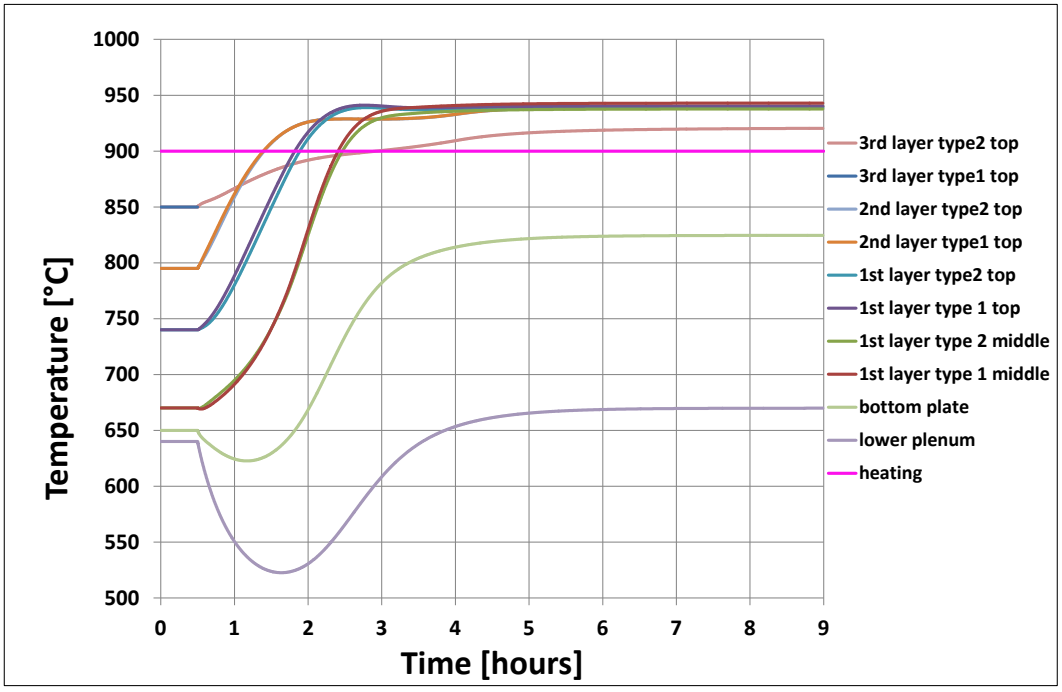

Figure 36: Temperatures calculated by ATTICA^{3D} for the NACOK corrosion experiment

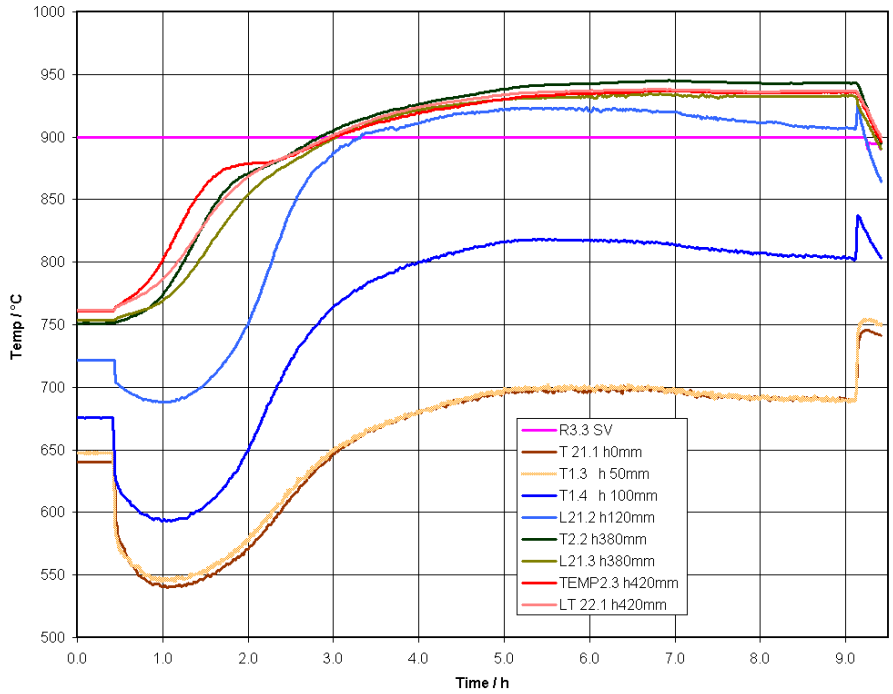

Figure 37: Measured temperatures of the NACOK corrosion case for the lowest layer [83]. The lowest curves correspond to the lower plenum and the isolation plate (dark red and yellow). The dark blue curve shows the lowermost layer of the graphite block. All curves above show the temperature subdivided in axial height. The pink temperature is the heating temperature for the experiment.

The experiment has a strong coupled character. In the corrosion reactions, the oxygen is consumed, but heat is deposited in the solid and/or gas phase. This leads to a temperature increase that in turn increases the corrosion rates. If oxygen is already consumed in a layer below, corrosion is not possible in the successive layers above. It becomes clear that the determination of temperature and the corresponding burn-off is a consequence of the initial temperature distribution, the on-going corrosion reaction and the flow distribution of the respective reflector material (2 large or 14 small holes). As stated in 4.8, different types of graphite are implemented at least for the air ingress case. For the calculation of the transient the graphite type V483T was selected. This selection is motivated by results published in [84]. Here, three different computer codes SPECTRA [43], TINTE [35], REACT/THERMIX [66] were used to determine burn-off as well as temperature distribution. The REACT/THERMIX and TINTE versions only had two-dimensional (cylindrical) capabilities. Therefore, the results produced use a uniform averaged porosity approach unable to determine local corrosion behaviour, i.e. the different blocks of type 1 and type 2 exhibit a difference of areas available for corrosion of a factor of 4. This geometric difference also leads to rather different corrosion rates for the two geometrical specimens. Since the graphite used was similar to the tested

ones, the mass loss of the two blocks of one geometrical specimen was averaged, see Table 9. It is obvious, that in layer 1 the corrosion is overestimated for the type 1 but yields acceptable agreement for type 2. Since the corrosion is a bit overestimated for layer 1/type 1, the mass loss for type 1reflector elements above is underestimated. This can be explained by the fact, that there is no oxygen present in the layer 2 for a type 1 reflector. The gaps between the layers of 2 cm height are made for instrumentation and do not allow cross-flow. Therefore, no oxygen can flow out of layer1/type2 element in x,y-direction, the oxygen supply is completely consumed. Since the temperatures also stay below 950 °C the Boudouard reaction does not take place. For the type 2 reflector elements, the results are in good agreement for the lower part. But since the mass loss in layer 1 is at the upper end of the experimental result, layer 2 is still in the experimental results range, the mass loss is underestimated for layer 3. Nevertheless, the results can be regarded validated. The mass loss per layer is displayed in Table 9.

What appears to be necessary is to repeat the experiments for the most likely candidates of nuclear graphite, both for fuel and for the reflector.

Table 10 presents the integral mass loss values for the experiment and the results obtained with the respective code system. Figure 38 shows a cross section of the first layer of graphite along with a 3-d view of the three layers with their respective burn-off. To emphasize the 3-d corrosion, the x,y-plane is depicted with maximum and minimum burn-off. It is obvious that type 1 is much stronger corroded than type 2. Type 2 gets parts of the chemical heat produced of its neighbour due to heat conduction through the solid. If temperatures are higher, so is the respective corrosion. Type 2 displays inhomogeneous corrosion behaviour, see Figure 38.

Table 9: Mass loss of graphite per layer and type after the corrosion experiment

		ATTICA^{3D}	Experiment
Layer 1	Type 1	28.84 %	23.8 – 24.3 %
	Type 2	16.44 %	11.5 – 16.5 %
Layer 2	Type 1	1.37 %	3.4 – 3.5 %
	Type 2	4.62 %	4.5 – 5.0 %
Layer 3	Type 1	0.14 %	0.8 – 1.5 %
	Type 2	1.53 %	2.6 – 2.8 %

Table 10: Integral mass loss over all blocks for the corrosion experiment

	Relative mass loss	Reference
Experiment	8.4 %	[83]
SPECTRA, Roes correlation	9.0 %	[84]
SPECTRA, CEA correlation	9.4 %	[84]
SPECTRA, NKL correlation	9.7 %	[84]
TINTE	9.9 %	[84]
REACT/THERMIX	10.9 %	[84]
ATTICA^{3D}	8.8 %	-

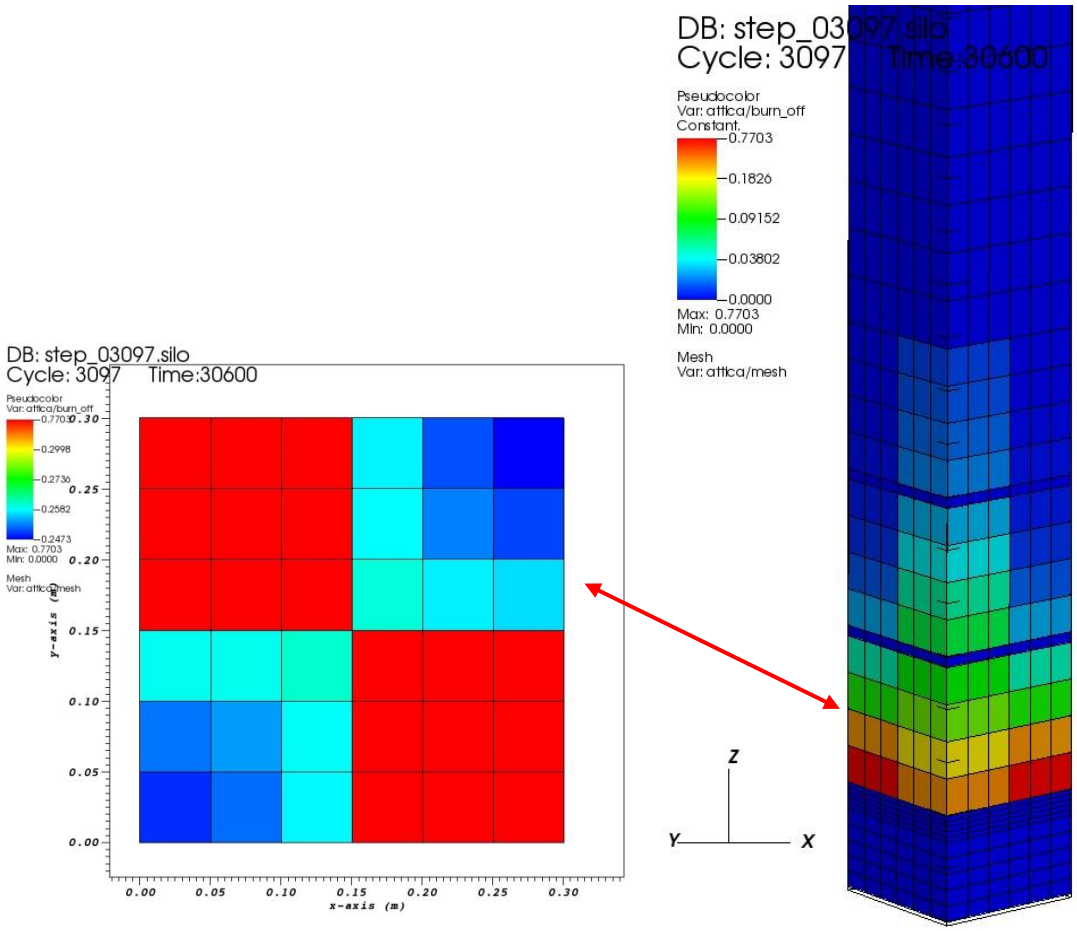

Figure 38: Burn-off of the first layer of graphite with “type 1” in the upper left and lower right corner, and “type 2” lower left and upper right. Legend is normalised to minimum and maximum graphite burn-off within the first layer. Right: 3-d view after the corrosion experiment.

5.3 Validation of the Coupled Simulation System with the Chinese Experimental Reactor HTR-10

The HTR-10 is a modular HTGR and a testing facility for HTGR technology. This experimental reactor was first critical in December 2000 and since then, is operated by the Institute of Nuclear and New Energy Technology of the Tsinghua University (INET). The reactor building is sited 40 km north of Beijing, China. The Design Criteria and the Safety Analysis Report of the HTR-10 were approved in August 1992 and March 1993, respectively. Ground was broken in 1994; construction works were completed in 2000. The first criticality was achieved in December 2000 [12].

The objectives of the Chinese HTR-10 project are to verify and to demonstrate the technical and safety features of the HTGR technology. Also, it is a testing facility for nuclear process heat applications and helium turbine cycle. Particular aims to achieve are [14]:

- to gain experience of HTGR technology,
- irradiation testing for fuel elements,
- to prove inherent safety features of the modular HTGR technology,

and later

- demonstration of electricity/heat co-generation, also a demonstration of the combined steam/gas turbine cycle
- development of a process heat utilisation

The primary circuit is depicted in Figure 39 below.

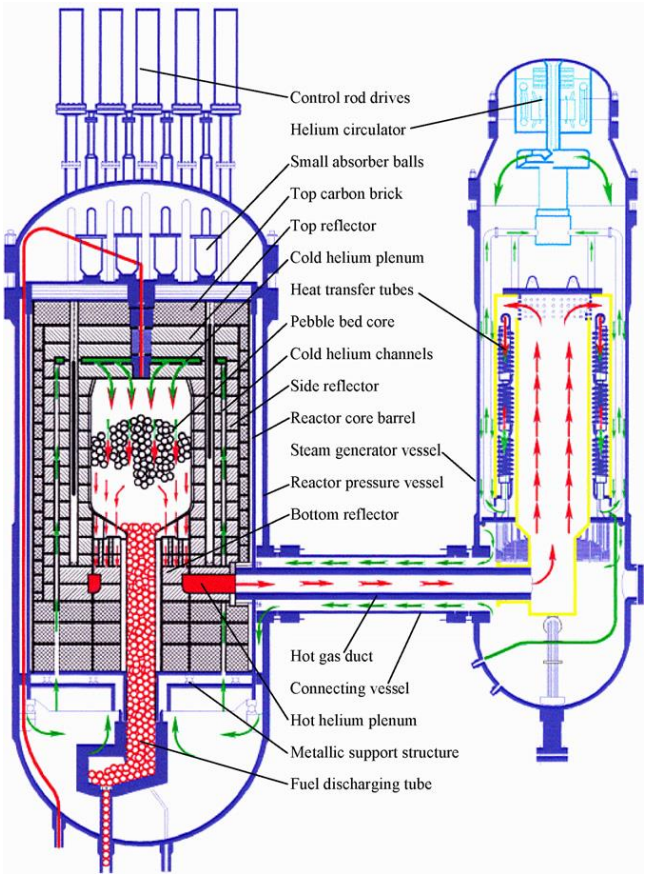

Figure 39: Primary circuit of the HTR-10, left: reactor pressure vessel with pebble bed core, right: steam generator with helium blower [56]

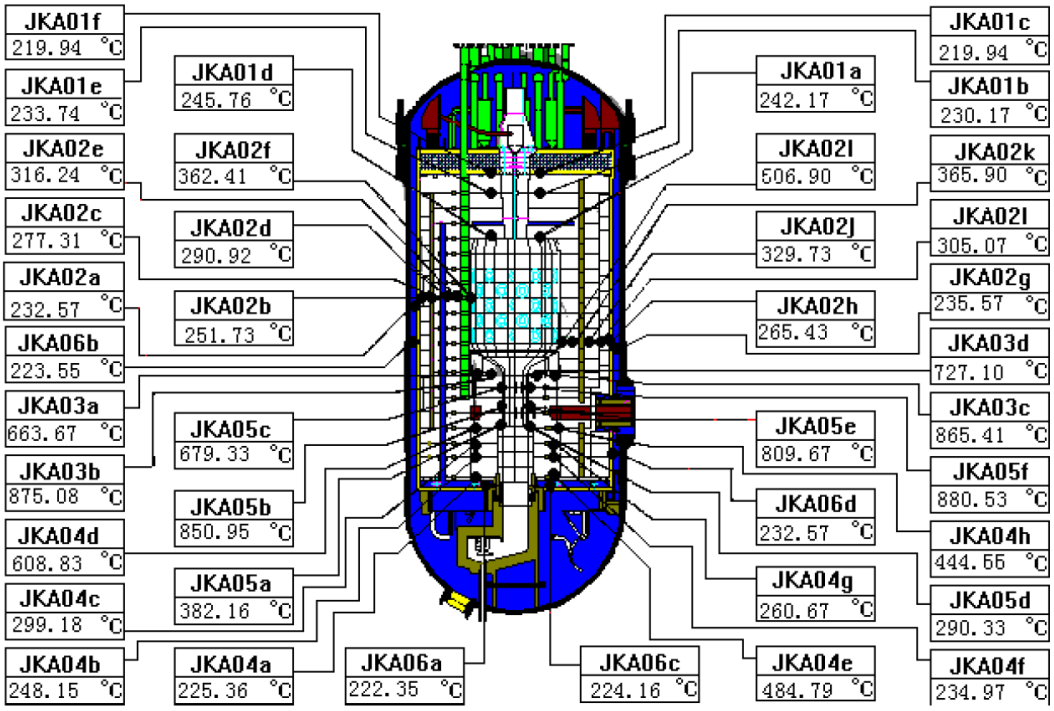

Figure 40: Location of thermocouples in the HTR-10 with temperatures [81]

The internals of the HTR-10 are instrumented with a multitude of thermocouples that measure the solid temperature of the reflector structures. It is, in fact, the only pebble bed reactor operational (even though not in constant operation) where validation is possible. With this instrumentation the temperature distribution within the reflectors can be measured. The location of the thermocouples is depicted in Figure 40.

For the HTR-10, both a 180°-model and a 30°-model was created. However, since the position exact location around in the HTR-10 could not be specified, a 2-dimensional representation of the HTR-10 was chosen for the comparison with temperatures of the full power experiment. For the neutronics, 13-neutron groups for the steady state were used applying the transport approach for TORT-TD led to a k_{eff} = 1.00368. The thermal hydraulic boundary conditions are provided in Table 11.

The thermal hydraulic zonal subdivisions for the HTR-10 are presented in Figure 41 along with the gas velocities. The pebble bed is the centre rectangle (cylinder) in red ranging from z = 1.8 – 0 metres. The corresponding power distribution and the gas temperatures are depicted beside. The position “A” in Figure 41 indicates the gas outlet. Here, the calculated gas temperature is 699.5°C. In the measurements of the gas temperature the result was 700.5 °C which agrees very well with the results produced with TORT-TD/ATTICA^{3D}.

Table 11: Main parameters for full power in the HTR-10

Thermal power	10 MW
System pressure	30 bar
Mass flow	4.32 kg/s
Inlet temperature	250 °C
Outlet temperature	≈ 700 °C

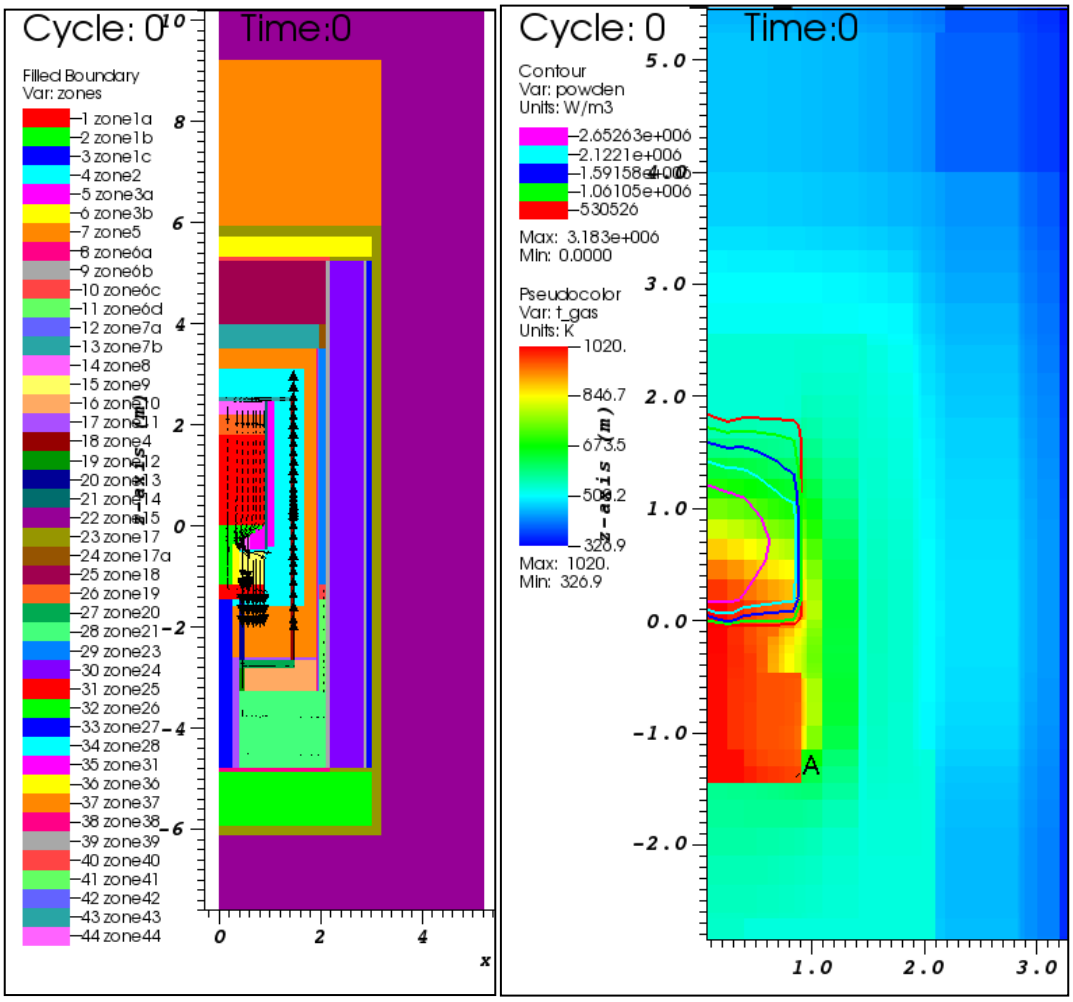

Figure 41: Left: Zonal subdivision of the HTR-10, gas flow direction is indicated by black arrows; right gas temperatures in colour, power density as isolines, the position “A” indicates the location of the gas outlet, where the temperature is 699.5°C.

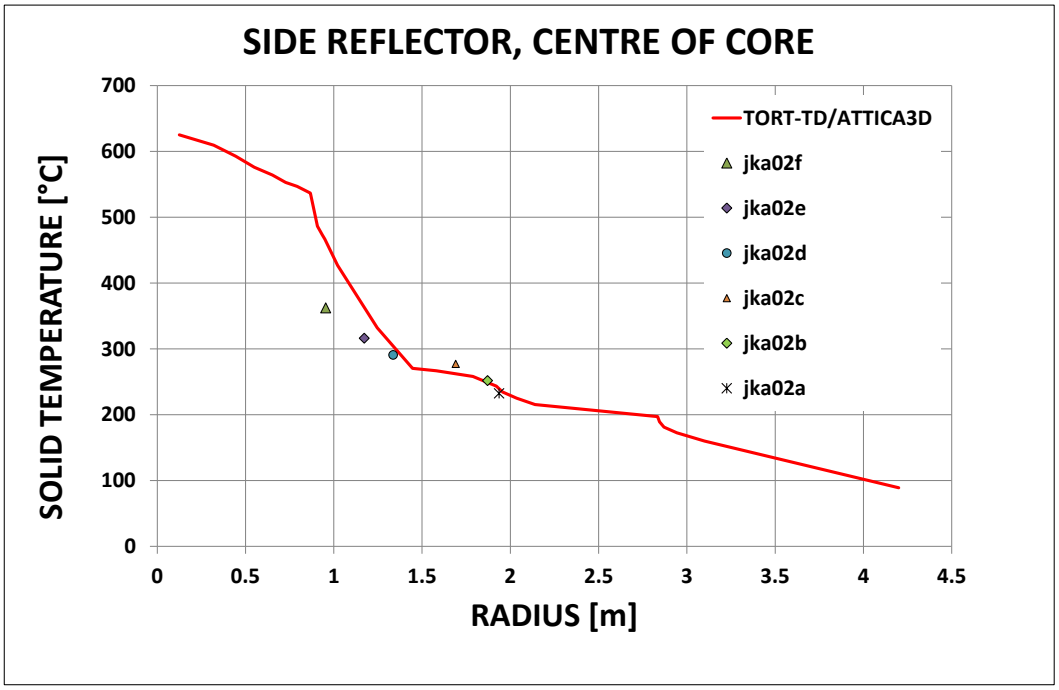

Figure 42: Comparison of TORT-TD/ATTICA3D results with the thermocouples jka02a, jka02b, jka02d, jka02d, jka02e and jka02f [81].

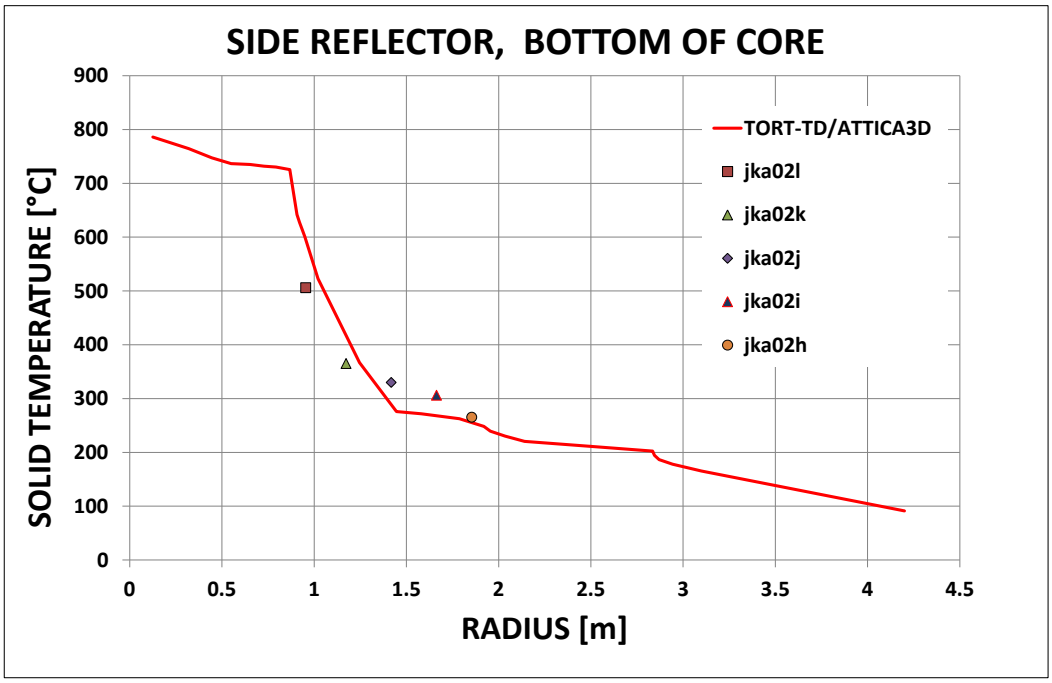

Figure 43: Comparison of TORT-TD/ATTICA3D results with the thermocouples jka02h, jka02i, jka02j, jka02k and jka02l [81].

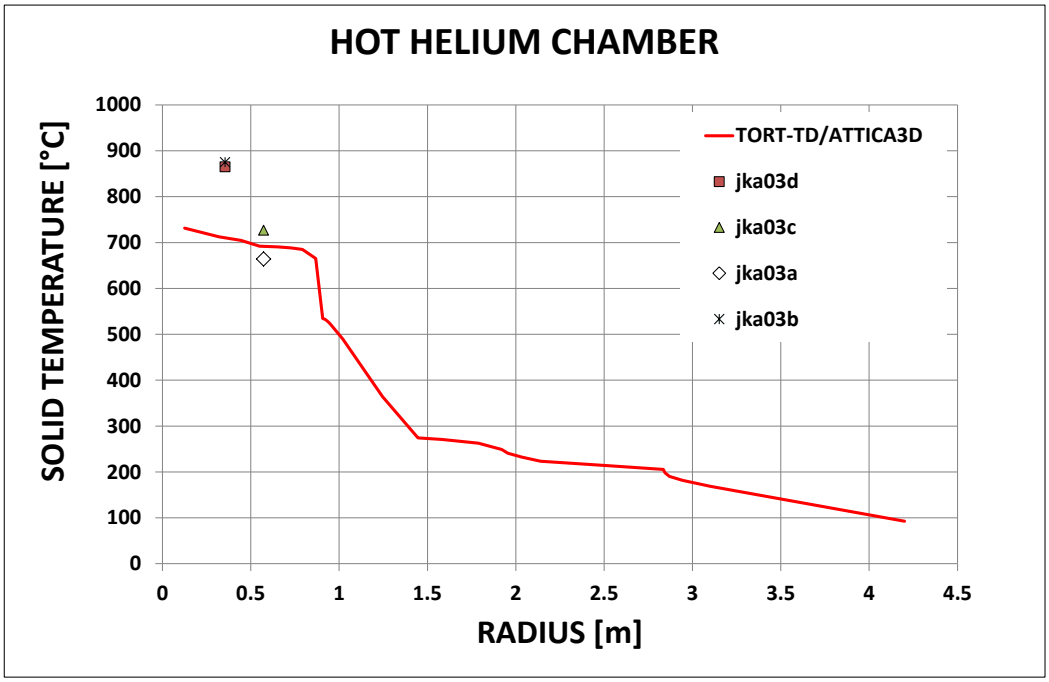

Figure 44: Comparison of TORT-TD/ATTICA^{3D} results with the thermocouples jka03a, jka03b, jka03c and jka03d, [81].

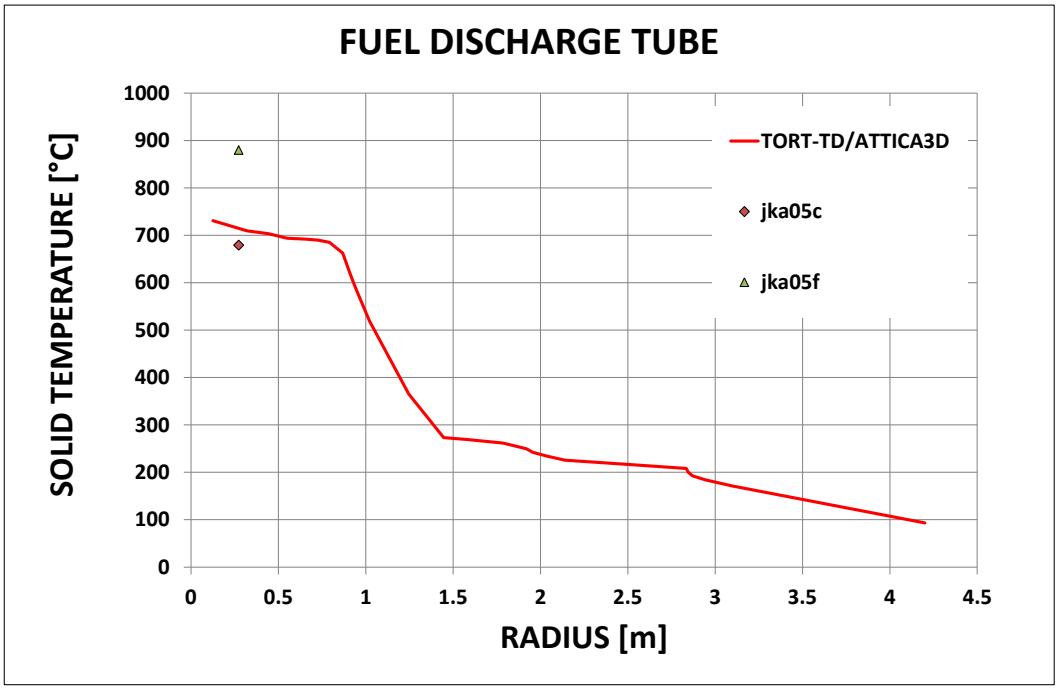

Figure 45: Comparison of TORT-TD/ATTICA^{3D} with thermocouples jka05c and jak05f at the fuel discharge tube, [81]

6 Application of the coupled simulation system

6.1 Spatially resolved control rods

The benchmark description provided nuclear two group cross sections. Since most of the exercises can also be solved in a 2-dimensional manner, the cross section for the control rod was provided as a grey curtain. The grey curtain approach is an equivalent cross section that is generated homogenising the control rods from a detailed model so that comparable reactivity increase is obtained. Lacking a detailed 3-D MCNP model that would be optimal as comparison case an inverse approach was applied. I.e. instead of applying a detailed MCNP model, the absorption and total cross section of the control rods was adjusted in a way that roughly the same power increase and consequently, the same temperature increase was obtained, while yielding comparable reactivities for the controlled and uncontrolled state (grey curtain case: 1.97 %; spatially resolved rods: 2.24 %).

Meier [27] simulated the control rod curve for the PBMR benchmark model with MCNP5 and obtained a reactivity increase from the nominal operational condition to the withdrawn condition of ~2.55%. With only 2 neutron groups used in the benchmark, it is questionable if the control rod ejection is adequately modelled, but the generation of cross section - especially for benchmark purposes - could not be performed within this work. However, for the HTR-PM, such a MCNP model exists and was used to adjust the efficiency of the absorber.

The PBMR-400 concept foresees 24 control rods [46]. The smallest unit with two neighbouring control rods is a 15° cake piece cut out of the PBMR geometry and is depicted in Figure 46 where the thermal flux is shown at the flux maximum and at the lower end of the control rods. In b) there is a clear depression of the neutron flux in the vicinity of the rods. In the reflector region between the rods the flux is higher. The control rods in this simulation model are halved. For the manipulation of the rod cross section, different factors for the weighting of the absorption and consequently the total cross section of the control rods where applied. The first approach used areal weighting. Areal weighting means that the rods now occupy the same area as a control rod (in a grey curtain case the control rod cross section is in each of the angular segments of Figure 46). This yields an opening angle of 2.95° for a single rod with a diameter of 12.5 cm, or a relative fraction within the absorber ring of 19.6 %. The correspond-

ing weight is the inverse value of the relative fraction, i.e. 5.08. This factor is the factor for areal weighting. However, with an areal weighting the corresponding k_{eff} was too big compared to the reference solution and the reactivity increase, and hence the power increase, were underestimated. The factor to multiply the absorption cross section of the control rod was now tested so that comparable power and temperature increase could be obtained. The factors tested were 10, 40, 100, and 1000. The results with the best agreement for both power increase as well as temperature increase were then used for the single control rod ejection in chapter 6.2.

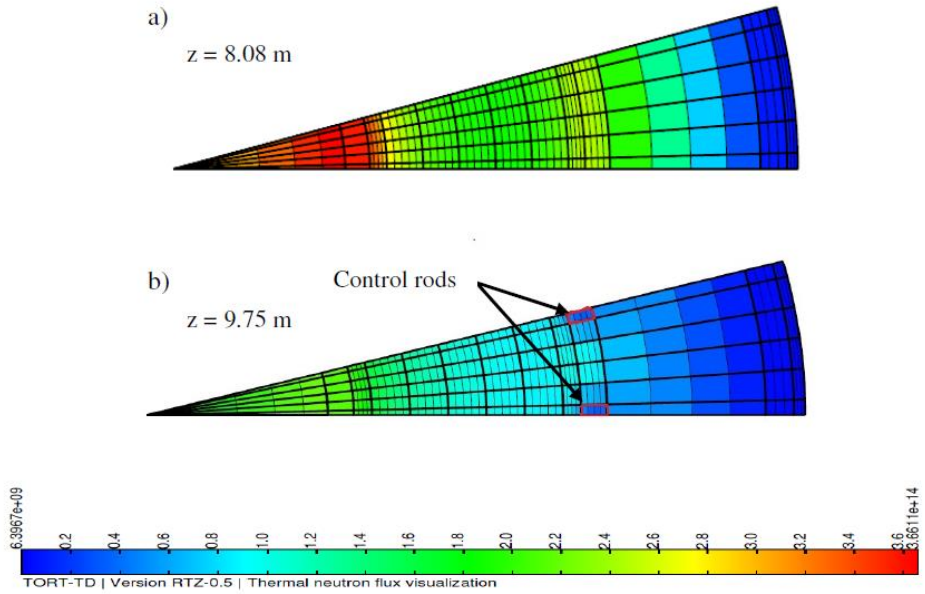

Figure 46: Thermal flux a) flux maximum b) at lower end of spatially resolved control rods for a 15° wedge with two control rod halves

In the following figures, the red curves with "TORT-TD/ATTICA^{3D} het" are the reference solutions, i.e. the results from the cylindrically symmetric modelling, compare 5.1.4. The other curves with modified cross section are referred to as "mod" with the corresponding multiplier attached, i.e. "mod10" for a multiplier of 10 etc.

The evolution of power of the cases with spatially resolved control rods is shown in Figure 48. For the multiplier "mod1000" the best agreement is obtained, but the power value is slightly overestimated yielding a power increase factor of 4.81 instead of 4.74 for the reference solution. When looking at Figure 49 and Figure 51, it becomes evident that the temperatures obtained for the "mod1000" case are still lower than in the reference solution, let alone "mod10" or "mod40" solutions. Taking a closer look at the average fuel temperature evolution for the first 0.4 seconds in Figure 50, different starting temperatures as well as different fuel temperature evolutions can be identified. The

starting temperatures of the reference case was 821.5°C, 820.7°C for the “mod10” case, 816.4 for the “mod40” and 813.4°C for the “mod1000” case. While the shape of the temperature evolution for mod10 and mod40 deviates from the reference shape, the “mod1000” solution basically preserves the initial temperature difference ($\Delta T \approx 8$ K). The first two seconds of each transient (-2 seconds to 0 seconds), the steady-state is calculated in the transient mode of TORT-TD/ATTICA^{3D}. The reactor period is shown for the “mod1000” case in Figure 47. Only absolute values are shown.

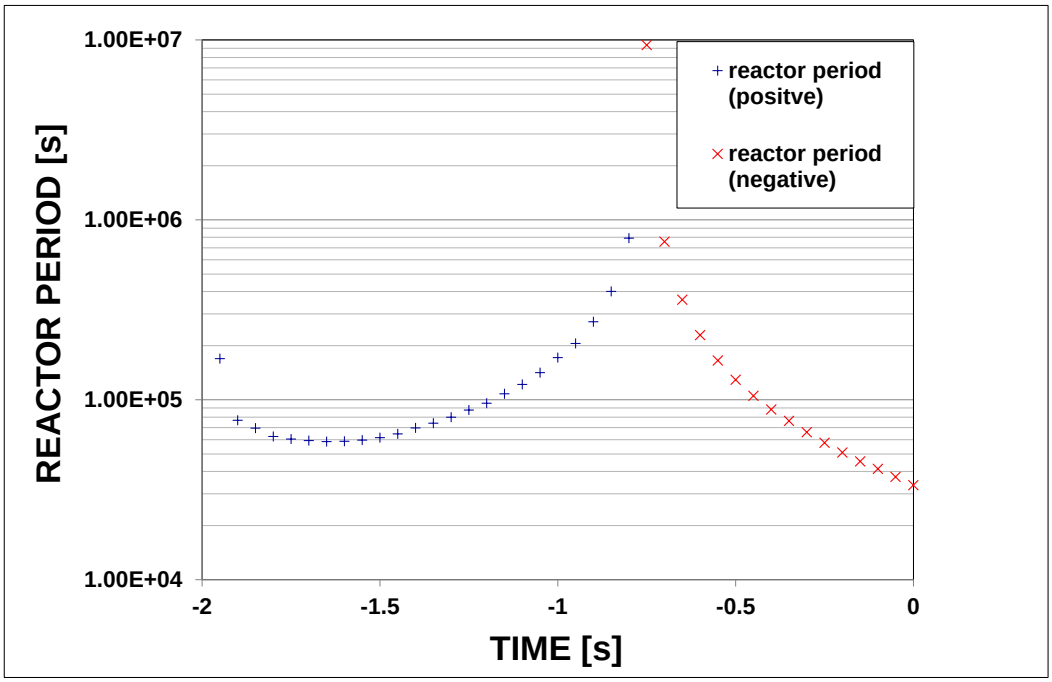

Figure 47: Reactor period for start of the transient calculation for the mod1000 case

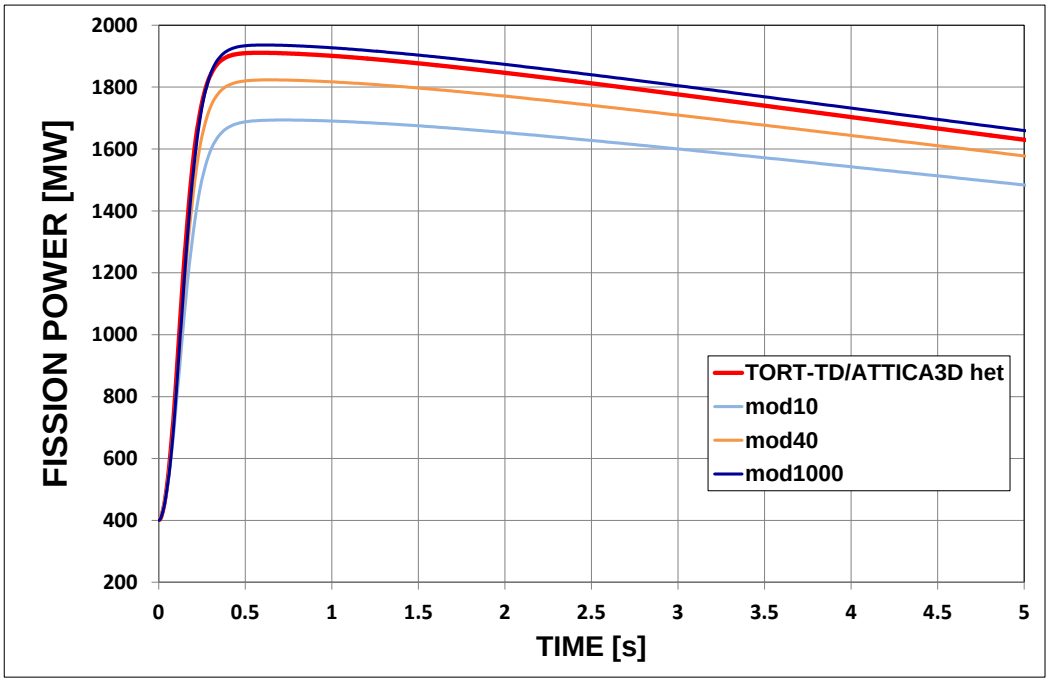

Figure 48: Power evolution for different factors (10, 40 and 1000) for absorption cross sections modification for the control rod cross section.

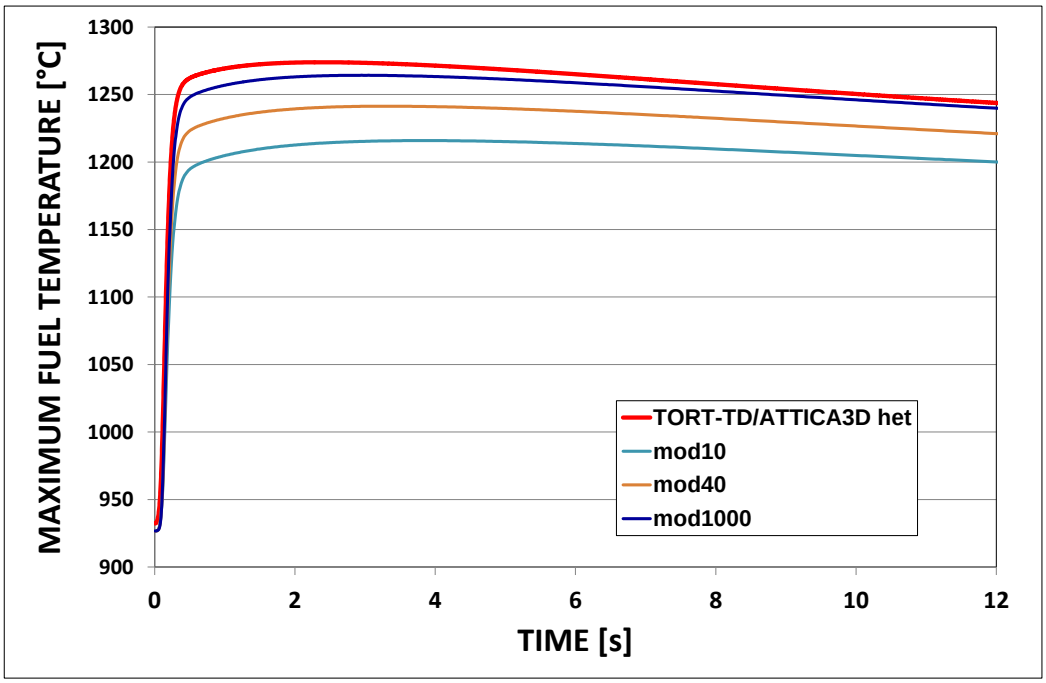

Figure 49: Maximum fuel temperatures for the total control rod ejection case with spatially resolved control rods.

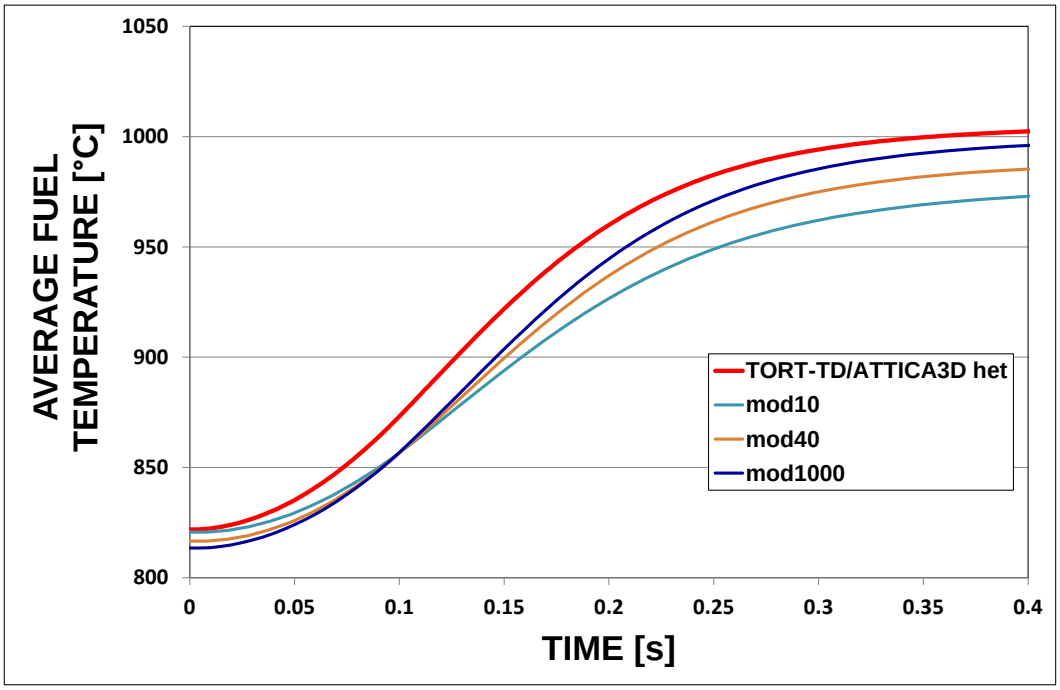

Figure 50: Average fuel temperatures for the total control rod ejection for different factors to modify the control rod absorption cross section.

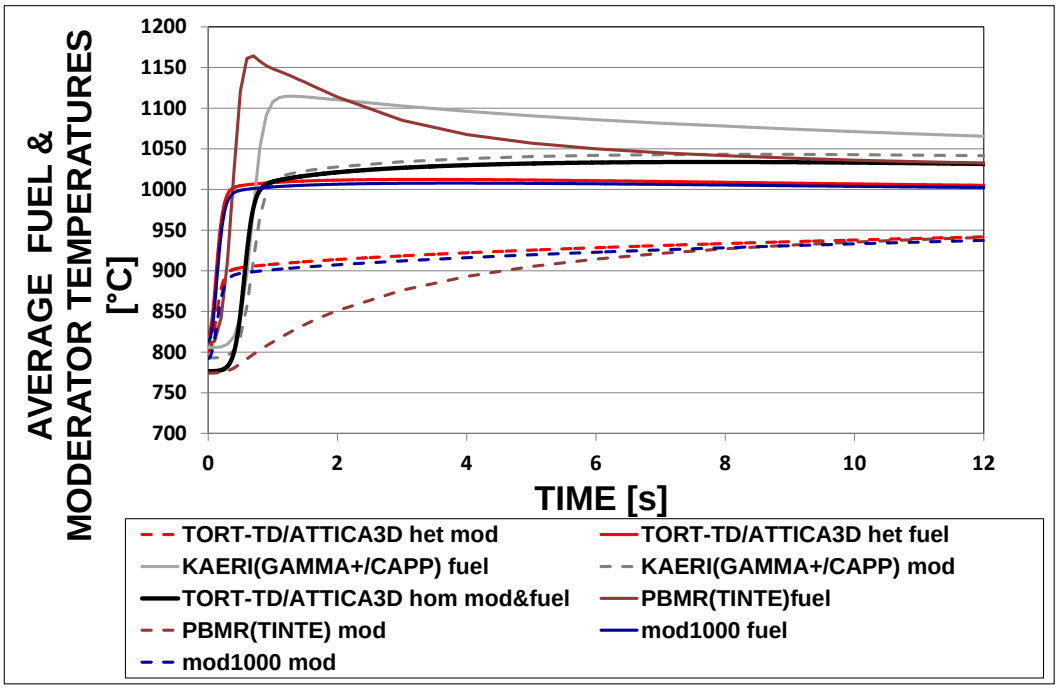

Figure 51: Average fuel and moderator temperatures for the control rod ejection case, with and without spatially resolved control rods.

6.2 Simulation of a Single Control Rod Ejection for the South African High Temperature Reactor concept (PBMR-400)

For the PBMR-400 benchmark, a single control rod ejection should be simulated. This transient can only be calculated if the rods are spatially resolved. Since the participants employed coupled codes that contain at least one two dimensional model for either neutronics or thermal fluid dynamics, results for that transient were not published. But this transient is used to demonstrate the computational capabilities of the coupled system TORT-TD/ATTICA^{3D}. As described for the case with spatially resolved control rods, the total and the absorption cross section of the control rods are modified in a way that the same reactivity increase occurs. The ejection time is 0.1 seconds, as in the total control rod ejection case. The previously determined modification factor of 1000 (chapter 6.1) for the absorption cross section will subsequently be used to perform this application calculation.

The reactivity value from one rod differs from the fractional value of the number of control rods, see Table 12. This is due to the self-shielding of absorbers. Self-shielding means that the influence of the ensemble of control rods is so strong that a removal of one rod is hardly detected by the reactor. The influence is less than the 1/24th of the control rod bank which would be 0.094 %, because the one withdrawn rod is shielded by its neighbouring absorber rods. Likewise for an insertion of a single absorber, the efficiency is higher than the mere fraction of a control rod. This was also tested by inserting one rod by 200 centimetres from the nominal position, similar to the ejection distance.

To determine the reactivity presented below, a steady-state solution was performed first. Then, the calculation is repeated but keeping the previously determined temperature and xenon distribution constant, i.e. without re-iterating fuel and moderator temperatures or xenon distribution but taking it from a restart file instead.

Table 12: Reactivity increase for rod ejection

Programme	Number of rods	Reactivity increase, $\Delta\rho$
MCNP5 [27]	24 rods out	2.55%
TORT-TD/ATTICA^{3D} (2D)	all rods out	1.95 %
TORT-TD/ATTICA^{3D}	24 rods out	2.256 %
TORT-TD/ATTICA^{3D}	1 rod out	0.030 %

TORT-TD/ATTICA^{3D}	1 rod in	- 0.27 %

Figure 52 shows the power evolution together with the average fuel temperature evolution for a single control rod ejection case. Since the reactivity inserted is only very small, the power increase is rather moderate with only 4.18 %. Using a previously determined integral temperature coefficient $\Gamma(T)$ from Meier [27] to make a rough estimate for the temperature increase that is to be expected for the uranium loaded PBMR-400 when inserting a reactivity of 0.03 % with

$$\Delta\rho = \Gamma \cdot \Delta T \tag{6-1}$$

with $\Gamma = 0.55 \cdot 10^{-4}\, K^{-1}$ yields a temperature increase by 5.4 K. Since there is a shift in power distribution towards the top of the reactor and not all zones experience the same temperature increase. The effective temperature increase for the coupled solution is only 4.5 K.

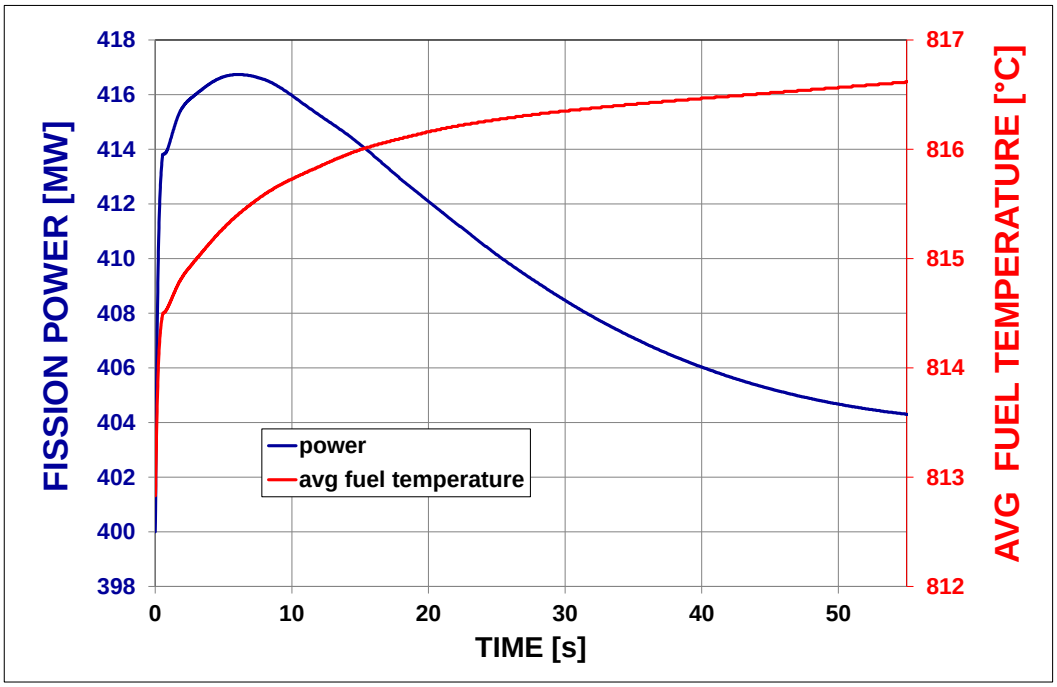

Figure 52: Power and fuel temperature evolution in a single control rod ejection case.

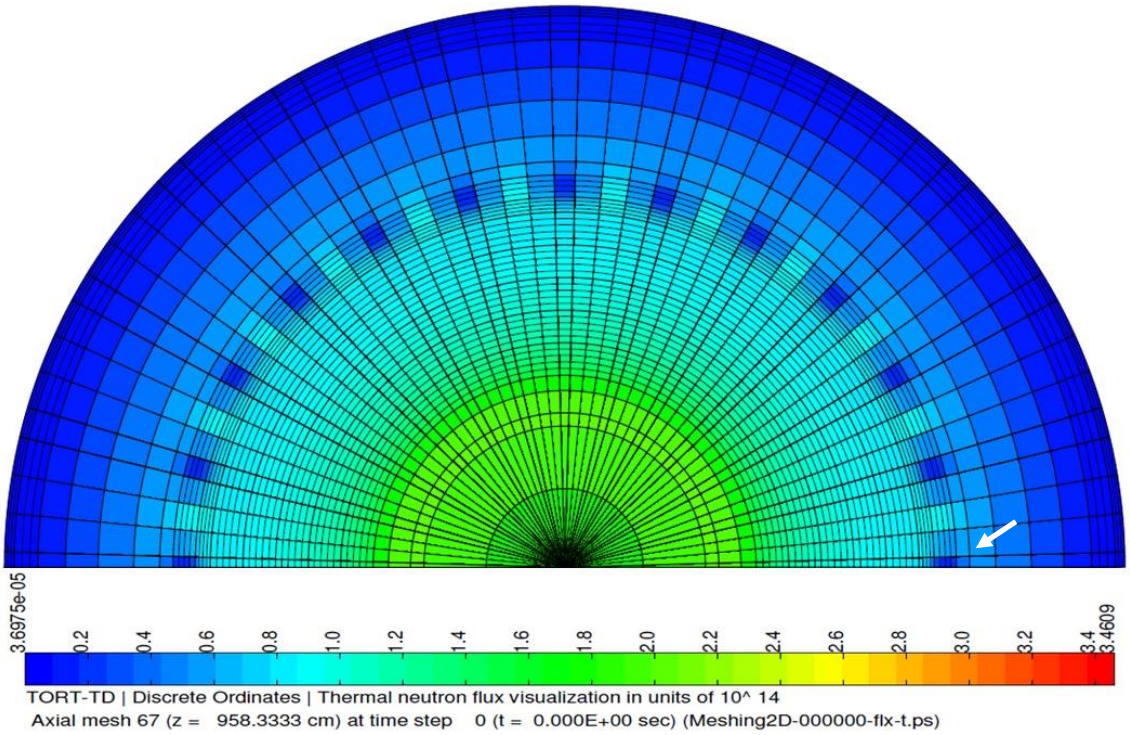

Figure 53: Thermal neutron flux at t = 0 seconds, with the position of the control rod to be ejected highlighted with a white arrow.

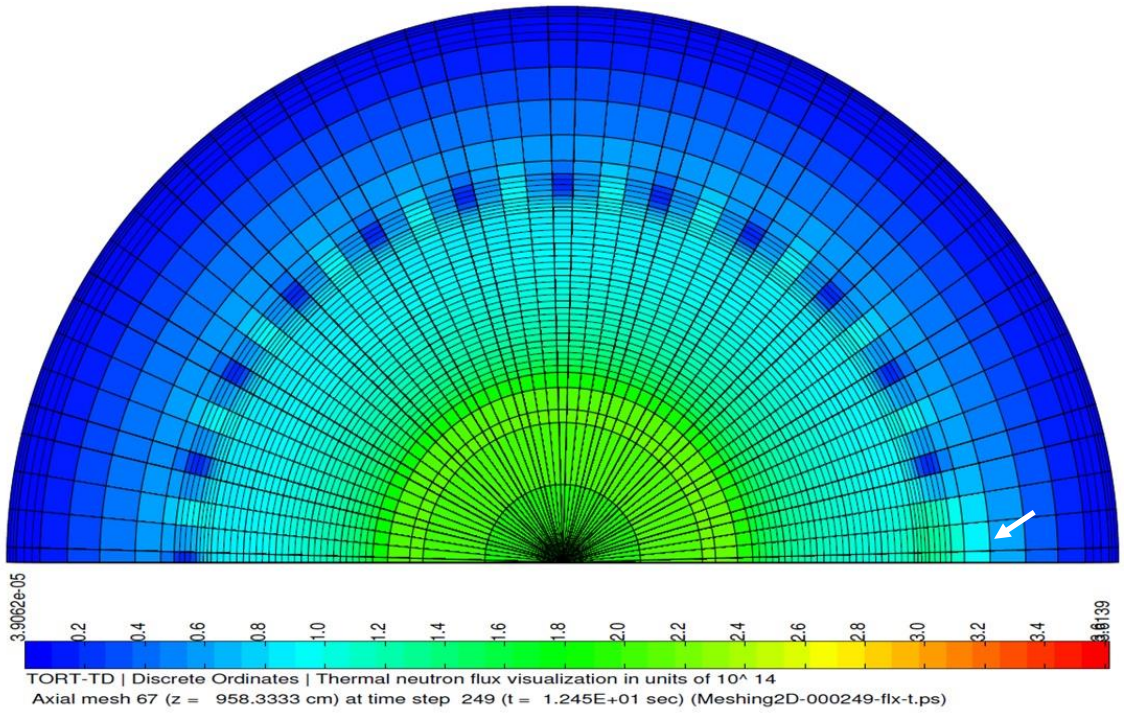

Figure 54: Thermal neutron flux at t = 12.45 s, on the right, the increase within the side reflector is visible and highlighted with a white arrow.

6.3 Simulation of a Single Control Rod Ejection for the Chinese High Temperature Reactor concept (HTR-PM)

The HTR-PM is the Chinese HTR concept where two reactor units are to drive one steam turbine. The thermal power of a single unit is 250 MW. It employs the side by side concept introduced by SIEMENS-INTERATOM, with the steam generator vessel and the integrated helium blower geodetically positioned below the reactor pressure vessel in order to obtain thermal fluid dynamic decoupling of heat source and sink. Like in the transient rod ejection analysis described in 5.1.4 the time of ejection is only 0.1 seconds. The HTR-PM however only uses 8 control rods instead of 24 in the PBMR. This increases the importance of a single control rod. In nominal operational conditions all control rods are inserted 290 cm from the top of the core.

When all 8 rods are ejected from there, the inserted reactivity is 1.3 %, in case of 3 rods ejected 0.433 % for both MCNP5 and TORT-TD/ATTICA^{3D} [30] and a single control rod worth is 0.115 %. This was determined comparing values with rods inserted at the nominal position and all rods, 3 rods and a single rod withdrawn but keeping the temperature and xenon distribution of the nominal case.

Figure 55 displays the thermal flux of the slowest (7th out of 7) neutron group at the position of the lower end of the control rods. The flux depression at the location of the control rods is obvious. The flux peak at the location of the control rods is the so-called reflector peak. The reflector peak is a consequence of fast neutrons going into the reflector where they experience a strong energy loss due to elastic scattering. This loss in the fast flux is a source term for neutron groups of lower energy. The reason for the smaller neutron flux inside the core region is that neutrons at these energies have a very high probability for absorption by fuel and are all absorbed in the fissile material.

After the control rod ejection, the power rises quickly to about 128 % within 7 seconds, see Figure 56. In the beginning (0 – 1 second), there is a steep rise of power by 20 % already, which, like in the PBMR-400 single control rod ejection case, is dampened by a fuel and moderator temperature increase. After the first second, the power increase until the following 7 seconds shows already the feedback effects, and without further actuation of control rod or shutdown system the power will approach the initial level.

Nevertheless, both control rod ejection scenarios lack the primary circuit feedback because increasing the power – even for a short time – will influence the whole plant behaviour. Say, the power increase will lead to significantly higher gas temperatures. Then, the steam generator cannot take all the heat and thereby the gas inlet tempera-

ture increases. However, an inlet temperature increase will also feed-back like an ingress of hotter coolant (opposite scenario of the cold helium ingress, see 5.1.2).

Figure 57 shows the position with the greatest increase in temperature. It is only 20 K, from the ejected control rod position to the position opposite of the ejected control rod.

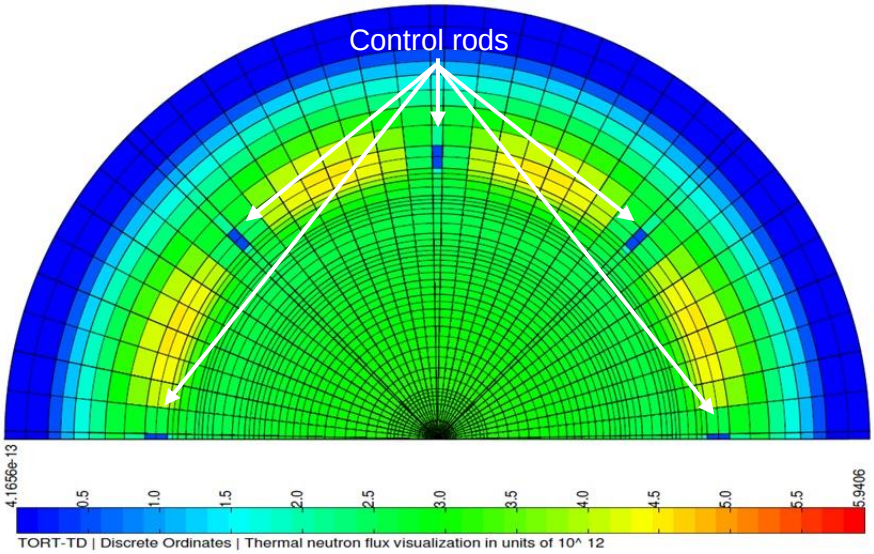

Figure 55: Thermal flux (7th neutron group out of 7) of the HTR-PM at the location of the lower end of the control rods at time t = 0 seconds (nominal state)

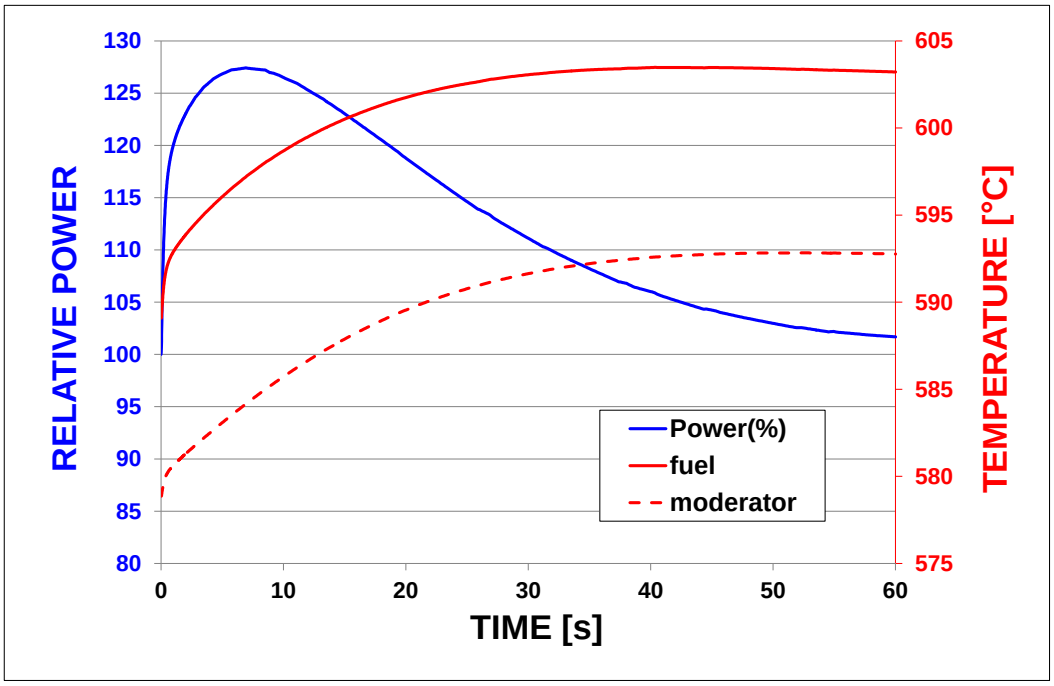

Figure 56: Power and temperature over time for the single control rod ejection case in the HTR-PM.

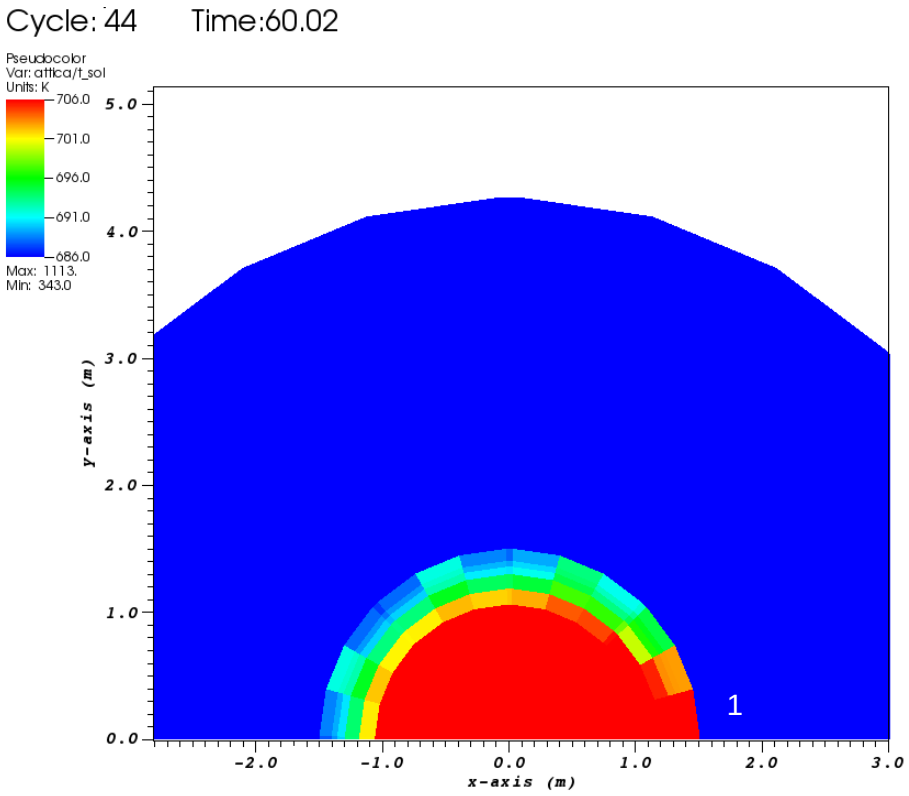

Figure 57: Temperature distribution at the plane where control rod ends were before the ejection; 1 is the location of the ejected control rod. Here, the greatest temperature increase was found. The increase due to the ejected control rod is around 20 K.

6.4 Simulation of Water Ingress Accidents for the Chinese High Temperature Reactor concept (HTR-PM)

The dynamics of water ingress accidents necessitate a simulation system that can not only model processes within the reactor pressure vessel or the primary circuit but must also cover the secondary circuit. As TORT-TD/ATTICA^{3D} lacks these abilities, use of pre-calculated boundary conditions is made. The dynamics of water pouring into the primary circuit of an HTR following steam generator tube rupture was investigated in [53]. Additionally, taking findings of [53], water ingress scenarios including neutronic response were investigated in [25]. The results produced with TORT-TD/ATTICA^{3D} for two water ingress scenarios – one with Scram, one anticipated transient without Scram (ATWS) – are compared to results of INET.

The first scenario to be examined is the case when a steam generator tube ruptures, steam enters and the blower flaps close to end coolant flow completely. The steam generator is quickly isolated by the steam generator isolation valves. Flow restrictors, an engineered safety feature, should prevent flow rates that are too high from entering the reactor. For the transient the steam generator isolation is assumed to work, effec-

tively separating the primary side from the secondary. The different boundary conditions with respect to time are [25]:

Time	Event	Difference to design basis accident
	Design basis accident	Anticipated transient without SCRAM
Initial situation	Reactor at 105 % of nominal power rating → 262.5 MW_{th}	Reactor at 100 %
0 – 10 sec	• break of one steam generator tube, approx. 600 kg of steam/water pour into the primary circuit • Primary pressure increase (70 → 74 bars), pressure increase over time including pressure relief taken from [25]	
10 – 40 sec	• humidity detector actuates blower shutdown • linearly decreasing blower power • control rods are inserted over 55 seconds	• control rods not moved
40 sec – 80 hrs	• onset of pressurised loss of forced cooling case including corrosion of graphite in steam atmosphere • short term effect: power increase due to improved moderation • long term effect: weakening of fuel and load-carrying graphite due to corrosive attack	
at 23 hrs	• pressure relief valve opens (set point 79 bar) to reduce pressure to 70 bar	

Additional boundary conditions for the TORT-TD/ATTICA3D simulation:

The pressure increase is a direct consequence of the increase of the primary inventory. Here, steam has the major contribution. During the course of the transient, the appearance of multiple gas components due to corrosion of steam will lead to a further increase in pressure. Since TORT-TD/ATTICA^{3D} can only simulate processes within the reactor pressure vessel and in such a way that reference pressure is an input parameter of the user, the pressure increase was approximated by using a time dependent pressure boundary condition. Since the major part of the flow will only occur inside the core (hot gas rises in the centre, transfers the heat to the top reflector graphite structure, and flows down on the outer core close to the side reflector), the outer helium risers are simulated as blocked (very high friction due to very small hydraulic diameter). This approach can underestimate corrosion in the side reflector. But comparison calculation showed that no significant corrosion occurs there anyway, nevertheless the time step size of the solution including corroding side reflector became unbearably small (less than 10^{-10} seconds).

Figure 58 shows the increase of power in case of the design basis accident where humidity is detected and appropriate measures, i. e. insertion of all control rods, are taken. The increase of total power amounts to 5 % after 10 seconds. The first five seconds are needed by the steam reach the core region in significant amounts (to have an impact). Then power increases until 10 seconds, when the control rods are inserted to end the power increase. The control rods are inserted over 55 seconds. The corresponding average fuel and moderator temperatures for the DBA case are shown in Figure 59

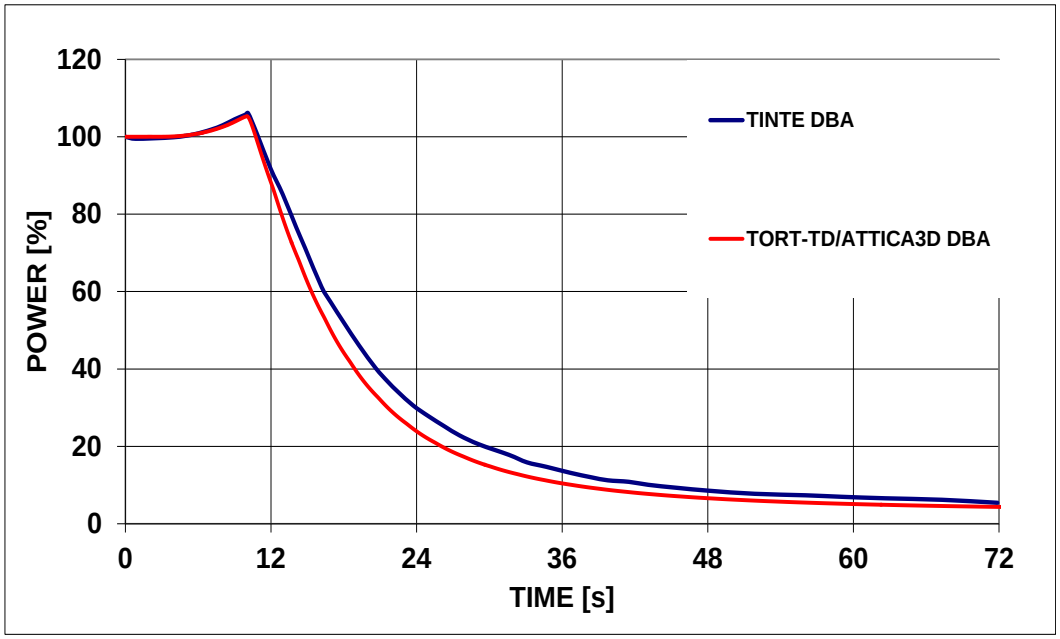

Figure 58: Short term power increase for the HTR-PM as a consequence of water ingress

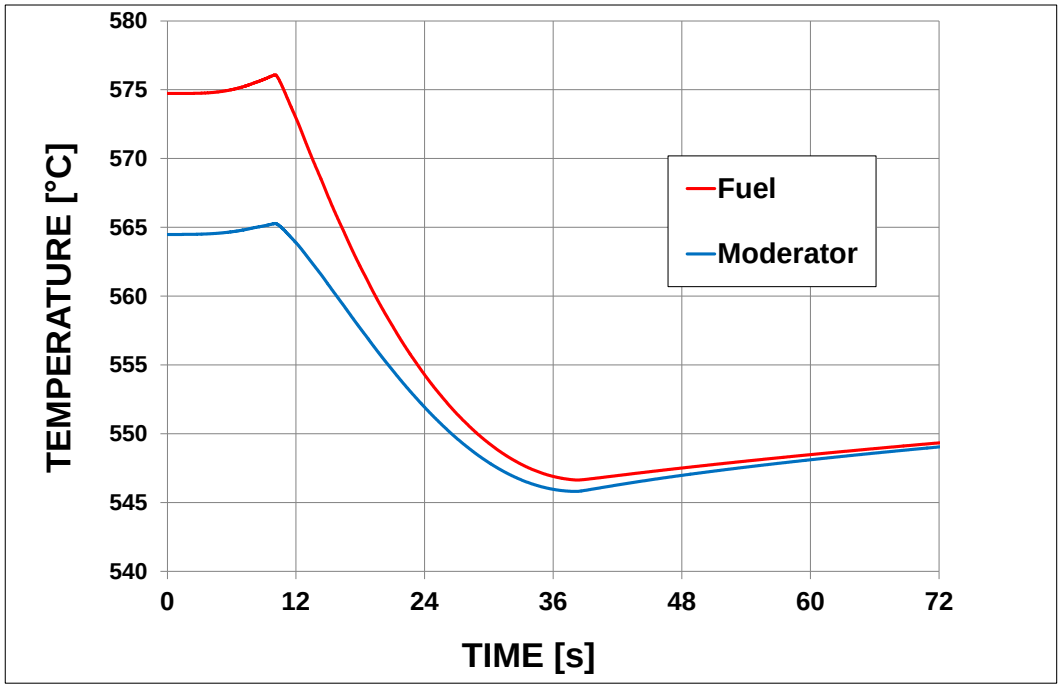

Figure 59: Short time effect on the average fuel and moderator temperature for the design basis water ingress accident, results from the TORT-TD/ATTICA^{3D} solution

After the steam is detected by the humidity sensors, the blower is turned off and the rods are inserted over 55 seconds ending the power increase for the design basis accident. The decay heat distribution of 105% of nominal conditions is taken from the ZIRKUS analysis. The short power increase in the range of seconds will not change

decay heat distribution significantly, and therefore will be taken as decay heat source for the long-term corrosion effects.

The long-time behaviour is characterised best by a pressurised loss of forced cooling case and is presented in Figure 60.

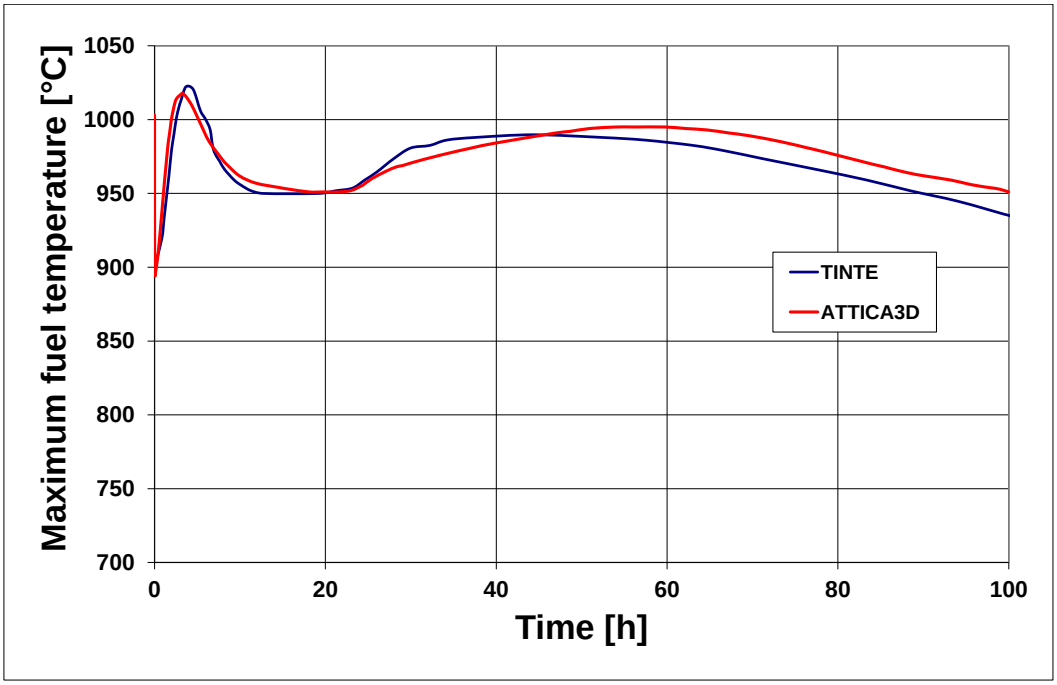

Figure 60: Maximum fuel temperatures for a design basis water ingress accident, TINTE results from [25].

In the beginning of the transient, the steam enters. However with the temperature distribution of nominal operation, even though at a higher level, the upper part of the reactor where the cold gas (250°C) enters is far below temperatures where corrosion takes place. Only at the outlet, where the solid temperatures reach (780°C) there is a minor corrosion attack. But the major part of corrosion due to steam in the core will take place in the course of hours. The reason is that the core first needs to heat up with the decay heat, so that temperatures are reached where corrosion becomes significant.

As mentioned above, the flow pattern in the water ingress design basis accident resembles the pressurised loss of forced cooling accident. After the blower stops, the bottom core and reflector are the hottest parts. The gas still under pressure heats up in the bottom and flows up in the central core. When the gas reaches cold top reflector (250°C in the beginning of the transient), it transfers its heat to the top reflector. The cooler gas flows downwards next to the side reflector in the outer part of the core.

In Figure 61 the flow patterns in steady state conditions and also after 11,800 seconds are shown. Here, the above described effect is visible.

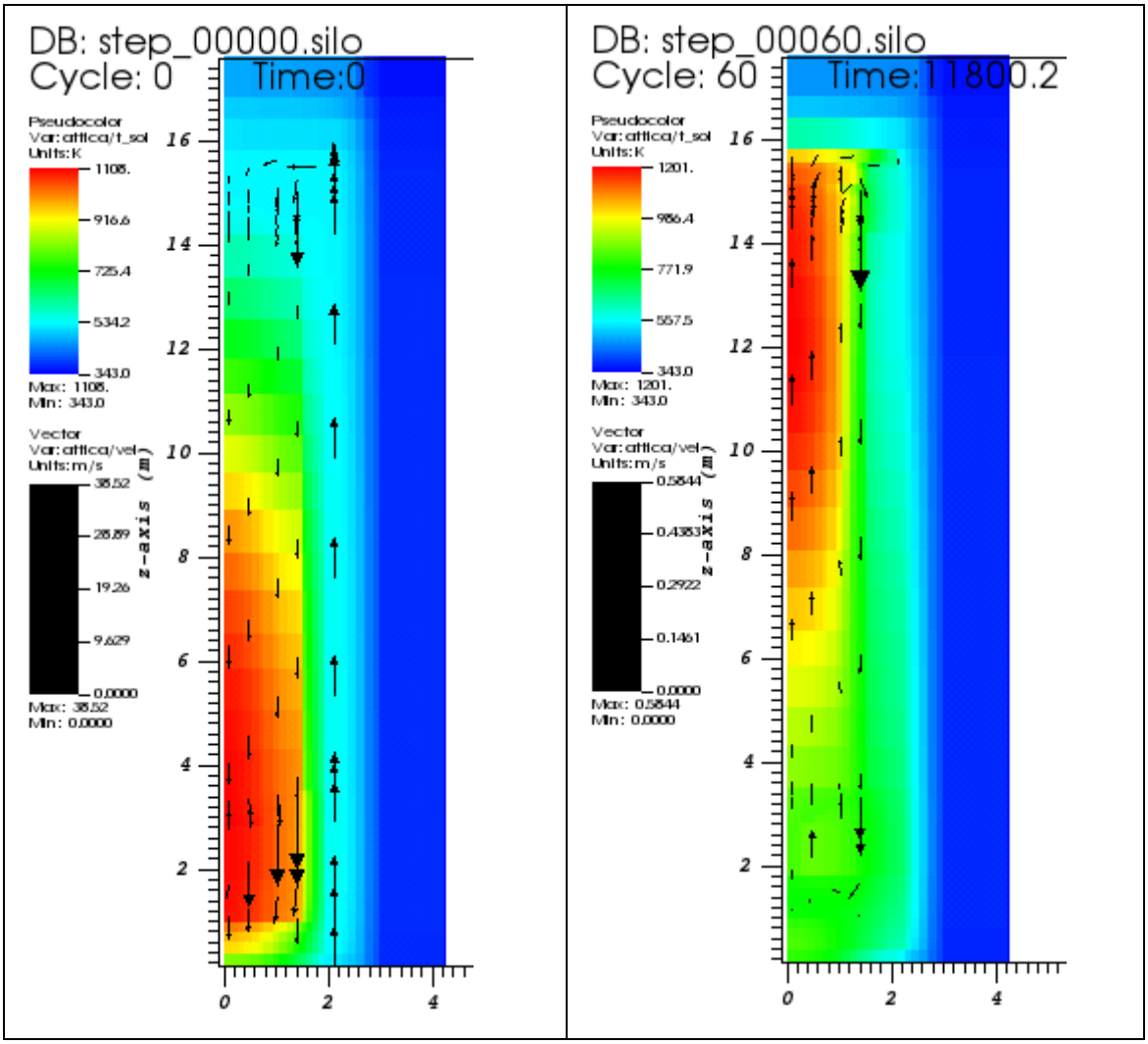

Figure 61 : Temperature distribution and velocities at t = 0 seconds (left) and after 11,800 seconds (right)

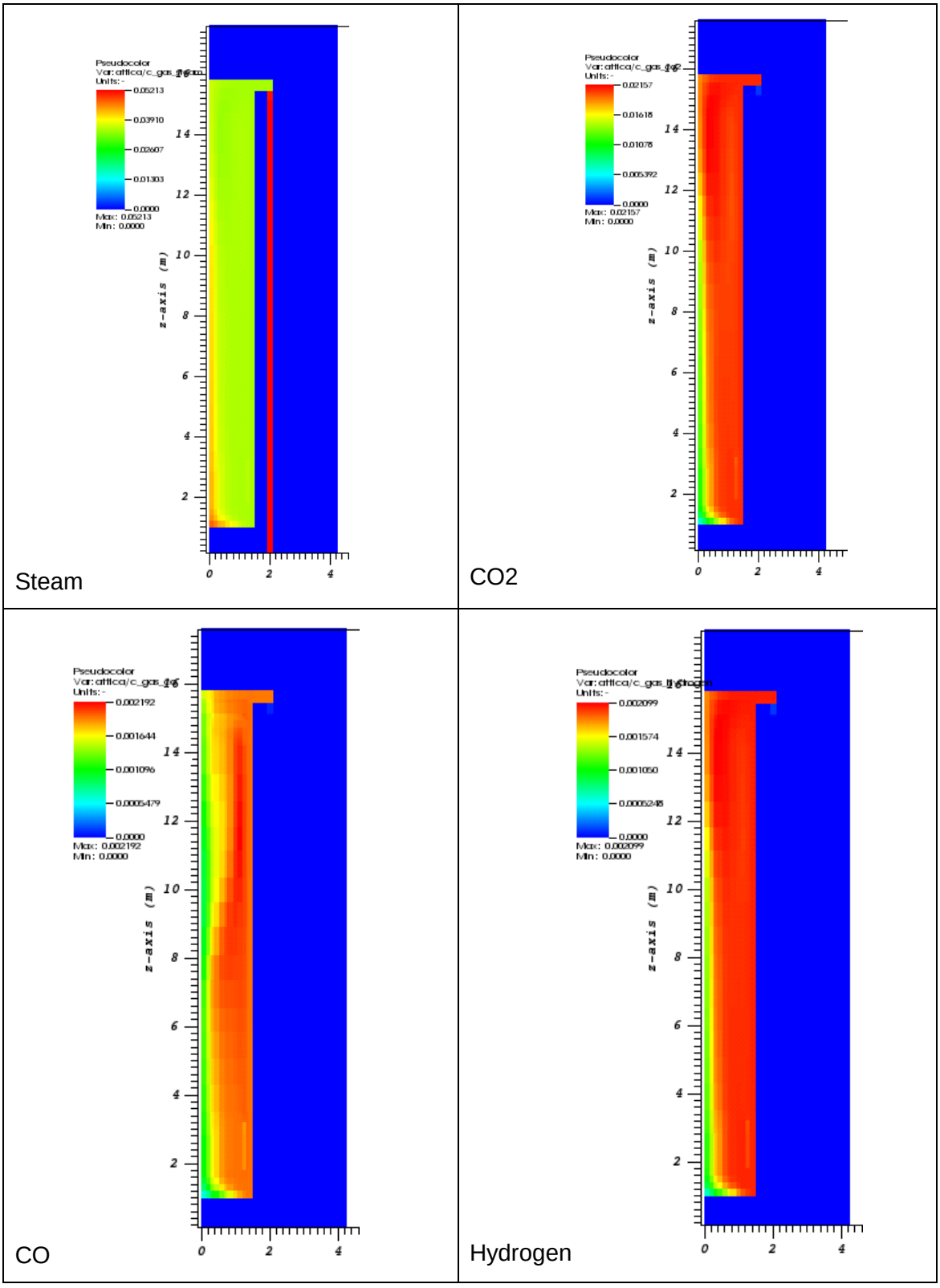

Figure 62: Steam and corrosion product distribution after 11,800 seconds (3.3 hours)

In Figure 62 above, the distribution of corrosion gases is presented. Here, it is to be noted, that the CO_2 is about five times higher than the corresponding CO concentration.

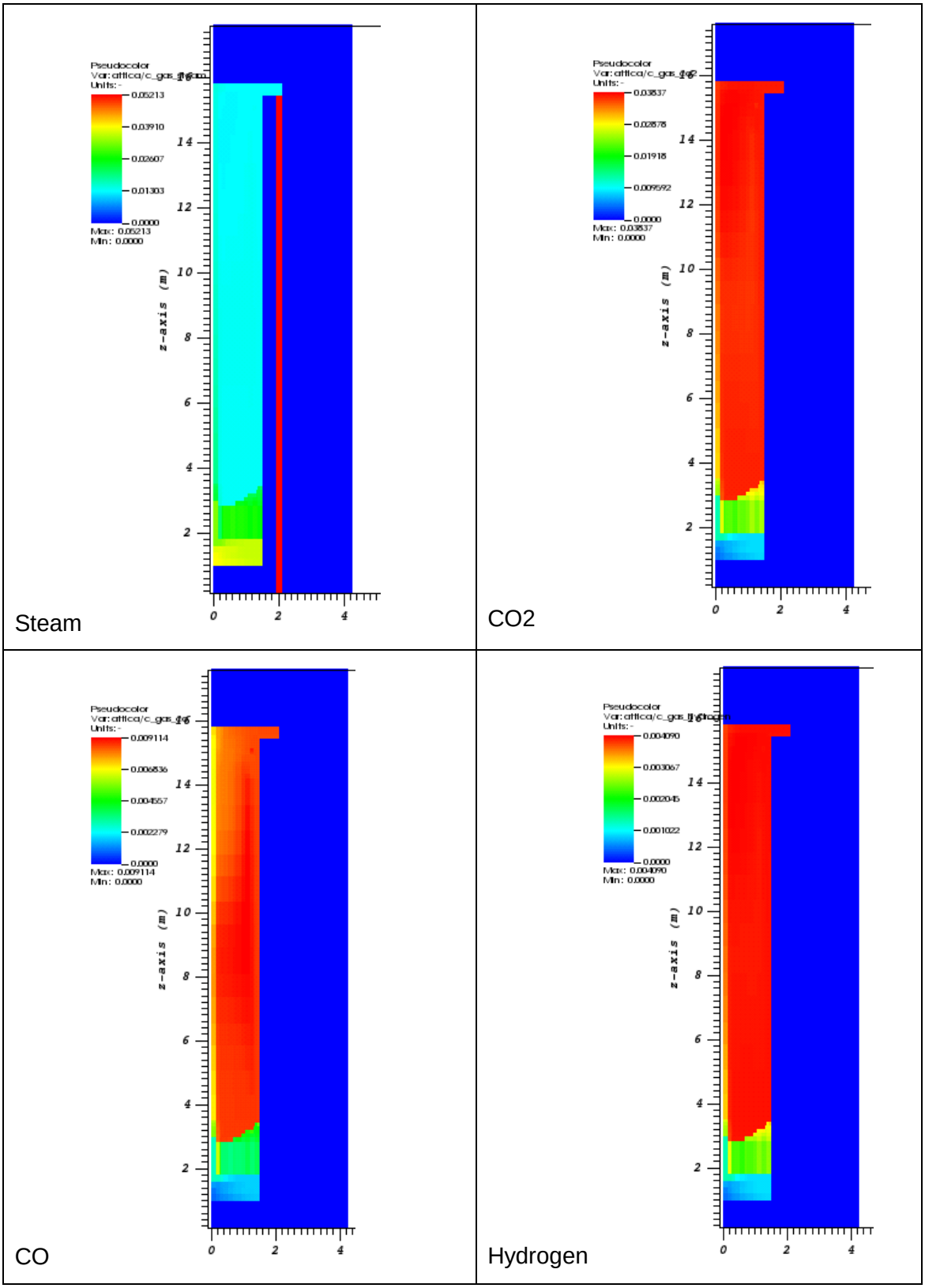

Figure 63 : Steam and corrosion gas distribution after 108,000 seconds (30 hours)

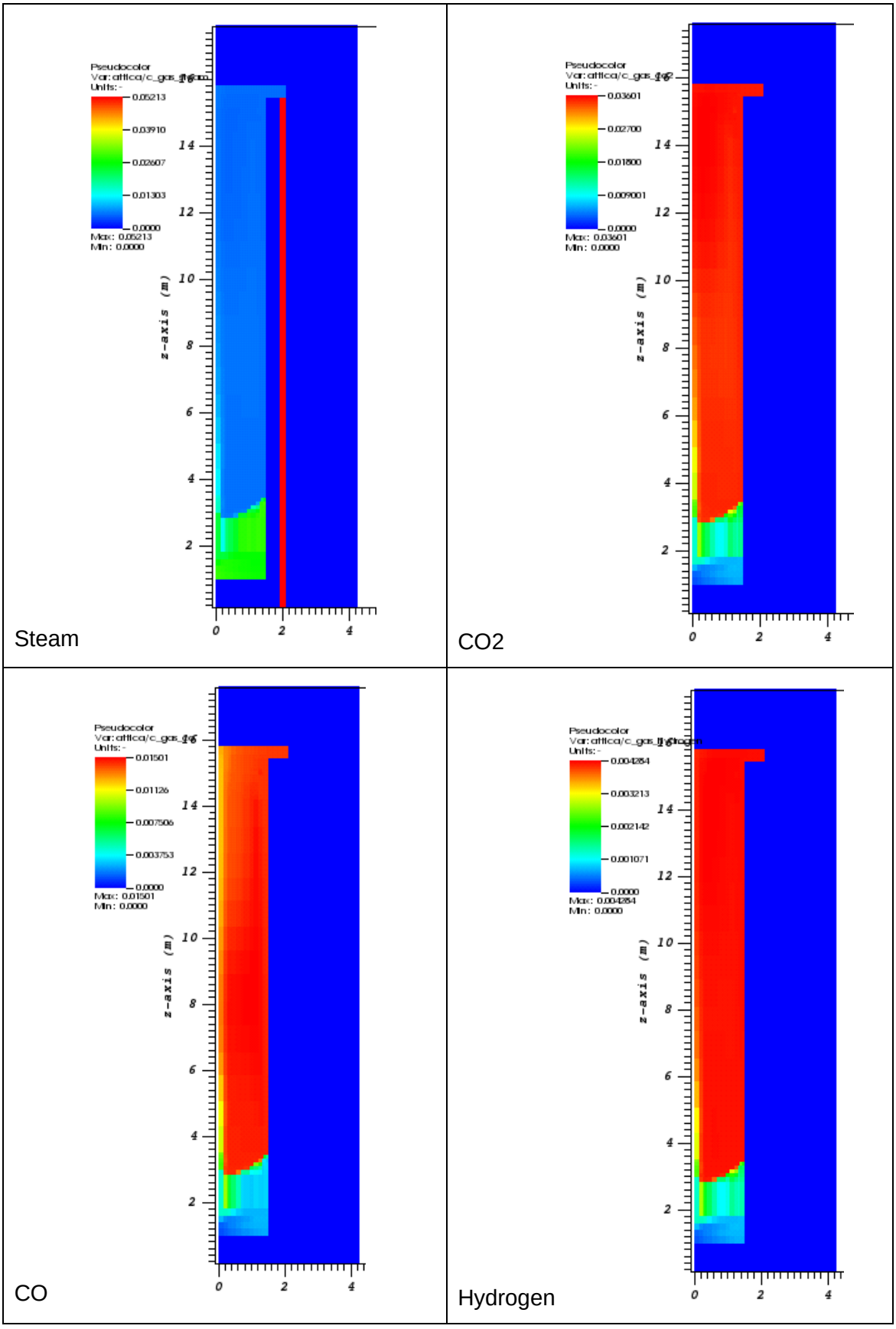

Figure 64: Steam and corrosion gas distribution after 216,000 seconds (60 hours)

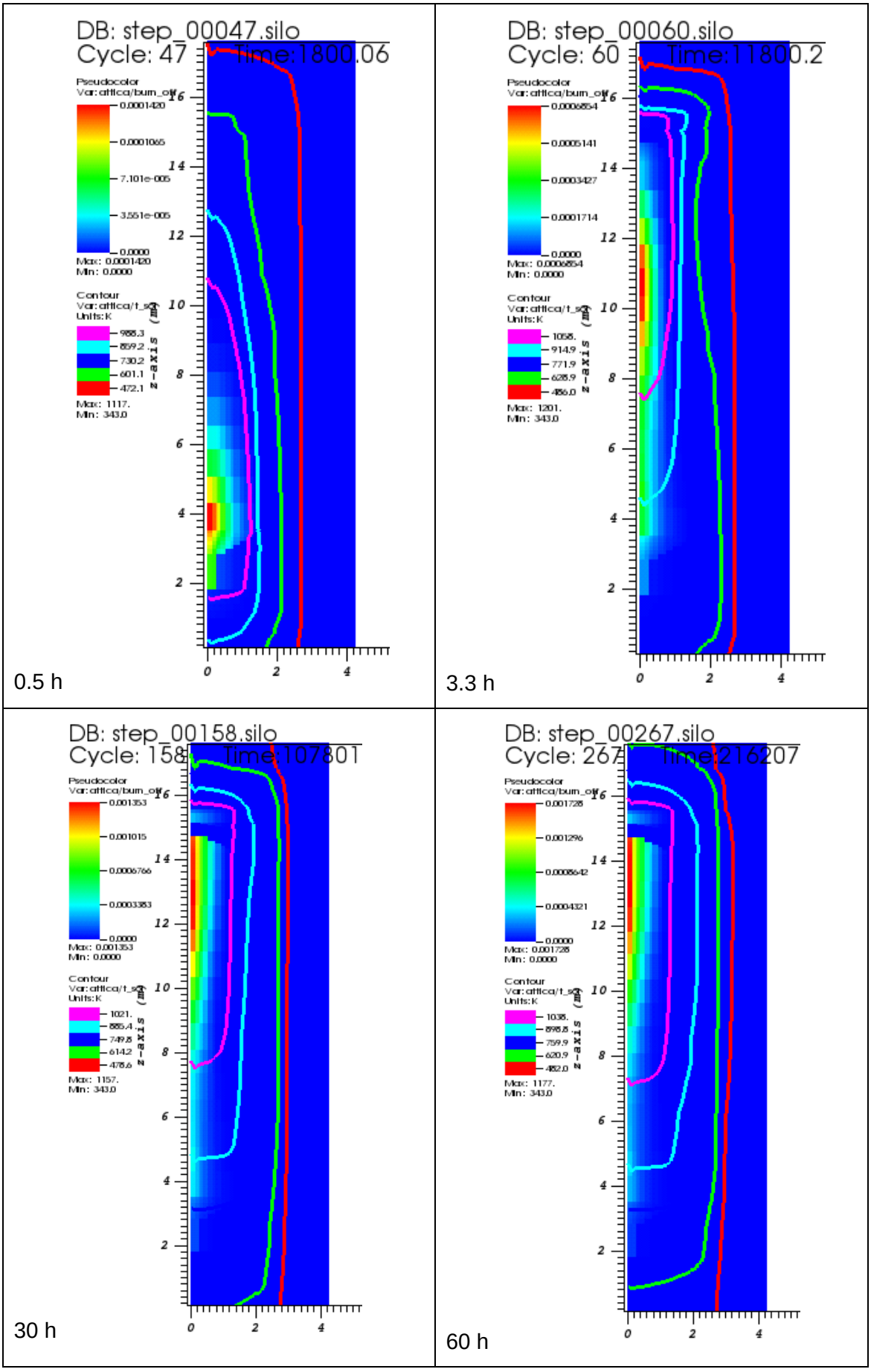

Figure 65: Relative burn-off of graphite after 0.5, 3.3, 30 and 60 hours

At the outlet, there is a concentration of steam present that corresponds to the 4 bar partial pressure out of 74 bar total pressure in the start of the transient. This steam concentration reduces linearly to 0 over 500,000 seconds.

The steam flow is corresponding to the gas flow of the helium. Since the core heats up and the temperature maximum shifts from bottom to top, the first centre of corrosion can be found in the lower part. With the re-distribution of the solid temperature and the cooling down of the lower part, the steam can now enter the core region and attack fuel elements. The centre of corrosion slowly shifts upwards and follows the temperature maximum.

The centre of corrosion starts at the bottom reflector where in steady state conditions the temperatures are high enough that corrosion can take place. This can be seen in Figure 66 and Figure 67, where 0 metre is the lower end of the pebble bed; 11 metres being the top of the core.

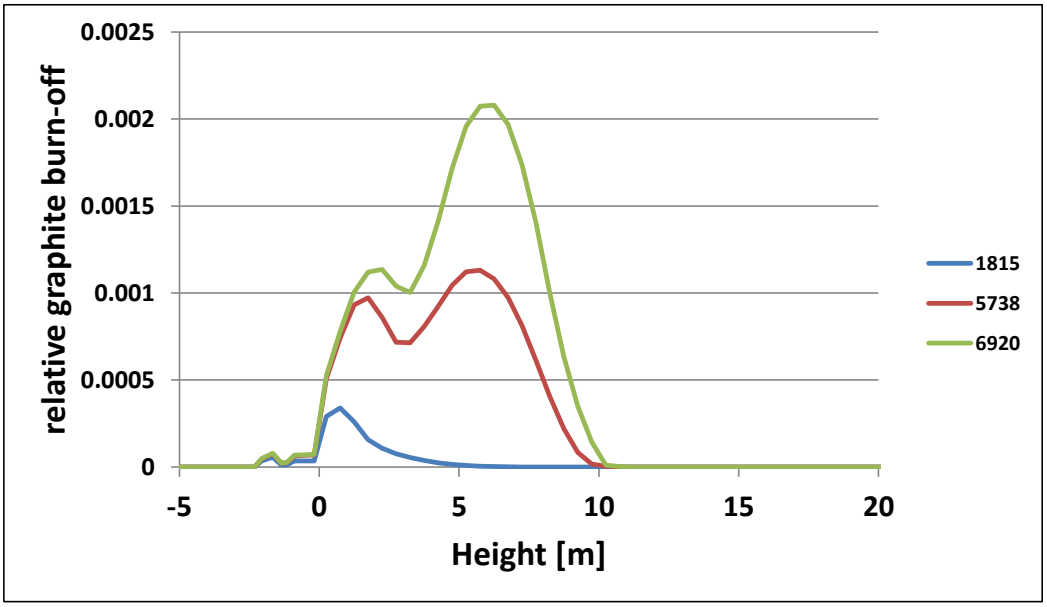

Figure 66: Relative graphite burn-off after 1,815 seconds, 5738 seconds and 6,920 seconds in the core zone next to the centre line (at radius = 0.058 m)

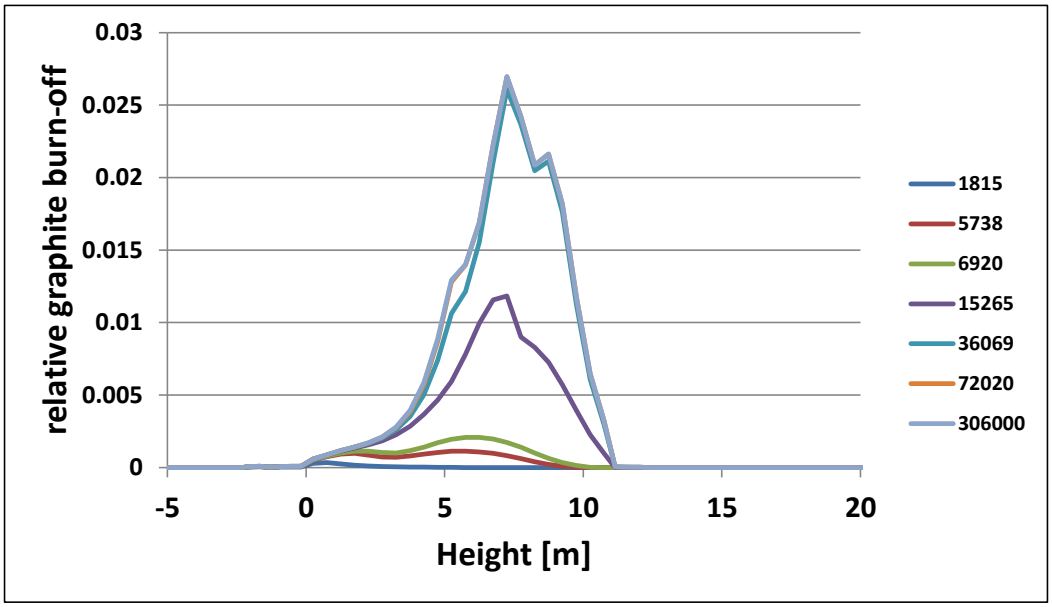

Figure 67: Relative graphite burn-off after 1,815 seconds, 5738 seconds, 6,920 seconds, 15,265 seconds, 36,069 seconds, 72,020 seconds and 306,000 seconds in the core zone next to the centre line (at radius = 0.058 m)

Figure 68 shows the power increase as a consequence of water ingress without the insertion of control rods. In this case, the increase in power is stopped by the fuel temperature effect, see Figure 69. In the TINTE result the power level increases a bit faster and hence, presumably fuel and moderator temperatures increase more rapidly which could explain why the maximum value of TORT-TD/ATTICA^{3D} lags around one second behind. Also one has to keep in mind that for our calculation assumptions for the increase of the steam at the inlet has to be made. Unlike the TINTE code, the steam transport has to be simulated by changing boundary conditions.

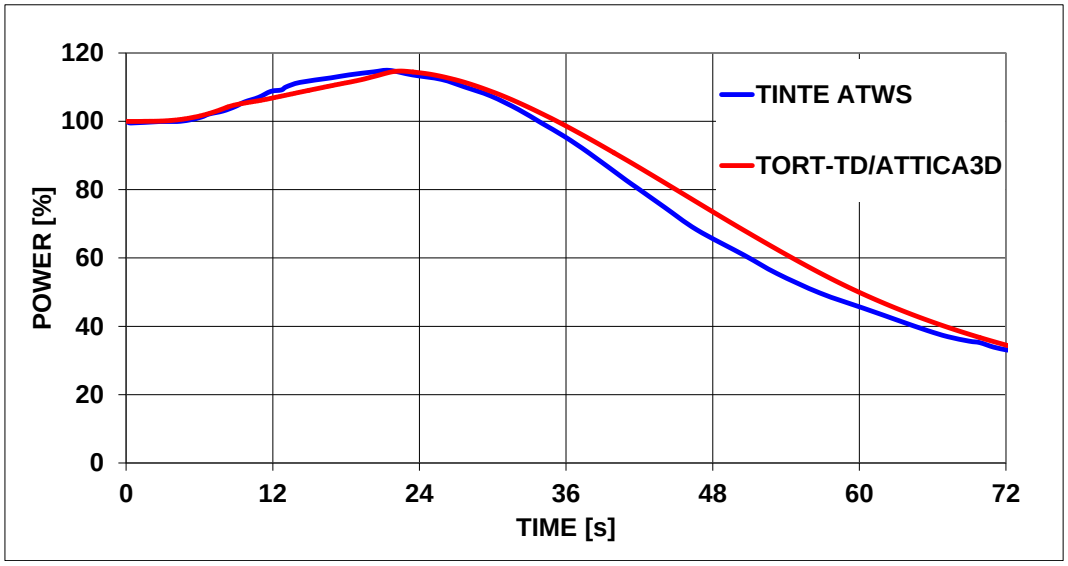

Figure 68: Short-term power increase in an anticipated transient without SCRAM case. The reactor is only shutdown by means of the fuel and moderator temperature effect.

Figure 69 below shows the total power again, but this time together with the decay heat which obviously does not change due to the short-term power increase. Also the fuel and moderator temperatures are presented which obviously start to rise as soon as the power increases.

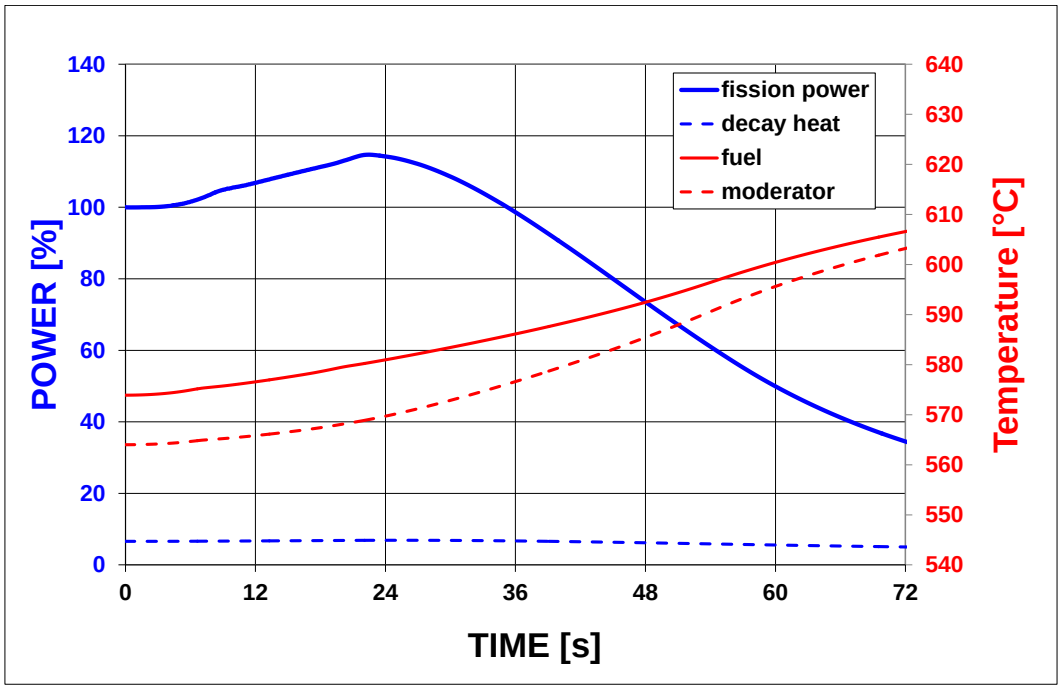

Figure 69: Fission and decay power (left axis), fuel and moderator (right axis) for the anticipated transient without Scram case.

A 3-dimensional case is analysed. The assumptions of the design basis accidents are adopted; with 105 % of nominal power, stopping of blower within 40 seconds and insertion of control rods to shut the reactor down. Additionally, a 90° piece is simulated with 6 angular subdivisions, see Figure 70.

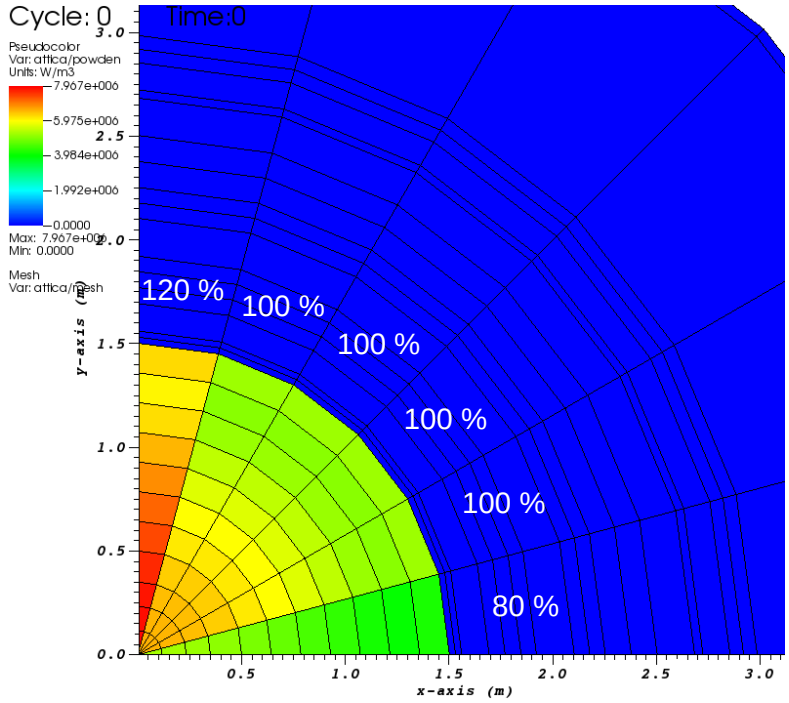

Figure 70: x,y-section of the maximum power plane. The percentages give the deviation from the 105 % of nominal power distribution

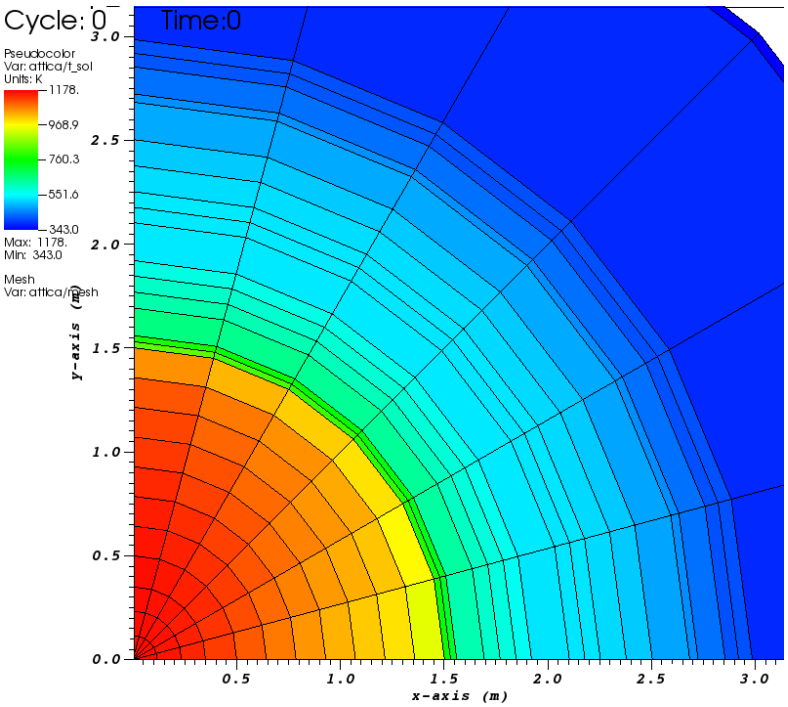

Figure 71: Asymmetric temperature distribution at core bottom

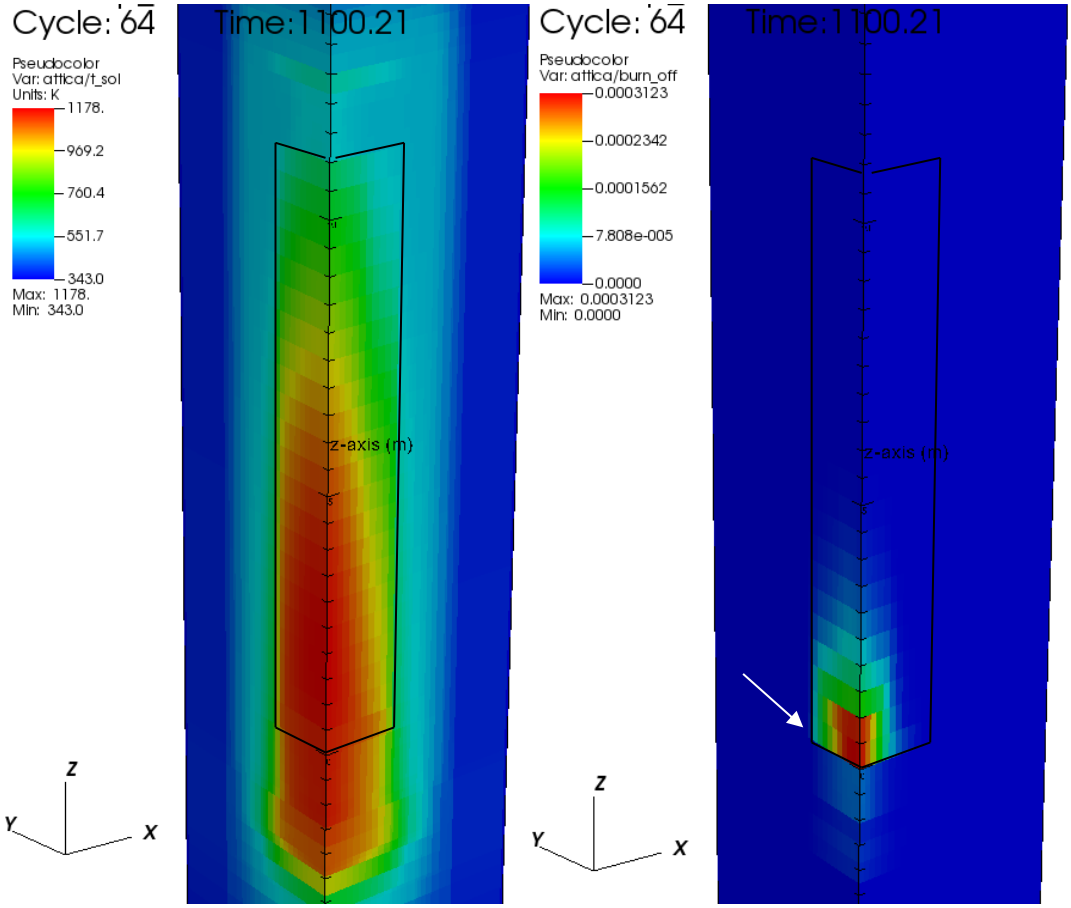

Figure 72: Left: 3-d temperature distribution; Right: 3-d burn-off distribution after 1,100 seconds; the black frame represents the pebble bed. White arrow: x,y-plane section.

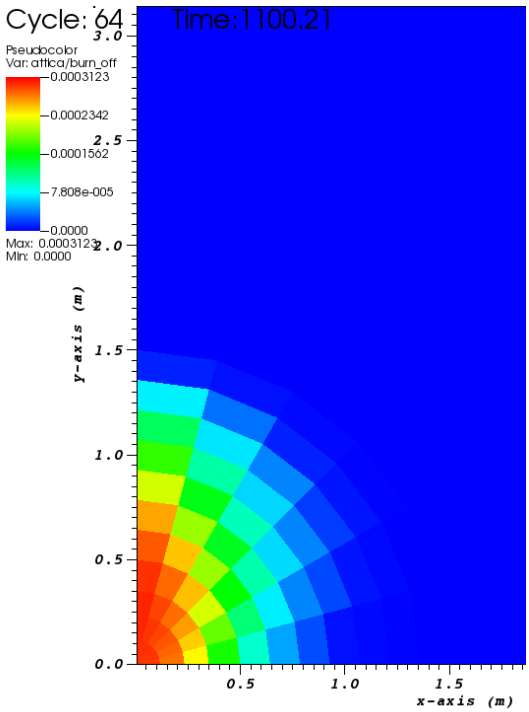

Figure 73: x,y-plane (Figure 72, white arrow) with asymmetric graphite burn-off after 1,100 seconds

Discussion of water ingress:

The relative graphite burn-off is a quantity that is normalised on the initial amount of graphite. When after 306,000 seconds the burn-off is 0.027, it means that only 2.7% of the graphite is corroded. Although the outer matrix graphite shell without fuel already comprises 42% of the fuel sphere volume, it is not the percentage of graphite that can be lost without reaching the first particles. In a pebble bed, the gas can only flow in the gas region. The fuel pebbles are always subjected to anisotropic corrosion since the part that is perpendicular facing a flow channel will be stronger corroded than in cases where the flow is parallel to the pebble surface. This fact can be accounted for by using a shape factor. In [25], it is stated that using a shape factor of 6 the admissible loss of graphite from the outer shell is 7%.

The results of TORT-TD/ATTICA^{3D} show a maximum corrosion within the core region of 2.7%. It is therefore far away from the fuel region and no coated particle will be attacked by the steam atmosphere.

The HTR-PM is designed with two helium purification systems to remove chemicals such as H_2O, O_2, CO, CO_2, N_2, H_2, CH_4 etc. within the coolant; one in operation, the other one serves as back-up if the first purification system fails.

For mitigation measures of the case of water ingress in the HTR-PM, there is a specially designed stand-by accident helium purification system line connected to both helium purification systems to remove chemical impurities. This purification system has special water separators and a throughput of 100% of the primary circuit inventory per hour. This would further decrease the steam and hydrogen content in the reactor for long-term corrosion effects. But it is not included in the safety related systems of the HTR-PM and is assumed not to work to give a conservative estimate.

Therefore, the corrosion attack of the core will be less severe if the helium purification system with the water separators operates as designed. See appendix 9.2 for results of air ingress calculation.

7 Summary and Conclusion

As three-dimensional time-depending modelling becomes more and more a standard in reactor analysis, it is to become state of the art for HTRs as well. This work addresses these needs by coupling a three dimensional time-dependent neutron transport code TORT-TD to a 3-dimensional time dependent thermal fluid dynamic code ATTICA^{3D} by means of a common interface exchanging power distributions and fuel and moderator temperatures, respectively. Along with the coupling, the single components are introduced. The major ideas in TORT-TD that solves the time-dependent neutron transport equations by transforming the set of equations into a source driven problem with the introduction of a time-dependent external neutron source were briefly explained. Also, an additional parameter, the hydrogen density, to vary the macroscopic cross sections as consequence of water ingress was introduced. For the thermal fluid dynamic component ATTICA^{3D} the principle transport equations for the porous medium approach were explained. These transport equations together with a set of constitutive equations, e.g. equations of state for the gas and gas mixtures, heat transfer coefficient, radiative heat transfer, effective heat conductivity of the pebble bed were presented. Interested readers may find the numerical solution of the equation system to be solved on a spatial grid applying the finite volume method, and a method of time integration with the help of the backward differentiation formulae in the appendix.

The thermal fluid dynamic component ATTICA^{3D} was enhanced for corrosive attacks by air and steam, which in case of the water ingress also transfers the hydrogen densities via the interface to account for a change of moderation in the TORT-TD calculation. For this case, parameterised cross section sets had to be made available. In the corrosion module, different experimentally determined corrosion rates were implemented. Depending on the nature of graphite as well as for the geometry (pebble bed surface vs blocks with boring holes), these differ quite significantly. While there is a huge data base for air ingress accidents, the corrosion under steam atmosphere has only limited data available and only for an unspecified fuel sphere graphite (A3).

The well-known mutual influence of neutronics and thermal fluid dynamics on each other is addressed by introducing an interface enabling the data exchange between the two components of the system. The interface between TORT-TD and ATTICA^{3D} automatizes the transfer of the power distribution for temperature computation, and in the other direction, the transfer of fuel and moderator temperatures and where needed the hydrogen densities. For a coupled neutronics/thermal fluid dynamic calculation, of

course, parameterised cross section sets must be available and re-evaluated at every neutronic time step.

As starting point for coupled calculations the steady-state of the PBMR-400 was selected for verification. Here the agreement of power and temperature distribution was well and can be regarded a good starting point for transient analysis.

The verification with the help of the PBMR-400 benchmark showed good agreement for the steady state case. This was important since it represents the starting conditions for subsequent transient analysis. The cold helium ingress case showed that the change in moderator temperature had an impact on the spectrum which softened and thereby increasing the fission rates and hence the power. For the case of withdrawal of the complete bank of control rods the results of TORT-TD/ATTICA3D, and even more so in the case of the total control ejection case, could present the difference of a detailed fuel model for the representation of the fuel element. In the withdrawal case, the homogeneous and heterogeneous solutions of the coupled system for the power evolution enveloped the results of others. Analysis of the fuel temperatures showed that in the homogeneous model (fuel and moderator temperature averaged over the whole fuel element) the fuel temperatures are the lowest, as well as the overall temperature increase. This corresponds well with theory. The heterogeneous model explicitly taking into account the fuel and moderator volumes has the highest average fuel temperatures. Therefore, the power increase in the heterogeneous model is the least of the participants (that also employed a different fuel model). For the case of ejection of all control rods, there was a huge spread in the results. Here, two reasons for the different results can be identified. First, the proposed fuel element model of the benchmark which subdivided the fuel element into 5 shells assigning the innermost 4 shells as average fuel temperature, the innermost sphere as the maximum fuel temperature, and all of the shell as moderator. This of course overestimates the volume of the coated particles where the heat is mostly deposited, real coated particle volume 0.89 % compared to 58 % of the volume in the proposed benchmark model. Secondly, TORT-TD/ATTICA^{3D} employs a quasi-steady-state heat conduction model while the results of KAERI and PBMR both employed a time dependent heat conduction model for the fuel, but both with different results. The reason for the – in comparison – moderate power excursion for the heterogeneous TORT-TD/ATTICA^{3D} results is a faster heat up of coated particles and limits the power increase in a drastic manner, explained by the detailed analysis of the average fuel temperatures where faster onset of temperature increase was presented.

The consequences of corrosion attacks were validated by means of an experiment performed within the RAPHAEL project co-funded by the European Comission in the NACOK facility at the Juelich Research Centre. Using different corrosion rates for fuel and reflector and also accounting for geometrical characteristics, 3-dimensional results could be produced as validation case. The determined time behaviour under corrosive atmosphere together with an external heating could be reproduced satisfactory. Given the complex nature of the experiment the corrosion behaviour in combination with the temperature development can be predicted.

The only experiment in a real high temperature reactor, the full power temperature distribution in the Chinese HTR-10, was performed in a coupled steady state. Compared with the experimental temperatures, the accordance is well except on locations where the porous medium approach has deficiencies, i.e. in outer core regions, where the actual porosity differs significantly from the homogeneous one. With an increased porosity at the side of the pebble bed an increased cooling is to be expected. However, the correlations implemented are only valid for a packed bed with the spheres of a radius at least 5 times less than the diameter of the column that is filled. In the discharge tube and the hot helium chamber, measured temperatures at the same r,z-location but at different angles lead to temperature differences of up to 200 K. Since the exact location of the measuring points was not provided, it is difficult to locate the exact positions within the reflector. Additionally, when using the porous medium approach the components are assumed to be homogeneously permeated by coolant. This can lead to averaging out temperature peaks which has to be remedied by more detailed component modelling. This should be done when more detailed locations become available. In summary, the agreement can be regarded very well.

As application cases, single rod control rod ejections where performed for the PBMR-400 as well as for the HTR-PM. The procedure to modify the cross section of control rods by an certain adjustment factor for the simulation of spatially resolved control rods yielded a comparable power and temperature increase as for the case with a grey curtain representation. Hence, it was concluded that the right efficiency for a single control rod was found. With the modified cross section for the spatial resolution, a single control rod ejection case was simulated for a 180° model that used 49 angular subdivisions for the TORT-TD model and 19 angles for the ATTICA^{3D} model, but with the ATTICA^{3D} model subdivisions densifying towards the control rod ejected. The reactivities determined for a rod ejection case were found to be 0.03 % which, with knowledge of the integral temperature coefficient of the PBMR-400, leads to a total temperature increase of 4.2 K; 4.9 K were predicted by an analytical method. However, of course the analytical method only accounts for global change. Local temperature changes can be much

higher, and hence, the averaging of a temperature distribution can introduce errors. The fuel and moderator temperature increase are shown together with the power evolution. Analysis of the thermal flux plots showed the increase in thermal flux for the position of the ejected control rod. Here, the 3-dimensional time dependent capabilities could be first demonstrated in a coupled manner. But simulating the reactor with spatially resolved control rods can also require the use of more than just two neutron energy groups.

This deficiency was overcome for the HTR-PM reactor by using 13 neutron groups for the spectral calculations without the questionable use of neutron bucklings. After obtaining a solution with the 13 energy groups for the steady state, they were condensed to seven neutron groups for transient calculations (for reasons of computational time). For the single rod ejection case, a detailed MCNP5 model was used to adjust the efficiencies of the control rods. After obtaining the right efficiencies, a single rod ejection case simulation was performed. The power increase went up to 25 % for a short time, quickly decreasing as the fuel and moderator temperatures increased by around 15 K. Analysis of the temperature distribution at the location with highest temperatures response to ejection revealed only a moderate local increase at the location of interest.

With the simulation of the water ingress, the whole interplay between neutron physics, cross section evaluation and thermal fluid dynamics could be demonstrated. TORT-TD was enhanced for an extra interpolation parameter for the macroscopic cross section outside this work by Seubert from the GRS. With the cross sections produced by Bader [30] including the hydrogen densities, the feedback due to steam in the core could be tested in the coupled system and yielded good agreement for both the short-term transient behaviour with the power increase and the long term behaviour.

For the 3-dimensional water ingress of a 90° piece of the HTR-PM, it could be shown that, of course, when assuming an asymmetric power distribution, an asymmetric temperature is the consequence. As the decay heat is proportional to the steady-state power distribution the corrosive attack corresponds to the temperature distribution.

In this work, it could be shown that with the coupling of the neutron transport code TORT-TD to ATTICA3D via a common interface produces comparable results of transient problem exercises of the PBMR-400 benchmark. From there on, it was shown that with some efforts put in cross-section processing or manipulating absorption and total cross sections of control rod elements, locally resolved results even for cases with a 180° angle can be obtained. The coupled HTR simulation system TORT-TD/ATTICA^{3D} is now available, tested and validated for the cases presented.

A logical development to continue to produce an integral HTR simulation system would be the coupling of TORT-TD/ATTICA3D to a programme that can simulate processes within the primary circuit and, if available, even of the secondary side.

8 References

[1] **Director General of the IAEA:** International Status and Prospects for Nuclear Power 2012, GOV/INF/2012/12-GC(56)/INF/6, (2012)

[2] **Editorial Office ATW International Journal for Nuclear Power,** "Kernenergie Weltreport 2012", 58, (6/2013)

[3] **U.S. Department of Energy,** "A Technology Roadmap for Generation IV Nuclear Energy Systems", Nuclear Energy Research Advisory Committee and the Generation IV International Forum, (2002)

[4] **W. von Lensa, M. Fütterer,** "Characteristics of an HTR", presentation within the ARCHER-"EUROCOURSE" (sub-project for education and training within the ARCHER project), ARCHER – Advanced Reactor for Cogeneration of Heat & Electricity-R&D, Co-funded by the European Comission under the Euratom Research and Training Program on Nuclear Energy within the 7th Framework Programme, Prague, (21st May 2013), www.archer-project.eu

[5] **K. P. Stewart,** "Final Summary Report on the Peach Bottom End-Of-Life Program, General Atomic Company, GA-A14404 UC-77, DoE, (1978)

[6] **R. Bäumer; H. Barnert; E. Baust, A. Bergerfurth; H. Bonnenberg; H. Bülling; St. Burger; C.-B. von der Decken; W. Delle; H. Gerwin; K.-G. Hackstein; H.-J. Hantke; H. Hohn; G. Ivens; N. Kirch; A. I. Kirjushin; W. Kröger; K. Krüger; N. G. Kuzavkov; G. Lange; C. Marnet; H. Nickel; P. Pohl; W. Scherer; J. Schöning; R. Schulten; J. Singh; W. Steinwarz; W. Theymann; E. Wahlen; U. Wawrzik; I. Weisbrodt; H. Werner; M. Wimmers; E. Ziermann,** AVR - Experimental High-Temperature Reactor, 21 Years of Successful Operation for a Future Energy Technology Association of German Engineers (VDI) The Society for Energy Technologies (Publ.) Düsseldorf, VDI-Verlag, (1990)

[7] **D. Schwarz, R. Bäumer,** "THTR Operating Experience", Nuclear Engineering and Design 109, pp. 199 – 205, (1988)

[8] **A. L. Habush, A. M. Harris,** "330 MW(e) Fort St. Vrain High Temperature Gas-Cooled Reactor", Nuclear Engineering and Design 7, pp. 312 – 321, (1968)

[9] **A. L. Habush, R. F. Walker,** “Fort St. Vrain Nuclear Generating Station - Construction and Design”, Nuclear Engineering and Design 26, pp. 16 – 26, (1974)

[10] **H. Reutler, G. H. Lohnert,** “Advantages of Going Modular in HTRs”, Nuclear Engineering and Design, 78, pp. 129 – 136, (1984)

[11] **H. Reutler,** “Plant Design and Safety Concept of the HTR-Module” Nuclear Engineering and Design, 108, pp. 335 – 340, (1988)

[12] **G.H.Lohnert,** “Technical design features and essential safety-related properties of the HTR-MODUL”, Nuclear Engineering and Design 121, pp. 259-276, (1990)

[13] **J. D. Bess, N. Fujimoto, B. H. Dolphin, L. Snoj, A. Zukeran,** “Evaluation of the Start-up Core Physics Tests at Japan’s High Temperature Engineering Test Reactor (Fully Loaded Core)” NEA/NSC/DOC(2006)1, Gas Cooled (Thermal) Reactor – GCR, HTTR-GCR-RESR-001, CRIT-SUB-REAC-COEF-KIN-RRATE

[14] **X. Jing, Y. Sun**, “Benchmark Problem of the HTR-10 Initial Core” prepared for the IAEA Coordinated Research Program (CRP-5) Evaluation of High Temperature Gas Cooled Reactor Performance, (March 2000)

[15] **Z. Wu, D. Lin, D. Zhong**, “The design features of the HTR-10”, Nuclear Engineering and Design, 218, pp. 25-32, (2002)

[16] **W. K. Terry, L. M. Montierth, S. S. Kim, J. J. Cogliati, A. M. Ougouag, Y. Sun, J. B. Briggs, H. D. Gougar, X. Jing, S. Xi, Z. Luo, V. F. Dean,** “Evaluation of the Initial Critical Configuration of the HTR-10 Pebble-Bed Reactor, NEA/NSC/DOC(2006), Gas-Cooled (Thermal) Reactor – GCR, HTR10-GCR-RESR-001 CRIT-REAC, (2006)

[17] **F. Li, Z. Zhang, Z. Wu, D. Wang, Y. Xu, Y. Sun, Y. Dong,** “Current Status and Technical Description of Chinese 1 x 250 MWth HTR-PM demonstration plant”, Nuclear Engineering and Design, 239, pp. 1212-1219, (2009)

[18] **J. Lapins,** “A Generic Parameter Study for a Power Upgrade of the Modular 200 MW_{th} High Temperature Reactor”, Universität Stuttgart, Diplomarbeit IKE 6D-113, (September 2008)

[19] **N. Kohtz, H. Haque,** “Meeting Fuel Temperature Limits in an HTR-Module Reactor during Depressurized Core Heat-Up”, Nuclear Engineering and Design, 137, pp. 115 – 124, (1992)

[20] **H. Nabielek, G. Kaiser, H. Huschka, M. Wimmers, W. Theymann,** "Fuel for Pebble-Bed HTRs", Nuclear Engineering and Design 78 pp. 155 – 166, (1984)

[21] **H. Nabielek, W. Kühnlein, W. Schenk, W. Heit, A. Christ, H. Ragoss,** "Development of Advanced HTR Fuel Elements", Nuclear Engineering and Design 121 pp. 199 – 210, (1990)

[22] **G. H. Lohnert, H. Nabielek, W. Schenk,** "The Fuel Element of the HTR-Module, a Prerequisite of an Inherently Safe Reactor", Nuclear Engineering and Design 109, pp. 257 – 263, (1988)

[23] **G. Brinkmann,** "Modular HTR confinement/containment and the protection against aircraft crash", Nuclear Engineering and Design, 236, pp. 1612 – 1616, (2006)

[24] **J. R. Lamarsh, A. J. Baratta,** "Introduction to Nuclear Engineering", 3rd edition, Prentice Hall, Upper Saddle River, New Jersey 07458, (2001)

[25] **Y. Zheng, L. Shi, Y. Wang,** "Water-ingress analysis for the 200 MWe pebble-bed modular high temperature gas-cooled reactor", Nuclear Engineering and Design 240, pp. 3095-3107, (2010)

[26] **F. Reitsma, K. Ivanov, T. Downar, H. de Haas, S. Sen, G. Strydom, R. Mphahlele, B. Tyobeka, V. Seker, H. D. Gougar,** "PBMR Coupled Neutronics/Thermal hydraulics Transient Benchmark The PBMR-400 Core Design", NEA/NSC/DOC(2007), Draft-V07, http://www.oecd-nea.org/science/wprs/pbmr400/participants/PBMR400-OECD-Draft-20June2007/PBMR400-OECD-Draft-20June2007.pdf (accessed on 20th June 2011)

[27] **A. Meier,** "Verbrennung von Aktiniden aus Leichtwasserreaktoren in modularen Hochtemperaturreaktoren zur Reduzierung langlebiger Nuklide", Universität Stuttgart, Dissertation IKE 6-209, (May 2012)

[28] **R. Moormann,** "AVR Prototype pebble bed reactor: a safety re-evaluation of its operation and consequences for future reactors", Juel-4275, (2008)

[29] **W. von Lensa,**"HTR Waste Management" Presentation of Waste Issues with the HTR, EUROCOURSE in the EU Project ARCHER, www.(May 2013)

[30] **J. Bader,** “Influence of Local Porosity Maxima on High Temperature Pebble-Bed Reactor Safety”, HTR-2014-61424-2, Proceedings of the HTR2014, Weihai, China, October 27-31 (2014)

[31] **T. Rademer, W. Bernnat, G. Lohnert,** “Coupling of Neutronics and Thermal-Hydraulics Codes for the Simulation of Transients of Pebble Bed Reactors“, C22, Proceedings of the 2nd International Topical Meeting on High Temperature Reactor Technology, Beijing, China, September 22-24, (2004)

[32] **W. Bernnat, W. Feltes,** “Models for reactor physics calculations for HTR pebble bed modular reactors”, Nuclear Engineering and Design, 222 pp. 331–347, (2003)

[33] **S. Becker, E. Laurien**, “Three-dimensional numerical simulation of flow and heat transport in high-temperature nuclear reactors”, Nuclear Engineering and Design 222, pp.189-201, (2003)

[34] **B. Tyobeka,** “Advanced Multi-Dimensional Deterministic Transport Computational Capability for Safety Analysis of Pebble-Bed Reactors”, Dissertation, Pennsylvania State University, (August 2007)

[35] **H. Gerwin, W. Scherer, A. Lauer, I. Clifford,** “TINTE – Nuclear Calculation Theory Description Report”, Institute for Energy Research (IEF-6), Jül-4317 (2010)

[36] **B. Boer,** “Optimized Core Design and Fuel Management of a Pebble-Bed Type Nuclear Reactor”, Dissertation, IOS press, Amsterdam, (2008)

[37] **H. Hiruta, A. M. Ouagoug, H. D. Gougar, J. Ortensi, D. W. Nigg, C. B. Davis, W. W. Weaver III,** “CYNOD: A Neutronics Code for Pebble Bed Modular Reactor Coupled Transient Analysis”; Proceedings of the 4th topical Meeting on High Temperature Reactor Technology HTR2008, Washington DC, USA, (September 28 – October 1 2008)

[38] **J. B. M. Haas, J. C. Kuijper,** “Feasibility of Burning First and Second Generation Plutonium in Pebble Bed Reactors”, Nuclear Technology, 151, pp. 192 – 200, (2005)

[39] **K. Hossain,** “Development of a fast running multidimensional thermal-hydraulic code to be readily coupled with multidimensional neutronic tools, applicable to

modular High Temperature Reactors", Dissertation, IKE 6-208, ISSN 0173 6892, (February 2011)

[40] **K. Hossain, M. Buck, N. Ben Said, W. Bernnat, G. Lohnert,** "Development of a fast 3D thermal-hydraulic tool for design and safety studies for HTRs", Nuclear Engineering and Design 238, pp. 2976–2984, (2008)

[41] **P. Mkhabela, K. Ivanov,** "DLOFC transient analysis for PBMR with NEM/THERMIX", Proceedings of PHYSOR 2008, Interlaken, Switzerland, (September 14 – 19 2008)

[42] **U. Rohde, S. Baier, S. Duerigen, E. Fridman, S. Kliem, B. Merk,** "Development and Verification of the Coupled 3D Neutron Kinetics/Thermal-Hydraulics Code DYN3D-HTR for the Simulation of Transients in Block-Type Reactors", Nuclear Engineering and Design, 251, pp. 412 – 422, (2012)

[43] **M. M. Stempniewicz,** "D22.21: Implementation of models and data for graphite-water interaction in SPECTRA" ARCHER project, contract number 269892, Deliverable 22.21, July 1, (2013)

[44] **A. Walter, A. Schulz, G. Lohnert,** "Comparison of Two Models for a Pebble Bed Modular Reactor Core Coupled to a Brayton Cycle", Proceedings of the 2nd International Meeting on High Temperature Reactor Technology, Beijing, China, September 22 – 24, (2004)

[45] **S. Kasselmann, C. Druska, S. Herber, S. Jühe, F. Keller, D. Lambertz, J. Li, S. Scholthaus, D. Shi, A. Xhonneux, H.-J. Allelein,** "Status of the Development of a fully integrated code system for the simulation of high temperature reactors", Nuclear Engineering and Design, 271, pp. 341 – 347, (May 2014)

[46] **W. A. Rhoades, D. B. Simpson,** "The TORT three-dimensional Discrete Ordinates Neuton/Photon Transport code", TORT (Version 3), ORNL/TM-13221, Oak Ridge (1997)

[47] **A. Pautz,** "Rechenmodellentwicklung für die Analyse von Reaktivitätstransienten mit Neutronentransporttheorie und gekoppelter Thermofluiddynamik für Hochfluss-Forschungsreaktoren", Technische Universität München, Lehrstuhl für Reaktordynamik und Reaktorsicherheit, Dissertation, (2001)

[48] http://atom.kaeri.re.kr/ton/nuc7.html, (Korean Atomic Energy Research Institute) accessed on the October 10, 2013

[49] **D. Emendörfer, K.-H. Höcker,** "Theorie der Kernreaktoren", Band 1: Der stationäre Reaktor, Bibliographisches Institut AG, Zürich (1982)

[50] **N. M. Greene,** "Bonami: Resonance Self-Shielding by the Method of Bondarenko", Manual of the SCALE6 Bonami Module, ORNL/TM-2005/39, Version 6, Vol. II, Sect. F1, Oak Ridge National Laboratory, (January 2009)

[51] **D. Mathews,** "An Improved Version of the MICROX-2 Code", Paul Scherrer Institute, Switzerland, PSI Bericht Nr. 97-11, (1997)

[52] **D. Emendörfer, K.-H. Höcker,** "Theorie der Kernreaktoren", Band 2: Der instationäre Reaktor, Bibliographisches Institut AG, Zürich (1982)

[53] **D. Yujie ,Zh. Zuoyi, W. Scherer,** "Assessments of Water Ingress Accidents in a Modular High Temperature Gas-Cooled Reactor", Nuclear Technology 149, pp. 253-264, (2005)

[54] **A. Seubert, K. Velkov, S. Langenbuch,** "The time-dependent 3D discrete ordinates code TORT-TD with thermal-hydraulic feedback by ATHLET models", International Conference on the Physics of Reactors "Nuclear Power: A Sustainable Resource" Casino-Kursaal Conference Center, Interlaken, Switzerland, September 14-19, (2008)

[55] **F. Reitsma, K. Ivanov, T. Downar, H. de Haas, H. D. Gougar**: The OECD/NEA/NSC PBMR Coupled Neutronics/Thermal Hydraulics Transient Benchmark: The PBMR-400 Core Design, Proceedings of PHYSOR 2006, Canadian Nuclear Society, (14.-16. September 2006)

[56] **F. Chen, Y. Dong, Z. Zhang, Y. Zheng, L. Shi, S. Hu**, "Post-test analysis of helium circulator trip without scram at 3 MW power level on the HTR-10", Nuclear Engineering and Design, 239, pp. 1010 – 1018, (2009)

[57] **Y. Zheng, J. Lapins, E. Laurien, L. Shi, Z. Zhang**, "Thermal hydraulic analysis of a pebble-bed modular high temperature gas-cooled reactor with ATTICA3D and THERMIX codes", Nuclear Engineering and Design 246, pp. 286-297, (2012)

[58] **L. Massimo,** "Physics of High Temperature Reactors", Pergamon Press, ISBN-0-08-019616-0, (1976)

[59] **M.B. Kuhlmann,** „Experimente zu Gastransport und Graphitkorrosion bei Lufteinbruchsstörfällen im Hochtemperaturreaktor," Dissertation, Jül-4003, (2002)

[60] **W. Graven, J. Long,** Kinetics and Mechanisms of the Two Opposing Reactions of the Equilibrium CO + H2O = CO2 + H2, Journal of the American Chemical Society, 76, pp. 2602-2607, (1954)

[61] **W. Graven, J. Long:** "Corrections of 'Kinetics and Mechanisms of the Two Opposing Reactions of the Equilibrium CO + H2O = CO2 + H2'", Journal of the American Chemical Society, 76, p. 6421, (1954)

[62] **Sabri Ergun, A. A. Orning**, "Fluid Flow through Randomly Packed Columns and Fluidized Beds", Industrial and Engineering Chemistry Vol. 41, No. 6, (1949)

[63] **K.-J. Loenißen**, Untersuchungen zur Druckabhängigkeit der Graphit/Wasserdampfreaktion im Porendiffusionsbereich im Zusammenhang mit Wassereinbruchsstörfällen in Hochtemperatur-Reaktoren, Juel-2159, (September 1987)

[64] **R. C. Reid, J.M. Prausnitz, B.E. Poling,** The Properties of Gases and Liquids, McGraw Hill, (1987)

[65] **R. Brokaw,** Approximate Formulas for the Viscosity and Thermal Conductivity of Gas Mixtures, Journal of Chemical Physics Vol. 29, No. 2, (August 1958)

[66] **R. Moormann, K. Petersen,** "REACT/THERMIX – Ein Computercode zur Berechnung der störfallbedingten Graphitkorrosion in Kugelhaufenreaktoren", Juel-1782, ISSN 0366-0885 (April 1982)

[67] **M. S. El-Genk, J.-M. Tournier, B. Travis,** "Graphite Oxidation Simulation in HTR Accident Conditions – 3rd year and Final Technical Report", Technical Report ISNPS-UNM-1-2012, (October 2012)

[68] **P. Kubaschewski, B. Heinrich,** "Graphitkorrosion durch Wasserdampf", Hochtemperaturreaktorbau GmbH, Juel-Conf-43, pp. 30- 42, (1981)

[69] **H.-K. Hinssen, W. Katscher, K.-J. Loenißen, R. Moormann,** "Korrosion von graphitischen Hochtemperatur-Werkstoffen mit Wasserdampf/Helium Mischungen im Druckbereich von 3-55 bar bei Temperaturen von 900-1150°C", Juel-2747, (March 1993)

[70] **W. Graven, J. Long,** “Kinetics and Mechanisms of the Two Opposing Reactions of the Equilibrium CO + H2O = CO2 + H2”, Journal of the American Chemical Society, 76, pp. 2602-2607, (1954)

[71] **W. Graven, J. Long,** “Corrections of ‘Kinetics and Mechanisms of the Two Opposing Reactions of the Equilibrium CO + H2O = CO2 + H2’”, Journal of the American Chemical Society, 76, p. 6421, (1954)

[72] **R. Moormann,** Effects of Delays in Afterheat Removal on Consequences of Massive Air Ingress Accidents in High-Temperature Gas-Cooled Reactors, Journal of Nuclear Science and Technology 21 (11), pp. 824 – 835, (November 1984)

[73] **P.L. Walker Jr., F. Rusinko Jr., L.G. Austin**, “Gas Reactions of Carbon, Advances in Catalysis”, IX, pp. 133-221, (1951)

[74] **M. Buck,** “Modelling of the Late Phase of Core Degradation in Light Water reactors”, Dissertation, IKE 2-153, (November 2007)

[75] **A. Seubert, S. Langenbuch, K. Velkov, W. Zwermann,** “Deterministic and Monte Carlo Transport Models with Thermal-Hydraulic Feedback”, Jahrestagung Kerntechnik, Proceedings of German Annual Nuclear conference, (May 2007)

[76] **A. Seubert, S. Langenbuch, K. Velkov, W. Zwermann,** “Applicability of Deterministic and Monte Carlo Neutron Transport Models Coupled with Thermal-Hydraulic Feedback”, Proceedings of EUROSAFE 2007, Berlin, (5^{th}-6^{th} November 2007)

[77] **A.-K. Krüssenberg,** “Experimentelle und analytische Untersuchungen zu Luft- und Wassereinbrüchen in das Vakuumgefäß eines Fusionsreaktors”, Jül-3333, (Dezember 1996), also Dissertation D294 (Universität Bochum)

[78] **J. Ortensi, A. M. Ougouag.** “Improved Prediction of the Temperature Feedback in TRISO-Fuelled Reactors”, Idaho National Laboratory, INL/EXT-09-16494, (August 2009)

[79] http://dante.phys.chemie.tu-muenchen.de/de/vorlesung/pc1/WS%200708/V2_Ideales_und_Reales_Gas_WS2007-08.pdf, **A. Ogrodnik**, Institut für biophysikalische Chemie (engl.: Institute of bio-physical chemistry), TU München, published lecture (accessed 1st November 2013)

[80] http://dante.phys.chemie.tu-muenchen.de/de/vorlesung/pc1/SS2006/3_Ideale%20und%20Reale%20Gase.pdf, A. Ogrodnik, Institut für biophysikalische Chemie (engl.: Institute of bio-physical chemistry), TU München, published lecture (accessed 1st November 2013)

[81] **S. Hu, X. Liang, L. Wei,** "Commisioning and Operation Experience and Safety Experiments on HTR-10, Proceedings HTR2006, 3rd international Topical Meeting on High Temperature Reactor Technology, Johannesburg, South Africa, (October 1-4, 2006)

[82] **Kerntechnischer Ausschuss (KTA),** "Auslegung der Reaktorkerne von gasgekühlten Hochtemperaturreaktoren", Sicherheitstechnische Regel des KTA 3102 (Engl.: German Committee of Nuclear Safety Standards), (1983)

[83] **H. Niessen, H. Hohn, H.-K. Hinssen, W. Jahn, K. Trollmann, K. Baginski, B. Schloegl,** "NACOK Experiment, Experimental set-up, execution of the test, experimental results, RAPHAEL Deliverable D-ST3.4", (May 2009)

[84] **Y. Zheng, M. Stempniewicz,** "Investigation of NACOK Air Ingress Experiment using Different System Analysis Codes", Nuclear Engineering and Design, 251, pp. 423–432, (October 2012)

[85] **J. R. Arthur,** "Reactions between Carbon and Oxygen", Transactions of the Faraday Society, 47, pp. 164-178, (1951)

[86] **M. Rossberg, E. Wicke,** "Transportvorgänge und Oberflächenreaktionen bei der Verbrennung graphitischen Kohlenstoffs", Chemie-Ing. Technik, 28, pp. 181-189, (1956)

[87] **M. L. Lomax,** "A review of graphite oxidation models", AEA FUS 99, (1991)

[88] **M. El-Glenk,** "Graphite Oxidation Simulation in HTR Accident Conditions" Reactor concepts RD&D, Technical Report ISNPS-UNM-1-2012, October, (2012)

[89] **P. L. Walker Jr., F. Rusinko Jr., L. G. Austin,** "Gas Reactions of Carbon", Advances in Catalysis, 9, pp. 249-327, (1951)

[90] **U. Nowak, L. Weinmann,** "A Family of Newton-Codes for Systems of Highly Non-Linear Equations – Algorithms, Implementation, Application", Konrad-Zuse-Zentrum für Informationstechnik Berlin, Technical Report, SC-89-NN, (1989)

[91] **E. Hairer, G. Wanner,** "Solving ordinary differential equations II: stiff and differential-algebraic problems" Springer Verlag, (1991)

[92] **L. R. Petzold,** "A description of DASSL: a differential/algebraic system solver", Proceedings of IMACS World Congress, Montreal, Canada, (1982)

[93] **W. Katscher, R. Moormann**, "Graphite Corrosion Under Severe Accident Conditions", IAEA Specialists' Meeting on Graphite Component Structural Design, JAERI, Tokai-mura, Japan, (September 8-11, 1986)

[94] **H.-K. Hinssen, W. Katscher, R. Moormann**: Kinetik der Graphit/Sauerstoff-Reaktion im Porendiffusionsbereich, Teil 1: Matrixmaterialien, Juel-1875, ISSN 0366-0885, (November 1983)

[95] **H.-K. Hinssen, W. Katscher, R. Moormann**: Kinetik der Graphit/Sauerstoff-Reaktion im Porendiffusionsbereich, Teil 2: Graphite V483T, ASR-1RS, ASR-1RG und ATR-2E, Juel-2052, ISSN 0366-0885, (April 1986)

[96] **H.-K. Hinssen, W. Katscher, K.-J. Loenißen, R. Moormann,** "Korrosion von graphitischen Hochtemperatur-Werkstoffen mit Wasserdampf/Helium Mischungen im Druckbereich von 3-55 bar bei Temperaturen von 900-1150°C", Juel-2747, ISSN 0366-0885, (March 1993)

[97] **J. B. Howard, G. C. Williams, D. H. Fine,** "Kinetics of Monoxide Oxidation in Postflame Gases", 14th Symposium on Combustion, The Combustion Institute, pp. 975 – 986, (1973)

[98] **J. Lapins, J. Bader, M. Buck,** "Deliverable D22.23: TORT-TD/ATTICA^{3D} water ingress models and assumptions for calculation" ", ARCHER – Advanced Reactor for Cogeneration of Heat & Electricity-R&D, Co-funded by the European Comission under the Euratom Research and Training Program on Nuclear Energy within the 7th Framework Programme, www.archer-project.eu

[99] **J. Lapins, M. Buck,** "Deliverable D22.24: Report on results of water ingress with TORT-TD/ATTICA^{3D}", ARCHER – Advanced Reactor for Cogeneration of Heat & Electricity-R&D, Co-funded by the European Comission under the Euratom Research and Training Program on Nuclear Energy within the 7th Framework Programme, www.archer-project.eu

[100] **M. Buck, J. Bader, J. Lapins,** “Documentation of ATTICA^{3D}, Volume II, Methods and Models”, Intermediate documentation for ATTICA^{3D}

[101] **S.V. Patankar,** “Numerical Heat Transfer and Fluid Flow, Hemisphere Publishing Corporation, New York, (1980)

[102] **G. Lohnert,** “The consequences of water ingress into the primary circuit of an HTR-Module – From design basis accident to hypothetical postulates”, Nuclear Engineering and Design, 134, pp. 159 – 176, (1992)

9 Appendix

9.1 Numerical solution methods

The general numerical solution approach is to solve the partial differential equation system that consists of the conservation equations of mass, momentum and energy of the phases, together with the constitutive equation introduced above. The approach for the numerical solution of this system in ATTICA^{3D} can be subdivided into two general steps:

- The spatial solution of the equation system: In order to map the three-dimensional space on a discrete grid, the solution domain is discretised spatially by making use of the finite volume method.
- The time integration is done by subdividing time into a sequence of time steps approximating the partial derivatives w.r.t. time of the solution variables by differences that are evaluated at the actual and previous time levels. In ATTICA^{3D} the method of backward differencing formulae is applied.

This description is described in more detail in [100].

9.1.1 Spatial discretisation by the finite volume method

Spatial discretisation of the conservation equations system is done by finite volumes techniques. The space is discretised on a 3-d rectangular grid. The finite volumes have the form of cubes or wedges (Cartesian or cylindrical geometry). For a cylindrical grid the volumes are given as

$$V_{i,j,k} = \frac{1}{2} \cdot \left(R^2_{i+½} - R^2_{i-½} \right) \cdot \left(z_{j+½} - z_{j-½} \right) \cdot \left(\theta_{k+½} - \theta_{k-½} \right) \tag{9-1}$$

where $V_{i,j,k}$ is the volume of cell radius i, height j and angle k. The subscripts $i \pm ½$, $j \pm ½$ and $k \pm ½$ indicate the boundaries of the cell. The faces of the volume that form the boundaries of this cell are given in radial direction as

$$A_{i\pm½,j,k} = R_{i\pm½} \cdot \left(z_{j+½} - z_{j-½} \right) \cdot \left(\theta_{k+½} - \theta_{k-½} \right), \tag{9-2}$$

in axial direction

$$A_{i,j\pm½,k} = \frac{1}{2} \cdot \left(R^2_{i+½} - R^2_{i-½}\right) \cdot \left(\theta_{k+½} - \theta_{k-½}\right) \tag{9-3}$$

and azimuthal direction

$$A_{i,j,k\pm½} = \left(z_{j+½} - z_{j-½}\right) \cdot \left(\theta_{k+½} - \theta_{k-½}\right). \tag{9-4}$$

It is common to use a staggered grid approach in fluid dynamics to solve for the properties of interest. Staggered grid means that all scalar quantities Φ (pressures, temperatures, concentrations) are computed for the cell centres whereas vector quantities like velocities, mass or enthalpy flows are computed at the volume faces.

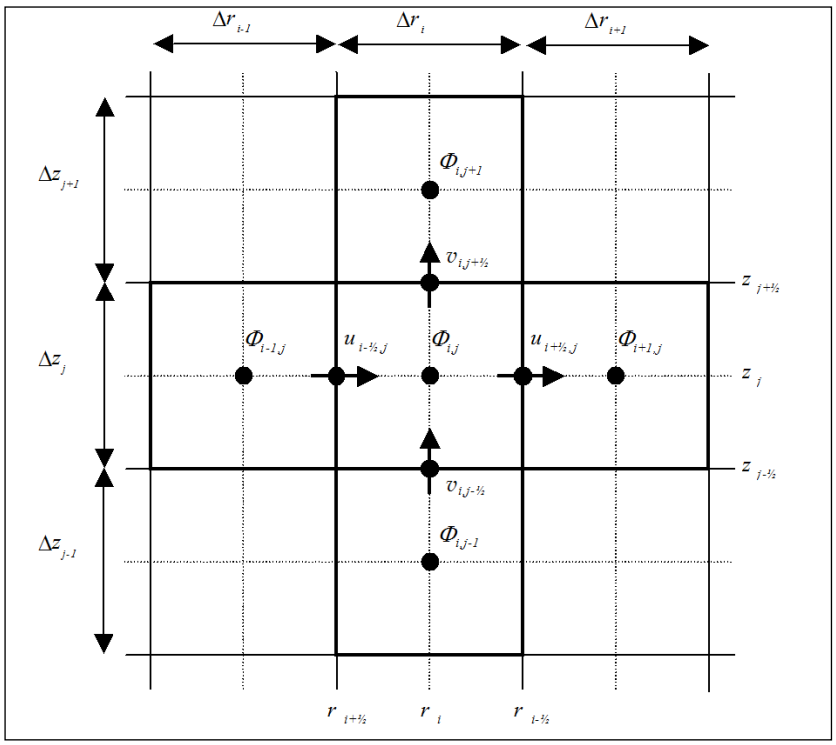

Figure 74: Discretisation of space using a staggered grid approach for the finite volume method in the r,z-plane.

In order to make the values needed at the cell centre or face available, the quantities are interpolated to the respective location (from cell centre to cell phases for the scalar quantity Φ and vice versa for the vector quantities). Depending on the nature of the parameter to be interpolated, different interpolation approaches are used. These are linear interpolation, geometrical interpolation (emphasizing the smaller values, e.g. in heat conduction problems) or up-wind interpolation for quantities with convective fluxes.

9.1.2 Discretisation of mass and energy conservation

The mass and energy conservation equations expressed in the general form are

$$\underbrace{\frac{\partial(\beta\rho\Phi)}{\partial t}}_{\text{changerate}} + \underbrace{\nabla\cdot\left(\beta\rho\Phi\vec{v}\right)}_{\text{convection}} = \underbrace{\nabla\cdot\left(D\cdot\nabla\Phi\right)}_{\text{diffusion}} + \underbrace{S}_{\text{source}} \tag{9-5}$$

where Φ is the quantity of interest, i.e. the mass fraction of the mass conservation, for the energy conservation Φ is the enthalpy of the gas or the solid, β is the respective volume fraction which is ε for the gas phase and $(1-\varepsilon)$ for the solid phase. For mass and energy conservation equations not all the terms are present. While for the mass conservation the diffusion term is neglected, the convection term is neglected for the energy equation of the solid. Integration of the equation over a volume cell with the help of the divergence theorem

$$\int_{\Delta V}\frac{\partial(\beta\rho\Phi)}{\partial t}\cdot dV + \oint_{\Delta A}\left(\beta\rho\Phi\vec{v} - D\cdot\nabla\Phi\right)\cdot d\vec{A} = \int_{\Delta V} S\cdot dV \tag{9-6}$$

For cylindrical coordinates for the control volume $V_{i,j,k}$.

$$\begin{aligned}\frac{\partial}{\partial t}\beta_{i,j,k}\rho_{i,j,k}\Phi_{i,j,k}V_{i,j,k} &= \left[\beta\rho\Phi u - D\nabla\Phi\right]_{i-½,j,k}A_{i-½,j,k} - \left[\beta\rho\Phi u - D\nabla\Phi\right]_{i+½,j,k}A_{i+½,j,k}\\ &+ \left[\beta\rho\Phi v - D\nabla\Phi\right]_{i,j-½,k}A_{i,j-½,k} - \left[\beta\rho\Phi v - D\nabla\Phi\right]_{i,j+½,k}A_{i,j+½,k}\\ &+ \left[\beta\rho\Phi w - D\nabla\Phi\right]_{i,j,k-½}A_{i,j.k-½} - \left[\beta\rho\Phi w - D\nabla\Phi\right]_{i,j,k+½}A_{i,j.k+½}\\ &+ S_{i,j,k}V_{i,j,k}\end{aligned} \tag{9-7}$$

Here, the change rate of the conserved quantity (mass, energy) equals the sum of the production rate due to sources and convective and diffusive fluxes entering or leaving the cell boundaries of the control volume. The change rates and source terms are calculated from the values of the variables at volume centres, while the fluxes are computed from values of variables defined at volume faces. Mass and energy fluxes leaving one cell enter the neighbouring cell. Summing up over the whole solution domain will cancel out contributions from the internal fluxes, such that mass and energy are conserved.

The convective and diffusive fluxes are discretised in a coupled way, depending on the mesh Peclet number. The Peclet number gives the ratio of convective to diffusive energy transport. If the condition Pe < 2 is fulfilled, linear interpolation is used for the calculation of convective and the diffusive terms. For other cases, the convective fluxes are calculated by up-wind interpolation, neglecting diffusive fluxes. This method yields numerically stable results in cases with low or stagnating velocities.

9.1.3 Discretisation of the momentum equation

The momentum equations for the gas according to the Ergun approach can be expressed in terms of the mass flow rates. In discretised form, this gives e.g. for the axial component of the gas momentum equation at the cell boundary *i,j±½,k*

$$\left[\frac{1}{\rho_g \mu_g}\right]_{i,j+½,k} \left|\dot{m}_{g,i,j+½,k}\right| \cdot \dot{m}_{g,i,j+½,k} + \left[\frac{\nu_g}{\kappa_g}\right]_{i,j+½,k} \dot{m}_{g,i,j+½,k} = -\frac{p_{g,i,j+1,k} - p_{g,i,j,k}}{\frac{\Delta z_j + \Delta z_{j+1}}{2}} - \rho_{g,i,j+½,k} \cdot g \tag{9-8}$$

with $\dot{m}_{g,i,j+½,k} = (\beta_g \rho_g v_g)_{i,j+½,k}$

The pressures and mass flow rates are already defined at the required grid locations. The density ρ_g, kinematic viscosity ν_g, permeability κ_g and passability μ_g have to be computed from interpolated values interpolated from cell centre to cell boundaries. Therefore, properties associated with the gas flow (volume fraction, density and viscosity) are evaluated using up-wind interpolation. The quantities associated with the solid matrix (porosity, particle diameter) are computed using geometric interpolation to assure that the mass flux at the boundaries of a completely blocked cell will be zero. The resulting mass flow rates at the cell boundaries can then be computed explicitly as a function of the properties in the adjoining cells. Analogously, the discretisation of the radial and the azimuthal components of the gas momentum equations is done.

9.1.4 Time integration method

The solution variables of ATTICA^{3D} are the solid enthalpy h_s, the gas pressure p, the gas temperature T_g, the gas component volume fractions $\chi_{g,k}$ for the components $k = 1 \ldots N_g$ and the velocity components u_r, u_z and u_θ.

In each control volume a system of ordinary differential equations results from the spatially discretised conservation equations. These are:

$$m_s \frac{dh_s}{dt} = \dot{E}_s \tag{9-9}$$

$$\varepsilon \cdot V \cdot \frac{d}{dt}\left(\rho_g \cdot e_g\right) = \dot{E}_g \tag{9-10}$$

$$\varepsilon \cdot V \cdot \frac{d\rho_{g,k}}{dt} = \varepsilon \cdot V \cdot \frac{d}{dt}\left(c_{g,k} \cdot \rho_g\right) = \dot{M}_{g,k} \quad k = 1 \ldots N_g \tag{9-11}$$

Instead of all individual mass conservation equations for the gas components, we work with the sum of the mass conservation equations

$$\varepsilon \cdot V \cdot \frac{d\rho_g}{dt} = \sum_{k=1}^{N_g} \dot{M}_{g,k} = \dot{M}_g \tag{9-12}$$

and $N_g - 1$ individual mass conservation equations

$$\varepsilon \cdot V \cdot \frac{d\rho_{g,k}}{dt} = \dot{M}_{g,k} \quad k = 1 \ldots N_g - 1 \tag{9-13}$$

From equation (9-10)we have

$$\varepsilon \cdot V \cdot \frac{d}{dt}\left(\rho_g \cdot e_g\right) = \varepsilon \cdot V \cdot \left(e_g \frac{d\rho_g}{dt} + \rho_g \frac{de_g}{dt} \right) = \dot{E}_g \tag{9-14}$$

By subtracting equation (9-12) multiplied by e_g from (9-14) we get

$$\frac{de_g}{dt} = \frac{\dot{E}_g - \dot{M}_g \cdot e_g}{\varepsilon \cdot V \cdot \rho_g} \tag{9-15}$$

Since our equation of state is based on enthalpy instead of internal energy, we use

$$\frac{de_g}{dt} = \frac{dh_g}{dt} - \frac{d\frac{p}{\rho_g}}{dt} = \frac{dh_g}{dt} - \frac{1}{\rho_g}\frac{dp}{dt} + \frac{p}{\rho_g^2}\frac{d\rho_g}{dt} = \frac{\dot{E}_g - \dot{M}_g \cdot e_g}{\varepsilon \cdot V \cdot \rho_g} \; . \tag{9-16}$$

With equations (9-15) and (9-16) this can be transformed to

$$\frac{dh_g}{dt} - \frac{1}{\rho_g}\frac{dp}{dt} = \frac{\dot{E}_g - \dot{M}_g \cdot e_g}{\varepsilon \cdot V \cdot \rho_g} - \frac{p}{\rho_g^2} \cdot \frac{\dot{M}_g}{\varepsilon \cdot V} = \frac{\dot{E}_g - \dot{M}_g \cdot \left(e_g + \frac{p}{\rho_g} \right)}{\varepsilon \cdot V \cdot \rho_g} = \frac{\dot{E}_g - \dot{M}_g \cdot h_g}{\varepsilon \cdot V \cdot \rho_g} \; . \tag{9-17}$$

Since h_g is not a differential solution variable, we have to express $\frac{dh_g}{dt}$ in terms of the time derivatives of the differential solution variables h_g that depends on: p, T_g and $\chi_{g,k}$. Hence, we have

$$\left(\frac{\partial h_g}{\partial p}-\frac{1}{\rho_g}\right)\cdot\frac{dp}{dt}+\frac{\partial h_g}{\partial T_g}\cdot\frac{dT_g}{dt}+\sum_{k=1}^{N_g-1}\left(\frac{\partial h_g}{\partial \chi_{g,k}}-\frac{\partial h_g}{\partial \chi_{g,N_g}}\right)\cdot\frac{d\chi_{g,k}}{dt}=\frac{\dot{E}_g-\dot{M}_g\cdot h_g}{\varepsilon\cdot V\cdot\rho_g} \tag{9-18}$$

Here, we have considered that $\chi_{g,N_g}=1-\sum_{k=1}^{N_g-1}\chi_{g,k}$, so $\frac{d\chi_{g,N_g}}{dt}=-\sum_{k=1}^{N_g-1}\frac{d\chi_{g,k}}{dt}$.

Similarly, we have from equation (9-12)

$$\frac{d\rho_g}{dt}=\frac{\partial\rho_g}{\partial p}\cdot\frac{dp}{dt}+\frac{\partial\rho_g}{\partial T_g}\cdot\frac{dT_g}{dt}+\sum_{k=1}^{N_g-1}\left(\frac{\partial\rho_g}{\partial\chi_{g,k}}-\frac{\partial\rho_g}{\partial\chi_{g,N_g}}\right)\cdot\frac{d\chi_{g,k}}{dt}=\frac{\dot{M}_g}{\varepsilon\cdot V} \tag{9-19}$$

From the equation (9-13), we have

$$\frac{d\rho_{g,k}}{dt}=\frac{\partial\rho_{g,k}}{\partial p}\cdot\frac{dp}{dt}+\frac{\partial\rho_{g,k}}{\partial T_g}\cdot\frac{dT_g}{dt}+\sum_{k=1}^{N_g-1}\left(\frac{\partial\rho_{g,k}}{\partial\chi_{g,k}}-\frac{\partial\rho_{g,k}}{\partial\chi_{g,N_g}}\right)\cdot\frac{d\chi_{g,k}}{dt}=\frac{\dot{M}_{g,k}}{\varepsilon\cdot V}, \tag{9-20}$$

with $k=1\ldots N_g-1$

Hence, the system of conservation equations for each volume considered is transformed into a linearly-implicit system of ordinary differential equations of the form

$$\mathbf{M}\cdot\dot{\mathbf{Y}}=\mathbf{f}(t,\mathbf{Y}) \tag{9-21}$$

with the array of solution variables

$$\mathbf{Y}=\begin{pmatrix}h_s\\p\\T_g\\\chi_{g,1}\\\vdots\\\chi_{g,N_g-1}\end{pmatrix}, \tag{9-22}$$

the array of derivatives

$$\dot{\mathbf{Y}} = \cdot \begin{pmatrix} \frac{dh_s}{dt} \\ \frac{dp}{dt} \\ \frac{dT_g}{dt} \\ \frac{d\chi_{g,1}}{dt} \\ \vdots \\ \frac{d\chi_{g,N_g-1}}{dt} \end{pmatrix}, \tag{9-23}$$

the matrix

$$\mathbf{M} = \begin{pmatrix} m_s & 0 & 0 & 0 & \cdots & 0 \\ 0 & \frac{\partial h_g}{\partial p} - \frac{1}{\rho_g} & \frac{\partial h_g}{\partial T_g} & \frac{\partial h_g}{\partial \chi_{g,1}} - \frac{\partial h_g}{\partial \chi_{g,N_g}} & \cdots & \frac{\partial h_g}{\partial \chi_{g,N_g-1}} - \frac{\partial h_g}{\partial \chi_{g,N_g}} \\ 0 & \frac{\partial \rho_g}{\partial p} & \frac{\partial \rho_g}{\partial T_g} & \frac{\partial \rho_g}{\partial \chi_{g,1}} - \frac{\partial \rho_g}{\partial \chi_{g,N_g}} & \cdots & \frac{\partial \rho_g}{\partial \chi_{g,N_g-1}} - \frac{\partial \rho_g}{\partial \chi_{g,N_g}} \\ 0 & \frac{\partial \rho_{g,1}}{\partial p} & \frac{\partial \rho_{g,1}}{\partial T_g} & \frac{\partial \rho_{g,1}}{\partial \chi_{g,1}} - \frac{\partial \rho_{g,1}}{\partial \chi_{g,N_g}} & \cdots & \frac{\partial \rho_{g,1}}{\partial \chi_{g,N_g-1}} - \frac{\partial \rho_{g,1}}{\partial \chi_{g,N_g}} \\ \vdots & \vdots & \vdots & \vdots & \ddots & \vdots \\ 0 & \frac{\partial \rho_{g,N_g-1}}{\partial p} & \frac{\partial \rho_{g,N_g-1}}{\partial T_g} & \frac{\partial \rho_{g,N_g-1}}{\partial \chi_{g,1}} - \frac{\partial \rho_{g,N_g-1}}{\partial \chi_{g,N_g}} & \cdots & \frac{\partial \rho_{g,N_g-1}}{\partial \chi_{g,N_g-1}} - \frac{\partial \rho_{g,N_g-1}}{\partial \chi_{g,N_g}} \end{pmatrix} \tag{9-24}$$

and the right hand side

$$\mathbf{f(Y)} = \begin{pmatrix} \dot{E}_s \\ \frac{\dot{E}_g - \dot{M}_g \cdot h_g}{\varepsilon \cdot V \cdot \rho_g} \\ \frac{\dot{M}_g}{\varepsilon \cdot V} \\ \frac{\dot{M}_{g,1}}{\varepsilon \cdot V} \\ \vdots \\ \frac{\dot{M}_{g,N_g-1}}{\varepsilon \cdot V} \end{pmatrix} \tag{9-25}$$

The required partial derivatives of the densities and mixture enthalpy follow from the equation of state of the gas mixture.

In order to determine the solution variables $\mathbf{Y}$ and their time derivatives $\dot{\mathbf{Y}}$ it is necessary to solve the array F of the form

$$\mathbf{F}\left(t, \mathbf{Y}, \dot{\mathbf{Y}}\right) = \mathbf{0} \tag{9-26}$$

which is composed of the discretised conservation equations for every control volume i,j,k. This gives 2 energy conservation equations, 3 momentum equations and N_g mass conservation equations for the gas. The solution variables $\mathbf{Y}$ and their time derivatives $\dot{\mathbf{Y}}$ are composed as described above. By algebraic manipulation it is possible to transform the equation system into an explicit set of differential equation such that

$$\dot{\mathbf{Y}} = \mathbf{f}\left(t, \mathbf{Y}\right) \tag{9-27}$$

Here, an implicit Euler method is selected in which the time derivatives are approximated by a first order difference quotient at previous and actual time levels.

$$\frac{\mathbf{Y}^{n+1} - \mathbf{Y}^{n}}{\Delta t} - \mathbf{f}(\mathbf{Y}^{n+1}) = \mathbf{0} \tag{9-28}$$

where the solution for the next time step depends on the new time step, again. This approach needs a larger effort for the solution since it can only be solved iteratively, but the time step size can be much larger compared to explicit methods such that this pays off especially for the stiff equation system present. In ATTICA3D a modified Newton-Raphson method [90] is applied which linearises the equation system w.r.t. the solution variables around the actual solution values. The resulting linear system is solved to obtain an improved solution each step and is iterated until the residuals fall below a certain threshold. The size of this algebraic system can be very large such that a stepwise approach can be applied where only single equations of the total equation system are linearized and then solved, e.g. mass conservation equations. The updated solution will be used for the solution of the next linearized single equations for e.g. momentum equations to determine the velocities, then the energy equations a.s.o. The whole sequence is repeated until convergence criteria are met. Some coupled processes like heat transfer between solid and gas can lead to oscillation of the solution and by that slows down the solution which is remedied by relaxation parameters that are based on experience and can be heavily problem dependent.

For the solution method in ATTICA3D, the backwards differencing formulae (BDF) method proposed by Petzold [92] is selected, since the largest part of the computational effort is needed for the evaluation of the Jacobian matrix which contain the partial derivatives of the solution variables. While other possible solution methods demand for a factorization of the Jacobian at each time step, the BDF method allows the re-use of

the factorization of the iteration matrix if time step size changes are less than a factor of 2 or 0.5, respectively. This re-use enables massive savings in computational times.

The BDF method solves differential algebraic equations of the form 4-64 in conjunction with a set of initial conditions $\mathbf{Y}(t^0) = \mathbf{Y}^0$, $\dot{\mathbf{Y}}(t^0) = \dot{\mathbf{Y}}^0$. The term algebraic refers to the possibility, that not all time derivatives $\dot{\mathbf{Y}}$ have to appear explicitly in the equations, i.e. algebraic equations may also be part of the total system. The BDF takes into account the solution and the partial derivatives of up to 5 of the last time steps which are adapted to the solution in a way to obtain optimum step sizes for the local discretisation error. For each time step an approximation of the solution of the variables and their derivatives at the new time step t^{n+1} are estimated by a predictor polynomial which interpolates the solutions at the last time steps (depending on the order). The new values obtained are re-evaluated by applying a predictor polynomial and its derivative that fulfills the equation system at the new time step level. After successful completion of a time step, the step size width and order for the next step are determined, depending on the previous solution sequence.

The iterative solution of the equation system requires the calculation of an iteration matrix. Since the nature of this matrix is diagonally-dominant and sparse, use of matrix decomposition in an upper and lower triangular matrix (LU-decomposition) is made. For solution of sparse matrices a number of numerical solver libraries are freely available. Here, interfaces for several solver packages are integrated into ATTICA3D, e.g. for band matrices the LAPACK library, for direct sparse solvers the UMFPACK, Super-LU libraries can be selected by the user.

The numerical solution of the equations system is done stepwise. First, the pressure field is calculated with other initial values, followed by a pressure and velocity calculation. Then, the pressure, velocity and gas temperatures are calculated with the initial solid temperatures before, in the last step, all variables are calculated. However, the user can also specify explicitly in the input which equations to be solved. This is iterated till finally convergence criteria (default or user-specified) are met and the next step can be executed.

9.3 Air ingress into the HTR-PM

For an air ingress accident, a precondition is the depressurisation scenario with a destruction of the main coaxial gas duct. Several scenarios can be thought of, e.g. lid and bottom are open (chimney effect) or the fuel discharge tube breaks. In [59] it is assumed that the helium that remains within the reactor pressure vessel will expand with the heat up of the reactor and its interiors. Only when the maximum temperatures are reached helium will contract making volume for air (79% Nitrogen, 21% oxygen) that will be sucked in (dive bell effect). In the scenario presented here, the assumption is that right after the break of the duct half of the gas concentration is made up by air. Therefore, the graphite structures will instantaneously undergo corrosion and will also experience corrosion in the time where the reactor still heats up with the decay heat. In the first mentioned scenario, the bottom reflector structures are already below 500°C and there is no significant corrosion to be expected. In order to initialise the transient, a steady-state calculation was performed and saved on a restart file. Then the transient was started with a reduced pressure of 1 bar. Now, at outlet and inlet the gas concentrations were modified to 50% helium, 39.5% nitrogen and 10.5% oxygen. Since the core is much hotter than the helium riser and further heats up with the decay heat, conditions as simulated with the NACOK experiment for temperature differences between core and helium risers are fulfilled – a natural convection loop, starting from the outlet through the core and then helium riser, will establish.

The simulation time is 365,000 seconds which corresponds to about 100 hours or more than 4 days.

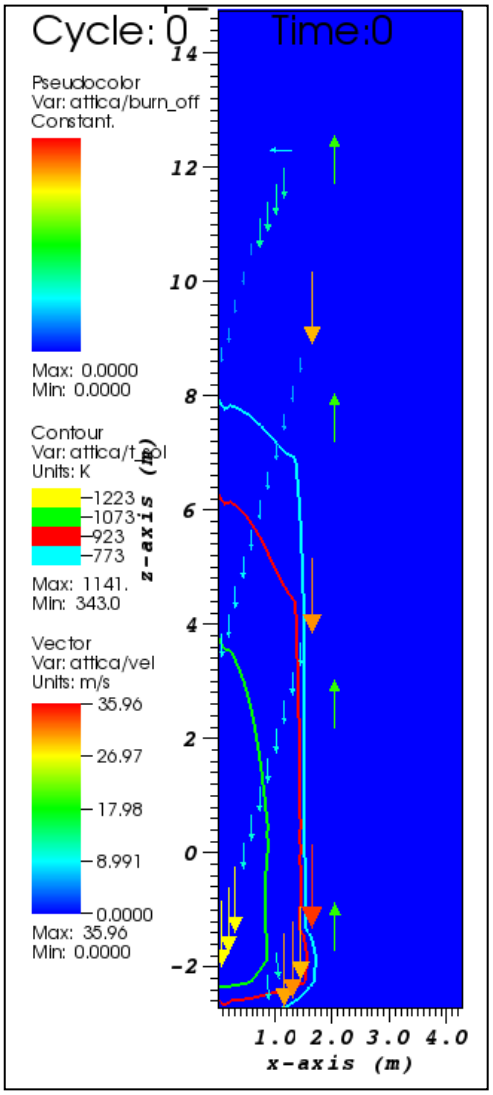

Figure 75: Starting condition before the depressurisation, there is no graphite burn-off, temperatures are shown as iso-lines, velocities as arrows

Figure 75 depicts the starting conditions before depressurisation. The temperatures are shown as iso-lines between 773 K (500°C) and 1223 K (950°C) in order to highlight regions where corrosion takes place. Temperatures within the 1223 K line show the region of Boudouard reaction. Additionally the velocities are shown as arrows. Figure 76 shows the conditions after 1,500 seconds. The flow direction reverses; air is sucked in at the outlet and corrosion starts. In the beginning, CO_2 is all over the reactor core. However, when temperatures exceed 1223 K the CO_2 is consumed gradually and the CO concentration increases, see Figure 78. The temperature in case of a depressurised loss of forced cooling rises to about 1500°C within 40 hours after depressurisation. At that time CO_2 is only present in the lower pebble bed. On the way through the core it reacts with C forming CO. Only in the control rod channels CO_2 is present, see Figure

78. It is obvious when the 1223 K temperature isoline is traversed the CO_2 content diminishes to zero.

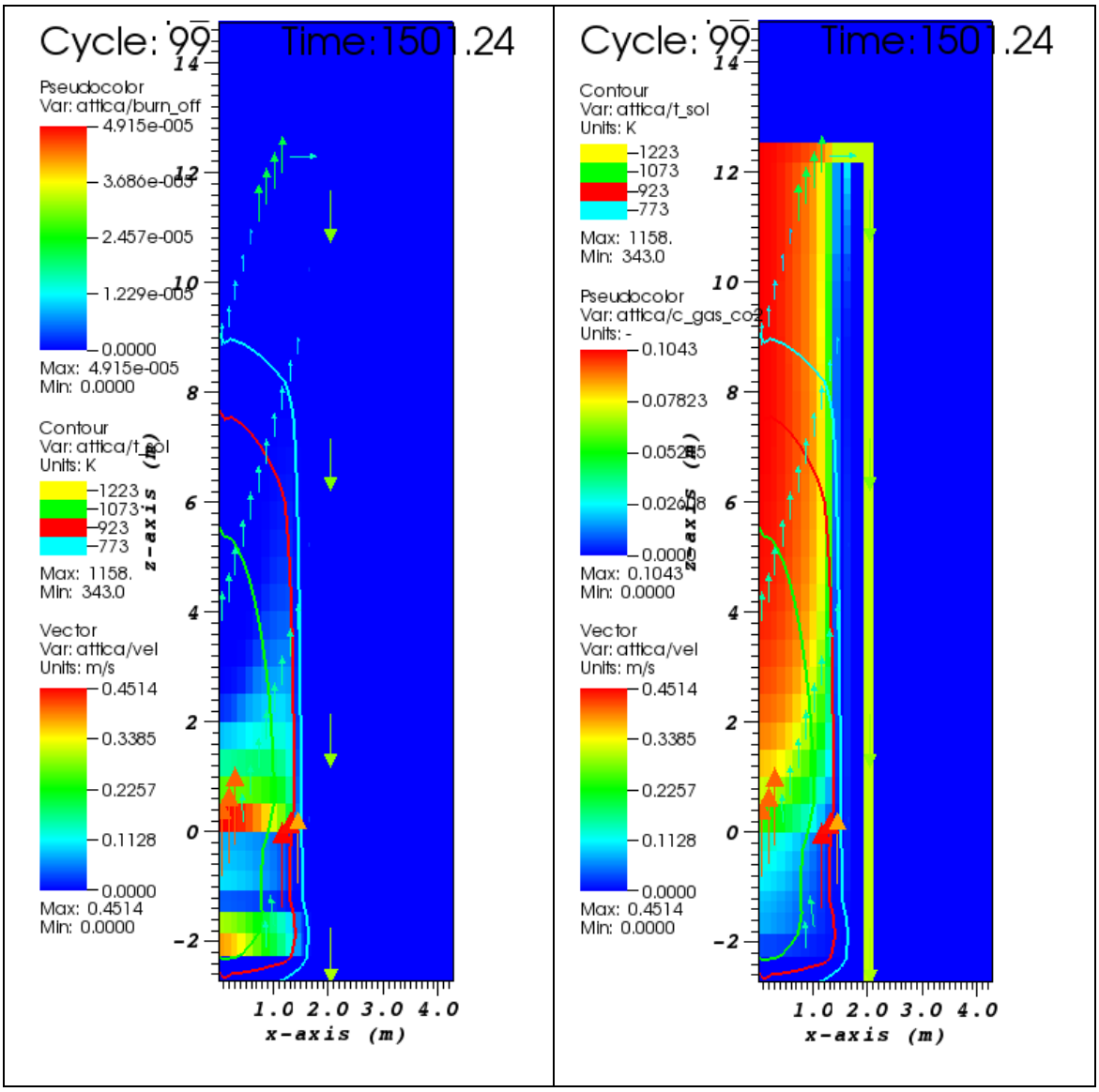

Figure 76: left: relative graphite burn-off, temperature in isolines and gas velocities; right CO_2 concentration, temperature isolines and gas velocities at t = 1501 seconds.

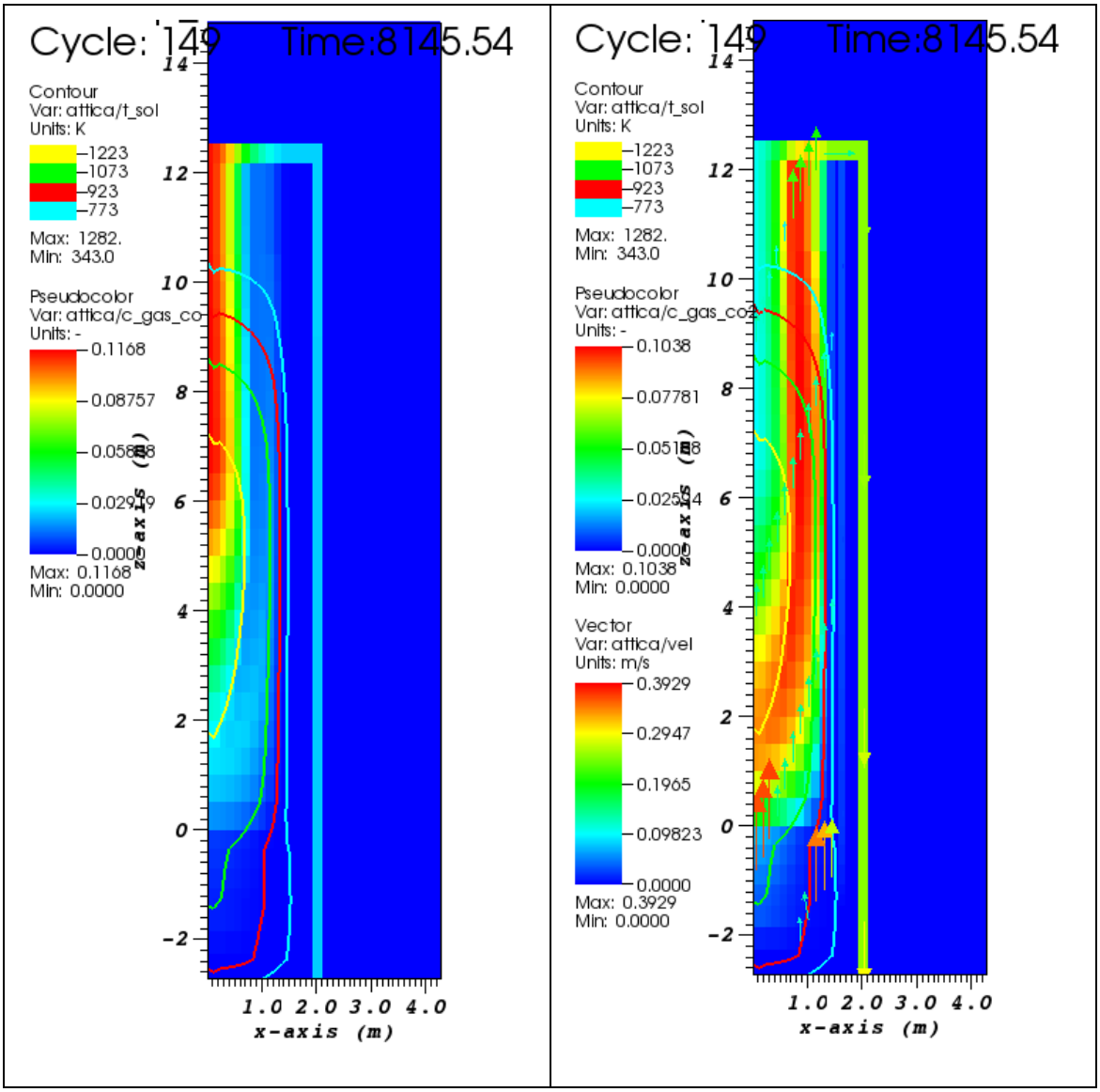

Figure 77: left CO distribution with isolines; right CO_2 distribution and solid temperature isolines at t = 8,145 sec

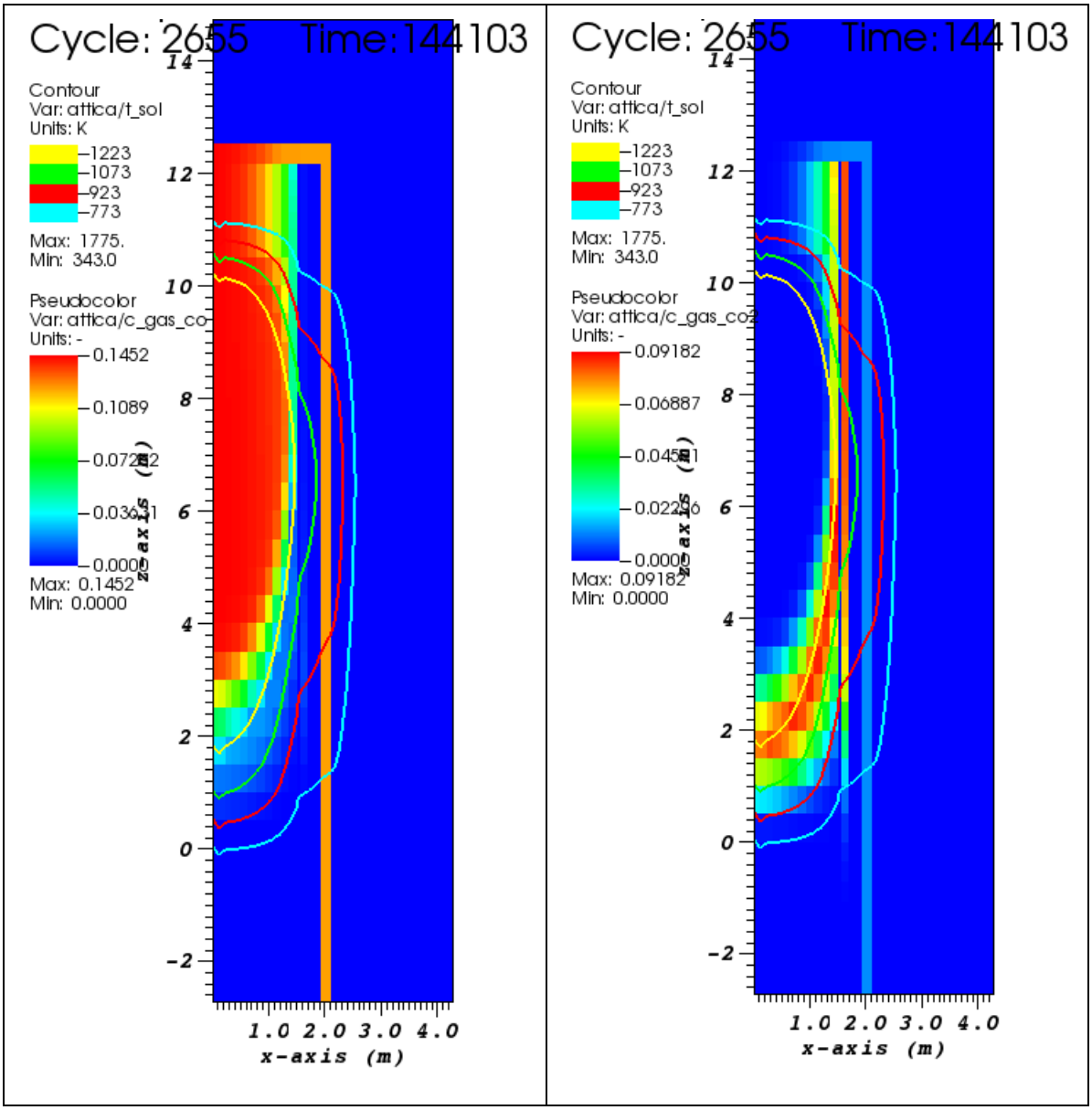

Figure 78: left CO distribution with solid temperature isolines; right CO_2 distribution and solid temperature isolines at t = 144,103 sec

After 365,000 seconds (~ 100 hours), there is two clearly distinguishable burn-off locations; a lower one where most of the CO_2 is formed, and a second one within the core which follows the 1223 K solid temperature isoline, see Figure 79. This second burn-off front is due to Boudouard reaction.

After the end of the transient the maximum burn-off is only 1.9 %. This burn-off value is in the lower core region. Like mentioned in the water ingress transient simulation, the graphite corrosion can reach the coated particles after 7 % burn-off assuming a shape factor of 6 as done in [25].

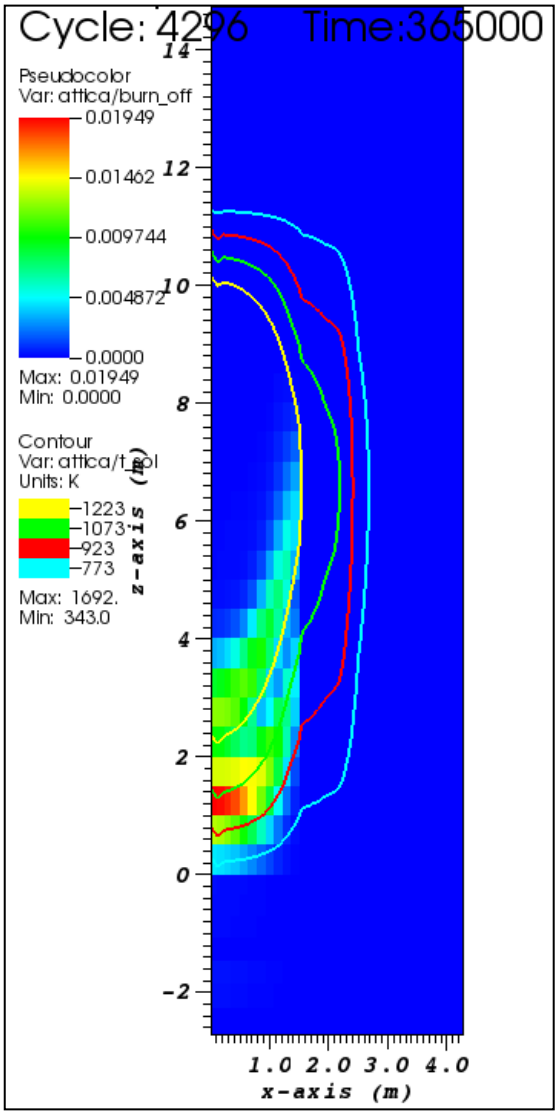

Figure 79: Graphite burn-off and temperature isolines at the end of the air ingress transient (365,000 seconds ~ 100 hours)